

EXPERIMENTAL INVESTIGATION OF MORPHING WING  
AERODYNAMICS BY FORCE MEASUREMENTS AND PARTICLE IMAGE  
VELOCIMETRY

A THESIS SUBMITTED TO  
THE GRADUATE SCHOOL OF NATURAL AND APPLIED SCIENCES  
OF  
MIDDLE EAST TECHNICAL UNIVERSITY

BY

ÖZGE SİNEM ÖZÇAKMAK

IN PARTIAL FULLFILLMENT OF THE REQUIREMENTS  
FOR  
THE DEGREE OF MASTER OF SCIENCE  
IN  
AEROSPACE ENGINEERING

NOVEMBER 2015



Approval of the thesis:

**EXPERIMENTAL INVESTIGATION OF MORPHING WING  
AERODYNAMICS BY FORCE MEASUREMENTS AND PARTICLE  
IMAGE VELOCIMETRY**

submitted by **ÖZGE SİNEM ÖZÇAKMAK** in partial fulfillment of the requirements for the degree of **Master of Science in Aerospace Engineering Department, Middle East Technical University** by,

Prof. Dr. Gülbin Dural Ünver  
Dean, Graduate School of **Natural and Applied Sciences** \_\_\_\_\_

Prof. Dr. Ozan Tekinalp  
Head of Department, **Aerospace Engineering** \_\_\_\_\_

Prof. Dr. Serkan Özgen  
Supervisor, **Aerospace Engineering Dept., METU** \_\_\_\_\_

**Examining Committee Members**

Prof. Dr. Nafiz Alemdaroğlu  
Dept. of Airframe and Powerplant Maintenance, Atılım Univ. \_\_\_\_\_

Prof. Dr. Serkan Özgen  
Aerospace Engineering Department, METU \_\_\_\_\_

Assoc. Prof. Dr. Oğuz Uzol  
Aerospace Engineering Department, METU \_\_\_\_\_

Assoc. Prof. Dr. Kürşad Melih Güleren  
Aeronautical Engineering Department, UTAA \_\_\_\_\_

Asst. Prof. Dr. Tuncay Yalçinkaya  
Aerospace Engineering Department, METU \_\_\_\_\_

**Date: 11.11.2015**

**I hereby declare that all information in this document has been obtained and presented in accordance with academic rules and ethical conduct. I also declare that, as required by these rules and conduct, I have fully cited and referenced all material and results that are not original to this work.**

Name, Last name : Özge Sinem Özçakmak

Signature :

## **ABSTRACT**

### **EXPERIMENTAL INVESTIGATION OF MORPHING WING AERODYNAMICS BY FORCE MEASUREMENTS AND PARTICLE IMAGE VELOCIMETRY**

Özçakmak, Özge Sinem

M.S., Department of Aerospace Engineering

Supervisor: Prof. Dr. D. Serkan Özgen

November 2015, 192 pages

Recently, new developments in on manufacturing technologies, aircraft materials, sensors, actuators, and other mechanisms raised the interest in morphing wings. Instead of conventional wings, which are optimized only for one flight condition, morphing wings can adapt themselves for different missions, mission segments and associated flight conditions.

The focus of this thesis is the experimental analysis of a morphing wing, the planform and airfoil shapes that were made available from a separate numerical study. Four half wing models, one of which is the base model, are manufactured separately and load cell measurements are performed in order to obtain the lift and drag values of these wings for seven velocity and twenty angle of attack values. The physical behavior of the flow is analyzed by performing oil flow visualization technique for one of the models and compared with the load cell experiments. According to the load cell measurements in level flight, for a fixed value of lift, the angle of attack and the drag trends of the wings are analyzed. Then, at these velocities and angle of attack values, particle image velocimetry (PIV) experiments are performed. Laser plane is placed perpendicular to the free stream velocity at the downstream of the wing in

order to analyze the wing tip vortices. The wing tip vortices of the four half wing models are recorded at two different downstream locations from the wing tip. Vector maps, velocity magnitude, vorticity, turbulence kinetic energy, Reynolds stress component and vortex core radii are analyzed.

The aim of this study is to validate the numerical results in a separate study with load cell and PIV measurements of a morphing wing. By this approach it is shown that, for level flight, the three morphing wing shapes are optimized from the base wing properly for the particular velocities they are designed for.

Keywords: Morphing Wing, Load Cell Measurements, Particle Image Velocimetry, Tip Vortex, Lift and Drag Measurements, Oil Flow Visualization, Experimental Aerodynamics, Experimentation for Numerical Validation

## ÖZ

# ŞEKİL DEĞİŞTİREBİLEN KANAT AERODİNAMİĞİNİN KUVVET ÖLÇÜMLERİ VE PARÇACIK GÖRÜNTÜLEME TEKNİĞİ İLE DENEYSEL OLARAK İNCELENMESİ

Özçakmak, Özge Sinem

Yüksek Lisans, Havacılık ve Uzay Mühendisliği Bölümü

Tez Yöneticisi: Prof. Dr. Serkan Özgen

Kasım 2015, 192 sayfa

Günümüzde üretim teknolojileri, havacılık malzemeleri, algılayıcılar, eyleyiciler ve diğer mekanizmalardaki yeni gelişmeler şekil değiştirebilen kanatlara olan ilgiyi arttırmıştır. Konvansiyonel kanat yapıları sadece tek bir uçuş durumu için tasarlanmışken, şekil değiştirebilen kanatlar farklı görev, görev bölümleri ve farklı uçuş koşullarına uyum sağlayabilmektedir.

Bu tezin odak noktasını daha önce yapılan sayısal bir çalışmadan elde edilmiş şekil değiştirebilen bir kanadın, kanat profili ve planformlarının, deneysel olarak analiz edilmesi oluşturmaktadır. Bir tanesi temel kanat olmak üzere, dört yarım kanat modeli üretilmiş, bu kanatlar ile yük hücreleri deneyleri gerçekleştirilmiş, yedi farklı hız ve yirmi farklı hücum açısı değerlerinde taşıma ve sürükleme kuvvetleri ölçülmüştür. Akışın fiziksel davranışı yağ akış görüntüleme tekniği ile modellerden biri için analiz edilmiş ve yük hücreleri deney sonuçları ile karşılaştırılmıştır. Yük hücreleri deneyleri sonuçlarına göre, düz uçuş koşullarında sabit bir taşıma kuvveti için sürükleme kuvveti ve hücum açısı eğrileri incelenmiştir. Daha sonra, bu hız ve hücum açıları parçacık görüntüleme tekniği deneyleri gerçekleştirilmiştir. Lazer düzlemi,

kanat uç girdaplarının incelenmesi amacıyla kanatların ařađı akım bölgesinde serbest akıř hızına dik olarak yerleřtirilmiřtir. Dört yarım kanat modelinin kanat uç girdapları, kanat ařađı akım bölgesinde, kanat ucundan iki farklı uzaklıkta ölçölmüřtür. Hız vektörleri, hız büyüklüđü, vortisite, türbölans kinetik enerji, Reynolds gerilme bileřeni ve girdap çekirdeđi yarıçapları analiz edilmiřtir.

Bu çalıřmanın amacı, daha önce gerçekteřirilmiş sayısal çalıřma sonuçlarının, řekil deđiřtirebilen kanatlarda yük hücresi ve parçacık görüntöleme tekniđi ölçümleri ile dođrulanmasıdır. Bu yöntemle, düz uçuř kořullarında temel bir kanattan eniyileřtirme yapılarak tasarlanmış řekil deđiřtirebilen üç kanat řeklinin optimize edildikleri hızlara uygun tasarlandıkları gösterilmiřtir.

Anahtar Kelimeler: řekil Deđiřtirebilen Kanat, Yük Hücresi Ölçümleri, Parçacık Görüntöleme Tekniđi, Kanat Uç Girdabı, Tařıma ve Sürökleme Kuvveti Ölçümleri, Yađ Akıř Görüntöleme Tekniđi, Deneysel Aerodinamik, Sayısal Dođrulama İçin Deneyleme



*To my grandmother Cemile*

*and*

*to freedom...*



## ACKNOWLEDGEMENTS

I would like to express my appreciation and gratitude to my advisor Prof. Dr. Serkan Özgen for his supervision during my research. His support for me to become a graduate research assistant and involving me in his project is invaluable for me.

I would like to thank to my jury members Prof. Dr. Serkan Özgen, Prof. Dr. Nafiz Alemdaroğlu, Assoc. Dr. Oğuz Uzol, Assoc. Dr. Kürşad Melih Güleren and Asst. Prof. Dr. Tuncay Yalçınkaya for reviewing my thesis and providing constructive suggestions.

I would like to thank to Assoc. Prof. Dr. Oğuz Uzol who is in the first place to make me choose this department to study and give his advices throughout the way. I would like to also thank him for his guidance and support during the PIV experiments.

I am profoundly grateful to Assoc. Prof. Dr. Demirkan Çöker to be always there to help, advice, cheer me up and provide any kind of logistics.

I would like to thank to Asst. Prof. Dr. Nilay Uzol who influenced me to be an aerospace engineer, to be an elder sister for me and even sometimes shape my destiny.

I would like to give special thanks to Burak for his support during my Bachelor years and influenced me to become a graduate research assistant by being a role model.

I would like to express my sincere gratitude to Hooman and Ezgi, our super PIV team! Sleepless nights spent together in the smell of olive oil and endless laser-smoke parties where we had the PIV madness and our ‘hangar keyfi’ breaks are unforgettable... It would be impossible to conduct the experiments alone without their support.

I would like to thank to Serkan Kaymak for his support in the load cell experiments, ability to operate a wind tunnel above its capabilities (velocity master!) and for the times we turned hangar into a dance floor or a stage together and for all the fun.

I would like to thank to Gökay Sedef for his invaluable support for the PIV software and the system. I would like to thank Anas, Derya and Yashar for their advice.

I would like to thank to Kenan for sharing all the good and bad times in the same room for three years, such a great roomie! I also want to thank Ufuk for checking my thesis progress even from abroad.

I would like to thank to my colleagues Harputlu, Emre & Tümüklü Reises, Özgür Y., Hazal, Pınar, Özcan, Oğuz, Arda and Yunus for the good times spent together.

I would like to thank to Alpay S. for making the coffee breaks joyful and Halil for waiting my thesis to end patiently to see me.

I would like to thank to Ufuk and Gülden, drama besties for their encouragement.

I would like to deeply thank to my high school teachers and at the same time my friends Kemal Ege, Halise, Rahime, Devrim, Nihat and many others I couldn't count here.

Heartfelt thanks go to my theatre group, Zeynep, Gülay, Barış, Ozan, Kubilay, Yasemin, Nazan, Deniz, Filiz, Ezgi, and Soner, for making the after work activities best!

I would like to especially thank to Yaso for his support and encouragement and belief in me. He never give up saying 'finish your thesis!' and cheer me up in the hardest times.

Lastly, but most importantly, I would like to express my endless thanks to my family, my relatives and especially my mother (and my teacher) Nahide for her love and eternal support throughout my life.

During the experimental works of this thesis, the facilities of RUZGEM were made available for me. I am grateful for this support.

This study was supported by The Scientific and Technological Research Council of Turkey (TÜBİTAK) with the project number 111M731. This support is gratefully acknowledged.

## TABLE OF CONTENTS

ABSTRACT .....	v
ÖZ .....	vii
ACKNOWLEDGEMENTS .....	xi
TABLE OF CONTENTS .....	xiii
LIST OF TABLES .....	xvi
LIST OF FIGURES.....	xvii
LIST OF SYMBOLS .....	xxv
CHAPTERS	
1 INTRODUCTION.....	1
1.1 Motivation .....	1
1.2 Literature Survey.....	1
1.2.1 Morphing Phenomenon .....	1
1.2.2 Applications of Morphing Wing .....	2
1.2.3 Experimentation for Numerical Validation.....	4
1.3 Objectives of the Study .....	8
2 WING MODELS AND MANUFACTURING.....	9
2.1 Wing Models Generation .....	9
2.2 Planforms of the Wing Models .....	11
2.2.1 Base Wing with NACA 4412 Airfoil Profile with Spline Method .	12
2.2.2 Optimized 14 Wing .....	13
2.2.3 Morphed 10 Wing .....	15
2.2.4 Morphed 16.5 Wing .....	16
2.3 Manufacturing.....	18
3 EXPERIMENTAL SET-UP AND MEASUREMENT TECHNIQUES .....	21
3.1 Introduction .....	21
3.2 METU Wind Tunnel .....	21
3.3 Load Cell Force Measurements .....	26

3.3.1	Experimental Methodology .....	26
3.3.2	Experimental Set-up .....	26
3.3.3	System Components .....	30
3.3.4	Power Unit.....	31
3.3.5	Load Cell Calibration .....	33
3.4	Error Analysis.....	34
3.4.1	Sources of Errors .....	35
3.5	Uncertainty Analysis .....	37
3.6	Surface Oil Flow Visualization Set-Up.....	41
3.7	Particle Image Velocimetry Experiments.....	42
3.7.1	Experimental Methodology .....	42
3.7.2	PIV Set-up and System Components .....	43
3.7.3	Wing Models and Laser Planes .....	48
3.7.4	Calibration .....	49
3.7.5	Image Quality .....	50
3.7.6	Analysis Parameters .....	51
3.7.7	PIV Processing .....	52
3.7.8	Image Visualization.....	52
4	EXPERIMENTAL RESULTS AND DISCUSSION.....	55
4.1	Introduction .....	55
4.2	Load Cell Experimental Results.....	55
4.2.1	Base Wing .....	58
4.2.2	Optimized 14 Wing .....	63
4.2.3	Morphed 10 Wing.....	73
4.2.4	Morphed 16.5 Wing.....	75
4.3	Comparison of the Experimental and Numerical Lift and Drag Curve Results of Load Cell Measurements.....	77
4.3.1	Comparison.....	77
4.3.2	Base Wing Results.....	78
4.3.3	Optimized Wing at 14 m/s.....	81

4.3.4 Morphed 10 Wing .....	83
4.3.5 Morphed 16.5 Wing .....	86
4.4 Drag Curve .....	88
4.5 Particle Image Velocimetry Experimental Results .....	90
4.5.1 Motivation .....	90
4.5.2 Results .....	91
4.5.3 Comparisons at 14 m/s Free Stream Velocity.....	92
4.6 Conclusion.....	111
5 CONCLUSION .....	113
REFERENCES.....	115
APPENDICES	
A COMPARISON AT 15 M/S .....	121
B VECTOR MAPS AND VELOCITY MAGNITUDE .....	135
C VORTICITY CONTOURS .....	143
D TURBULENCE KINETIC ENERGY CONTOURS.....	165
E REYNOLDS STRESS COMPONENT CONTOURS .....	187

## LIST OF TABLES

Table 2.1 Nomenclature for the Wing Models.....	11
Table 2.2 Base Wing Properties .....	12
Table 2.3 Optimized Wing Properties .....	13
Table 2.4 Properties of the 10 m/s Morphed Wing .....	15
Table 2.5 Properties of the Morphed 16.5 Wing .....	16
Table 2.6 Wing Manufacturing Properties .....	18
Table 3.1 METU Aerospace Engineering Dept. wind tunnel properties .....	21
Table 3.2 Sections of the METU Aerospace Engineering Dept. Wind Tunnel [25]	22
Table 3.3 ATI Gamma Load Cell metric calibrations.....	30
Table 3.4 Load Cell calibration.....	34
Table 3.5 Three Axis Force Statistics of the Noise in Load Cell.....	40
Table 3.6 Three Axis Torque Statistics of the Noise in Load Cell .....	40
Table 3.7 Random uncertainty of the mean in x and y direction forces.....	41
Table 4.1 Mean Aerodynamic Chords of the Wings.....	56
Table 4.2 Ambient Conditions and Flow Properties .....	57
Table 4.3 Reynolds Numbers .....	58
Table 4.4 List of the cases yielding 2.5 N Lift Force .....	89
Table 4.5 Angle of attack values at 14 m/s and 15m/s that create 2.5 N lift.....	92
Table 4.6 Vortex Core Radius.....	97
Table 4.7 Induced Drag of the Tip Vortices at 14 m/s .....	111



## LIST OF FIGURES

Figure 1.1 Various wing shapes of a seagull at different flight conditions [2].....	2
Figure 1.2 Local and Global Morphing [5].....	3
Figure 1.3 Blowing Type Wind Tunnel [8] .....	5
Figure 1.4 Drag vs freestream velocity [18] .....	7
Figure 2.1 Drag vs velocity curves of the Baseline Wing, Optimum Wing with planform and airfoil shape changes, Morphing wing with only airfoil shape change, Morphing wing with only planform change and Morphing Wing with both planform and airfoil shape change [23].....	9
Figure 2.2 Planforms of the four wing models .....	11
Figure 2.3 Base Wing airfoil profile .....	12
Figure 2.4 Base Wing top view .....	12
Figure 2.5 Isometric view of the Base Wing.....	13
Figure 2.6 Optimized 14 Wing airfoil profile .....	14
Figure 2.7 Optimized 14 Wing top view.....	14
Figure 2.8 Isometric view of the Optimized 14 Wing .....	14
Figure 2.9 Airfoil profile (side view) of Morphed 10 Wing .....	15
Figure 2.10 Top view of Morphed 10 Wing .....	15
Figure 2.11 Isometric view of Morphed 10 Wing.....	16
Figure 2.12 Side view of Morphed 16.5 Wing .....	17
Figure 2.13 Top view of the Morphed 16.5 Wing .....	17
Figure 2.14 Isometric view of the Morphed 16.5 Wing.....	17
Figure 2.15 Manufactured wings top view (from top to bottom: Base Wing, Optimized Wing at 14 m/s, Morphed Wing at 10 m/s, Morphed Wing at 16.5 m/s) .....	18
Figure 2.16 Manufactured wings side view from the root chord (from left to right: Base Wing, Optimized Wing at 14 m/s, Morphed Wing at 10 m/s, Morphed Wing at 16.5 m/s).....	19

Figure 2.17 Manufactured wings side view from the tip chord (from left to right: Base Wing, Optimized Wing at 14 m/s, Morphed Wing at 10 m/s, Morphed Wing at 16.5 m/s) .....	19
Figure 3.1 METU Aerospace Engineering Dept. low speed wind tunnel .....	23
Figure 3.2 Motor controller device.....	23
Figure 3.3 Dywer 471 Thermo-Anemometer .....	24
Figure 3.4 METU Aerospace Engineering Dept. wind tunnel freestream velocity vs frequency .....	24
Figure 3.5 (a) Axial velocity distribution, (b) turbulence intensity distribution, (c) total pressure distribution at the exit of the contraction section [25]. .....	25
Figure 3.6 Measurement and assessment procedure of load cell experiment .....	26
Figure 3.7 Angle of attack plates.....	27
Figure 3.8 The drawing of the angle of attack mechanism, load cell and the wing [27] .....	28
Figure 3.9 Angle of attack mechanism, load cell and the wing .....	28
Figure 3.10 Load cell measurements set-up .....	29
Figure 3.11 Schema of the acquisition and data process set-up .....	29
Figure 3.12 The drawing and the photo of the ATI Gamma load cell .....	30
Figure 3.13 Power unit and amplifier.....	31
Figure 3.14 Data Acquisition System.....	31
Figure 3.15 NI 9205 Module .....	32
Figure 3.16 LabVIEW interface .....	33
Figure 3.17 Load Cell x-axis force (drag) bias .....	38
Figure 3.18 Load Cell y-axis force (lift) bias .....	38
Figure 3.19 Oil Visualization Set-Up.....	41
Figure 3.20 Measurement chain of the PIV experiments .....	42
Figure 3.21 PIV Set-Up.....	43
Figure 3.22 PIV Set-Up Schema (Top View) .....	44
Figure 3.23 Camera Protection.....	45
Figure 3.24 Distance Measurement Device .....	46

Figure 3.25 Litron laser.....	46
Figure 3.26 Phantom CCD Camera .....	47
Figure 3.27 Fog Generator .....	47
Figure 3.28 Painting Process of the Half Wing Models.....	48
Figure 3.29 Laser Sheet Plane Lines.....	49
Figure 3.30 Laser Sheet Plane at the Downstream of the Wing Model.....	49
Figure 3.31 Calibration of the images.....	50
Figure 3.32 Particle Density.....	50
Figure 3.33 Correlation Peak .....	51
Figure 3.34 Wing and wing tip vortex in the tunnel test section .....	53
Figure 3.35 Wing tip vortices of optimized 14 wing at 2C location.....	53
Figure 4.1 Base Wing in Wind Tunnel .....	58
Figure 4.2 Lift (N) vs AOA (degrees) curves of the Base Wing .....	59
Figure 4.3 Drag (N) vs AOA (degrees) curves of the Base Wing .....	60
Figure 4.4 Numerical Stream function (left) and vorticity contours (right) for AG24 airfoil (Re=60000) [44] .....	61
Figure 4.5 Lift curve of AG24 airfoil at Re=60000 [43] .....	61
Figure 4.6 Separation Bubble Formation [46] .....	62
Figure 4.7 Laminar Separation Bubble [47] .....	63
Figure 4.8 Optimized 14 Wing in the wind tunnel.....	63
Figure 4.9 Lift vs AOA curves of Optimized 14 Wing.....	65
Figure 4.10 Drag vs AOA curves of Optimized 14 Wing.....	65
Figure 4.11 Laminar separation bubble at low Reynolds number [45].....	66
Figure 4.12 Classification of lift curves .....	66
Figure 4.13 Oil flow Visualizations of the upper surface of Optimized 14 Wing at 14 m/s .....	68
Figure 4.14 Attachment and separation locations of Optimized 14 Wing at 5 AOA .....	69
Figure 4.15 Oil accumulation lines of Optimized 14 Wing at 11 AOA .....	69

Figure 4.16 Oil flow accumulation and PIV of a wing at AOA=10 degrees, Re=64000 [49].....	70
Figure 4.17 Oil flow Visualizations of the upper surface of Optimized 14 Wing at 15 m/s .....	71
Figure 4.18 E423 Airfoil at Re=1.2x10 <sup>5</sup> at 0 degree AOA (at left) and 12 degrees AOA (at right) [50].....	72
Figure 4.19 Lift and drag values of Optimized 14 Wing at 15 m/s.....	72
Figure 4.20 Morphed 10 Wing in the tunnel .....	73
Figure 4.21 Lift vs AOA curves of Morphed 10 Wing .....	74
Figure 4.22 Drag vs AOA curves of Morphed 10 Wing .....	74
Figure 4.23 Morphed 16.5 Wing in the tunnel .....	75
Figure 4.24 Lift vs AOA curves of Morphed 16.5 Wing .....	76
Figure 4.25 Drag vs AOA curves of Morphed 16.5 Wing.....	76
Figure 4.26 Lift curve of AG24 airfoil at Re=6000 with 0.18% free stream turbulence [35].....	77
Figure 4.27 Figure 4.28 Lift vs AOA (left) and Drag vs AOA (right) curves of Base Wing at 10 m/s.....	79
Figure 4.29 Lift vs AOA (left) and Drag vs AOA (right) curves of Base Wing at 12 m/s .....	79
Figure 4.30 Lift vs AOA (left) and Drag vs AOA (right) curves of Base Wing at 13 m/s .....	80
Figure 4.31 Lift vs AOA (left) and Drag vs AOA (right) curves of Base Wing at 14 m/s .....	80
Figure 4.32 Lift vs AOA (left) and Drag vs AOA (right) curves of Base Wing at 15 m/s .....	80
Figure 4.33 Lift vs AOA (left) and Drag vs AOA (right) curves of Base Wing at 16.5 m/s .....	81
Figure 4.34 Lift vs AOA (left) and Drag vs AOA (right) curves of Optimized 14 Wing at 10 m/s.....	81

Figure 4.35 Lift vs AOA (left) and Drag vs AOA (right) curves of Optimized 14 Wing at 11 m/s .....	82
Figure 4.36 Lift vs AOA (left) and Drag vs AOA (right) curves of Optimized 14 Wing at 12 m/s .....	82
Figure 4.37 Lift vs AOA (left) and Drag vs AOA (right) curves of Optimized 14 Wing at 13 m/s .....	82
Figure 4.38 Lift vs AOA (left) and Drag vs AOA (right) curves of Optimized 14 Wing at 14 m/s .....	83
Figure 4.39 Lift vs AOA (left) and Drag vs AOA (right) curves of Optimized 14 Wing at 15 m/s .....	83
Figure 4.40 Lift vs AOA (left) and Drag vs AOA (right) curves of Optimized 14 Wing at 16.5 m/s .....	83
Figure 4.41 Lift vs AOA (left) and Drag vs AOA (right) curves of the Morphed 10 Wing at 10 m/s .....	84
Figure 4.42 Lift vs AOA (left) and Drag vs AOA (right) Drag Force curves of the Morphed 10 Wing at 11 m/s.....	84
Figure 4.43 Lift vs AOA (left) and Drag vs AOA (right) Drag Force curves of the Morphed 10 Wing at 12 m/s.....	84
Figure 4.44 Lift vs AOA (left) and Drag vs AOA (right) Drag Force curves of the Morphed 10 Wing at 13 m/s.....	85
Figure 4.45 Lift vs AOA (left) and Drag vs AOA (right) Drag Force curves of the Morphed 10 Wing at 14 m/s.....	85
Figure 4.46 Lift vs AOA (left) and Drag vs AOA (right) Drag Force curves of the Morphed 10 Wing at 15 m/s.....	85
Figure 4.47 Lift vs AOA (left) and Drag vs AOA (right) Drag Force curves of the Morphed 10 Wing at 16.5 m/s.....	86
Figure 4.48 Lift vs AOA (left) and Drag vs AOA (right) Drag Force curves of the Morphed 16.5 Wing at 10 m/s.....	86
Figure 4.49 Lift vs AOA (left) and Drag vs AOA (right) Drag Force curves of the Morphed 16.5 Wing at 11 m/s.....	87

Figure 4.50 Lift vs AOA (left) and Drag vs AOA (right) Drag Force curves of the Morphed 16.5 Wing at 12 m/s .....	87
Figure 4.51 Lift vs AOA (left) and Drag vs AOA (right) Drag Force curves of the Morphed 16.5 Wing at 13 m/s .....	87
Figure 4.52 Lift vs AOA (left) and Drag vs AOA (right) Drag Force curves of the Morphed 16.5 Wing at 14 m/s .....	88
Figure 4.53 Lift vs AOA (left) and Drag vs AOA (right) Drag Force curves of the Morphed 16.5 Wing at 15 m/s .....	88
Figure 4.54 Lift vs AOA (left) and Drag vs AOA (right) Drag Force curves of the Morphed 16.5 Wing at 16.5 m/s .....	88
Figure 4.55 Drag Curve of the Morphing Wing.....	90
Figure 4.56 Steady level flight force balance [18] .....	90
Figure 4.57 Vortex Velocity Profile .....	93
Figure 4.58 Velocity Magnitude Contours on one mean chord downstream plane at 14 m/s; Base Wing (Top Left), Optimized 14 Wing (Top Right), Morphed 10 Wing (Bottom Left) and Morphed 16.5 Wing (Bottom Right). Note that all cases are at different angles of attack as given in Table 4.5 but all producing the same 2.5 N lift force .....	94
Figure 4.59 Velocity Magnitude Contours on two mean chord downstream plane at 14 m/s; Base Wing (Top Left), Optimized 14 Wing (Top Right), Morphed 10 Wing (Bottom Left) and Morphed 16.5 Wing (Bottom Right). Note that all cases are at different angles of attack as given in Table 4.5 but all producing the same 2.5 N lift force .....	95
Figure 4.60 Velocity Magnitude at 14 m/s on one chord downstream plane.....	96
Figure 4.61 Velocity Magnitude at 14 m/s on two chord downstream plane .....	97
Figure 4.62 Vorticity Contours on one mean chord downstream plane at 14 m/s; Base Wing (Top Left), Optimized 14 Wing (Top Right), Morphed 10 Wing (Bottom Left) and Morphed 16.5 Wing (Bottom Right). Note that all cases are at different angles of attack as given in Table 4.5 but all producing the same 2.5 N lift force .....	99

Figure 4.63 Vorticity Contours on two mean chord downstream plane at 14 m/s; Base Wing (Top Left), Optimized 14 Wing (Top Right), Morphed 10 Wing (Bottom Left) and Morphed 16.5 Wing (Bottom Right). Note that all cases are at different angles of attack as given in Table 4.5 but all producing the same 2.5 N lift force .....	100
Figure 4.64 Mean out of Plane Vorticity along the Vortex on one mean chord downstream plane at 14 m/s .....	101
Figure 4.65 Mean out of Plane Vorticity along y direction on two mean chord downstream plane 2C Location at 14 m/s .....	101
Figure 4.66 In-Plane Turbulence Kinetic Energy Contours on one mean chord downstream plane at 14 m/s; Base Wing (Top Left), Optimized 14 Wing (Top Right), Morphed 10 Wing (Bottom Left) and Morphed 16.5 Wing (Bottom Right). Note that all cases are at different angles of attack as given in Table 4.5 but all producing the same 2.5 N lift force .....	104
Figure 4.67 In-Plane Turbulence Kinetic Energy Contours on two mean chord downstream plane at 14 m/s; Base Wing (Top Left), Optimized 14 Wing (Top Right), Morphed 10 Wing (Bottom Left) and Morphed 16.5 Wing (Bottom Right). Note that all cases are at different angles of attack as given in Table 4.5 but all producing the same 2.5 N lift force .....	105
Figure 4.68 In Plane Turbulence Kinetic Energy along y direction at 14 m/s on one mean chord downstream plane .....	106
Figure 4.69 Turbulence Kinetic Energy along y direction at 14 m/s on two mean chords downstream plane .....	106
Figure 4.70 $u'v'$ Contours on one mean chord downstream plane at 14 m/s; Base Wing (Top Left), Optimized 14 Wing (Top Right), Morphed 10 Wing (Bottom Left) and Morphed 16.5 Wing (Bottom Right). Note that all cases are at different angles of attack as given in Table 4.5 but all producing the same 2.5 N lift force .....	109
Figure 4.71 $u'v'$ Contours on two mean chord downstream plane at 14 m/s; Base Wing (Top Left), Optimized 14 Wing (Top Right), Morphed 10 Wing (Bottom	

Left) and Morphed 16.5 Wing (Bottom Right). Note that all cases are at different angles of attack as given in Table 4.5 but all producing the same 2.5 N lift force ..... 110



## LIST OF SYMBOLS

$Re$		Reynolds Number
$\rho_{\infty}$	$kg/m^3$	Density of the free stream
$\mu_{\infty}$	$kg/ms$	Free stream dynamic viscosity
$F_x$	N	Force in x direction
$F_y$	N	Force in y direction
$F_z$	N	Force in z direction
$T_x$	Nm	Torque in x direction
$T_y$	Nm	Torque in y direction
$T_z$	Nm	Torque in z direction
$\epsilon_{absolute}$		Absolute error
$\sigma$		Standard deviation
$x_i$		Instantaneous quantity
$\bar{x}$		Mean quantity
$\sigma_m$		Mean standard deviation
$N$		Number of samples
$f_s$	Hz	Samples per second
$K$		Coverage factor
$U$		Random uncertainty
$l$	M	Characteristic length
$\bar{c}$	M	Mean aerodynamic chord
$\lambda$		Taper ratio
$Re_x$		Local Reynolds number

$c_t$	m	Tip chord
$c_r$	m	Root chord
$T_0$	°R	Reference temperature
$T$	°R	Temperature
$\mu_0$	cP	Reference dynamic viscosity
$C$	°K	Sutherland's constant
$L$	N	Lift
$D$	N	Drag
$T$	N	Thrust
$W$	N	Weight
$V$	m/s	Velocity
$P$	Pascal	Pressure
$\omega$	1/s	Vorticity
$\omega_z$	1/s	Out-of-plane vorticity
$\nu$	m <sup>2</sup> /s	Kinematic viscosity
$u, v, w$	m/s	Velocities in x, y, z directions respectively
$u', v', w'$	m/s	Velocity fluctuations in x, y, z directions respectively
$y_c$	m/s	Tip vortex center
$K$	(m/s) <sup>2</sup>	Turbulence kinetic energy
$k_{ip}$	(m/s) <sup>2</sup>	In-plane Turbulence kinetic energy
$\tau_{ij,turbulent}$	(m/s) <sup>2</sup>	Reynolds Stress tensor
$\tau_{ij,turbulent,ip}$	(m/s) <sup>2</sup>	In-Plane Reynolds Stress tensor

# CHAPTER 1

## INTRODUCTION

### 1.1 Motivation

Inspired by the birds, mankind tried various ways of flying throughout the history. However, the lack of advanced technology did not allow to fully simulate flight of the birds. This led to fixed wing configurations designed for only one or two missions and compromising all the others. During the mission, there are also several mission segments such as take-off, climb, cruise, loiter, descent and landing to be considered during the design of the aircraft. Conventional fixed wing configurations are optimized for only one of these segments and compromise other mission segments.

Recently, new developments in manufacturing technologies, aircraft materials, sensors, actuators and other mechanisms raised the interest in morphing wings. With the development of the morphing wings, optimized wing shapes can be used during the flight for each mission or mission segment. With the development of technology, morphing wing mechanisms such as stretching and sliding skins, telescopic systems, chord expansion mechanisms, shape memory alloys, sweep changes, span extension, airfoil changing mechanisms, etc. have been studied by many researchers and the industry.

### 1.2 Literature Survey

#### 1.2.1 Morphing Phenomenon

In nature, flying animals adjust their wings for different missions at different flight conditions. With their flexible morphology, they can change their wing shapes through movement of joints and overlapping feathers without compromising the efficient aerodynamic shape [1]. Figure 1.1 shows the wing shapes of a seagull at various flight conditions.



Figure 1.1 Various wing shapes of a seagull at different flight conditions [2]

Getting inspiration from the nature, morphing wing concept is implemented for the flying vehicles, most commonly to the unmanned aerial vehicles (UAVs) because of their reduced scale and lower risk to human life.

Increasing role of the unmanned aerial vehicles in military and civil applications, where the morphing wing technologies are mostly applied has resulted in a growing interest in low Reynolds number aerodynamics.

Micro aerial vehicle designers and model aircraft builders have great interest on the range  $30000 \leq Re \leq 70000$ . In this range, airfoil choice is very important since thick airfoils ( $\geq 6\%$  or above) can cause late transition to turbulent flow because of laminar separation [3]. Most airfoils with a Reynolds number higher than 50000, laminar separation bubbles occur resulting in a rapid drop in performance, in other words, reduction in lift to drag ratio. Therefore, an efficient design at low Reynolds number wings is crucial.

### 1.2.2 Applications of Morphing Wing

Shape morphing is the change of shape of the wings during the flight to adapt to particular type of missions. Therefore, morphing wing aircraft can perform multiple missions and perform multiple maneuvers with improved fuel efficiency and reduced drag [4]. There are two types of morphing, namely local and global. Local morphing is the airfoil change such as camber and thickness, whereas global morphing is the

change along the wing span [5]. Examples to global and local morphing mechanisms are shown in Figure 1.2.

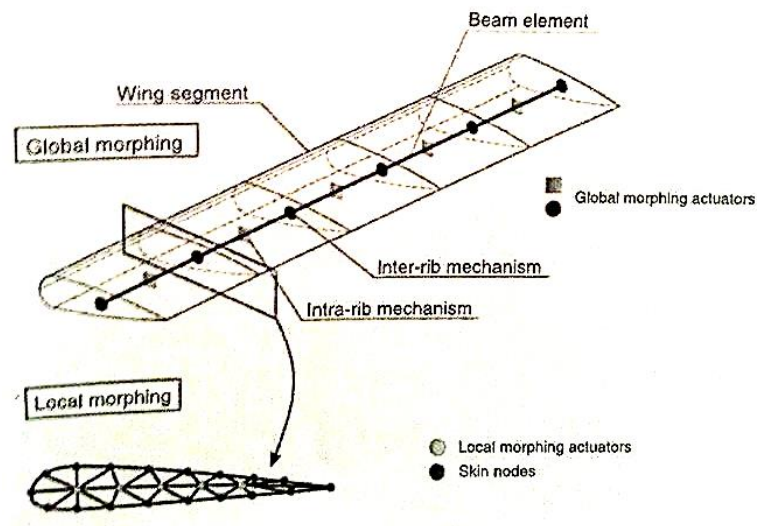


Figure 1.2 Local and Global Morphing [5]

There is wide range of implementations of morphing wings such as planform change, sweep change, twist change, taper change, area change, folding wing arrangements, wing extensions (symmetrical or asymmetrical), etc. Moreover, differential span change between wingtips can generate a roll moment by replacing the ailerons of aircraft. Buckle wing morphing is another approach. There is a single thick wing composed of two thin wings fused together. While flying it looks like a normal wing but when both wings are on, the wing morphs into biplane configuration and generates maximum lift and becomes more agile. Another morphing wing application is the variform wing. In order to maximize the lift to drag ratio, wing changes its shape as fuel is consumed. By this way range of the aircraft increases with less fuel consumption. Furthermore, inflatable wing morphing is another method. This wing can inflate and deflate and can change the shape of its tips [4]. Most of the morphing wing applications mentioned in this section requires a good and efficient structural design to provide the shape changes.

By the morphing mechanisms, the performance of the aircraft increases by increasing its flight range. Moreover, the heavy and complex conventional control surfaces and

high lift devices for flight control are replaced. Performance and stealth capability of the aircraft improves. Drag, vibration and control flutter are also reduced.

In order to improve morphing wings, development of the design and optimization strategies are needed that does not compromise the design space [5] [6]. By developing a morphing wing optimization computational tool, the shape optimization and conceptual design of the morphing wings can be performed more properly. Moreover, validating these codes by experiments can contribute to this research area extensively.

### **1.2.3 Experimentation for Numerical Validation**

Experimentation is very significant in order to have reliable numerical tools for the design of the morphing wings. Moreover, unmanned aerial vehicles, because of their reduced scale, operates in low Reynolds number range. In this study, Reynolds number values are between 30000 and 90000. Thus, experimentation in this range can provide guidance to low speed aerodynamics designs. Low speed wind tunnel selection for the experiments is important to analyze these designs more properly. For the aerodynamic performance analysis, balance systems are widely used since they can provide aerodynamic force and moment data of the wings. Moreover, Particle Image Velocimetry, a non-intrusive technique, is a reliable experimental method in order to analyze the flow structures comprising turbulence characteristics, mean velocity and vorticity properties in the near field.

#### **1.2.3.1 Wind Tunnels**

Low speed wind tunnels are the tunnels, where the velocity is lower than about 100 m/s. Moreover, compressibility effects caused by the pressure can be neglected [7]. There are two types of open circuit wind tunnels, namely suction and blowing types.

Suction wind tunnels are cost efficient and take a small place in laboratories, whereas it is free of disturbances caused by an upstream fan due to external obstructions and recirculation in the laboratories [7].

The fan of the blowing type wind tunnels is arranged upstream of the test section. This improves the flow control compared with the suction type wind tunnels [7]. Thus,

blowing type wind tunnel is chosen for the experiments. An illustration of a blowing type wind tunnel is shown in Figure 1.3.

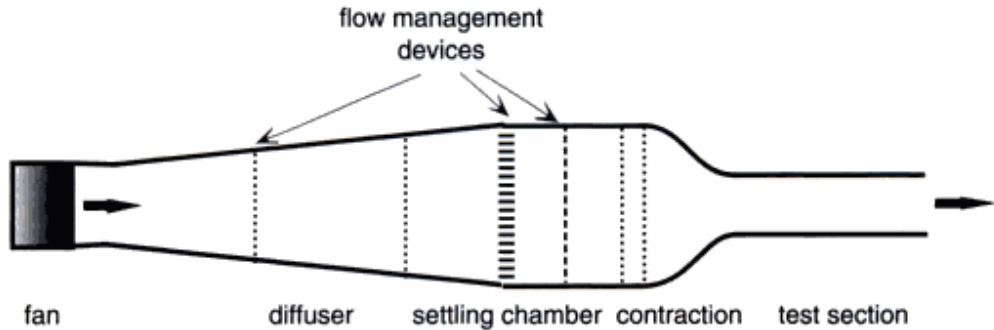


Figure 1.3 Blowing Type Wind Tunnel [8]

### 1.2.3.2 Balance Systems

A model which is connected to balance system is subjected to forces and moments in the wind tunnel. These forces and moments create elastic deformations which are measured by strain gauges on the balance system.

Balance systems are classified according to the location they are placed and the number of force/moment components that they simultaneously measure. If the balance system is placed inside the model it is called as an internal balance. On the contrary, if the balance system is placed outside the model or the wind tunnel, then it is named as an external balance [9].

External balances which are used in this study are divided into two types. First type consists of single force transducers connected to a framework and the second type is a one piece external balance equipped with strain gauges. External balances give possibility to change the model wings easily providing high flexibility to the experiments. Moreover the ones that are at the outside of the wind tunnel do not influence the fluid flow. Thus, in this study external balance is used for analyzing four wing models.

Balance systems are one of the most efficient methods to precisely measure forces and moments in three dimensions with high accuracy and reliable hardware and software components [10] [11]. Therefore, balance systems, pressure systems or their

combination are the most widely used aerodynamic measurement techniques for airfoils [12] [3]. The most flexible ones among all the balance systems are the six component external balances in terms of usability [13]. Consequently, a six component load cell is used in this study.

### **1.2.3.3 Surface Oil Flow Visualization**

In low Reynolds regime, one of the most important flow behaviors is the formation of laminar separation bubbles due to adverse pressure gradients. Laminar separation bubbles are formed on the upper surface of the airfoils especially at high angles of attack [14]. The presence of laminar separation bubbles and laminar separation regimes directly effects the lift and drag data. In order to validate this lift and drag data and understand the underlying physics of the flow behavior, flow visualizations are performed.

There are a lot of flow visualization techniques in application. In this study, surface oil visualization is taken into consideration because it is an effective, fast method and it enables to see separation and reattachment points of the flow on the surface. The main principle of this technique is to apply pigmented oil to the airfoil surface and running the tunnel at the desired Reynolds number [14]. By this way, oil accumulates on the surface showing the flow patterns.

### **1.2.3.4 Particle Image Velocimetry (PIV)**

Particle Image Velocimetry is a whole flow field, non-intrusive measurement technique. It allows recording of a complete velocity field in a plane selected within microseconds. It can measure instantaneous flow fields. Moreover, Particle Image Velocimetry has a superiority over other measurement techniques in providing information about unsteady flow fields [15]. On the other hand, conventional methods, such as Hot Wire Anemometry and Laser Doppler Velocimetry, are single point measurements and only turbulence statistics can be obtained from them. They need a traversing of the flow domain. Furthermore, in fixed probe measurements of the velocity, if there is a meandering of the vortices, then the measured velocity is not reliable at distances more than one chord downstream of the wing [15]. They fail to detect the maximum tangential and axial velocities in the core correctly [16].



PIV is a very useful experimental technique in order to understand the flow behavior and mean and turbulent characteristics. Since it is a non-intrusive technique, it does not disturb the flow field and is suitable for conducting experiments in the near flow field.

The balance system data of lift, drag and moment can be compared and validated by the PIV data. Keeping lift constant, equal to weight of the aircraft, in level flight, drag forces can be examined and compared with the PIV data. In order to make a decision on the field of interest for the PIV experiments, low speed aerodynamics behavior of the flow should be considered.

Drag force is composed of parasite drag and the induced drag. Parasite drag is composed of skin friction drag and pressure drag, which is a result of boundary layer separation. For low Reynolds number wings, drag due to lift, in other words, induced drag is greater in magnitude than parasite drag. Figure 1.3 illustrates this phenomena. In this study, due to low speed, induced drag is expected to be much higher than parasite drag and almost equal to the total drag so that the minimization of drag is focused on the induced drag [17].

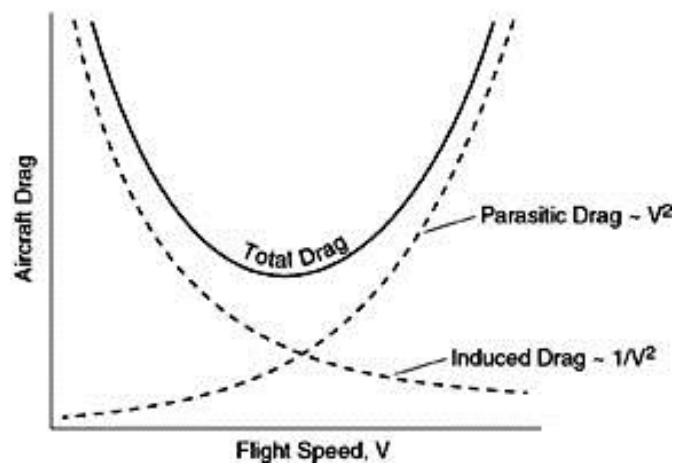


Figure 1.4 Drag vs freestream velocity [18]

Induced drag is also known as the vortex drag [19]. This is because, the wing produces lift by the pressure difference on upper and lower surfaces. The higher pressure on the lower surface of the wing tends to accelerate around the wing tip towards the upper

surface where low pressure exists, so that a wing tip vortex is generated, which in turn leads the production of the induced drag [20]. Wingtip vortices are the main source of the induced drag so that the weakest tip vortices yield the minimum induced drag.

Thus, the near field behavior of the tip vortices is significant in wing aerodynamics [21]. Particle Image Velocimetry can be used to analyze the vector maps, velocity magnitudes, vorticity, turbulence kinetic energy and Reynolds stress components of the tip vortices. In order to analyse the tip vortices, PIV measurement technique is selected for this study.

### **1.3 Objectives of the Study**

By the morphing wing concept, aircraft can perform multiple missions and maneuvers without complex and heavy control surfaces and devices. Moreover, developing morphing wing mechanisms such as improved health monitoring, structural enhancements, noise reduction and flow separation can improve the aircraft performance. By these improvements, damage tolerance, safety improvement, noise control, environmental compatibility, drag reduction, take-off and landing systems with lighter and simpler mechanisms, flutter and gust reduction can also be achieved [22]. Thus, the aim is to reduce this complexity, supply a smoother flow around the wing, increasing lift and decreasing drag, reducing the empty weight so that the payload capacity is increased, reducing the cost and fuel consumption with better performance by the morphing wing concept.

In this study, morphing wing concept is analyzed using two different experimental methods, namely load cell aerodynamic force measurements and particle image velocimetry (PIV) tip vortex measurements. By this way, the numerical tool can be validated and data, which are much closer to the real flight conditions can be obtained. Therefore, with the improving morphing technology, the results of this study can be a guide to implement these designs to real applications.

## CHAPTER 2

### WING MODELS AND MANUFACTURING

#### 2.1 Wing Models Generation

In a previous study of Körpe [23], the developed FORTRAN code with boundary layer modeling and optimization solver is used in order to obtain morphing wing shapes.

In the study of Körpe, drag values of the morphing wings are compared for only airfoil shape change and only planform change, where it is seen that the planform change has a significant role in drag reduction. When the planform is changed, the angle of attack and the lift coefficient required for obtaining the desired lift is less, reducing the induced drag significantly. On the other hand, this effect is less significant when only the airfoil shape changes because the variations in camber and thickness are limited for this shape change [23]. The effect of only planform change, only airfoil change and combination of them on wing total drag is presented in Figure 2.1.

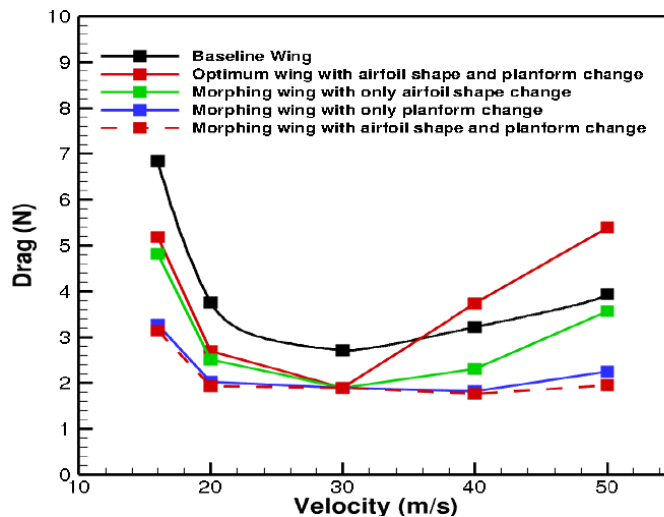


Figure 2.1 Drag vs velocity curves of the Baseline Wing, Optimum Wing with planform and airfoil shape changes, Morphing wing with only airfoil shape change, Morphing wing with only planform change and Morphing Wing with both planform and airfoil shape change [23]

Planform morphing alone supplies the major aerodynamic performance improvement and airfoil morphing improves this performance slightly further. Therefore, both the planform change and the airfoil shape change is applied in order to obtain resultant morphing wing shapes. Following the decision of changing both the airfoil shape and planform of the wings in the morphing process, the calculations are performed for level flight.

The Baseline wing is selected to have NACA 4412 airfoil profile and the span and chord values are selected accounting for the dimensions of the wind tunnel for the experimental studies. In the level flight, by fixing the lift value, starting from the baseline wing, fixed wing optimization is performed by changing both the airfoil shape and the planform at 14 m/s free stream velocity. The Optimized Wing at 14 m/s is used as the initial wing for morphing wing optimizations. After various allowances for the airfoil physical thickness change of the optimized wing are tried, 10% allowance is selected for the morphing wing optimization due to its efficiency in terms of drag reduction performance and energy demand for morphing mechanisms. Applying this allowance, the morphing wing shapes are obtained at 10 m/s and 16.5 m/s free stream velocities

Therefore, according to the numerical results of the previous study, Base Wing, Optimized Wing at 14 m/s and Morphed Wings which are optimized at 10 m/s and 16.5 m/s are obtained. During a level flight, the wing optimized for the flight conditions of 14 m/s free stream velocity change its shape by the morphing mechanism at 10 m/s and 16.5 m/s free stream velocities.

The Nomenclature for these four wings are introduced in Table 2.1 in order to prevent confusion for the oncoming sections.

Table 2.1 Nomenclature for the Wing Models

<i>Wing</i>	<i>Nomenclature</i>
Baseline Wing with NACA 4412 Airfoil Profile	Base Wing
Optimized Wing at 14 m/s free stream velocity	Optimized 14 Wing
Morphing Wing (Optimized for 10 m/s free stream velocity)	Morphed 10 Wing
Morphing Wing (Optimized for 16.5 m/s free stream velocity)	Morphed 16.5 Wing

## 2.2 Planforms of the Wing Models

The top views of the four half wing models are illustrated in Figure 2.3.

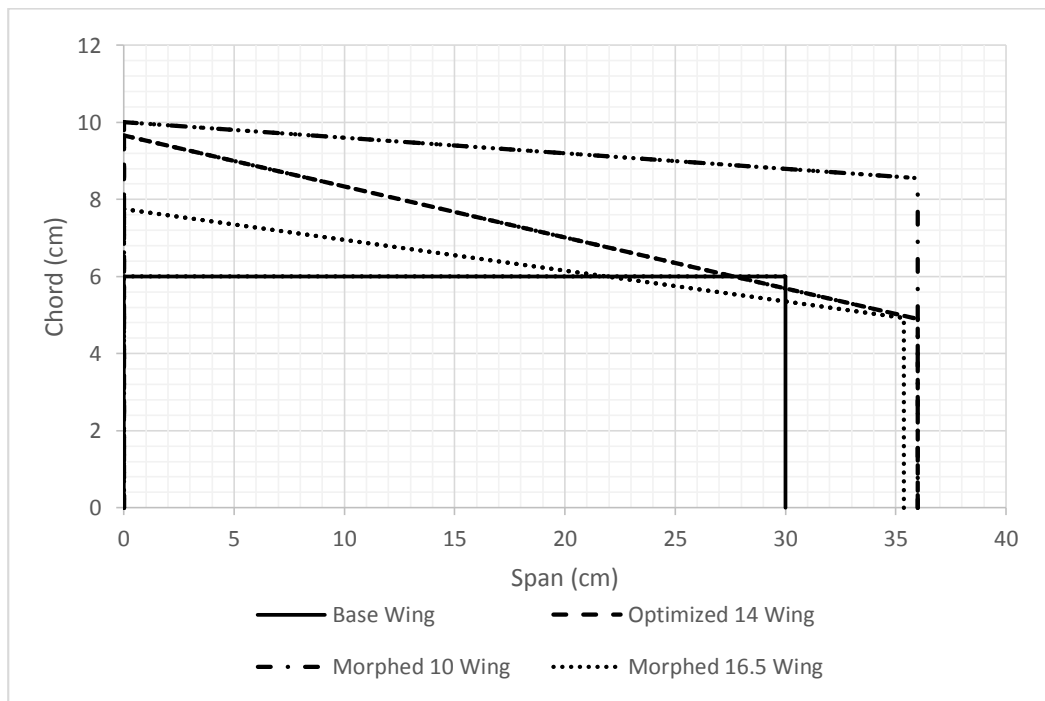


Figure 2.2 Planforms of the four wing models

### 2.2.1 Base Wing with NACA 4412 Airfoil Profile with Spline Method

Base wing airfoil is chosen as the NACA 4412 profile and the airfoil is regenerated by spline method in the previous study so there is a slight difference between the NACA 4412 airfoil profile and the actual Base Wing airfoil profile.

The wings are plotted by Catia V5R18 software. The base wing is plotted by using the values in Table 2.2.

Table 2.2 Base Wing Properties

<i>Base Wing Properties</i>	<i>Chord</i>	<i>Half Span</i>
<i>(mm)</i>	6	300

Base Wing airfoil profile is shown in Figure 2.3.

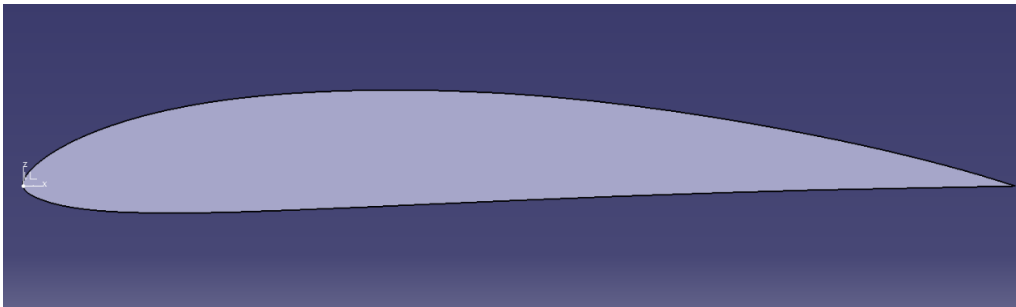


Figure 2.3 Base Wing airfoil profile

The top view of the wing is presented in Figure 2.4.

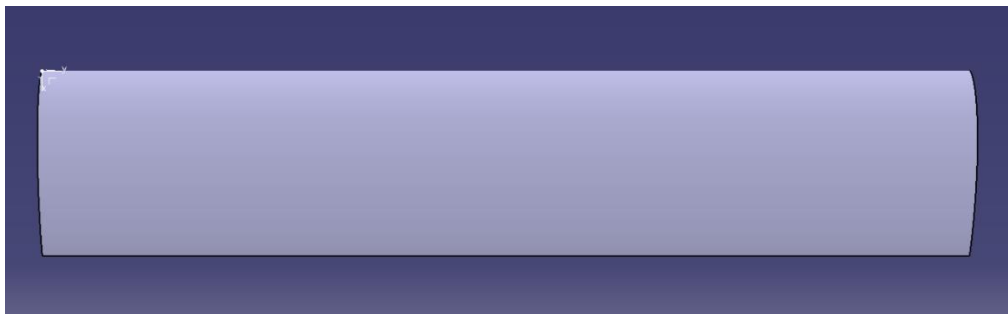


Figure 2.4 Base Wing top view

Isometric view of the base wing is presented in Figure 2.5.

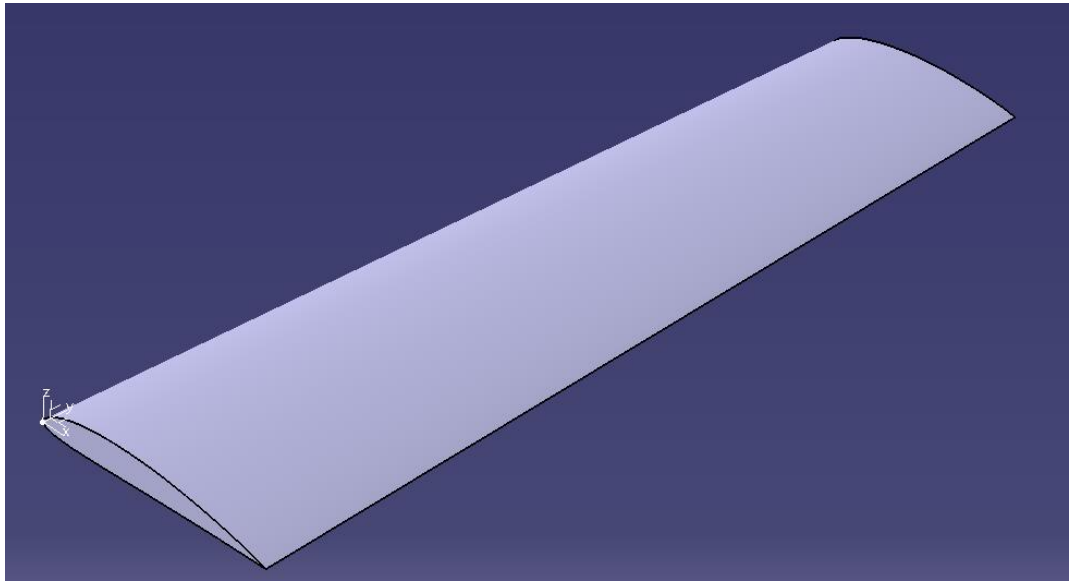


Figure 2.5 Isometric view of the Base Wing

### 2.2.2 Optimized 14 Wing

According to the numerical results, the wing that is optimized starting from the Base Wing at velocity of 14 m/s is drawn. The airfoil is generated using 150 data points.

The three dimensional optimized wing is plotted according to the values in Table 2.3.

Table 2.3 Optimized Wing Properties

<i>Optimized Wing at 14 m/s</i>	<i>Root Chord</i>	<i>Tip Chord</i>	<i>Half Span</i>
<i>(mm)</i>	96.6	49	360

The airfoil profile, top view and the isometric view of the optimized wing is illustrated in the Figures 2.6, 2.7 and 2.8, respectively.

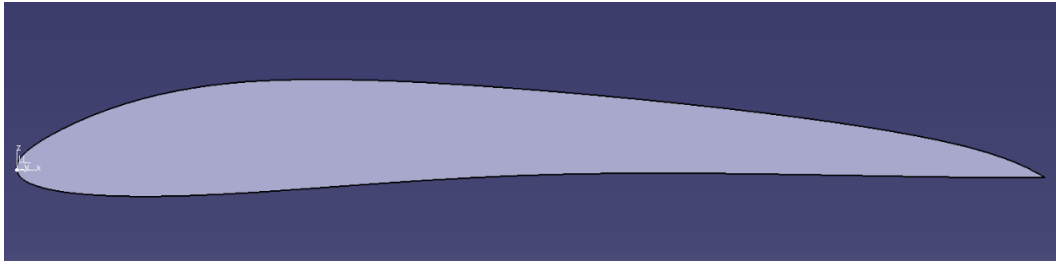


Figure 2.6 Optimized 14 Wing airfoil profile

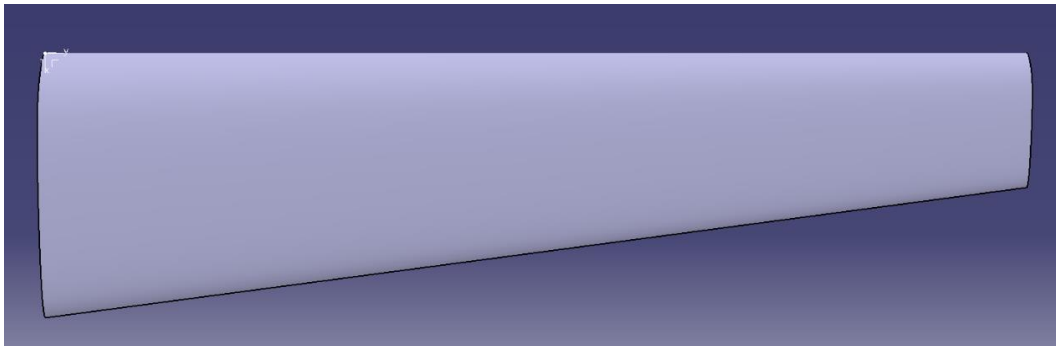


Figure 2.7 Optimized 14 Wing top view

Optimum wing at 14 m/s is obtained as a tapered wing according to numerical results.

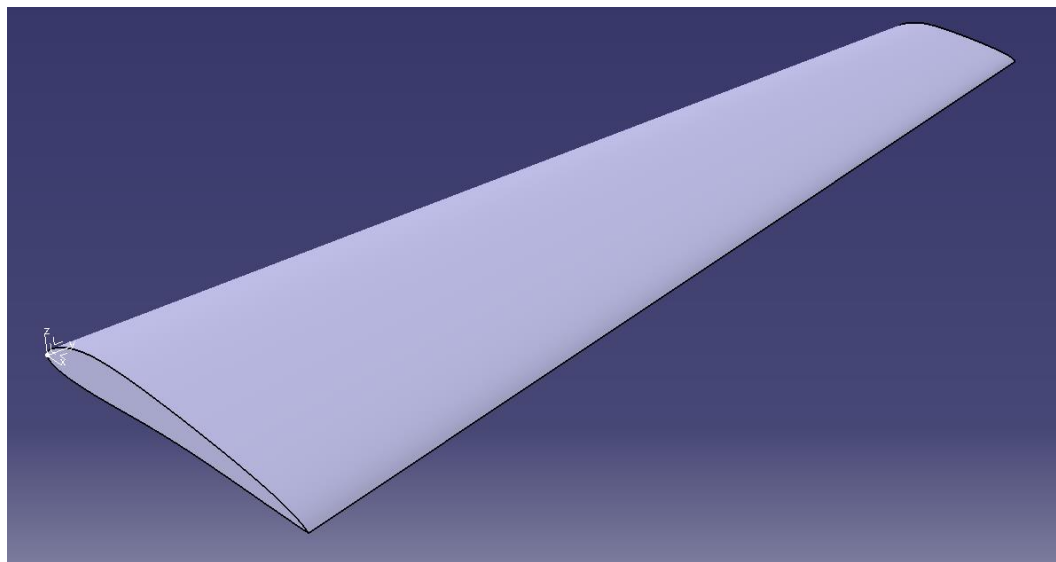


Figure 2.8 Isometric view of the Optimized 14 Wing



### 2.2.3 Morphed 10 Wing

The optimum wing obtained at 14 m/s is morphed at 10 m/s by changing both the airfoil shape and the planform while staying within the limits of the wind tunnel cross-section area. The airfoil of this morphed wing also has 150 data points.

The three dimensional morphed wing is plotted according to the values in Table 2.4.

Table 2.4 Properties of the 10 m/s Morphed Wing

<i>Morphed Wing at 10 m/s</i>	<i>Root Chord</i>	<i>Tip Chord</i>	<i>Half Span</i>
<i>(mm)</i>	100	85.5	360

The drawn airfoil profile (side view), top view and isometric views are illustrated in Figures 2.9 2.10 and 2.11, respectively.

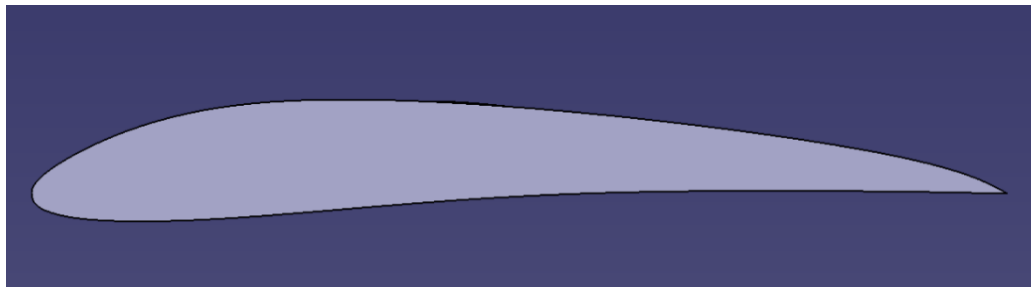


Figure 2.9 Airfoil profile (side view) of Morphed 10 Wing



Figure 2.10 Top view of Morphed 10 Wing

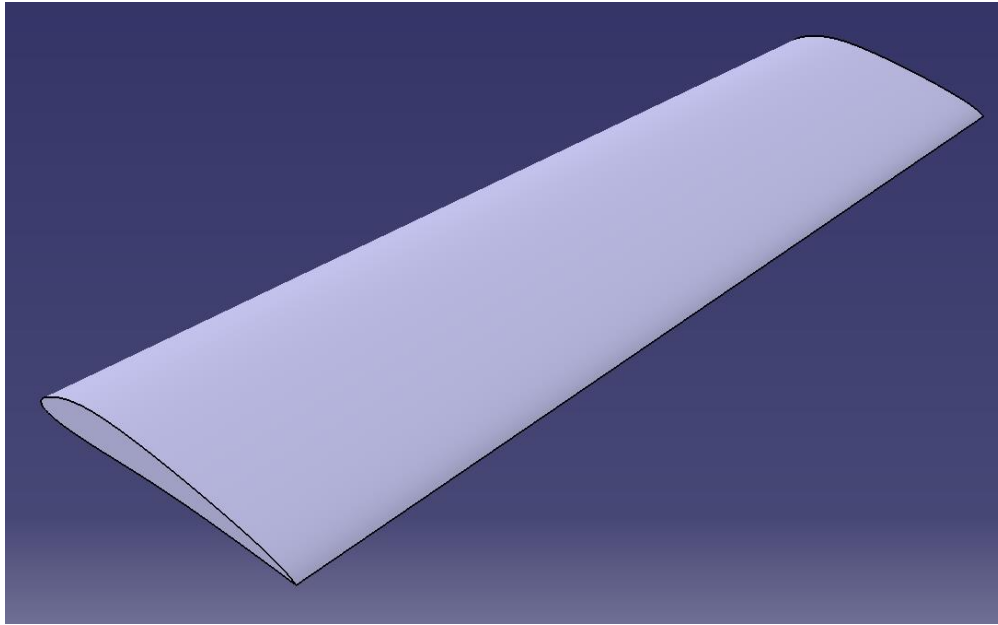


Figure 2.11 Isometric view of Morphed 10 Wing

### 2.2.4 Morphed 16.5 Wing

The optimum wing obtained at 14 m/s is morphed at 16.5 m/s, also considering the maximum speed of the wind tunnel with same procedure done for the morphed wing at 10 m/s. This morphed wing airfoil profile has also 150 data points.

The three dimensional optimized wing is plotted according to the values in Table 2.5.

Table 2.5 Properties of the Morphed 16.5 Wing

<i>Morphed Wing at 16.5 m/s</i>	<i>Root Chord</i>	<i>Tip Chord</i>	<i>Half Span</i>
<i>(mm)</i>	77.5	49.3	353.7

The drawn airfoil profile (side view), top view and isometric views are illustrated in Figures 2.12, 2.13, and 2.14, respectively.

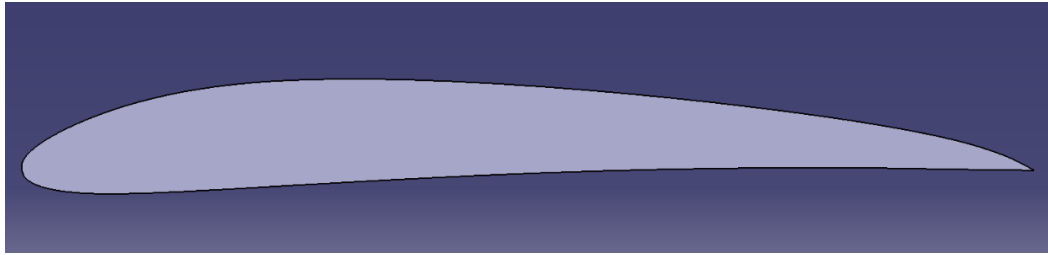


Figure 2.12 Side view of Morphed 16.5 Wing

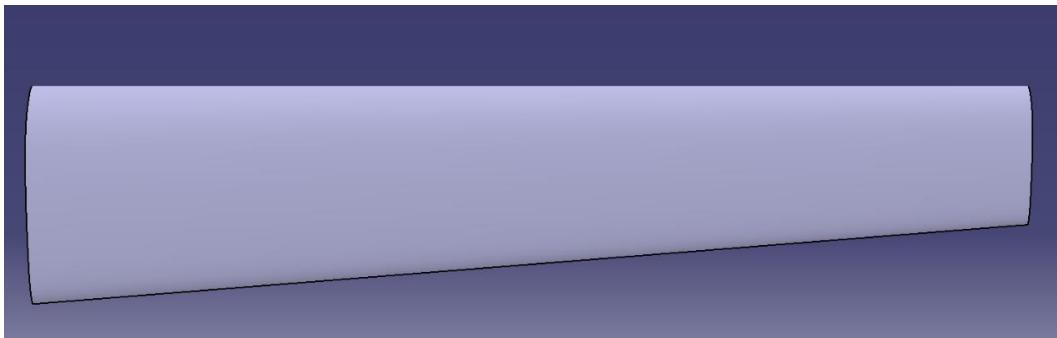


Figure 2.13 Top view of the Morphed 16.5 Wing

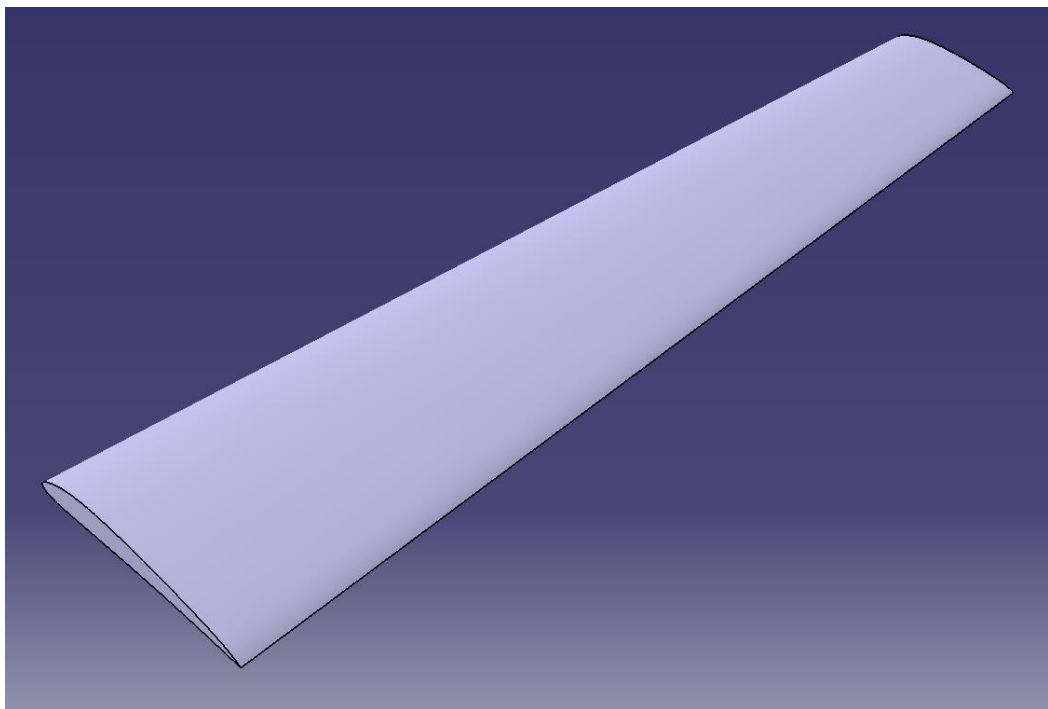


Figure 2.14 Isometric view of the Morphed 16.5 Wing

### 2.3 Manufacturing

The wings are manufactured by CNC milling machine. Manufacturing details are presented in Table 2.6.

Table 2.6 Wing Manufacturing Properties

<i>Wing Manufacturing</i>	<i>Material</i>	<i>Tolerance Limitation</i>
	Aluminum 6061-T6	0.05 mm

Aluminum 6061 is selected because of its high strength, high resistance and good workability. It has good surface finish. Moreover, T6, which is the most common temper of Aluminum 6061, solution heat treated and artificially aged, is selected [24]. It has high corrosion resistance to atmospheric conditions. Tolerance limitation is chosen very low in order to have a more precise and smooth surface.

Manufactured wings are presented in Figures 2.15, 2.16 and 2.17.

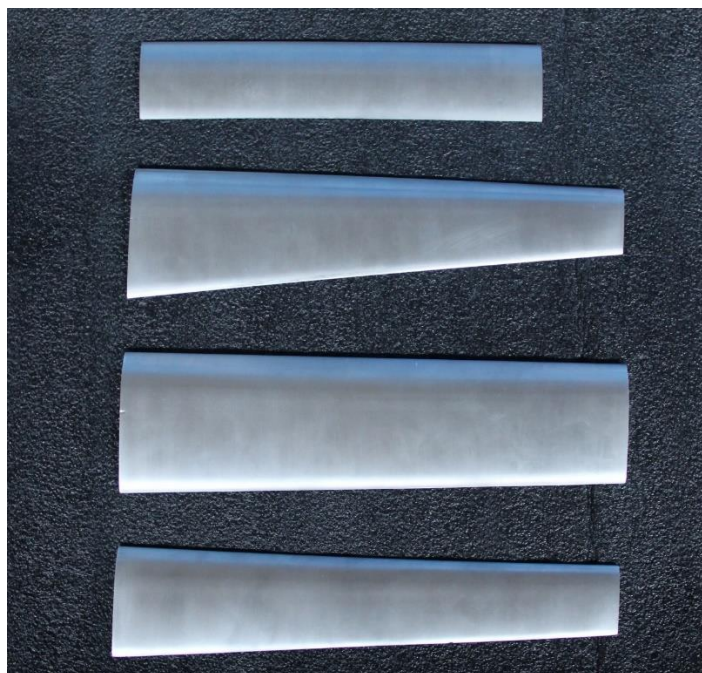


Figure 2.15 Manufactured wings top view (from top to bottom: Base Wing, Optimized Wing at 14 m/s, Morphed Wing at 10 m/s, Morphed Wing at 16.5 m/s)

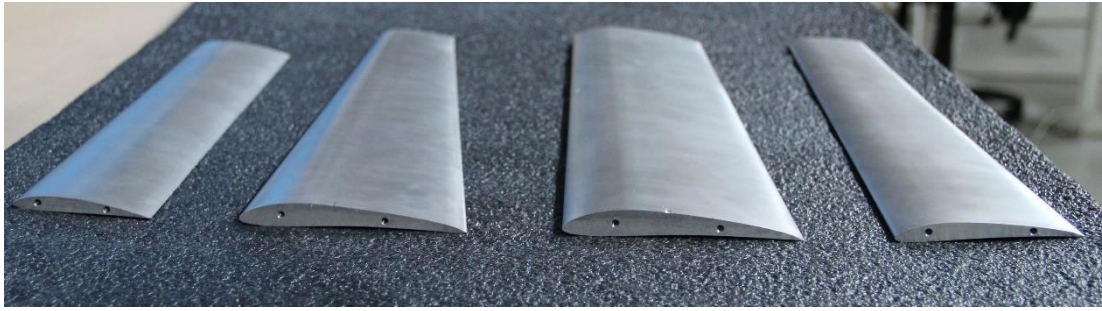


Figure 2.16 Manufactured wings side view from the root chord (from left to right: Base Wing, Optimized Wing at 14 m/s, Morphed Wing at 10 m/s, Morphed Wing at 16.5 m/s)



Figure 2.17 Manufactured wings side view from the tip chord (from left to right: Base Wing, Optimized Wing at 14 m/s, Morphed Wing at 10 m/s, Morphed Wing at 16.5 m/s)



## CHAPTER 3

### EXPERIMENTAL SET-UP AND MEASUREMENT TECHNIQUES

#### 3.1 Introduction

In this section, the wind tunnel used in the experiments and its properties, experimental methodology of the force measurements, force measurement set-up and its components, load cell calibration, possible sources of error and uncertainty analysis are explained. Then, oil flow visualization set-up is presented. Finally, particle image velocimetry experimental set-up, methodology, system components, analysis parameters, processing tools and image visualization results are explained and presented.

#### 3.2 METU Wind Tunnel

Experiments are done at METU Aerospace Engineering Dept. low speed wind tunnel at the METU Aerospace Engineering Department Lab Building. Wind tunnel properties are given in Table 3.1.

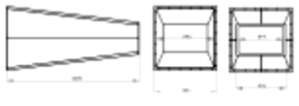
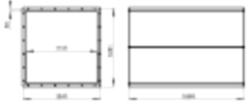

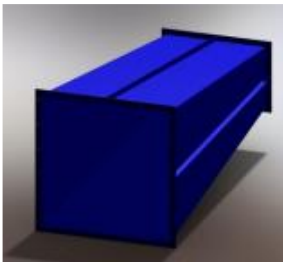
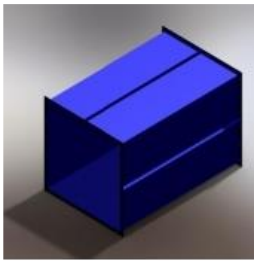
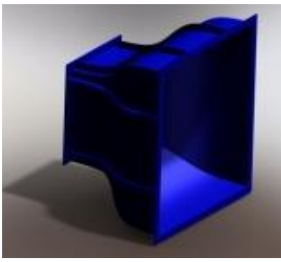
Table 3.1 METU Aerospace Engineering Dept. wind tunnel properties

<i>METU Wind Tunnel</i>	<i>Type</i>	<i>Fan</i>	<i>Test Section</i>	<i>Maximum Velocity</i>
	Blowing	Radial fan with 18.5 kW computer driven AC motor	60 x 60 cm	16.5 m/s

METU low speed wind tunnel has three main parts, namely, diffuser section, straight section and contraction section. The sections and their properties are presented in

Table 3.2. The contraction section is designed in order to provide low turbulence levels in the test section.

Table 3.2 Sections of the METU Aerospace Engineering Dept. Wind Tunnel [25]

<i>Sections of the Tunnel</i>	<i>Diffuser Section</i>	<i>Straight Section</i>	<i>Contraction Section</i>
2D Geometry			
3D Geometry			
Length (m)	2.6	1.85	0.915
Cross-section	Rectangular inlet and 1.1 x 1.1 m <sup>2</sup> square outlet	1.1 x 1.1 m <sup>2</sup> straight square cross-section	1.1 x 1.1 m <sup>2</sup> square cross section inlet changes to 0.6 x 0.6 m <sup>2</sup> square cross-section
Cross-section change	Changes with diffusion angle of 7 degrees	No change	Tangent Hyperbolic contraction profile with area ratio of 3.36

At the outlet of the wind tunnel, 140 cm long transparent test section is attached. The cross sectional area of the test section is 60x60 cm. The wind tunnel is presented in Figure 3.1.



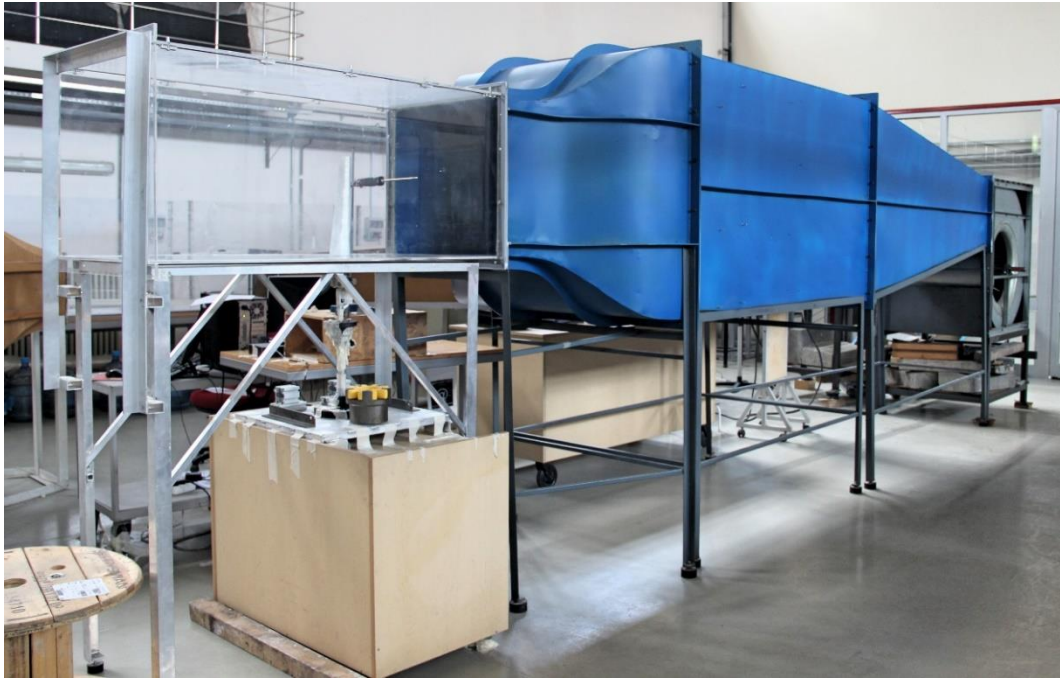


Figure 3.1 METU Aerospace Engineering Dept. low speed wind tunnel

The wind tunnel has a motor controller electronic device shown in Figure 3.2, on which the frequency can be adjusted. By changing the frequencies from the controller, the motor speed, so the airflow velocity of the wind tunnel can be changed.



Figure 3.2 Motor controller device

Velocity measurements are done with Dywer 471B Thermo-Anemometer. It has a range of 0 to 30 m/s. It has air velocity accuracy of +/- 3% at temperature range of 4 to 32 °C [26]. Dywer 471 Thermo Anemometer is shown in Figure 3.3.



Figure 3.3 Dywer 471 Thermo-Anemometer

The velocity and frequency relation is obtained with Dywer 471 Thermo Anemometer at the exit of the contraction section of the wind tunnel. Velocity vs frequency graphs are presented in Figure 3.4. The tunnel speed can reach up to 17 m/s by changing the speed of the motor. However, it cannot maintain its speed steadily for velocities above 15 m/s.

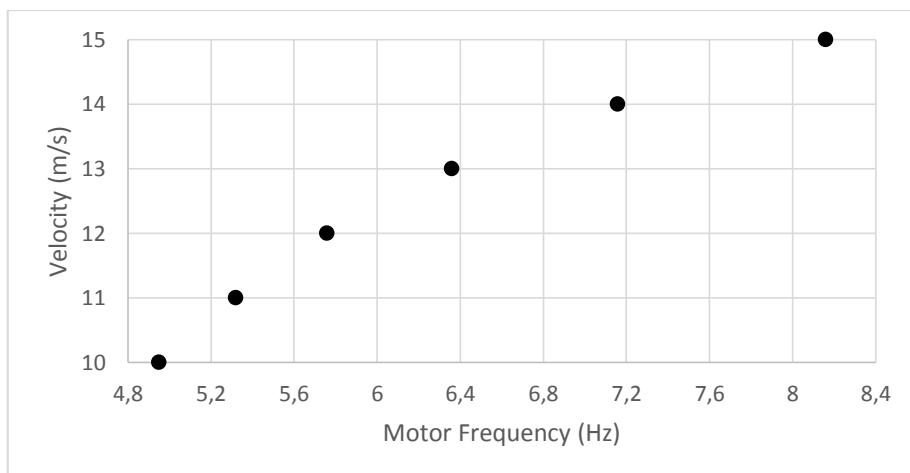


Figure 3.4 METU Aerospace Engineering Dept. wind tunnel freestream velocity vs frequency

Low turbulence levels within the wind tunnel test section are necessary to make sure that laminar flow does not transition to turbulent flow prematurely since low Reynolds number airfoil performance is highly dependent on the behavior of the laminar boundary layer [12]. Therefore, the measurements that are performed in a previous study [25] at the exit of the contraction section are considered. Traversing a single sensor hot wire probe and a Kiel probe in the perpendicular plane to the flow direction, velocity distribution, turbulence intensity and total pressure distributions are measured at 10 m/s freestream velocity adjusted by the corresponding frequency. Figure 3.5 shows these distributions.

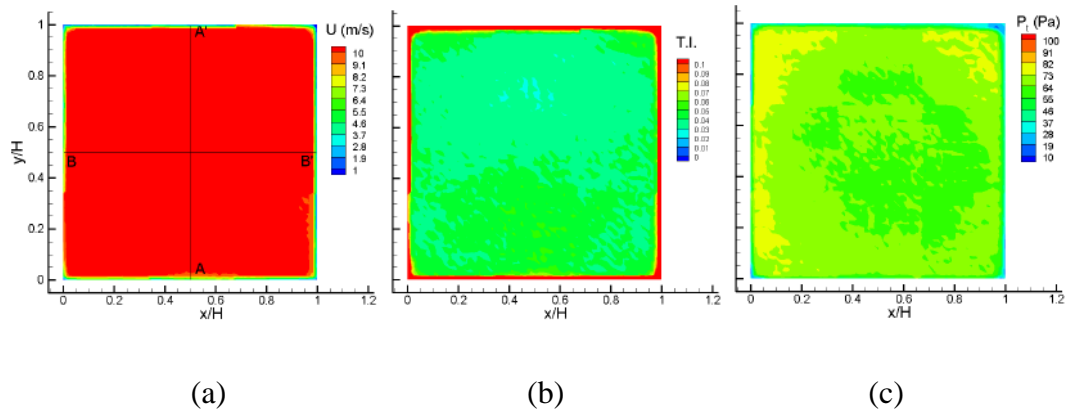


Figure 3.5 (a) Axial velocity distribution, (b) turbulence intensity distribution, (c) total pressure distribution at the exit of the contraction section [25].

Desirable variation in dynamic pressure in the working range of the test section is less than 0.5% of the mean [12]. The measurement indicates a uniform free stream velocity, total pressure distribution and proper dynamic pressure distribution. Turbulence intensity levels are at maximum 0.1, which are at the walls of the test section because of the boundary layer growth along the tunnel walls. Previous calibrations and measurements show that the wind tunnel is reliable for the low speed aerodynamic measurements.

### 3.3 Load Cell Force Measurements

#### 3.3.1 Experimental Methodology

The procedure followed for the experimentation is presented in Figure 3.6.

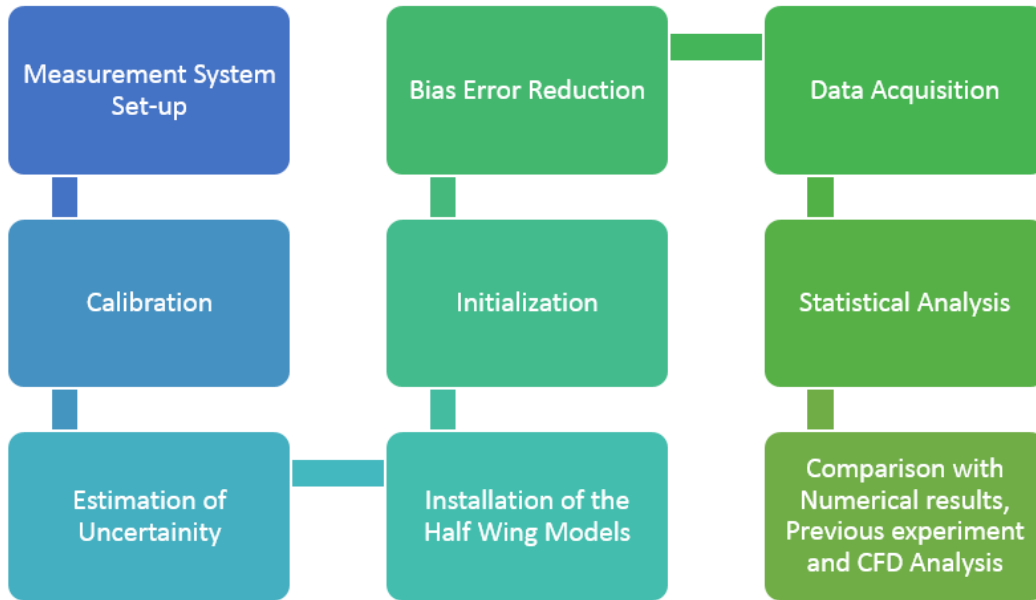


Figure 3.6 Measurement and assessment procedure of load cell experiment

#### 3.3.2 Experimental Set-up

Experiments are done with six axis force/torque ATI Gamma load cell. The wings are attached to the load cell from the lower side of the test section. In between, an angle of attack mechanism is used for adjusting the angle of the wing. The angle of attack plates are shown in Figure 3.7.



Figure 3.7 Angle of attack plates

Angle of attack of the wings can be changed from -15 degree to +15 degree with 1 degree increments. The upper plate with less holes at Figure 3.7 can rotate on the other plate with more holes and a pin is used to fasten them to the desired angle.

The angle of attack mechanism is attached to the load cell so that the X axis of the load cell coincides with the zero angle of attack. The other side of the angle of attack mechanism is attached to the wing from the lower side of the tunnel test section. The wing is attached to a circular plate which is attached to the angle of attack plates.

The set-up of angle of attack mechanism, load cell and the wing is shown in Figures 3.8 and 3.9.

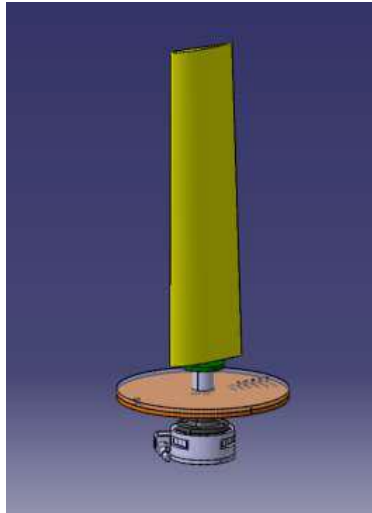


Figure 3.8 The drawing of the angle of attack mechanism, load cell and the wing [27]

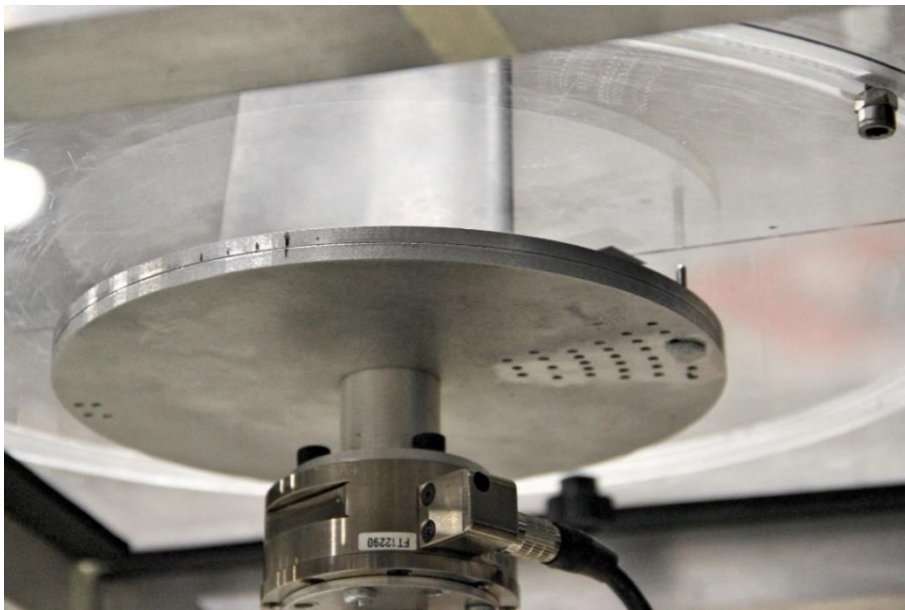


Figure 3.9 Angle of attack mechanism, load cell and the wing

The load cell is connected to the data acquisition system and data acquisition system sends the signals to the computer. The set-up and the set-up schema are presented in Figures 3.10 and 3.11, respectively.



Figure 3.10 Load cell measurements set-up

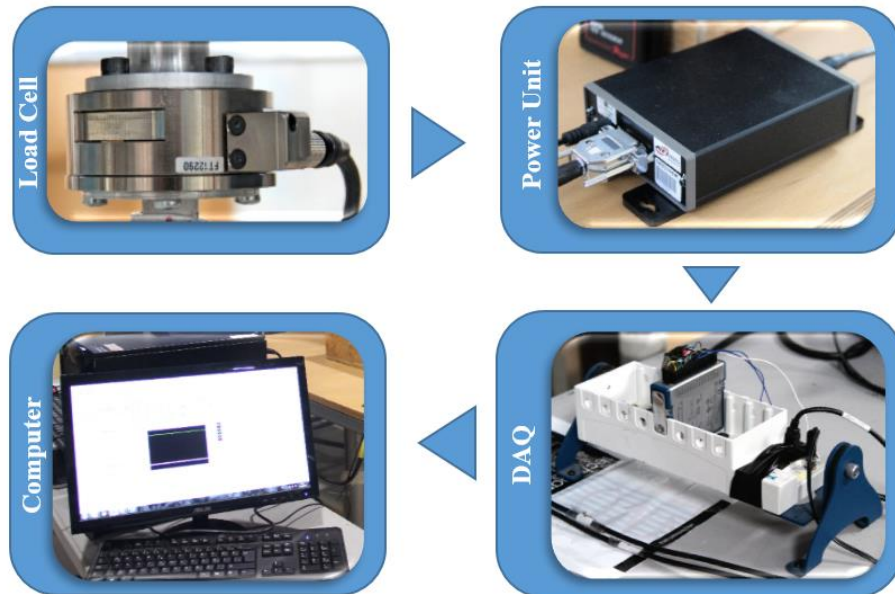


Figure 3.11 Schema of the acquisition and data process set-up

### 3.3.3 System Components

#### 3.3.3.1 ATI GAMMA Load Cell

Strain gauge sensors, also called as load cells, measure shear stress to determine the applied force or torque moment. The applied force or moment causes a mechanical deformation and the load cells generate an electrical signal through this deformation.

In the experiments, ATI Gamma load cell, which can measure six components of force and torque is used at the lower side of the models. The drawing of the load cell and the photo of it are illustrated in Figure 3.12 [28].



Figure 3.12 The drawing and the photo of the ATI Gamma load cell

ATI Gamma load cell is machined from high-strength aircraft aluminum. It consists of silicon strain gages, which make them deliver 75 times stronger signal compared to conventional ones. Presence of the signal amplification provides almost zero noise distortion [28]. The ATI Multi-Axis Force/Torque Sensor system consists of a transducer, interface electronics and cabling. The transducer has silicon strain gages that provide high noise immunity and allow overload protection.

The sensing ranges and resolutions are presented at Table 3.3.

Table 3.3 ATI Gamma Load Cell metric calibrations

	$F_x, F_y (N)$	$F_z (N)$	$T_x, T_y (Nm)$	$T_z (Nm)$
Sensing Ranges	$\pm 32$	$\pm 100$	$\pm 2.5$	$\pm 2.5$
Resolution	0.00625	0.0125	0.0005	0.0005



In this study, only 18% of the maximum balance range in x and y directions is used.

### 3.3.4 Power Unit

Load cell is operated with a power supply and amplifier unit shown in Figure 3.13.



Figure 3.13 Power unit and amplifier

#### 3.3.4.1 Data Acquisition System

Data Acquisition System digitalizes the signal coming from the power unit and sends it to the computer. Electronic data acquisition systems allow the data to be analyzed and manipulated easily and be sampled at higher rates while reducing the human errors [29]. In this study, National Instruments cDAQ-9172 data acquisition system is used, which is shown in Figure 3.14.

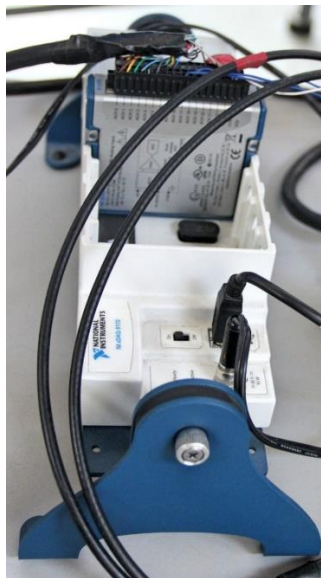


Figure 3.14 Data Acquisition System

The cDAQ-9172 is a eight-slot USB chassis which is capable of measuring broad range of analog and digital I/O signals and sensors. It has a maximum sample rate of 3.2 MS/s and 50 ns resolution [30]. In the chassis, NI 9205 C Series Analog Input Module is used. The module is shown in Figure 3.15. It features 32 single ended or 16 differential analog inputs. Each channel has programmable input ranges from  $\pm 200$  mV to  $\pm 10$  V. 16 bit resolution module has a maximum sampling rate of 250 kS/s. It has overvoltage protection, channel-to-earth-ground double isolation and noise immunity [31].

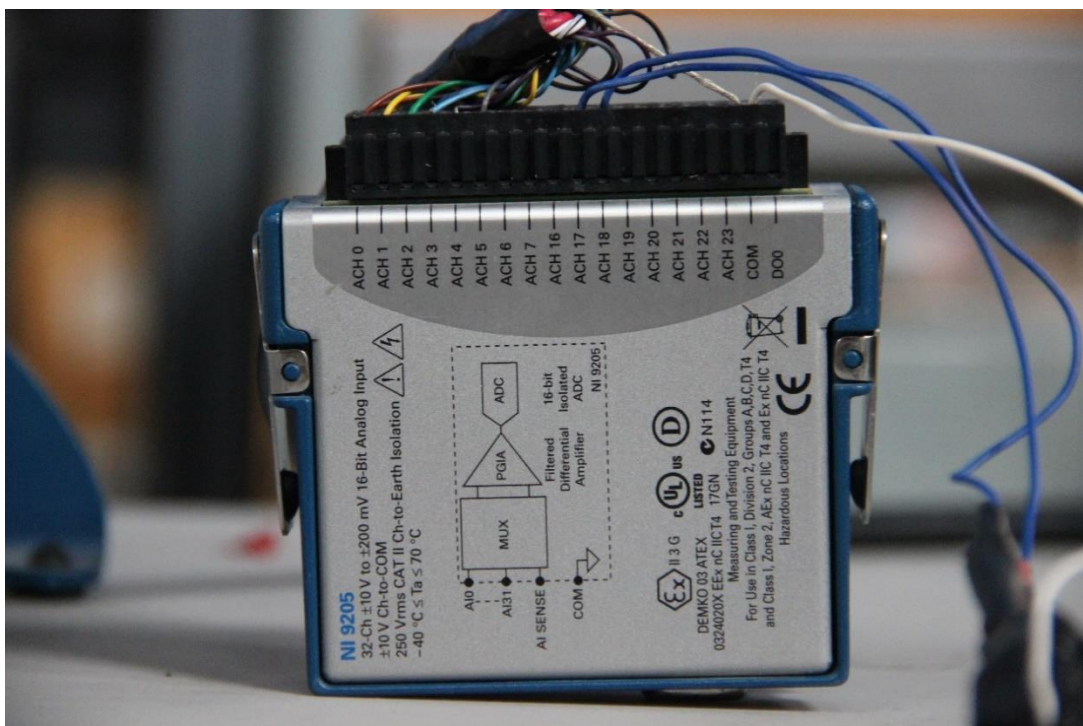


Figure 3.15 NI 9205 Module

### 3.3.4.2 Software

In the computer, National Instruments LabVIEW software is used with a code for the ATI Gamma load cell. The bias error of the data gathering can be controlled manually before starting the measurements and updated for new measurements. The sampling rate and number of samples to be read can be selected in the software. The voltages and force/torque readings in N/N.m can be seen on the screen simultaneously. The software interface is shown in Figure 3.16.

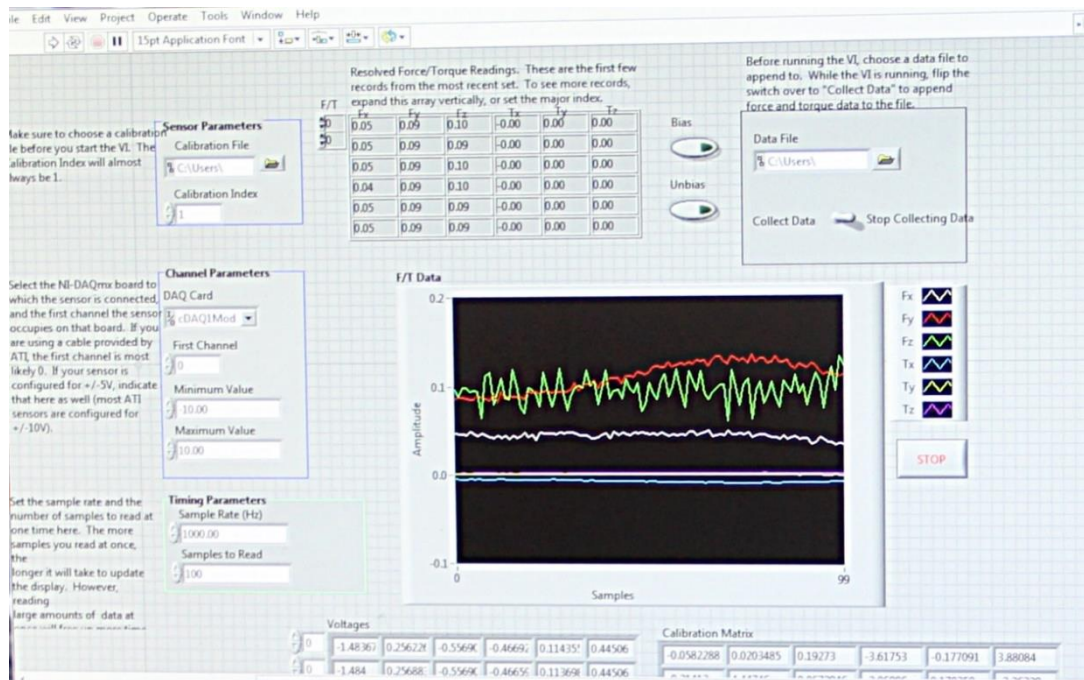


Figure 3.16 LabVIEW interface

Sampling rate, which is the number of samples obtained in one second is selected as 1000 Hz. Sampling rate formula is as follows;

$$f_s = \frac{\text{samples}}{\text{second}} \quad (3.1)$$

Number of samples to be read is selected as 100,

$$f_s = \frac{\text{samples}}{\text{second}} = 1000 = \frac{100}{\text{seconds}} \xrightarrow{\text{yields}} 0.1 \text{ seconds}$$

Thus, every 0.1 seconds 100 data is collected and every second 1000 data is collected and recorded. In most cases data acquisition is done for at least 10 seconds, in other words, at least 10000 samples are collected for each case. For more fluctuating data, this number is increased.

### 3.3.5 Load Cell Calibration

Known masses are applied in order to calibrate the load cell. 5, 50, 100, 500 and 1000 gr masses are applied and the percent error in measurements is calculated.

Absolute error is defined as the difference between the real load acting on the model, which is also called as true value, and the load detected by the balance [9]. Therefore, in the second step of the calibration process, known masses are applied to verify the calibration of the load cell. The percent errors are calculated from the following equations and presented in Table 3.4.

$$\epsilon_{absolute} = \text{Measured value} - \text{True Value} \quad (3.2)$$

$$\text{Relative Error} = \frac{\epsilon_{absolute}}{\text{True Value}} \quad (3.3)$$

$$\text{Percent Error} = \text{Relative Error} * 100 \quad (3.4)$$

Table 3.4 Load Cell calibration

<i>Applied Weight (gr)</i>	<i>Load Cell measurement (N)</i>	<i>Load Cell Measurement (gr)</i>	<i>Percent Error (%)</i>
5	-0.0501	5.1100	2.2018
50	-0.4785	48.7727	2.4546
100	-0.9944	101.3639	1.3639
500	-4.8659	496.0234	0.7953
1000	-9.8109	1000.0968	0.0097

It is seen that, although the vibration of the other test equipment creates noise and effects the measured values, the percent errors of the measurement are relatively low and decreases as the applied force increases. The calibration matrix of the software functions as desired and the load cell is thus calibrated.

### 3.4 Error Analysis

For the velocities above 15 m/s it is hard to maintain the free stream velocity because of the vibration of the old wind tunnel motor which causes big ampere changes and reduction in velocity while operating in a constant frequency. Thus, it is hard to obtain

reliable data when the velocity is higher than 15 m/s. For the 15.5 m/s and 16.5 m/s velocities the tunnel cannot be operated for long durations because of the heating problem. Thus, for 16.5 m/s, the data are taken at -5, 0, 5, 10 and 15 degrees angle of attack, while for the other seven velocities, data at twenty angles from -5 to 15 degrees in steps of one degree are collected. Because of the instability and heating of the wind tunnel motor, at high velocities the vibration of the test section is a significant issue to be solved. Although several precautions are taken during experiments, small vibrations could not be prevented. Moreover, load cell measurements are affected easily from the outside noise in the lab area. During the experiments, it is highly avoided.

After the data is acquired, both mean, median and moving average of the data sets are calculated so that the noise and disturbances in the data are avoided.

### **3.4.1 Sources of Errors**

In this section, possible sources of errors and the precautions taken to eliminate them are discussed.

During the wind tunnels tests, model oscillates especially at high free stream velocities because of the unbalanced motor of the tunnel. Although some holding mechanisms and axial joint slope of the wind tunnel motor are changed, wing model vibrations may have induced inertia forces on the balance.

Moreover, aerodynamic interference between the model support and model may be another source of error [13]. During the experiments, the support placed at the lower side of the wind tunnel test section from outside and the holes are closed so that the wing behaves as if there is no joint points and touches the lower side of the wind tunnel section.

Another source of error in wind tunnels is originating from the increasing velocity over the model due to confining effect of the wind tunnel section boundaries, the model itself and its wake. Consequently, secondary forces may be generated on the wing model. These interactions are reduced when the model is relatively small

compared to the test section. In this study, the maximum span of the wings is 36 cm so that it is small enough to eliminate these effects.

Furthermore, small time dependent fluctuations in the speed of tunnel may be caused by the inertia of the fan system and the air, particularly at low Reynolds number measurements.

In the wind tunnel experiments, the presence of the wind tunnel walls increases the measured values of lift, drag and pitching moment because of the accelerating velocity on the wing model due to buoyancy solid blockage, wake blockage and streamline curvature [12]. This should also be kept in mind during the assessment of the lift and drag curves.

Boundary layer growth at the walls causes the static pressure to decrease along the test section. Consequently, an additional drag force is created, also called as buoyancy. For the test sections with constant cross section area it becomes insignificant [12]. Thus for the METU Aerospace Engineering Dept. wind tunnel, this error source does not have an influence.

The existence of the model in the test section reduces the effective area within the constant test section, also called solid blockage. Accounting the Bernoulli equation, the velocity must increase over the model so that all the aerodynamic forces and moments are increasing [12]. This effect should also be taken into consideration while assessing the results of lift and drag values.

At the downstream of the wing, the free stream velocity decreases at some point where the wake of the wing exists. This is called wake blockage and the velocity on the model outside of the wake must increase in order to satisfy the continuity equation. Thus this is another effect that changes measured drag values proportional to the wake size [12]. This wing wake effect is discussed during the PIV Experiment results in the following chapters.

For the closed test sections, the walls create additional curvature by creating closer streamlines over the model, which increases the effective camber. Therefore, the lift and the pitching moment data is measured higher than the real case, whereas drag is

not affected by this [12]. Thus, in the lift curves of the wing models, this phenomena should be kept in mind.

According to the previous studies, it is seen that reducing the data acquisition time at each measurement, maintains system reliability at an acceptable level especially if the power supply consistency is low [10]. Moreover, the data must not be taken immediately after the wind tunnel is operated to have a more stable freestream velocity profile in the test section. Therefore, after the wind tunnel is operated for a while to obtain smoother flow, the data is taken considering the reliability of the power supply.

### **3.5 Uncertainty Analysis**

Errors and uncertainties may come from the measurement instruments, environmental conditions, measurement process, calibration of the instruments etc. [32]. There are two types of uncertainty in measurements. The systematic uncertainty (for each repeated measurement, same error is repeated) and the other one is the random uncertainty where repeating measurements give randomly different results. For the systematic uncertainty, velocity measurements are taken into account. Since the calibration of the load cell is already done it isn't included in this analysis.

In the random uncertainty analysis, first the noise of the load cell is measured when there is no load applied. By this way only the error coming from the load cell noise can be calculated. Moreover, the balance system analysis without any applied load can eliminate balance system interferences.

In this study, only the lift and drag forces, in other words  $F_x$  and  $F_y$  forces, are the main interests. Thus the bias of the load cell in x and y directions are presented in Figure 3.17 and Figure 3.18.

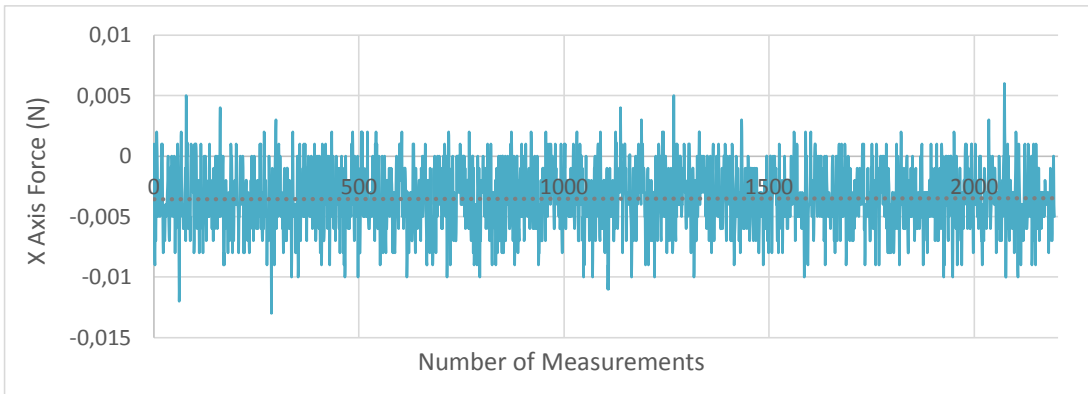


Figure 3.17 Load Cell x-axis force (drag) bias

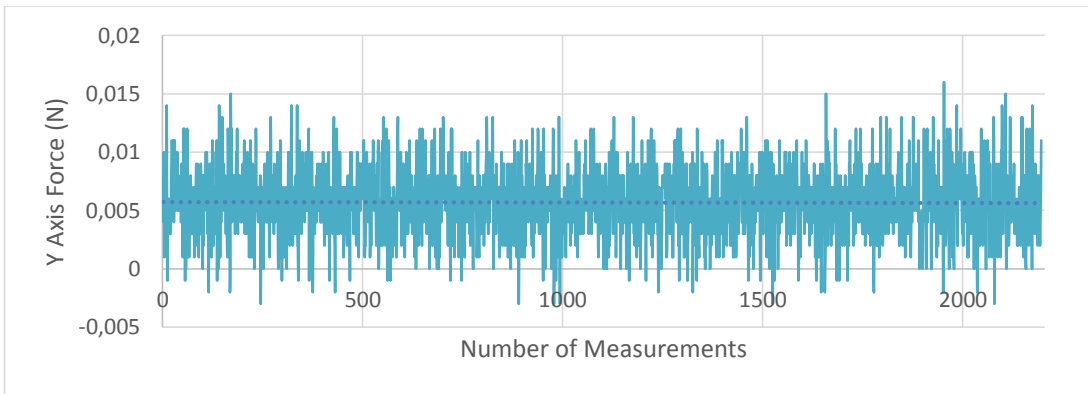


Figure 3.18 Load Cell y-axis force (lift) bias

The noise of the X, Y and Z axis forces and torques are analyzed and the results are presented in Tables 3.5 and 3.6.

Mean of the acquired data is computed by the following equation [26]:

$$\bar{x} = \frac{1}{N} \sum_{i=1}^N x_i \quad (3.5)$$

where  $x_i$  are the measured data, N is the number of the total data within a measurement.



Standard deviation is computed according to equation 3.6 [33].

$$\sigma = \sqrt{\sum_{i=1}^n \frac{(x_i - \bar{x})^2}{N-1}} \quad (3.6)$$

Where  $\bar{x}$  is the mean value of the measured data.

Thus, if the measurements are repeated, the next measurement has 68% probability of lying within  $\bar{x} \pm \sigma$  [34].

The standard deviation of the mean is calculated according to the Equation 3.7 [35].

$$\sigma_m = \frac{\sigma}{\sqrt{N}} \quad (3.7)$$

Where  $\sigma_m$  is the mean standard deviation. It is the standard error of the mean. Meaning that, in our case 35500 data are presented and the error of the mean will be 188.41 times less than the error of each measurement [34].

In general, standard deviation is the random uncertainty, but should be rescaled in order to calculate the combined uncertainty. Standard deviation and mean standard deviation to find random uncertainties are rescaled. For 95% confidence level, the corresponding coverage factor of 2 is applied [32]:

$$U = k \cdot \sigma \quad (3.8)$$

Where k is the coverage factor,  $\sigma$  is the standard deviation and U is the random uncertainty.

Table 3.5 Three Axis Force Statistics of the Noise in Load Cell

<b><i>Forces</i></b>	<i>F<sub>x</sub> (N)</i>	<i>F<sub>y</sub> (N)</i>	<i>F<sub>z</sub> (N)</i>
<i>Mean</i>	-0.0032	0.0060	-0.0040
<i>Standard Deviation</i>	0.002497	0.002998	0.01174
<i>Mean Standard Deviation</i>	0.00001325	0.00001591	0.00006230
<i>Median</i>	-0.003	0.006	-0.004
<i>Maximum</i>	0.008	0.016	0.044
<i>Minimum</i>	-0.014	-0.005	-0.053
<i>Random Uncertainty</i>	0.004994	0.005996	0.02348
<i>Random Uncertainty of the Mean</i>	0.00002650	0.00003182	0.00012462

Table 3.6 Three Axis Torque Statistics of the Noise in Load Cell

<b><i>Torques</i></b>	<i>T<sub>x</sub> (Nm)</i>	<i>T<sub>y</sub> (Nm)</i>	<i>T<sub>z</sub> (Nm)</i>
<i>Mean</i>	-0.00000245	0.000566	0.00000323
<i>Standard Deviation</i>	0.0001575	0.0004957	0.00005925
<i>Mean Standard Deviation</i>	0.000000836	0.000002631	0.000000315
<i>Median</i>	0	0.001	0
<i>Maximum</i>	0.001	0.002	0.001
<i>Minimum</i>	-0.001	0	-0.001
<i>Random Uncertainty</i>	0.0003150	0.0009916	0.0001185
<i>Random Uncertainty of the Mean</i>	0.00000167	0.00000526	0.00000063

Thus the load cell random uncertainty of the mean in percentages of the mean in the x and y directions, where the lift and drag forces are measured in the interest of this study are listed in Table 3.7.

Table 3.7 Random uncertainty of the mean in x and y direction forces

	$F_x$	$F_y$
<i>Random Uncertainties of Load Cell (%)</i>	0.827	0.534

Considering the range of the measured data for lift and drag forces, the bias of the load cell is acceptably small and the random uncertainties of the mean shows that the measurements are highly reliable.

### 3.6 Surface Oil Flow Visualization Set-Up

Surface Oil Flow Visualizations are conducted in the same wind tunnel that is used for force balance measurements. In the oil flow visualization experiments 15w40 motor oil is mixed with titanium dioxide powder and the optimum mixture is obtained by trial and error method. In order to capture the images, Canon 600D camera with 18-135 mm Canon lens is used. The set-up for the oil flow visualizations are shown in Figure 3.19.



Figure 3.19 Oil Visualization Set-Up

### 3.7 Particle Image Velocimetry Experiments

Particle Image Velocimetry, as discussed in the first chapter, is used to analyse wing tip vortices of the four half wing models at the angles of attack and free stream velocities that yield 2.5 N Lift force.

#### 3.7.1 Experimental Methodology

Basic principle of the particle image velocimetry experiments starts with illumination. Instantaneous velocity fields of the fluid are analysed by creating a laser sheet on the region of interest so that the tracer particle displacements are determined. The particles in the measurement plane are recorded by a camera, which is synchronized with the laser, and then analysed in the computer to find displacements of the particles. Thus, the PIV system consists of particles to trace, illumination system (laser), camera, synchronizer and host computer. In the host computer several operations are done to obtain final velocity vectors.

The measurement chain of the PIV measurements is illustrated in Figure 3.20.

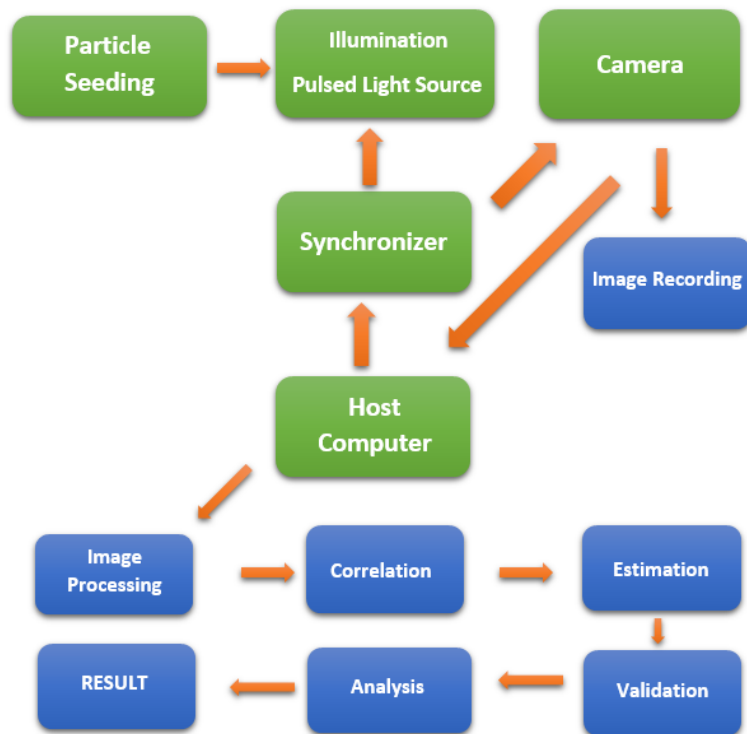


Figure 3.20 Measurement chain of the PIV experiments

### 3.7.2 PIV Set-up and System Components

The PIV experiments are performed at the wind tunnel that is used in load cell experiments. This is preferred in order to compare the data of load cell with PIV without having an additional error source coming from different wind tunnels. Moreover, the blowing type METU wind tunnel is very favourable for the PIV measurements since it can mix the fog particles properly with its rotating fan. During the measurements, the set-up is covered with black curtains in order to prevent any light source coming to the measurement plane from the environment. Figures 3.21 and 3.22 show the PIV set-up and schema used in this study.



Figure 3.21 PIV Set-Up

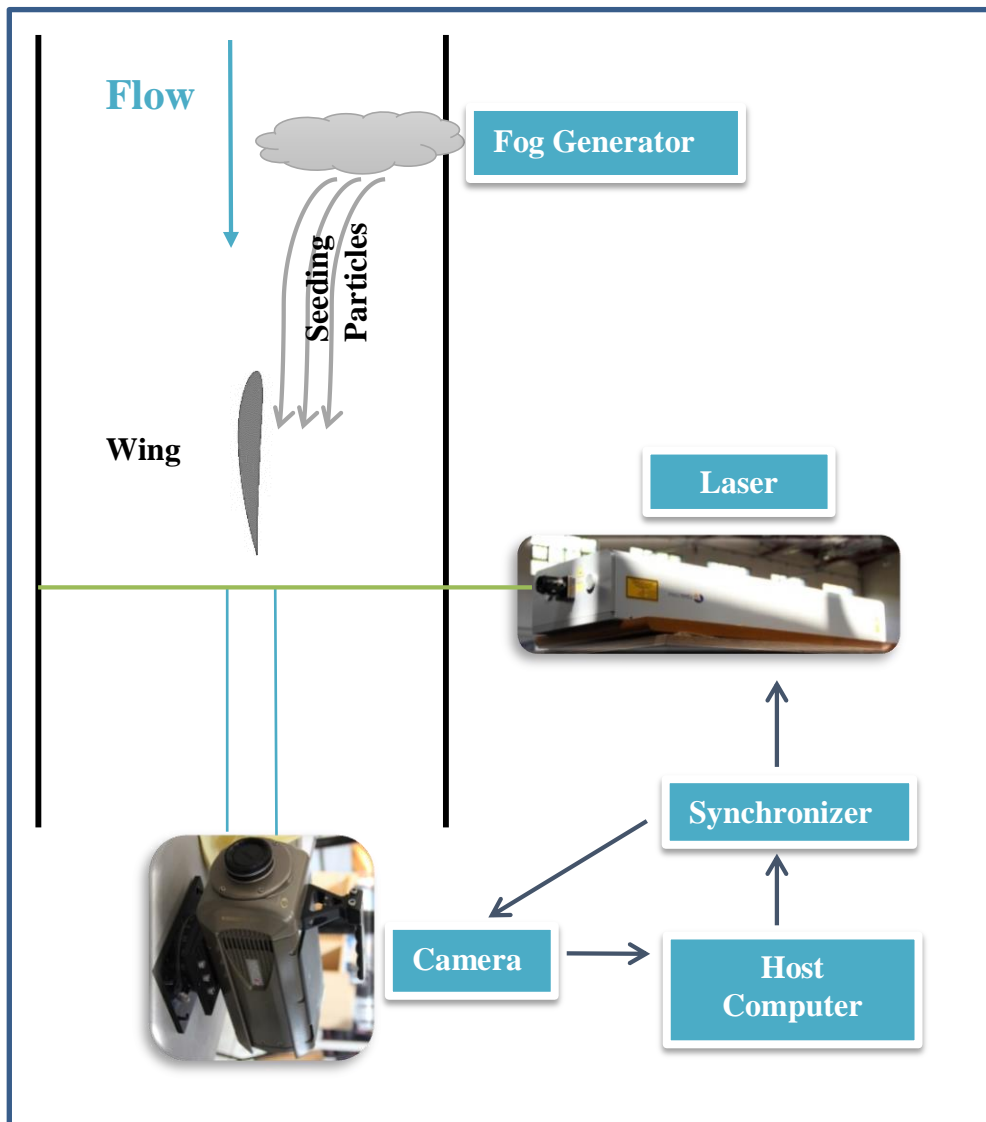


Figure 3.22 PIV Set-Up Schema (Top View)

The place of the laser is adjusted vertically so that the maximum laser light location coincides with the region of interest and it is adjusted horizontally for each measurement plain from the downstream. Since the mean aerodynamic chords of the wing models and their one chord and two chord downstream locations are different, camera location is changed in every measurement by a traverse system for different downstream chord locations for four wing models.

Another important issue is the risk of damaging the camera since it is located downstream of the seeding particles in the blowing wind tunnel. Thus, mirror usage

is tried. The images are mirrored to the camera. Influence of the mirror in the downstream low is studied before by Zhang et al and it is found that once the distance of the mirror exceed two chord distance from the wing the influence is less than 5% on scattering of vortex centers and 2% on maximum vorticity [36]. During the experiments, it is seen that mirror usage does not affect the images of the wing tip vortices. However, in order to avoid double reflection which may cause small losses in the data, a Plexiglas is cut and placed in front of the camera so that the camera does not get affected from the seeding particles. Moreover, camera is placed at the exit of the wind tunnel test section in order not to disturb the flow and prevent vibration of the camera caused by wind tunnel operation. The camera set-up with Plexiglas is presented in Figure 3.23.



Figure 3.23 Camera Protection

All the adjustments and distance measurements for laser and camera are double checked with Bosch electronic length measurement device shown in Figure 3.24.



Figure 3.24 Distance Measurement Device

### 3.7.2.1 Laser

Litron LDY304-PIV Nd:YLF laser is used as an illuminating source in the experiments. It has 30 mJ output energy per laser per pulse at 1 kHz, and a wave length of 527 nm. The laser is shown in Figure 3.25. Laser is operated at 80% power during the experiments.



Figure 3.25 Litron laser

### 3.7.2.2 Camera

Phantom V640 Vision Research Camera, presented in Figure 3.26, is used in the experiments for image capturing. The resolution of the camera is selected as 1024x768 pixels to get the optimum image area in the experiments. Furthermore, four different lenses are tried and finally, 50 mm Nikon Nikkor lens is chosen and used in the experiments. The Plexiglas in front of the camera is cleaned before each measurement. Exposure time of the camera is fixed to 158.169 micro seconds for the resolution at which it is operating.





Figure 3.26 Phantom CCD Camera

### 3.7.2.3 Timer Box

At the beginning of the experiments the synchronizer that is used is found to be broken and do not work in straddle mode. Thus, Dantec timer box is used for the synchronization of the camera and laser.

### 3.7.2.4 Fog Generator

In order to supply tracer particles three different fog generators are tried with different density fluids. Finally oil generator is selected because of the diameter of the vaporised oil particles. The oil generator is presented in Figure 3.27.



Figure 3.27 Fog Generator

### 3.7.2.5 Software

In the host computer, Dynamic Studio 2015 software is used.

### 3.7.3 Wing Models and Laser Planes

The wing models are painted in black with a spray painter in order not to create a reflection for the laser sheet. Painting process is presented in Figure 3.28.

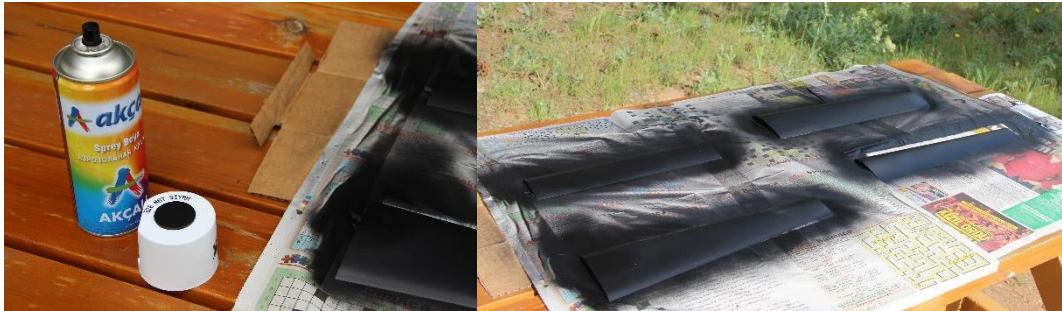


Figure 3.28 Painting Process of the Half Wing Models

The roll-up of the tip vortex is complete at the downstream location less than one chord. The overall circulation of the vortex remains nearly constant throughout the range from trailing edge of the wing to 6.7 chords downstream from the wing [16]. Furthermore, according to another study, vortex strength is found to grow dramatically behind the airfoil and reach a constant value at  $1.5 \times \text{Chord}$  suggesting the roll-up of the tip vortex [21]. Therefore, the measurements are done at one mean chord (C) and two mean chord downstream (2C) from the trailing edge of the tip chord. Since all wings except the Base Wing are tapered, the mean aerodynamic chord of each wing is taken into account. The lines at these C and 2C locations for each wing are determined and drawn on the wind tunnel for adjusting the laser sheet planes. The location of the laser according to a drawn sheet plane and illuminated sheet plane for Optimized 14 Wing 2C downstream locations are presented in Figures 3.29 and 3.30, respectively.

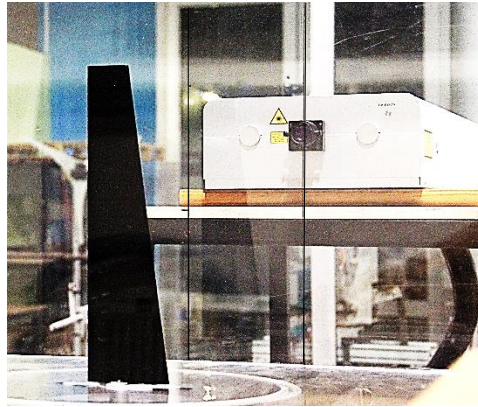


Figure 3.29 Laser Sheet Plane Lines

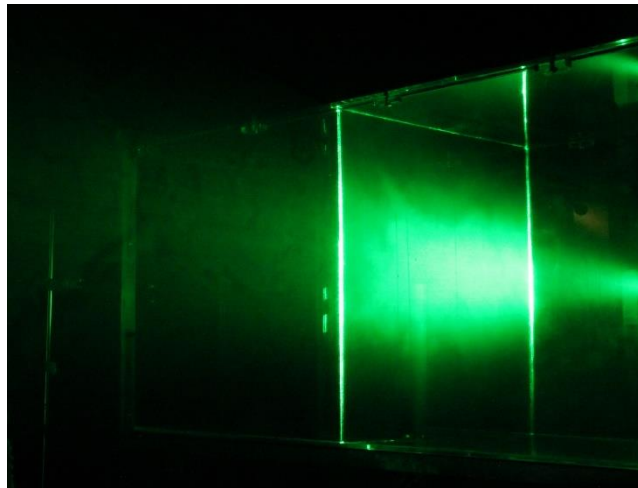


Figure 3.30 Laser Sheet Plane at the Downstream of the Wing Model

#### **3.7.4 Calibration**

The calibration of the images are done by putting a ruler in the measurement plane each time at different downstream locations. The calibration ruler at the laser sheet plane and the calibration image in the software is presented in Figure 3.31.

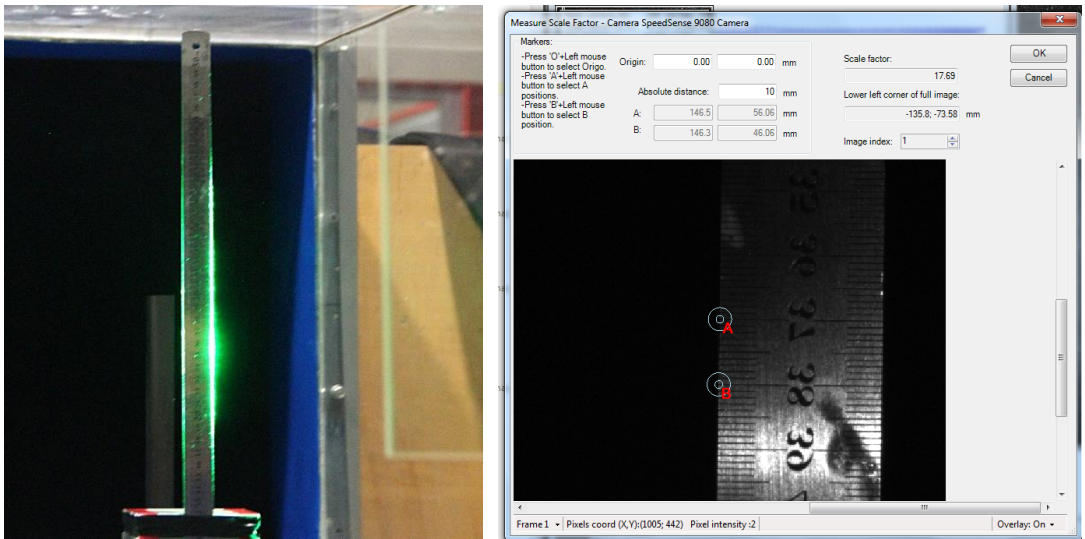


Figure 3.31 Calibration of the images

### 3.7.5 Image Quality

The captured images are checked for the seeding intensity, since this is very important for PIV measurements. Generally within an interrogation area there should be 5 to 15 particles. The process of controlling the seeding density is presented in Figure 3.32. The region with particles seen in the figure consists of 9 interrogation areas.

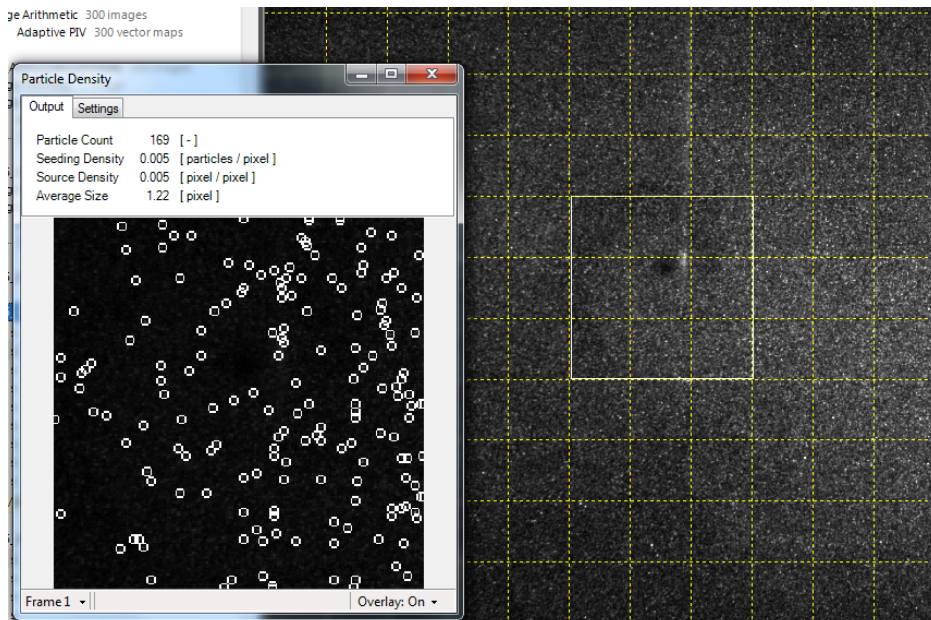


Figure 3.32 Particle Density

Moreover, correlation peak of the image pairs are checked so that the proper calculation of the particle displacement is ensured. An example of correlation peak is presented in Figure 3.33. The selected area is shown by a square.

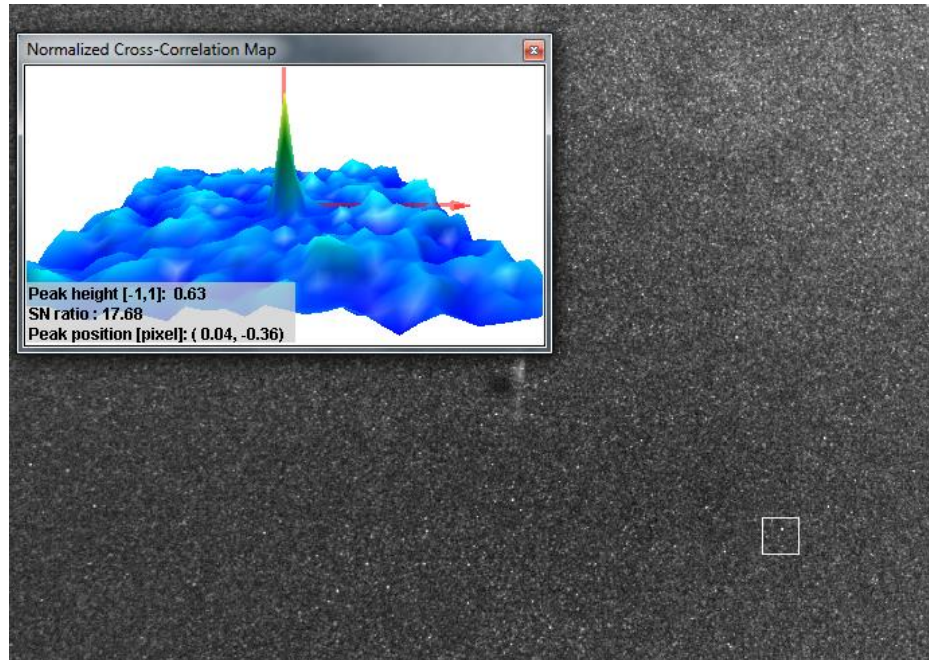


Figure 3.33 Correlation Peak

The quality of the particles are also checked by looking at the image values. The whitest ones (grayscale peaks) with the highest value corresponds to real particles while the gray ones with low magnitudes are noise.

### 3.7.6 Analysis Parameters

After choosing the camera resolution as 1024x768, the exposure time is fixed to 158.169 micro seconds. Trigger rate (sampling frequency of the PIV set-up) is limited by the camera and is selected as 700 Hz.

Since analysis in this study are performed at the plane perpendicular to free stream velocity, the particle movements are not very big so that the camera resolution is reduced from its maximum. By this way time between pulses can be reduced. It should be noted that the time delay between successive pulses ( $\Delta t$ ) should be selected such that the displacements of particles should be one fourth of the interrogation area.

Therefore,  $\Delta t$  is selected as 40 microseconds so that the particle displacements can be detected properly by the software.

### **3.7.7 PIV Processing**

After capturing images, the images are processed to have optimum results. First, the mean of the images are determined. This mean of grayscale values in a time series is the estimated background. This mean is the noise and the wing, which is common in all the 300 images. Then this mean (background) is subtracted from the all images by Image Arithmetics tool. Then Adaptive PIV is selected as a processing tool. Adaptive PIV tool iteratively adjusts the size and shape of the individual interrogation areas to adapt local seeding densities and flow gradients. Grid step size is chosen as 16x16 so that more interrogation areas will be present in the calculation area. Starting from 128x128, the adaptive PIV tool reduces the interrogation area to 64x64. Then the validation is performed by using Universal outlier detection where each vector is compared with its neighbours. Adaptive interrogation area size is used at each step for the particle density and velocity gradients [37]. Finally, Vector statistics is selected. It calculates the mean velocity vector of 300 image pairs, the standard deviations, variance, covariance etc.

Vector Statistics is performed for all valid vectors and substituted ones are not included so that the more realistic case can be obtained.

### **3.7.8 Image Visualization**

During the experiments, the wing tip vortex of the wing models are observed clearly and visualized by Canon 600D camera with 150 mm lens. The wing, tunnel test section and the wing tip vortex can be seen clearly in Figure 3.34. The different snapshots of the same vortex of Optimized 14 Wing at 2 C Location is presented in Figure 3.35. The rotation of the vortex is counter clockwise.

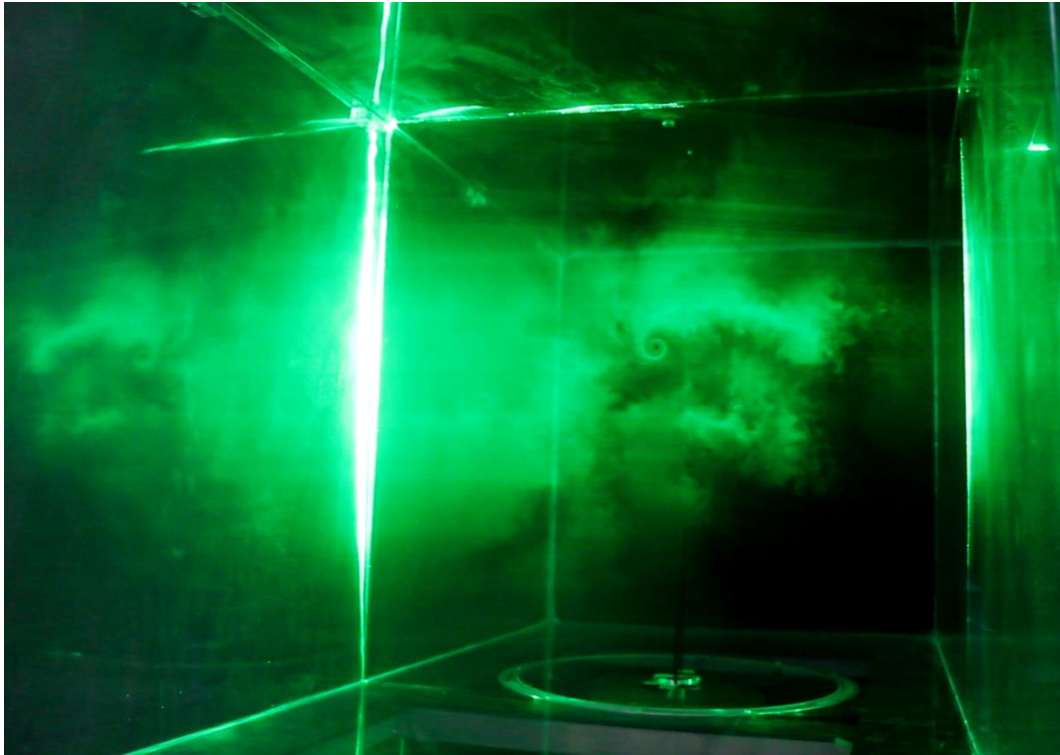


Figure 3.34 Wing and wing tip vortex in the tunnel test section

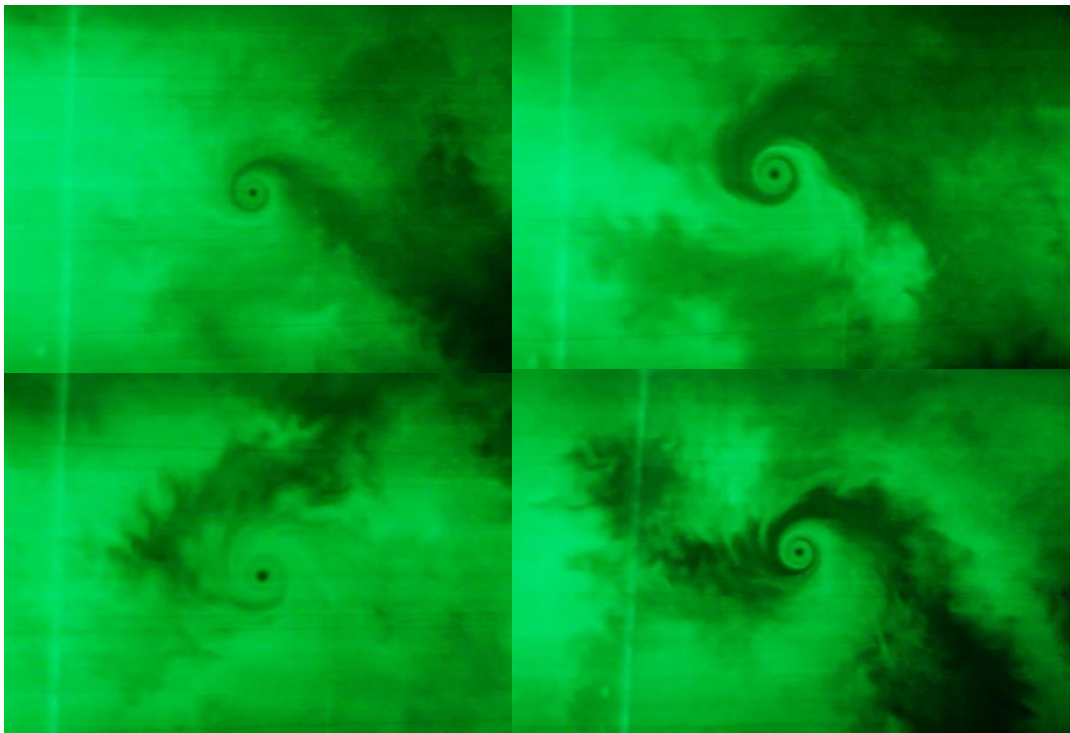


Figure 3.35 Wing tip vortices of optimized 14 wing at 2C location





## CHAPTER 4

### EXPERIMENTAL RESULTS AND DISCUSSION

#### 4.1 Introduction

In this section, the load cell experimental results for the four half wing models are presented and compared with the numerical results of previous studies and previous experiments. In the second part of this chapter, the particle image velocimetry results are presented and the results of the four half wing models are compared for the purpose of validating the morphing wing design.

#### 4.2 Load Cell Experimental Results

For each angle of attack, free stream velocity is checked to maintain a fixed Reynolds number. All the half wing models are analyzed at 8 velocities (10, 11, 12, 13, 14, 15, 15.5 and 16.5 m/s) and at 21 angles of attack from  $-5^\circ$  to  $15^\circ$  with  $1^\circ$  increments for each velocity. Only at 16.5 m/s 5 angles of attack are analyzed from  $-15^\circ$  to  $5^\circ$  with  $5^\circ$  increments because of the instability of the tunnel at 16.5 m/s caused by heating and excess vibration of the motor.

In this section, the lift and drag forces of the four half wing models at different velocities are presented in force vs angle of attack (AOA) graphs. All the force units are Newton and units of all the angles are degrees.

Reynolds number is the ratio of inertial forces to viscous forces in the flow. When viscosity is dominant, viscosity transports and dissipates momentum throughout the flow so that the flow is laminar and smooth. Since the viscous terms are in the denominator, Reynolds number is small when the viscous forces are high [38].

The Reynolds numbers for each wing at different velocities are computed according to following formula.

$$Re = \frac{\rho * V * l}{\mu} \quad (4.1)$$

Where  $\rho$  is the density of air inside the tunnel,

$V$  is the free stream velocity provided by the tunnel,

$\mu$  is the dynamic viscosity,

$l$  is the characteristic length. For wings, it is the mean aerodynamic chord length [17].

Since the Optimized 14, Morphed 10 and Morphed 16.5 wings are tapered, the characteristic length is the mean aerodynamic chord for these wings.

Mean aerodynamic chord is calculated according to the following formula [39]:

$$\bar{c} = \frac{2}{3} * c_r \frac{1+\lambda+\lambda^2}{1+\lambda} \quad (4.2)$$

where  $\lambda$  is the taper ratio;

$$\lambda = \frac{c_t}{c_r} \quad (4.3)$$

and  $c_r$  is the root chord length of the wing and  $c_t$  is the tip chord of the wing.

Mean Aerodynamic chords of the wings are presented in Table 4.1.

Table 4.1 Mean Aerodynamic Chords of the Wings

	<i>Base</i>	<i>Optimized 14</i>	<i>Morphed 10</i>	<i>Morphed 16.5</i>
MAC (cm)	6	7.5359	9.2943	6.4408

The ambient temperature measurements are done day by day and the flow temperature inside the tunnel is measured with Dywer 471 Thermo-Anemometer. The humidity of the air and air pressure is taken from weather forecasting source [40]. The altitude of Ankara, which is 938 meters, is used for the calculations. Dynamic viscosity is primarily effected by temperature and effect of pressure is negligible, so it isn't included in the calculations [41].

The viscosity is calculated by Sutherland's formula as follows [41]:

$$\mu = \mu_0 * \left( \frac{0.555 * T_0 + C}{0.555 * T + C} \right) * \left( \frac{T}{T_0} \right)^{3/2} \quad (4.4)$$

Where T is the temperature (in degrees Rankine),

T<sub>0</sub> is the reference temperature (in degrees Rankine),

C is the Sutherland's constant.

μ<sub>0</sub> is the reference viscosity (in cP (centipoise), 1cP= 0.001 kg/m-s) at temperature T<sub>0</sub>

μ is the resultant dynamic viscosity of the air in cP

Reference values and Sutherland's constant is taken as; C= 120, T<sub>0</sub>= 524.07 ° R and μ<sub>0</sub>= 0.01827 cP [41] [42].

The properties of ambient conditions and calculated dynamic viscosity is presented in Table 4.2.

Table 4.2 Ambient Conditions and Flow Properties

<i>Properties</i>	<i>Base</i>	<i>Optimized 14</i>	<i>Morphed 10</i>	<i>Morphed 16.5</i>
<i>Flow Temperature (°C)</i>	21.6- 23.4	26 - 27	21.3 - 23	21.5 - 25.5
<i>Ambient Temperature (°C)</i>	14	23	21	18
<i>Density of the air (kg/m<sup>3</sup>)</i>	1.06	1.045	1.061	1.054
<i>Humidity (%)</i>	75	49	68	73
<i>Ambient Pressure (hPa)</i>	1008.47	1011.38	1016.93	1008.66
<i>Dynamic viscosity (kg/m-s)</i>	1.8468E-05	1.8690E-05	1.8468E-05	1.8542E-05

According to the calculated mean aerodynamic chords and flow properties the Reynolds Number for each experiment free stream velocity for the four half wing models are calculated according to the Equation 5.1 and presented in Table 5.3.

Table 4.3 Reynolds Numbers

Free Stream Velocity	<i>Base</i>	<i>Optimized 14</i>	<i>Morphed 10</i>	<i>Morphed 16.5</i>
<i>10 m/s</i>	34437.62	42135.70	53396.16	36611.51
<i>11 m/s</i>	37881.38	46349.27	58735.78	40272.66
<i>12 m/s</i>	41325.14	50562.84	64075.40	43933.81
<i>13 m/s</i>	44768.90	54776.41	69415.01	47594.96
<i>14 m/s</i>	48212.67	58989.98	74754.63	51256.11
<i>15 m/s</i>	51656.43	63203.55	80094.25	54917.26
<i>15.5 m/s</i>	53378.31	65310.33	82764.06	56747.84
<i>16.5 m/s</i>	56822.07	69523.90	88103.67	60408.99

#### 4.2.1 Base Wing

Base Wing in the Tunnel during the experiment is shown in Figure 4.1.



Figure 4.1 Base Wing in Wind Tunnel

The lift and drag curves of the Base Wing are presented in Figures 4.2 and 4.3. As it can be seen from the lift curve, at low angles of attack values, the lift curve slope is different from the higher angle of attack values. This is suggested to be a result of the trailing edge separation at the lower surface of the airfoil at low angles of attack.

In the lift curve of the Base Wing, it is seen that from 13 m/s to 14 m/s free stream velocity, there is a jump in the lift curve. As free stream velocity decreases, boundary layer thickness also increases, which changes the effective airfoil shape. Furthermore, low Reynolds number flows are more prone to flow separation. When the flow is laminar, boundary layer thickness is proportional to  $1/Re_x^{0.5}$  and when it is turbulent, it is proportional to  $1/Re_x^{0.2}$ . Thus, after some point, as the free stream velocity so the Reynolds Number increases, the boundary layer becomes thinner, which causes a jump in the lift curve.

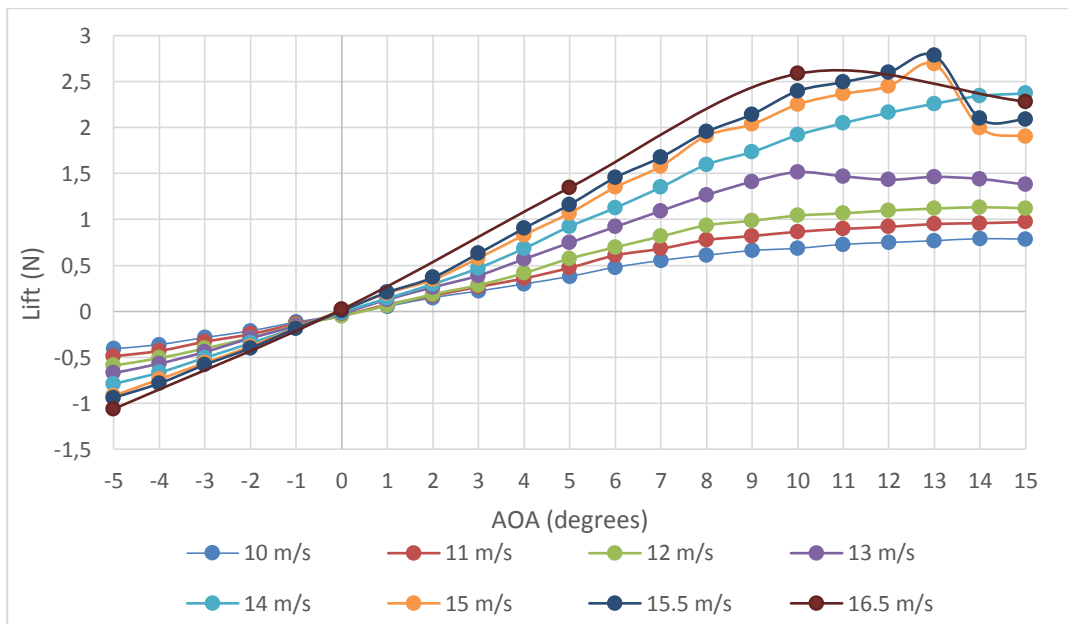


Figure 4.2 Lift (N) vs AOA (degrees) curves of the Base Wing

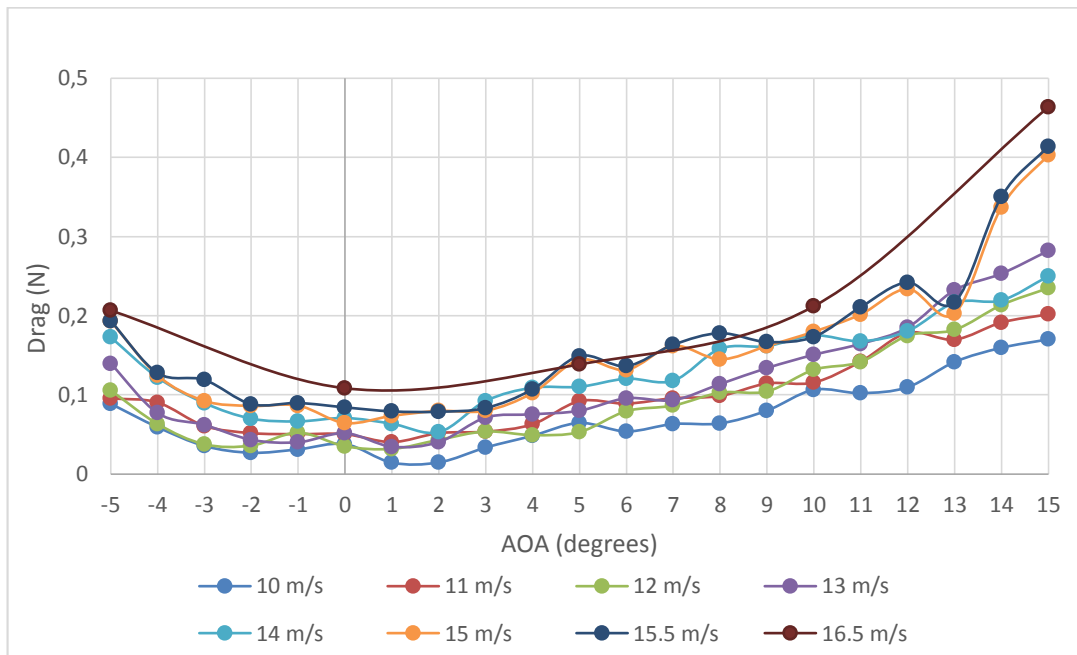


Figure 4.3 Drag (N) vs AOA (degrees) curves of the Base Wing

According to the numerical studies of Bagade, Krishnan and Sengupta [43], near negative stall angles, unsteady bubbles are observed on the lower surface and their intensity decreases as angle of attack increases where at all negative angles of attack including 0 degrees, flow on the upper surface of the airfoil is attached [44]. The lower surface separation at low angles of attack graph from this study is revised and presented in in Figure 4.4. As the angle of attack increases from negative values the separation moves to trailing edge and then disappears and flow starts to attach to the lower surface of the wing. The lift curve of this wing at  $Re=60000$ , which is close to that of the Base Wing case, is shown in Figure 4.5 for low angle of attack values. Lift curve slope variation of this wing has similar characteristics to the Base Wing of the present study. Thus, it is most probable that the Base Wing experiences a trailing edge separation on the lower surface at low angle of attack values.

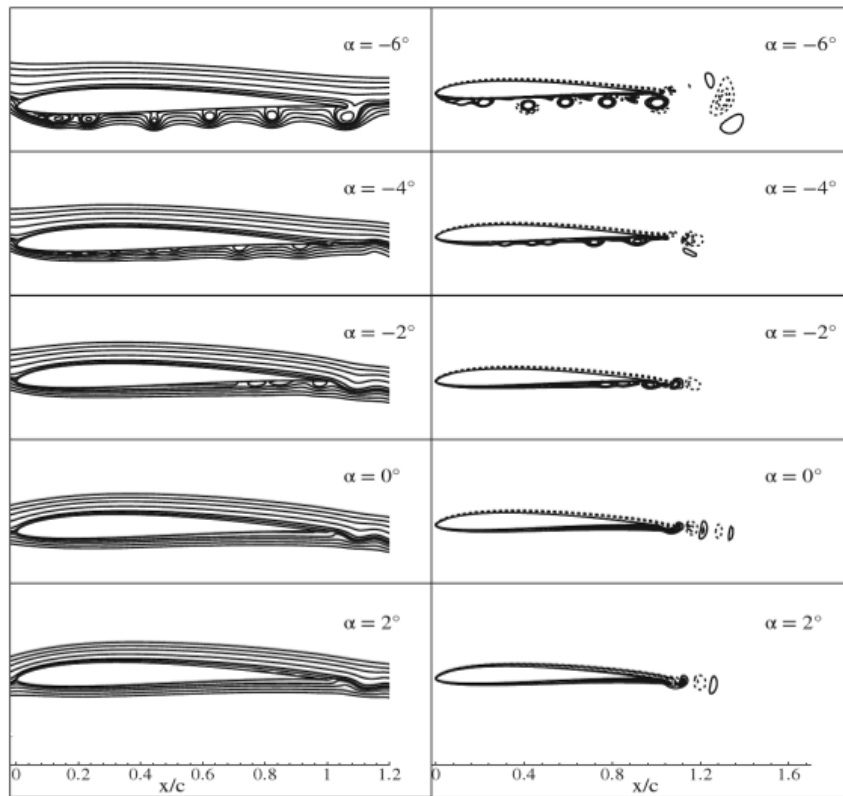


Figure 4.4 Numerical Stream function (left) and vorticity contours (right) for AG24 airfoil ( $Re=60000$ ) [44]

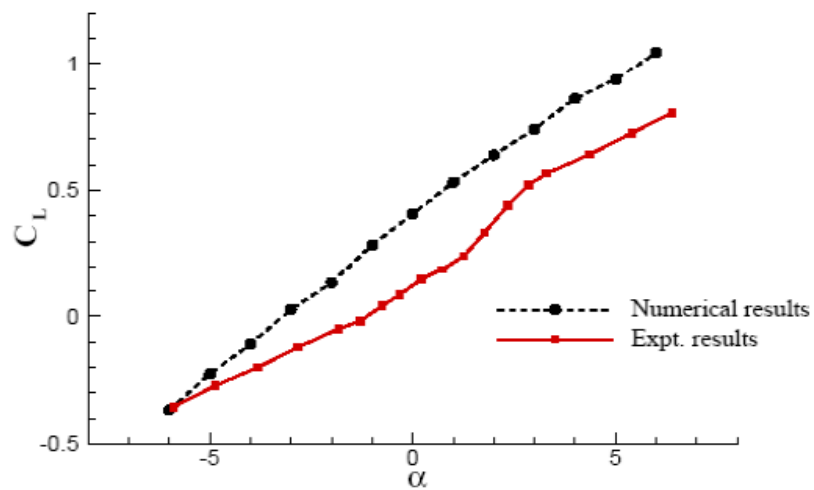


Figure 4.5 Lift curve of AG24 airfoil at  $Re=60000$  [43]

It is seen from Figure 4.2 that, for low velocities the lift curves are very smooth. With the increasing velocity after 13 m/s there is a large increase in the lift value at high

angle of attack values. 15.5 m/s and 15 m/s free stream velocities has the similar trend and the lift decreases after 13 degrees instantly. In the drag curves, it is also observed that there is a sudden increase in the drag value at these velocities. Although 16.5 m/s is analyzed at 5 angle of attack values, the trend between 10 degrees to 15 degrees is also expected to be similar at 15 m/s and 15.5 m/s velocities since there is also a drop in lift and increase in drag. It is a strong indication of separation.

For the low velocities at low angles of attack values the laminar boundary layer stays attached to the airfoil surface. However, as the angle of attack increases, when a laminar boundary layer comes across an adverse pressure gradient, it generates enough strength so that laminar boundary layer separates from the airfoil. This happens at point S in Figure 4.6. Then, due to this separation, a shear layer is formed over the bubble. The shear layer becomes very unstable and flow reversal occurs near the surface. Shear layer make a transition to turbulent flow at point T. The region before T is called dead-air region because the reversal flow is very slow in this region. After transition, the reverse flow magnitude increases and vortex type flow forms. When the turbulent shear layer entrains high energy external flow, pressure can be recovered and bubble reattaches, which results in a formation of the separation bubble. Point R in the Figure 4.4 indicates this reattachment point [45] [46]. Laminar separation bubble can be seen from a different angle in Figure 4.7.

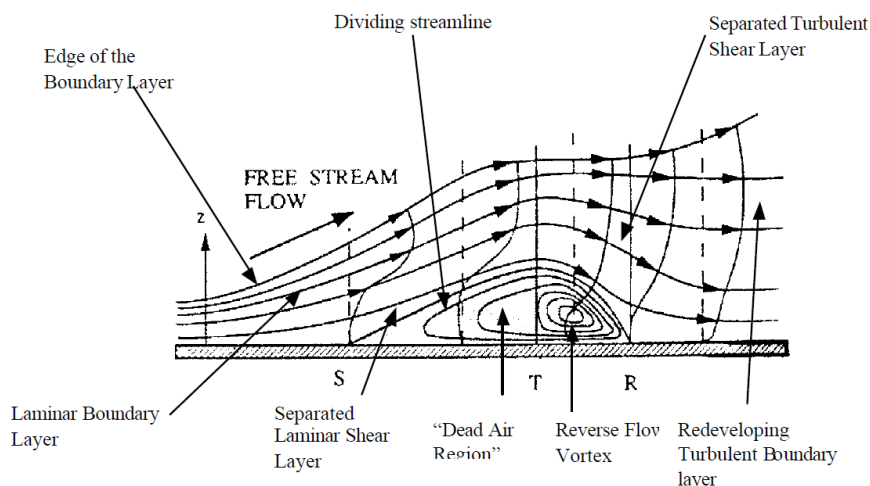


Figure 4.6 Separation Bubble Formation [46]



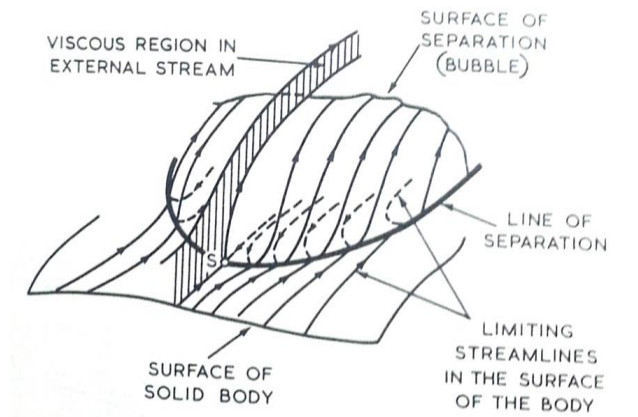


Figure 4.7 Laminar Separation Bubble [47]

Thus, at high angles of attack laminar separation bubble is formed on the airfoil upper surface and when the velocity gets higher, external flow energy is increasing so that the flow reattaches. This separation and reattachment behavior can be seen in 15 and 15.5 m/s and expectedly at 16.5 m/s between 13 to 14 and 14 to 15 degrees, respectively.

#### 4.2.2 Optimized 14 Wing

Optimized 14 wing is shown in Figure 4.8.

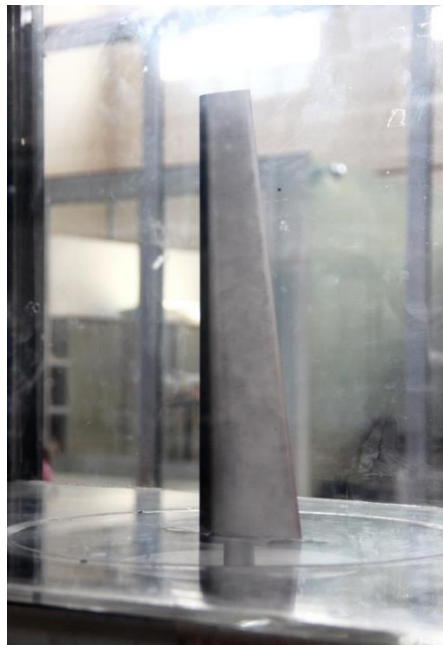


Figure 4.8 Optimized 14 Wing in the wind tunnel

Optimized 14 wing has a smooth lift curve at low velocities, shown in Figure 4.9. This is because, at low angles of attack flow streams can attach to the wing surface and leave the trailing edge smoothly. Moreover, at low angles of attack, adverse pressure gradient is low and no separation occurs on the upper surface [45].

At the lower surface, a separation at trailing edge, which is discussed in Base Wing results, is also observed in this wing with the change of lift curve slope at low angle of attack values.

At 13 m/s, 14 m/s and 15 m/s free stream velocities, lift force value decreases at 10 degrees angle of attack and at 15.5 m/s, the lift decreases at 11 degrees angle of attack. At the same time, drag curve slope which is shown in Figure 4.10 increases for these free stream velocities. For 13 m/s and 14 m/s, the flow starts to reattach to the upper surface between 13 degrees to 14 degrees. The lift curve for 15.5 m/s free stream velocity show the same characteristics with 15 m/s. For the 16.5 m/s free stream velocity, the trend looks similar with other velocities until 10 degrees and the trend between 10 to 15 degrees is not certain because of lack of data, but expected to be similar as 15 m/s and 15.5 m/s free stream velocities.

This behavior of the lift and drag curve can be explained by the laminar separation and also the existence of the laminar separation bubbles. When the angle of attack increases, separation bubble will be generated on the upper surface of the wing. Then, after some point, at the downstream of the separation bubble, the separated laminar boundary layer reattaches on the upper surface of wing as explained in the Base Wing section.

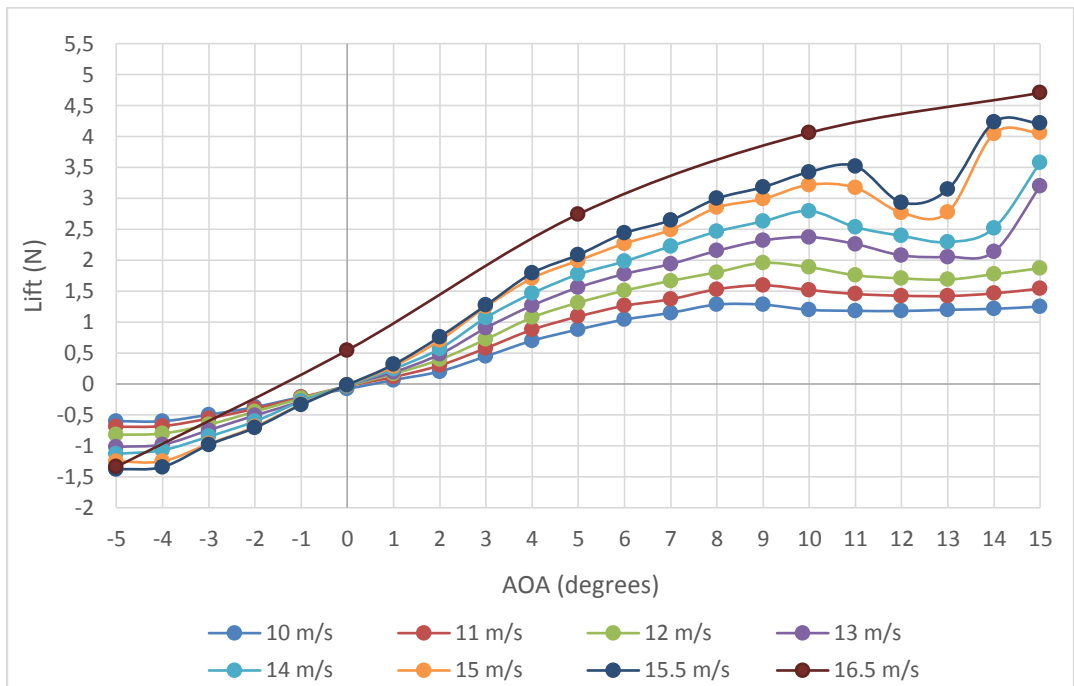


Figure 4.9 Lift vs AOA curves of Optimized 14 Wing

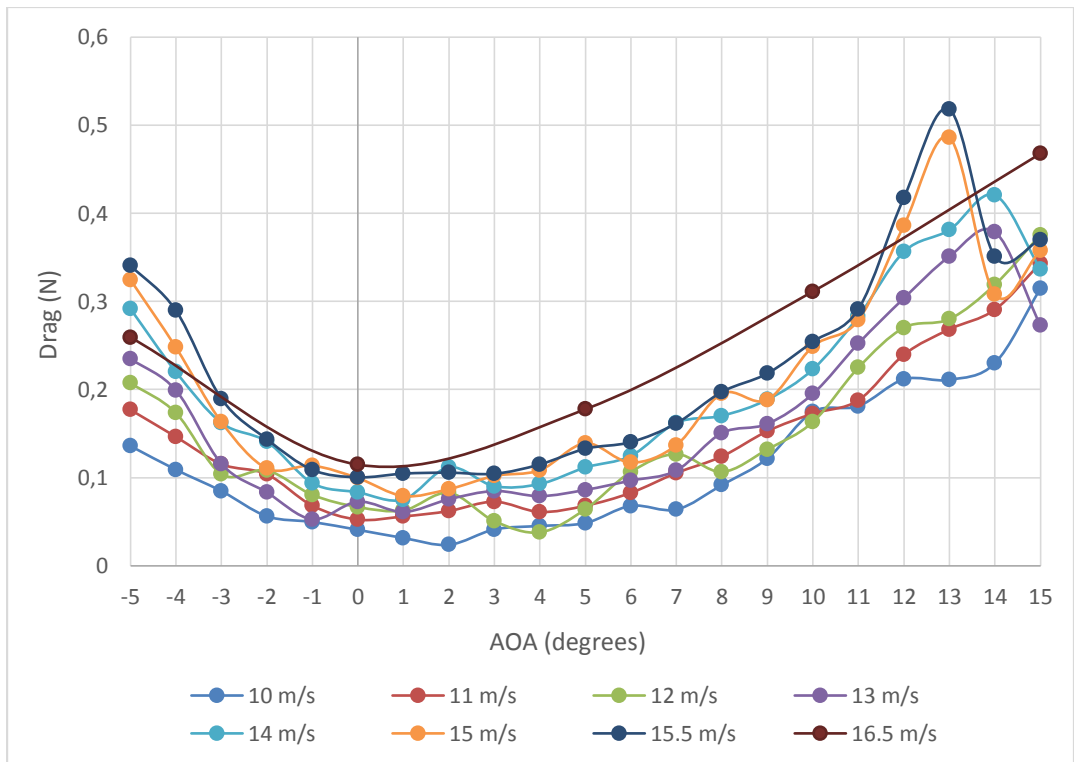


Figure 4.10 Drag vs AOA curves of Optimized 14 Wing

The bubble moves forward as the angle of attack increases and at high velocities, in other words with high kinetic energy flow around the bubble, the external fluid is entrained into the vortex in the bubble and reattaches again to the airfoil surface. Separation and reattachment points are shown in Figure 4.11.

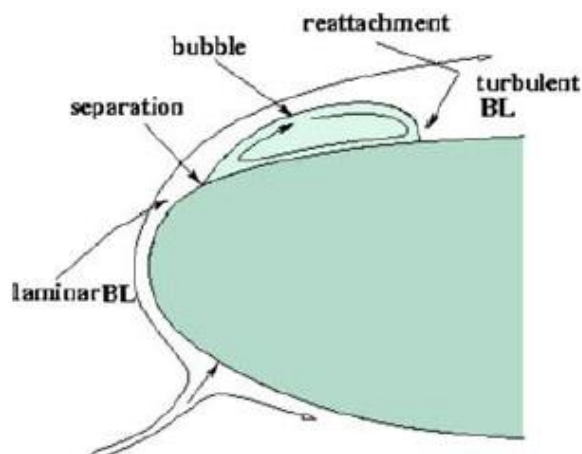


Figure 4.11 Laminar separation bubble at low Reynolds number [45]

According to a previous study of Lee et al. [46], this type of lift curve is called ‘recover’ type. In this study the lift curves of the various wings are analyzed and named abnormal if they do not look like the conventional lift curves. This categorization is redrawn in another study of Chen and Bernal [48] and presented in Figure 4.12.

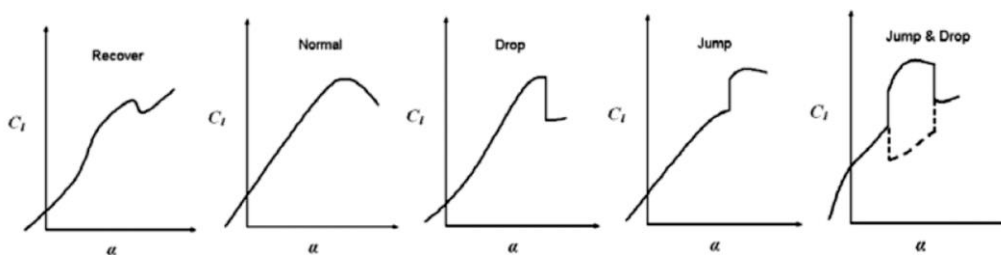


Figure 4.12 Classification of lift curves

Optimized 14 wing shows the recover trend in this categorization especially at high free stream velocities. According to a previous study [46], practically all airfoils exhibit recovery tendency. Some of them recover more obviously and some do not. Camber and thickness of the airfoil are significant parameters for the recovery characteristics. Low camber, moderate thickness (8% to 12%) airfoils have good recovery characteristics.

#### **4.2.2.1 Oil Flow Visualization**

In order to support the idea of the laminar separation and laminar separation bubble, oil flow visualization is conducted for Optimized 14 Wing, where these effects are more obvious on the lift and drag curves. The experiments are conducted at 14 m/s and 15 m/s free stream velocities.

##### **4.2.2.1.1 At 14 m/s**

The oil visualization is conducted at 14 m/s free stream velocity at angle of attack values of 5 degrees to 15 degrees with one degree increments.

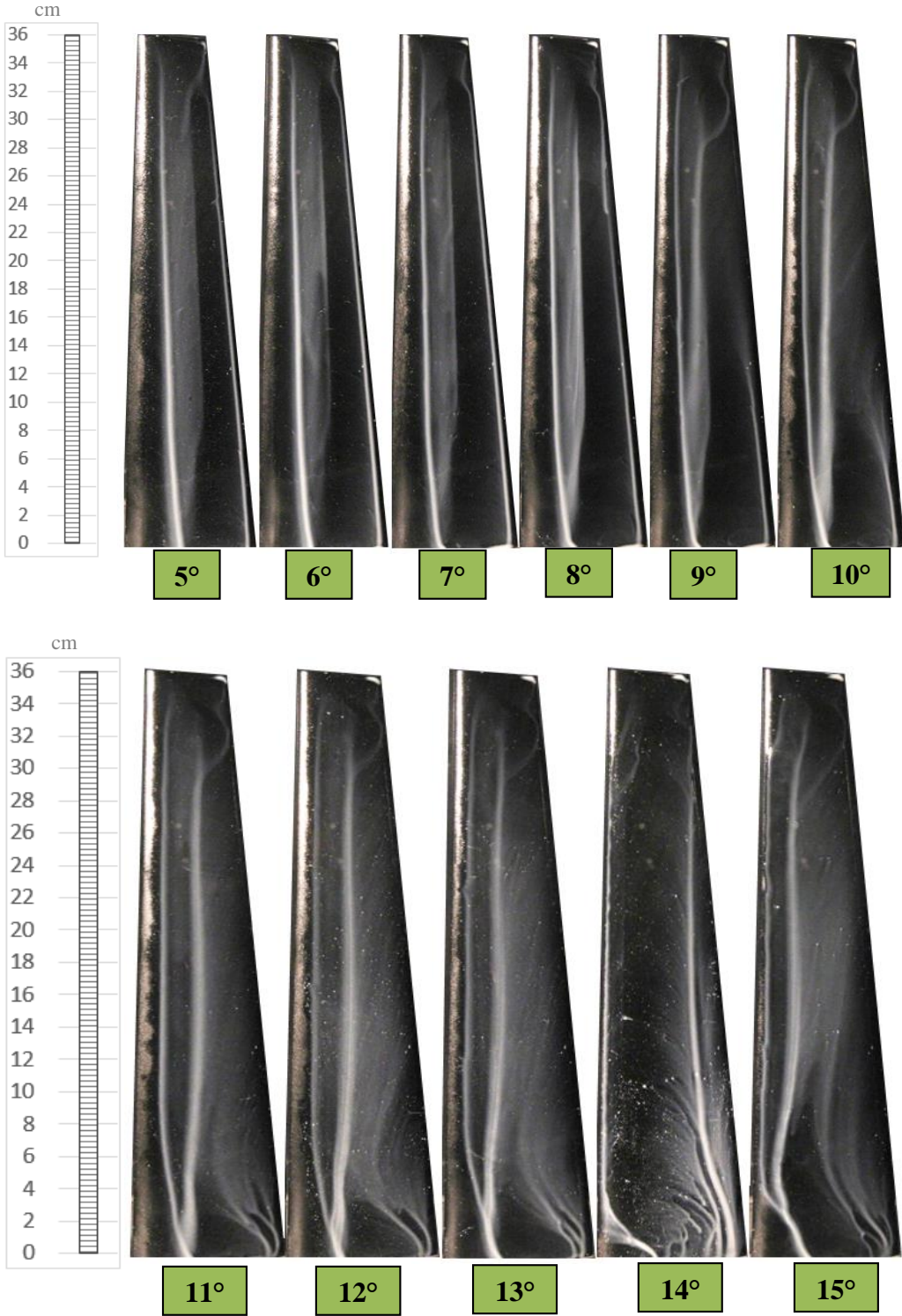


Figure 4.13 Oil flow Visualizations of the upper surface of Optimized 14 Wing at 14 m/s

Looking at Figure 4.13, it is seen that from 5 to 10 degrees, weak laminar separation is observed. As the angle of attack increases, the separation point moves forward to the leading edge. The drag increases with the increasing lift at these angle of attack values. The separation and attachment regions are shown in Figure 4.14.

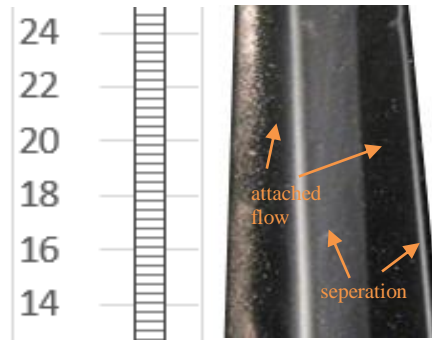


Figure 4.14 Attachment and separation locations of Optimized 14 Wing at 5 AOA

After 10 degrees it is seen that there are two lines of accumulation of the oil. The first one is the separation and sudden reattachment while the second accumulation line is the accumulation of the reverse velocity gradients of the bigger separation region. This region enlarges with the increasing angle of attack and lift reduces drag increases in this region until 14 degrees as supported by the load cell experiments. Between these two accumulation lines there is an attached flow. Oil accumulations are shown in detail in Figure 4.15 for 11 degrees.

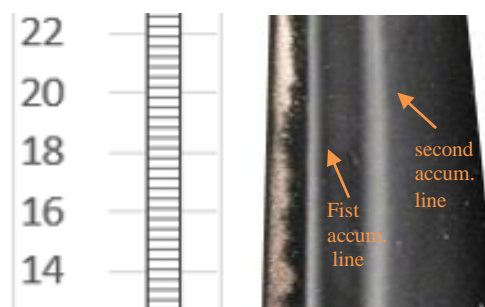


Figure 4.15 Oil accumulation lines of Optimized 14 Wing at 11 AOA

Same behavior seen in 9, 10, 11, 12 and 13 degrees is also observed in a study of Thake [49], which is in the close Reynolds Number range with Optimized 14 Wing. In the oil flow visualization results and the PIV results of that study, presented in

Figure 4.16, two lines of separation and reverse flow accumulation can be seen on the upper surface of the wing.

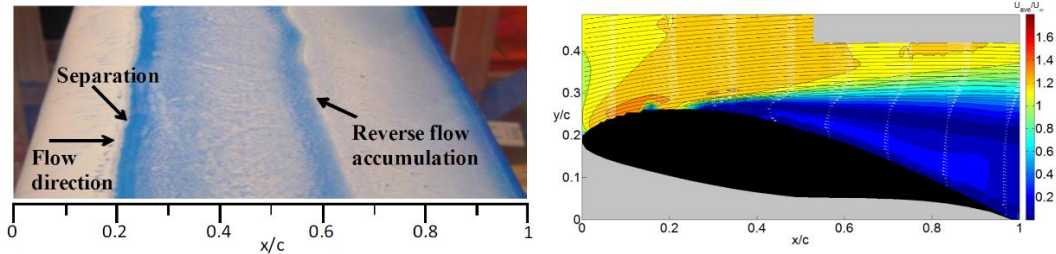


Figure 4.16 Oil flow accumulation and PIV of a wing at AOA=10 degrees, Re=64000 [49]

At 14 degree angle of attack in Figure 4.13, separation bubble is formed on the leading edge of the airfoil and after transition, the boundary layer is attached as a turbulent boundary layer. Since the turbulent boundary layer has more resistance to adverse pressure gradients, it separates later closer to the trailing edge of the airfoil [49]. After this point, lift increases and drag decreases at 15 degrees and the bubble disappears while the drag curve falls back into curve of laminar separation. As the angle of attack increases the separation bubble burst may result in airfoil stall.



#### 4.2.2.2 At 15 m/s

The oil flow visualizations are performed in the angle of attack values at the regions at which most of the lift and drag curve changes are observed according to the load cell experimental results at 15 m/s.

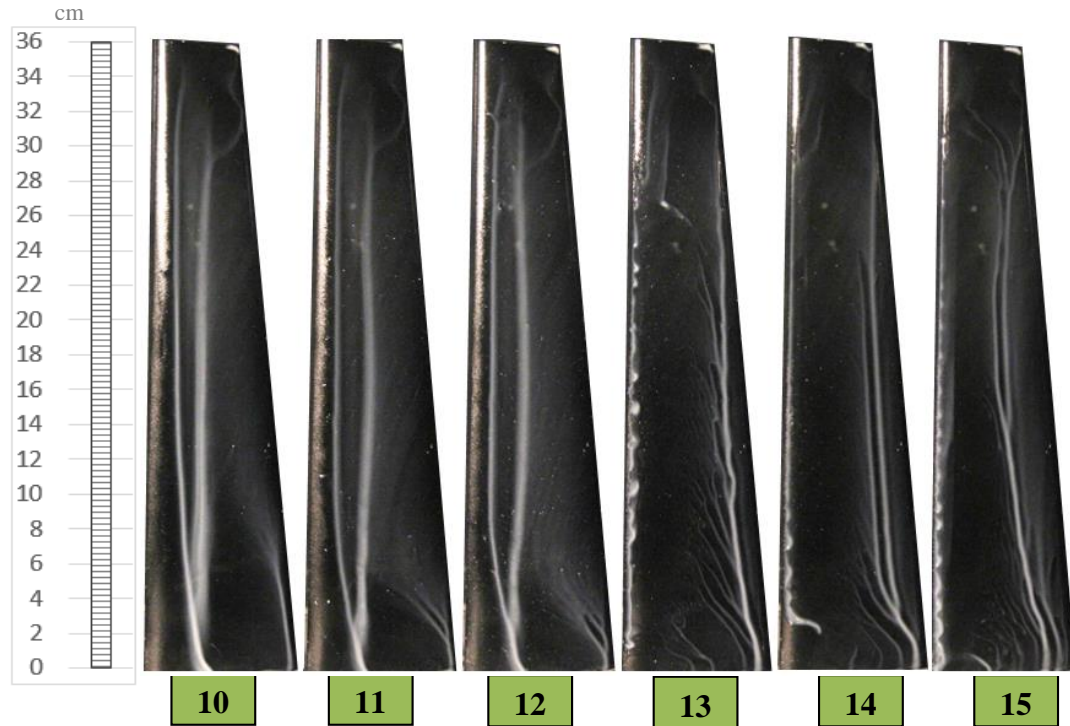


Figure 4.17 Oil flow Visualizations of the upper surface of Optimized 14 Wing at 15 m/s

As it can be seen from Figure 4.17, At 10 degrees to 12 degrees, there are two lines of accumulation of the oil. The first line is the laminar separation and the flow instantly reattaches. The second accumulation is because of the strong recirculation of the reverse flow which is separated. In this region as angle of attack increases the separation point moves forward to the leading edge. Lift decreases and drag force increases as presented in the load cell experimental results.

At 13 and 14 degrees, the laminar separation bubble is formed at the leading edge. Over this bubble, boundary layer transitions into turbulent boundary layer and this turbulent boundary layer separates further downstream due to its resistivity to adverse pressure gradient. Since the majority of the flow is attached this causes an increase in

the lift and decrease in drag value. As the angle of attack increases the bubble moves upstream enabling the boundary layer to reattach, improving lift. In the study of Jones et.al [50], similar phenomenon is observed such that separation bubble moves forward with the increasing angle of attack, and similarly, at the trailing edge of the wing there is a turbulent separation region, which is shown in Figure 4.18.

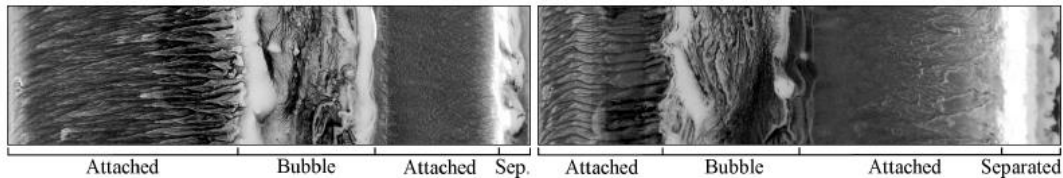


Figure 4.18 E423 Airfoil at  $Re=1.2 \times 10^5$  at 0 degree AOA (at left) and 12 degrees AOA (at right) [50]

The turbulent separation region increases as angle of attack increases from 14 degrees to 15 degrees resulting in a drop in lift and corresponding increase in the drag. The lift and drag curves starts come back into curve of laminar separation, which is clearly illustrated in Figure 4.19, whereas the disappearance of the laminar separation bubble is not seen as in the case of 14 m/s 15 degrees, and could be seen at higher angle of attack values.

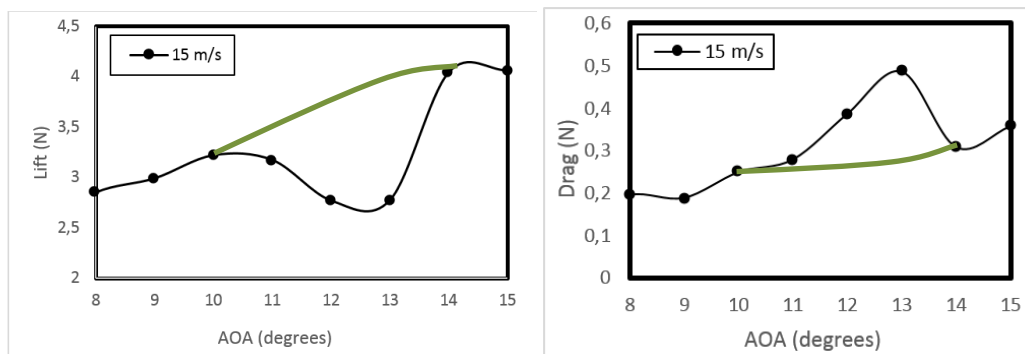


Figure 4.19 Lift and drag values of Optimized 14 Wing at 15 m/s

It should be noted that change in the surface roughness of the wings after painting into black for PIV measurements and wind tunnel free stream turbulence changes may have affected the results.

### 4.2.3 Morphed 10 Wing

Morphing 10 wing attachment to the wind tunnel is shown in Figure 4.20.



Figure 4.20 Morphed 10 Wing in the tunnel

The lift curve of the Morphed 10 wing, which is presented in Figure 4.21, is very smooth for all the velocities. It has to be noted that this wing yields the highest Reynolds numbers among the four wing models tested due its greater chord and size. At low angles of attack, the slope of the lift curve is different due to lower surface trailing edge separation. At 10 m/s and 11 m/s, at angle of attack values greater than 9 degrees slight decrease in lift is observed and recovering at 13 degrees. The drag curve at 10 m/s, presented in Figure 4.22, shows only slope changes but still increasing drag force, while for 11 m/s decrease in lift causes an increase in drag (increasing slope) and sudden decrease when the lift recovers at 13 degrees. At these velocities flow separation occurs at angles of attack around 9 degrees and the flow attaches again at angles of attack around 13 degrees. At 12, 13 and 14 m/s free stream velocities flow separation region is thought to be confined and has little effect on lift and drag curves at least until 14 degrees angle of attack. It is seen that there is a sudden drop of the drag value at 15 degrees in some of the velocities. This behavior may be caused by the instability of the flow based upon the vibration of the wind tunnel at high velocities. As discussed before, the wind tunnel cannot run for long durations at high velocities. Thus, the unexpected reductions in the drag values are probably because of

the experimental issues. The behavior of the lift and drag values at 16 m/s is expected to be similar to 15 m/s and 15.5 m/s looking at the closeness of the values at the measured angles at both lift and drag curves. Morphed 10 Wing has a normal lift profile referencing to Figure 4.12.

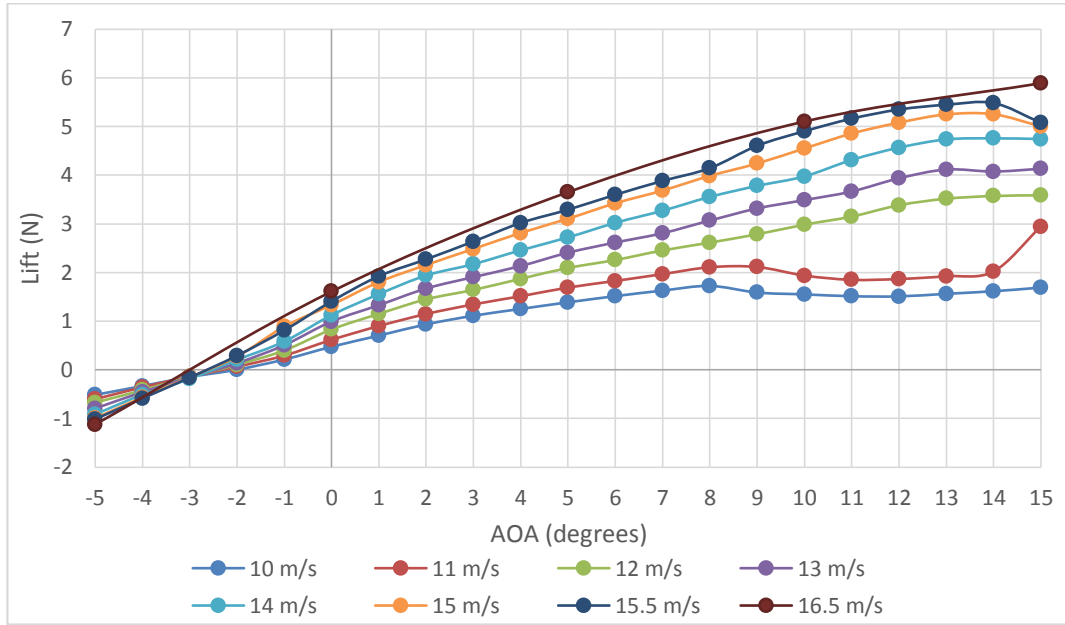


Figure 4.21 Lift vs AOA curves of Morphed 10 Wing

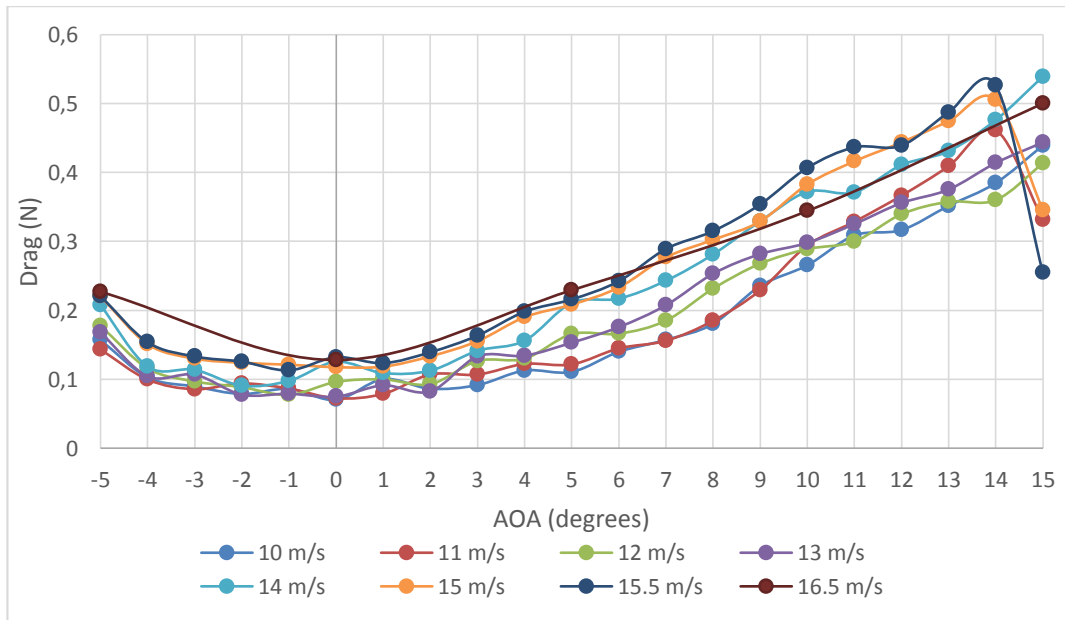


Figure 4.22 Drag vs AOA curves of Morphed 10 Wing

#### 4.2.4 Morphed 16.5 Wing

The morphed 16.5 wing during the experiments is shown in Figure 4.23.

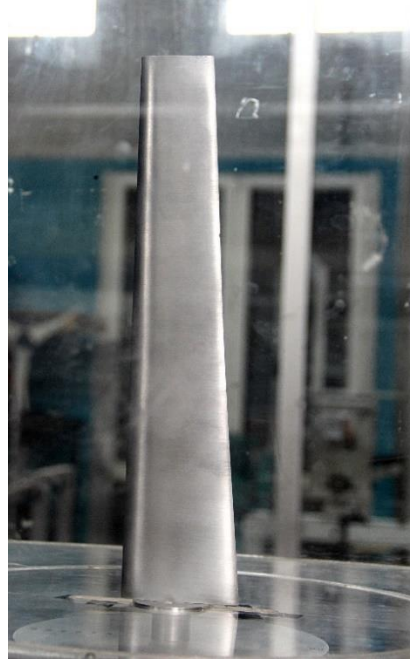


Figure 4.23 Morphed 16.5 Wing in the tunnel

For Morphed 16.5 Wing, there are small drops and rises in the lift curve as it can be seen in Figure 4.24. It has to be pointed out that this wing yields the lowest Reynolds number values among the four wing models tested. The drag curve of the morphed 16.5 Wing is presented in Figure 4.25. Flow separation region is thought to be confined and has little effect on lift and drag curves.

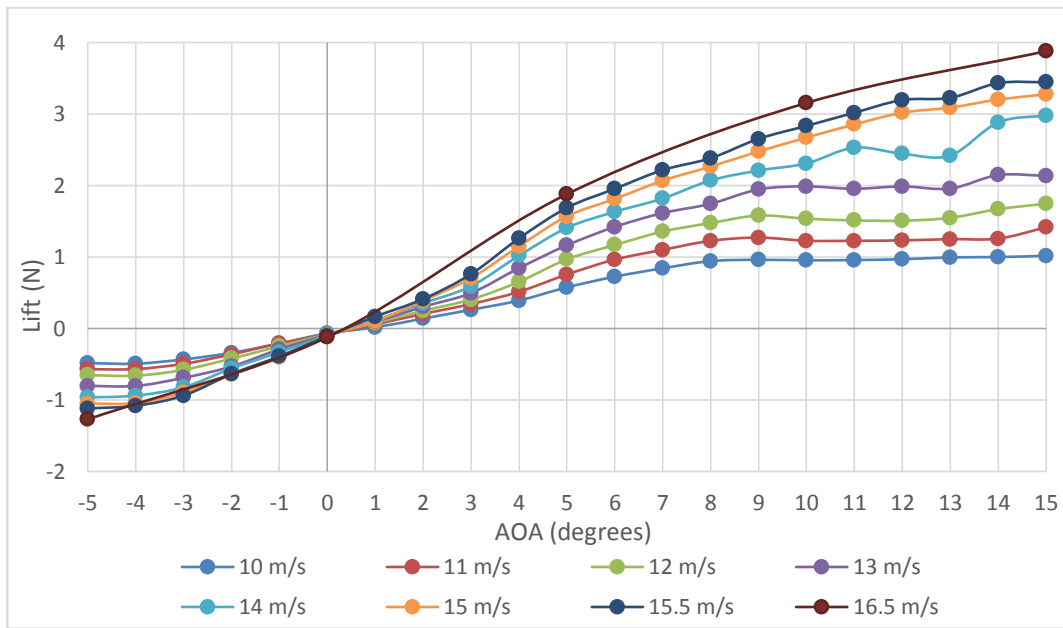


Figure 4.24 Lift vs AOA curves of Morphed 16.5 Wing

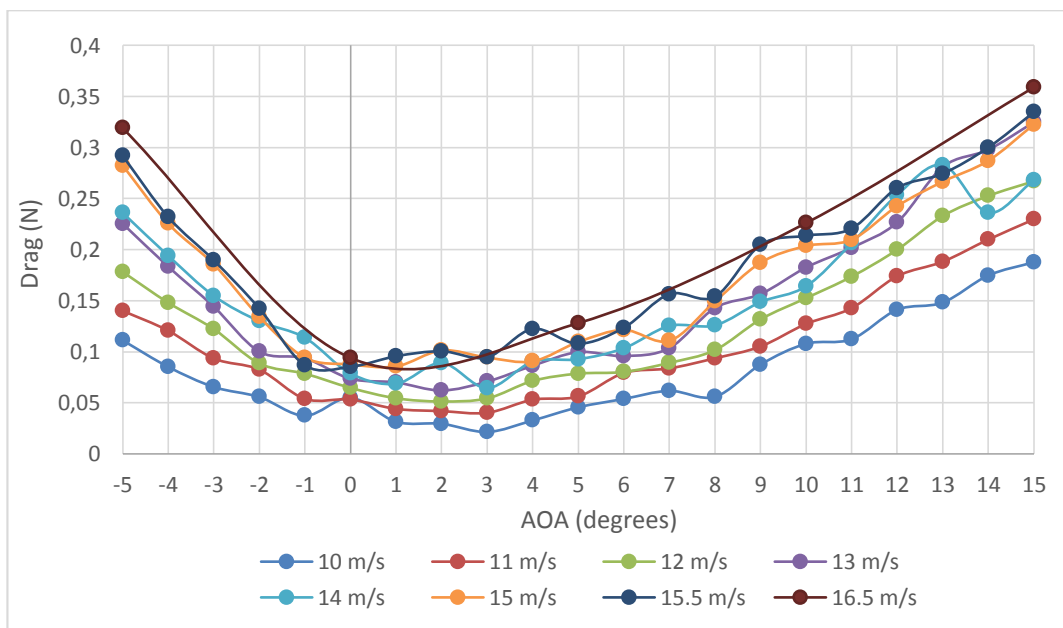


Figure 4.25 Drag vs AOA curves of Morphed 16.5 Wing

At low angle of attack values, lift curve slope is smaller than in the high angle of attack values for all velocities. This is due to the lower surface separation at the trailing edge which is discussed in Base Wing section. Figure 4.26 shows the lift curve from the study of Bagade, Krishnan and Sengupta [43], but with free stream turbulence.

Their wing encounters separation on the lower surface at low angles of attack and low Reynolds number similar to Morphed 16.5 Wing.

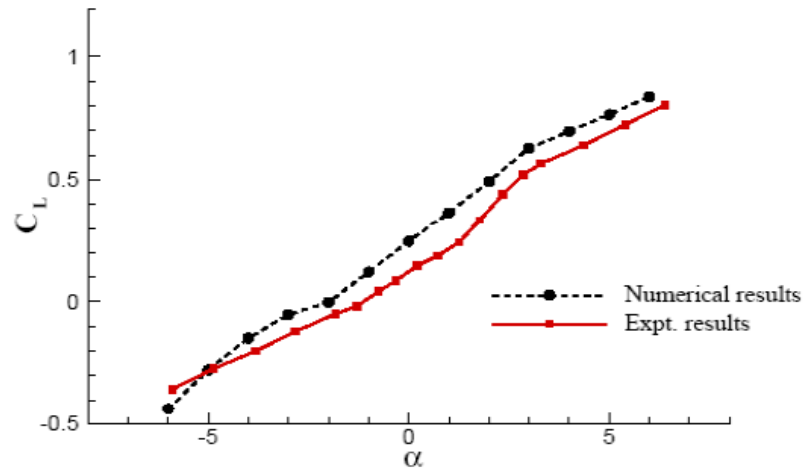


Figure 4.26 Lift curve of AG24 airfoil at  $Re=6000$  with 0.18% free stream turbulence [35]

The classification of the lift curve is ‘normal’ according to Figure 4.12. At high angle of attack values, separation behaviour is not prominent. The results show that Morphed 16.5 Wing operates satisfactorily at high velocities.

### 4.3 Comparison of the Experimental and Numerical Lift and Drag Curve Results of Load Cell Measurements

#### 4.3.1 Comparison

In this section, experimental results of drag and lift values obtained by load cell measurements are compared with the numerical results obtained by 3D Panel Method and 2D Boundary Layer solver in a previous study of Körpe [23], named as ‘Panel Method’ and CFD results obtained by ANSYS Fluent software in a previous study of Özkanaktı [27] named as ‘CFD’. There are two experimental results; ‘Experiment’ is results of the current study, whereas the ‘Previous Experiment’ is the previous experiment conducted by Özkanaktı [27]. Slight differences observed between the two experimental data sets are most probably due to the data acquisition system for

acquiring data, table set-up attachment of the wings (vibrations due to wind tunnel on the model is reduced by more rigid attachment) and the new adjustments on the motor shaft and wind tunnel stabilization. The data acquisition (DAQ) system (NI6211) used in the previous experiments has 2.69mV and 0.088 mV accuracy whereas the DAQ used in current experiment (NI9205) has 6.22 mV and 0.157 mV accuracy in maximum and minimum voltage ranges respectively. However, their resolution and sampling rate are the same. Since the accuracy range is low compared to the order of the magnitude of the measurements, changes in the set-up adjustment and motor shaft improvements and wind tunnel stabilization has the major effect on the results. Therefore, with these differences in two experiments, no repeatability problem should be sought for.

#### **4.3.2 Base Wing Results**

For low velocities, the lift force and drag force values of the experimental results are lower than the Panel Method and CFD results as can be seen in Figures 4.27, 4.28, 4.29, 4.30, 4.31, 4.32 ad 4.33. As the free stream velocity increases, the experimental lift values of the Base Wing almost coincides with the numerical results. Moreover, trend of the lift curves of experimental and numerical results in all velocities are very similar. The laminar separation on the upper surface at high velocities, cannot be predicted by 'Panel Method'. The 'CFD' analysis is the closest in terms of the magnitudes and also reduction in lift slope at high angles of attack values.

It can be deduced that the drag estimation of the numerical results are in very good agreement with the experimental results perfectly. The drag estimation is highly accurate. The laminar separation can be better observed in drag estimation of the numerical solutions. Moreover, in the drag curves, 'Panel Method' is close to estimate the trailing edge separation on the lower surface for low angles of attack values. Experimental results are highly close to the Half condition in magnitude and Tunnel condition in terms of the drag slope trends.



The effect of flow separation over the trailing edge of the lower surface and its effect on the lift curve slope at low angles of attack seems does not seem to be well predicted by Panel Method and CFD results.

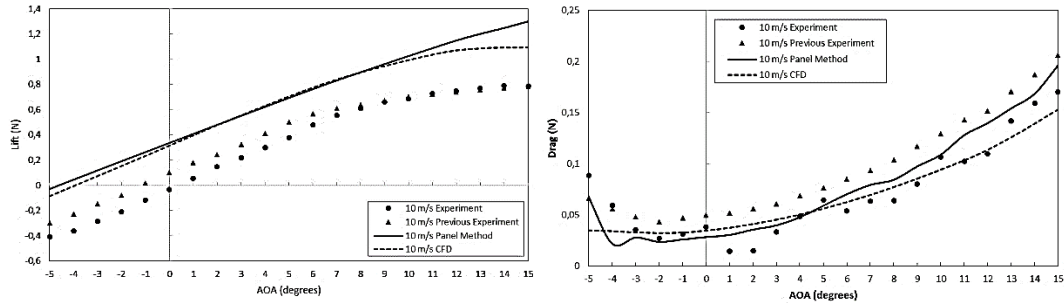


Figure 4.27 Figure 4.28 Lift vs AOA (left) and Drag vs AOA (right) curves of Base Wing at 10 m/s

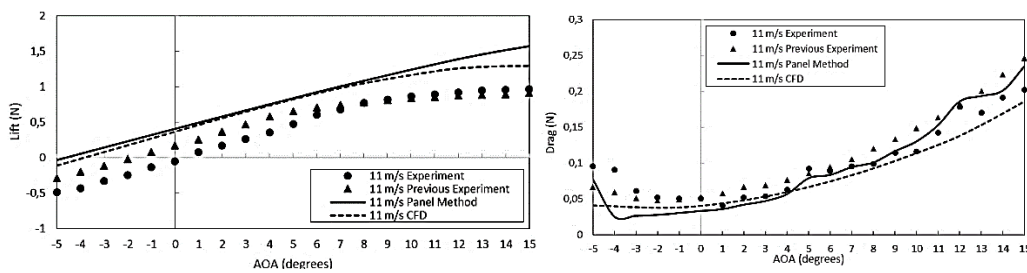


Figure 4.26 Lift vs AOA (left) and Drag vs AOA (right) curves of Base Wing at 11 m/s

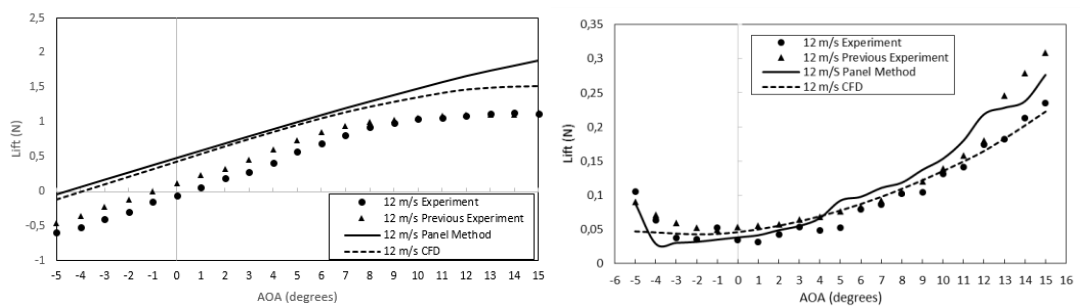


Figure 4.29 Lift vs AOA (left) and Drag vs AOA (right) curves of Base Wing at 12 m/s

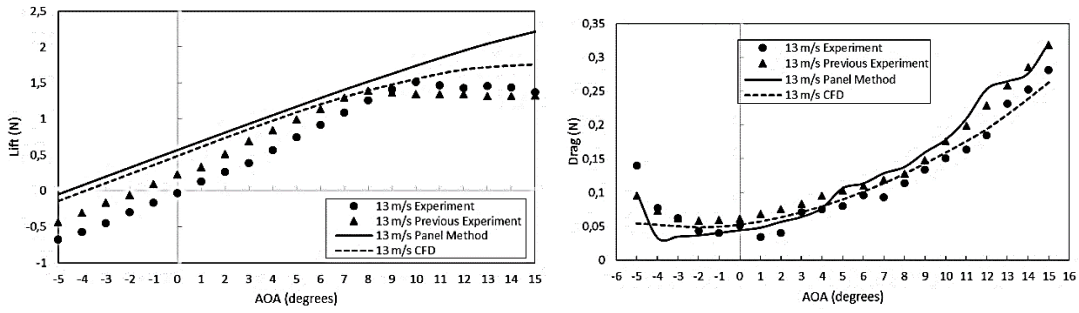


Figure 4.30 Lift vs AOA (left) and Drag vs AOA (right) curves of Base Wing at 13 m/s

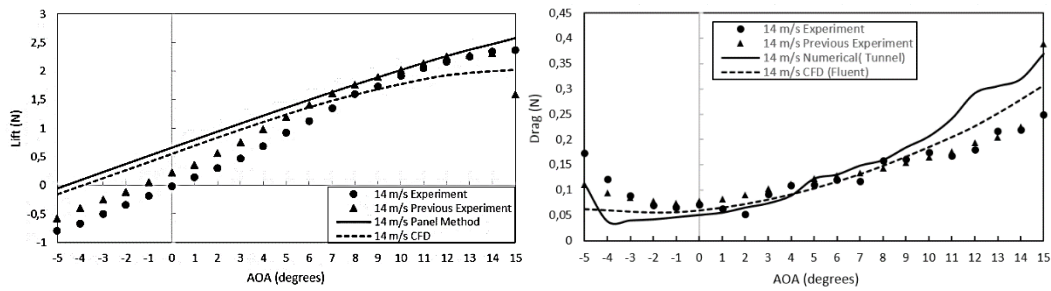


Figure 4.31 Lift vs AOA (left) and Drag vs AOA (right) curves of Base Wing at 14 m/s

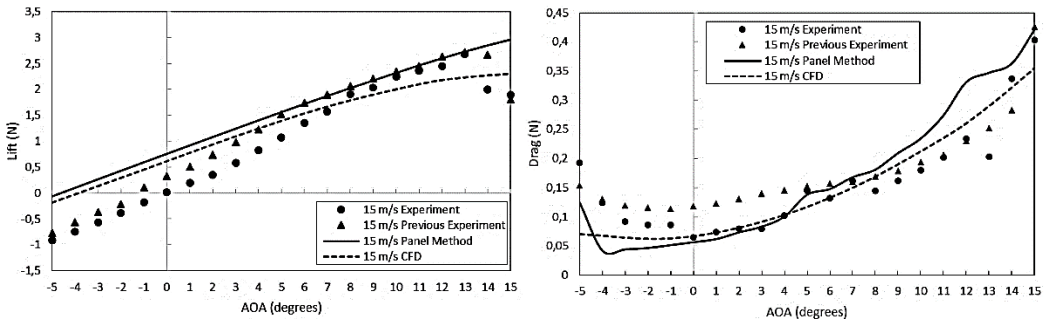


Figure 4.32 Lift vs AOA (left) and Drag vs AOA (right) curves of Base Wing at 15 m/s

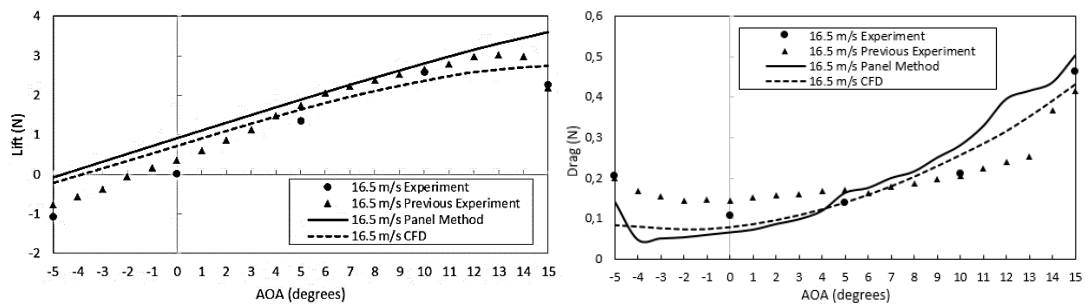


Figure 4.33 Lift vs AOA (left) and Drag vs AOA (right) curves of Base Wing at 16.5 m/s

### 4.3.3 Optimized Wing at 14 m/s

Optimized 14 Wing lift and drag curves are presented in Figures 4.34, 4.35, 4.36, 4.37, 4.38, 4.39, and 4.40.

As can be seen, the laminar separation on the upper surface can be observed in lift curves of the Panel Method. In CFD solution, drag curves overlap with the experimental results especially at 10 m/s, 11 m/s and 12 m/s. The numerical results cannot estimate the separation at the trailing edge of the lower surface at low angle of attack values, whereas in two experimental results it is obviously apparent. For the lift values at 13, and 14 m/s the behaviour of the two experimental results at high angles of attack are different. At 15 m/s previous experimental result starts to show the same trend with the current experiments. Considering the numerical solutions and also laminar separation and recovery behaviour, the current experiment is suggested to be more reliable. Moreover, the previous experimental data is not present for 16.5 m/s free stream velocity.

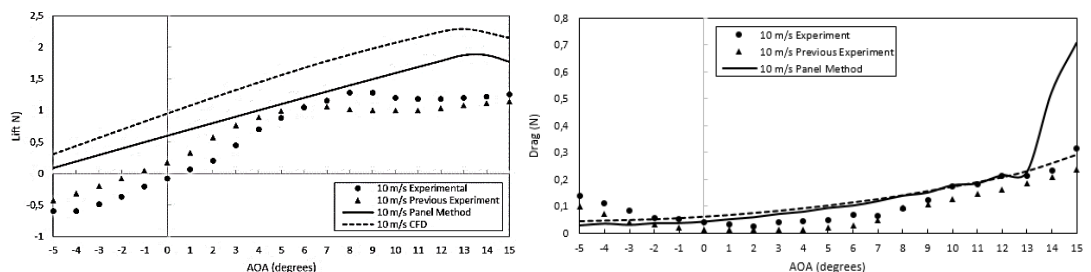


Figure 4.34 Lift vs AOA (left) and Drag vs AOA (right) curves of Optimized 14 Wing at 10 m/s

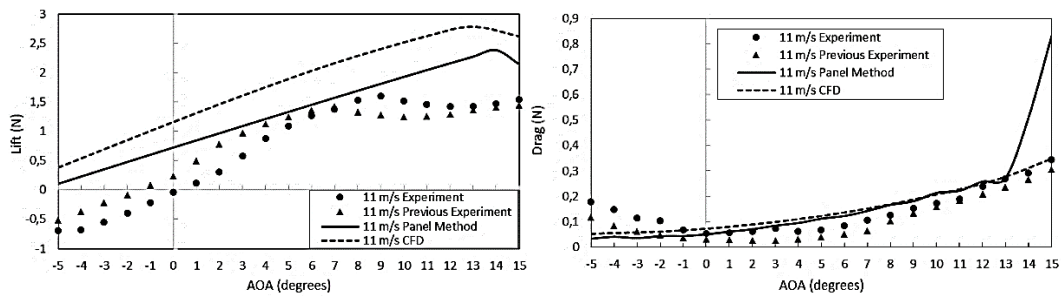


Figure 4.35 Lift vs AOA (left) and Drag vs AOA (right) curves of Optimized 14 Wing at 11 m/s

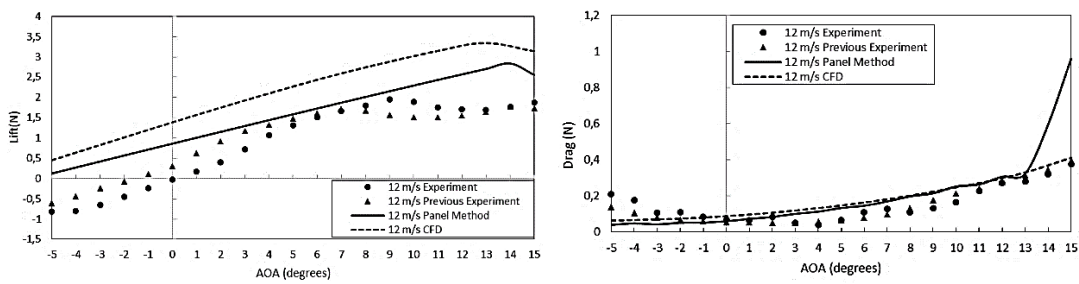


Figure 4.36 Lift vs AOA (left) and Drag vs AOA (right) curves of Optimized 14 Wing at 12 m/s

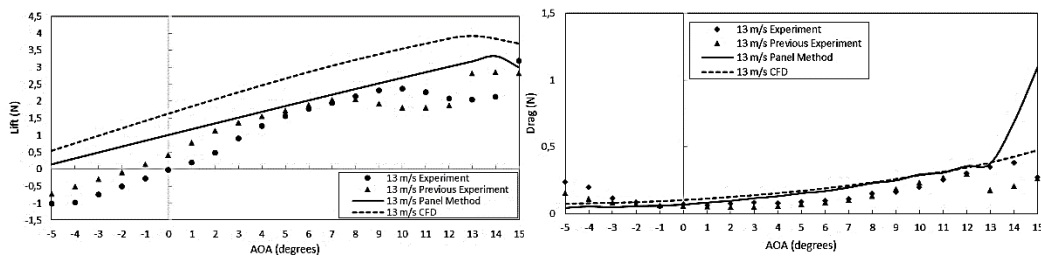


Figure 4.37 Lift vs AOA (left) and Drag vs AOA (right) curves of Optimized 14 Wing at 13 m/s

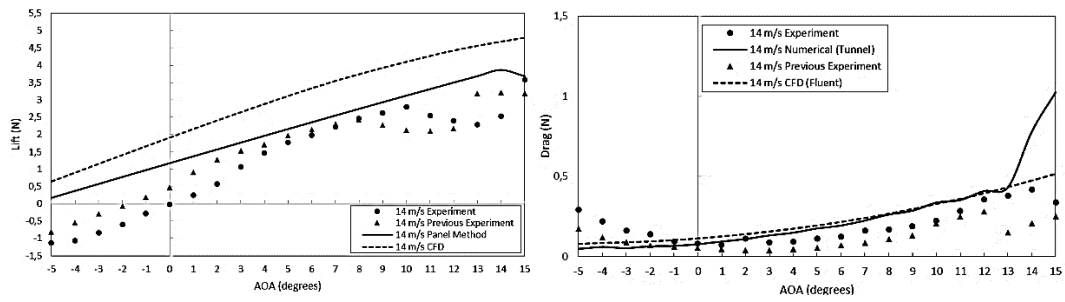


Figure 4.38 Lift vs AOA (left) and Drag vs AOA (right) curves of Optimized 14 Wing at 14 m/s

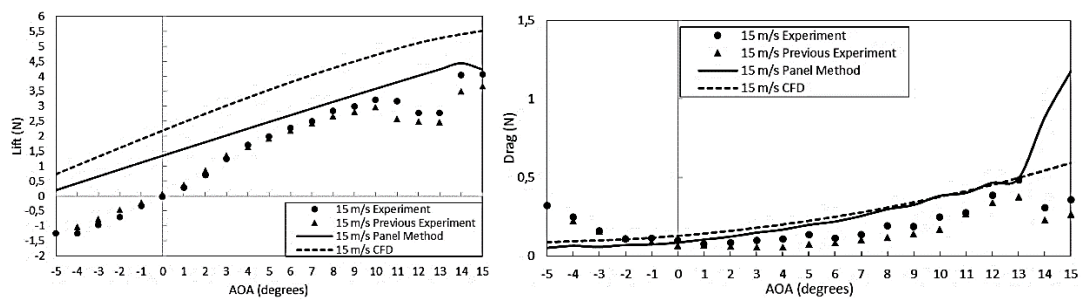


Figure 4.39 Lift vs AOA (left) and Drag vs AOA (right) curves of Optimized 14 Wing at 15 m/s

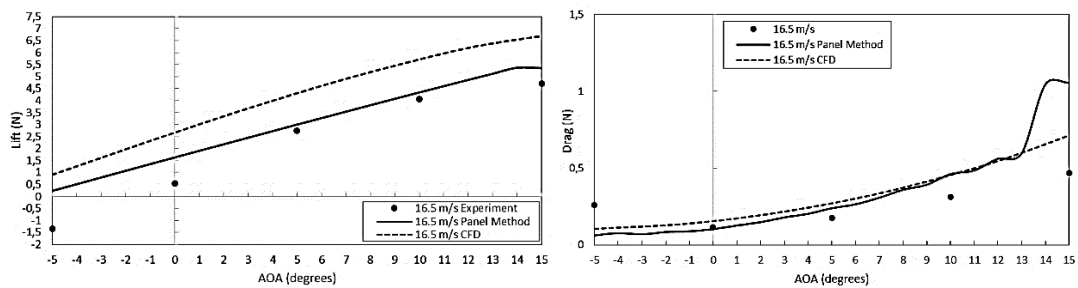


Figure 4.40 Lift vs AOA (left) and Drag vs AOA (right) curves of Optimized 14 Wing at 16.5 m/s

#### 4.3.4 Morphed 10 Wing

The Lift and Drag Curves of the Morphed 10 Wing are presented in Figures 4.41, 4.42, 4.43, 4.44, 4.45, 4.46, and 4.47. The separation at high angle of attack values can be seen in CFD calculations. When the velocity increases the lift curves of all conditions come closer and show good agreement. As in the other wings, trailing edge

separation on lower surface at low angle of attack values cannot be predicted by the numerical results, and can only be seen in experimental results. Drag estimation of the numerical results are significantly close to the experimental results. The drag and lift curve of the current experiment overlaps more with the numerical results than the previous experiments.

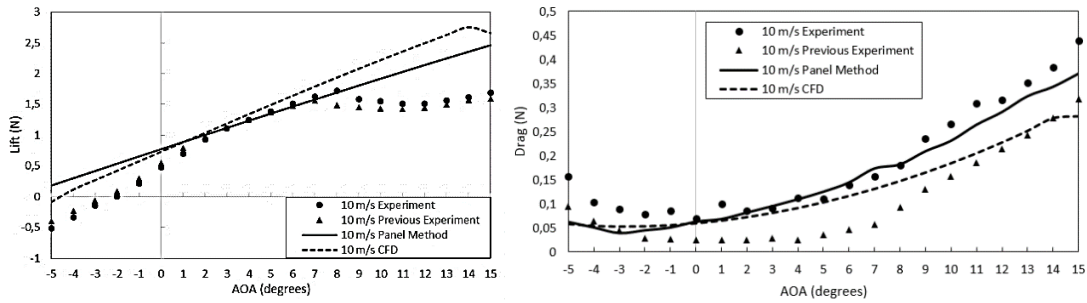


Figure 4.41 Lift vs AOA (left) and Drag vs AOA (right) curves of the Morphed 10 Wing at 10 m/s

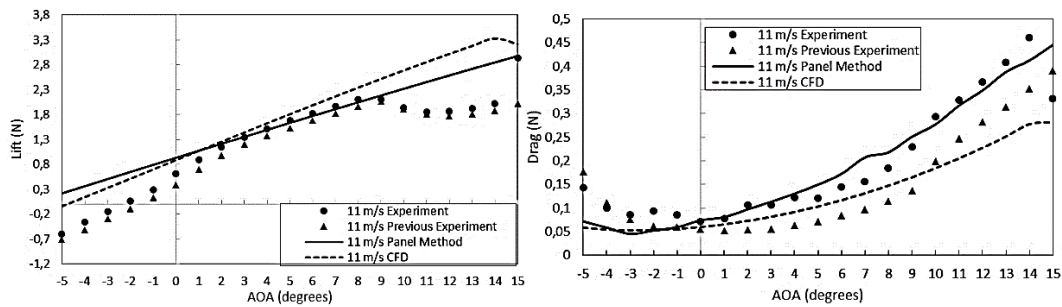


Figure 4.42 Lift vs AOA (left) and Drag vs AOA (right) Drag Force curves of the Morphed 10 Wing at 11 m/s

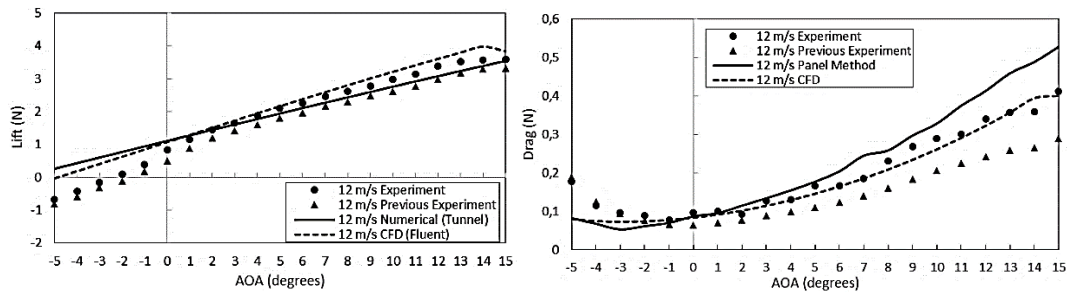


Figure 4.43 Lift vs AOA (left) and Drag vs AOA (right) Drag Force curves of the Morphed 10 Wing at 12 m/s

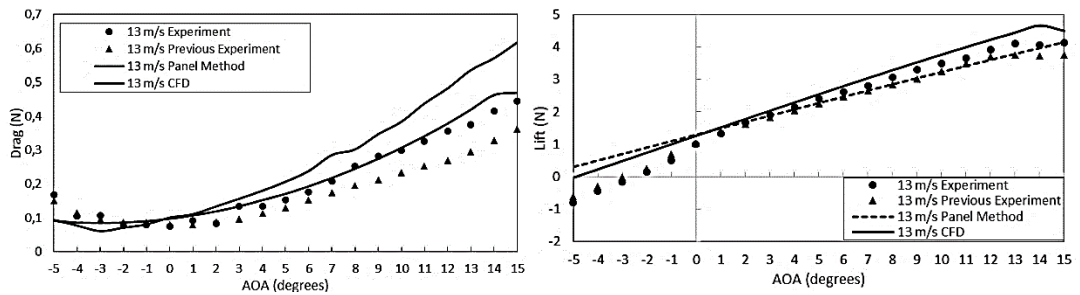


Figure 4.44 Lift vs AOA (left) and Drag vs AOA (right) Drag Force curves of the Morphed 10 Wing at 13 m/s

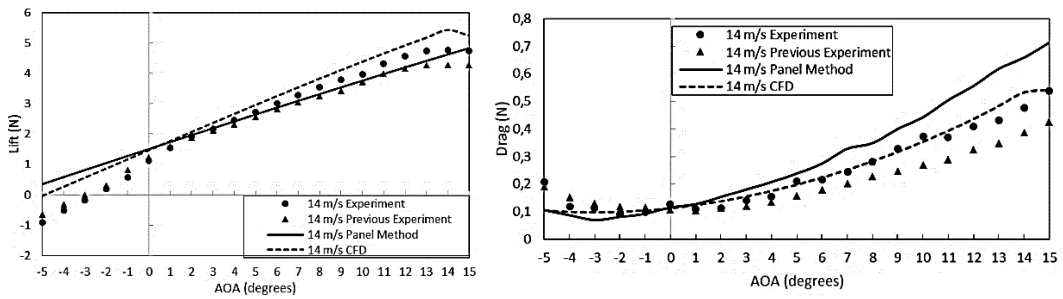


Figure 4.45 Lift vs AOA (left) and Drag vs AOA (right) Drag Force curves of the Morphed 10 Wing at 14 m/s

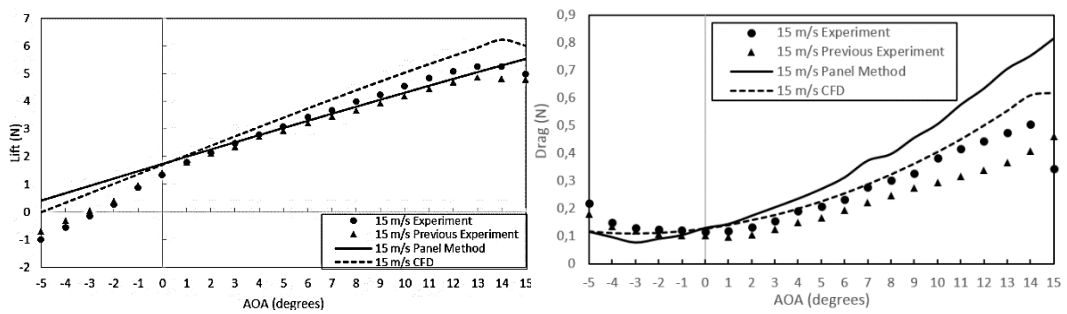


Figure 4.46 Lift vs AOA (left) and Drag vs AOA (right) Drag Force curves of the Morphed 10 Wing at 15 m/s

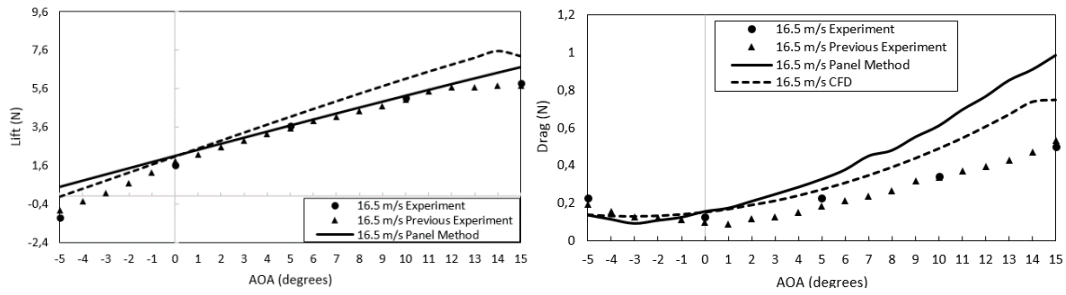


Figure 4.47 Lift vs AOA (left) and Drag vs AOA (right) Drag Force curves of the Morphed 10 Wing at 16.5 m/s

### 4.3.5 Morphed 16.5 Wing

Lift and drag curves of the Morphed 16.5 Wing are presented in Figures 4.48, 4.49, 4.50, 4.51, 4.52, 4.53 and 4.54.

In the Lift curves, for Panel Method results, separation is observed only at low velocities. For Morphed 16.5 Wing the lift values come closer at moderate angles of attack but do not coincide with the numerical results.

Experimental Drag curves of the Morphed 16.5 are close to numerical drag curves except the trailing edge separation regions at low angles of attack. Furthermore, Panel Method condition overestimates the drag at high angle of attack values but as the velocity increases, it decreases and comes closer to experimental values. CFD results are much closer than Panel Method results in the drag curves whereas Panel Method results are closer in the lift curves at all velocities.

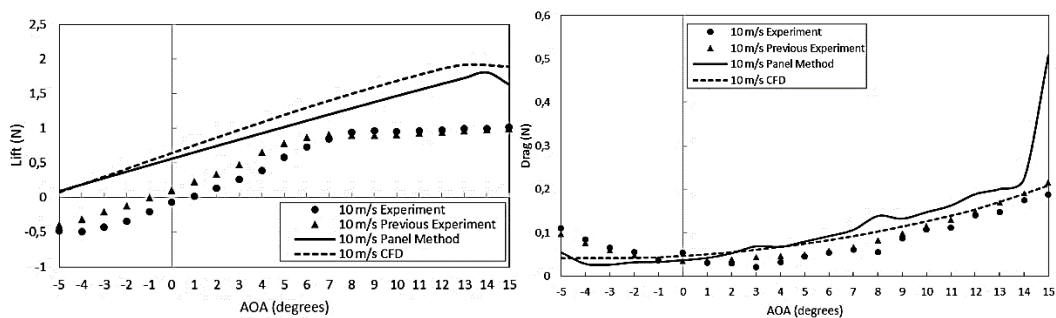


Figure 4.48 Lift vs AOA (left) and Drag vs AOA (right) Drag Force curves of the Morphed 16.5 Wing at 10 m/s



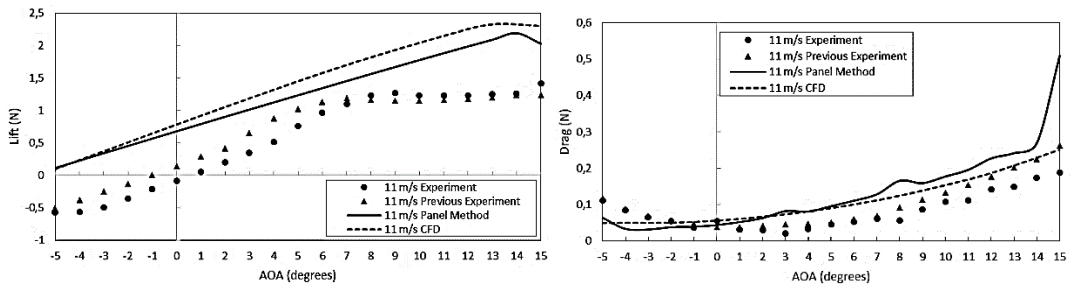


Figure 4.49 Lift vs AOA (left) and Drag vs AOA (right) Drag Force curves of the Morphed 16.5 Wing at 11 m/s

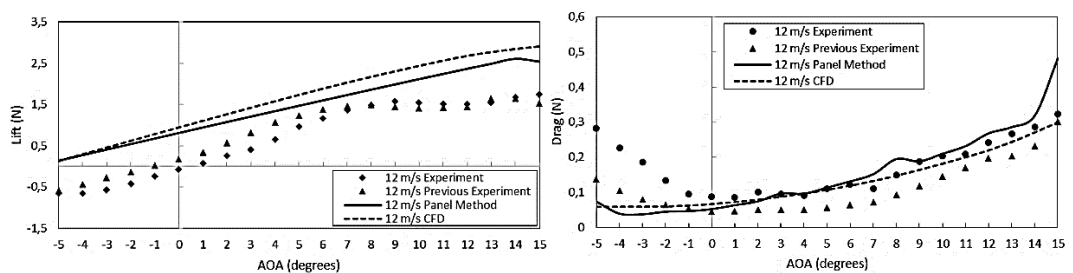


Figure 4.50 Lift vs AOA (left) and Drag vs AOA (right) Drag Force curves of the Morphed 16.5 Wing at 12 m/s

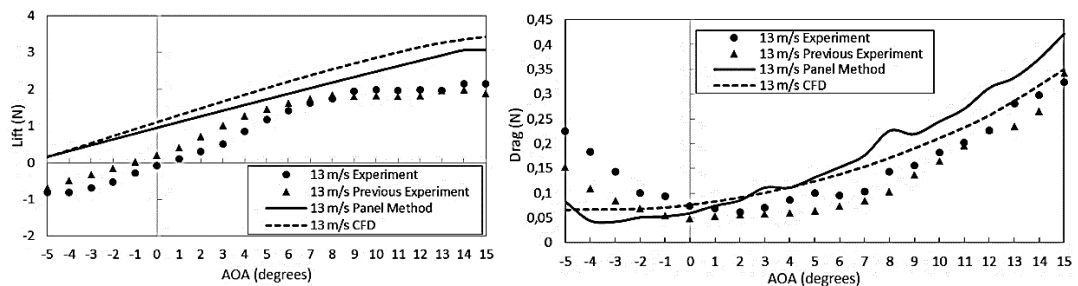


Figure 4.51 Lift vs AOA (left) and Drag vs AOA (right) Drag Force curves of the Morphed 16.5 Wing at 13 m/s

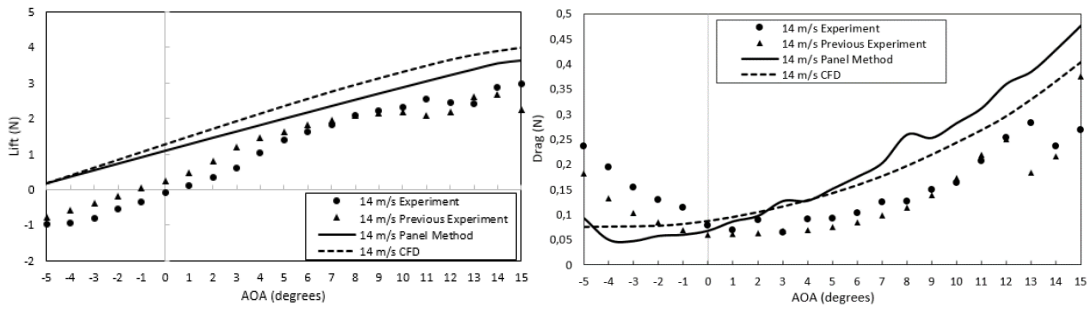


Figure 4.52 Lift vs AOA (left) and Drag vs AOA (right) Drag Force curves of the Morphed 16.5 Wing at 14 m/s

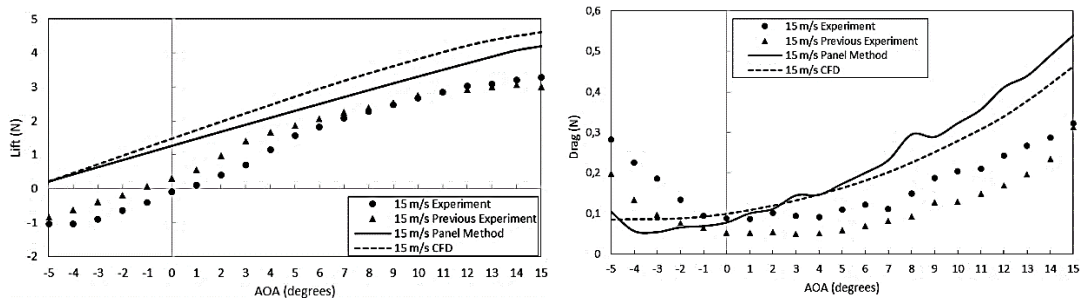


Figure 4.53 Lift vs AOA (left) and Drag vs AOA (right) Drag Force curves of the Morphed 16.5 Wing at 15 m/s

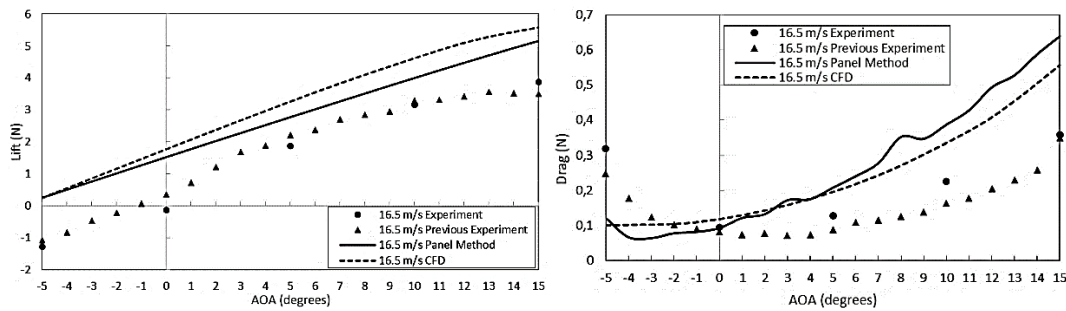


Figure 4.54 Lift vs AOA (left) and Drag vs AOA (right) Drag Force curves of the Morphed 16.5 Wing at 16.5 m/s

#### 4.4 Drag Curve

The Drag Curve of the resultant morphing wing is obtained by choosing the free stream velocities and angle of attack values for each wing that yields the required lift of 2.5N, at which the wings are optimized for. Then, the drag force values of this cases are plotted for each wing.

According to Table 4.3 where the angle of attack values and the velocities that yields 2.5 N are listed, the drag curve of the resultant morphing wing is plotted and presented in Figure 4.55.

The resultant morphing wing has the shape of Morphed 10 Wing at low velocities, Optimized 14 Wing for moderate velocities and Morphed 16.5 Wing at high velocities. As the numerical results suggest, Morphed 10 Wing gives the least drag force at low velocities and Optimized 14 Wing has minimum drag at 14 m/s. Moreover, at high velocities, morphing wing at 16.5 m/s has the minimum drag. The resultant morphing wing, which is drawn according to the three half wing models, has minimum drag values while keeping 2.5 N lift force constant in all velocity conditions. Therefore, the wings that are manufactured according to the numerical results are fairly the optimum wing shapes at the velocities they are designed for.

Table 4.4 List of the cases yielding 2.5 N Lift Force

<i>Wings</i>	<i>Velocity(m/s)</i>	<i>AOA (degrees)</i>
<i>Base Wing</i>	14	15
	15	12
	16.5	10
<i>Optimized 14 Wing</i>	13	10
	14	8
	15	8
<i>Morphed 10 Wing</i>	12	7
	13	6
	14	5
	15	4
	16.5	3
<i>Morphed 16.5 Wing</i>	14	11
	15	9
	16.5	8

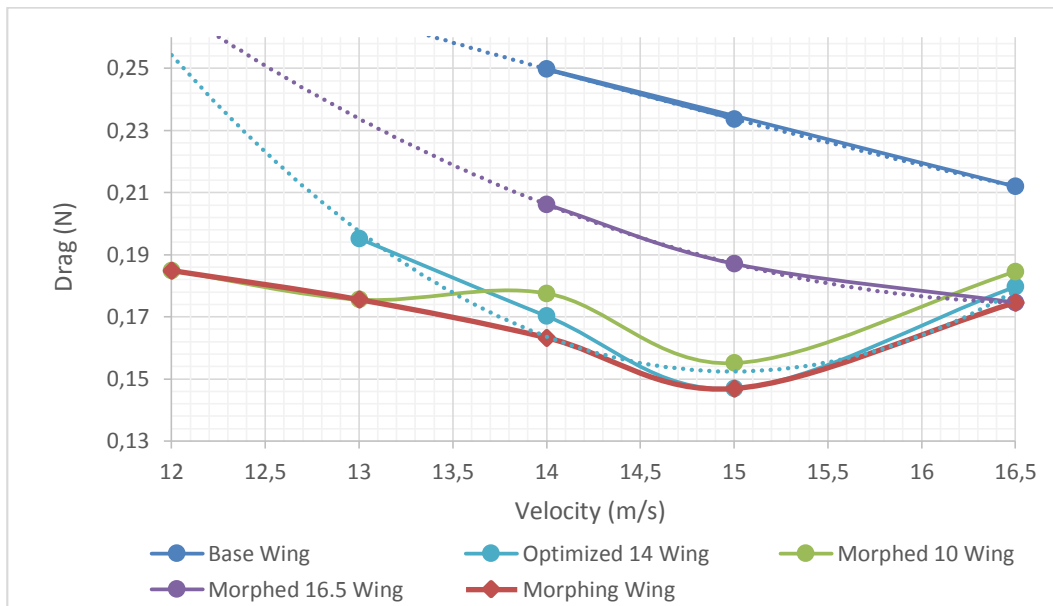


Figure 4.55 Drag Curve of the Morphing Wing

## 4.5 Particle Image Velocimetry Experimental Results

### 4.5.1 Motivation

In the numerical analysis, the optimized and morphed wings are obtained for a level flight at different velocities. In a level flight, lift equals to the drag force, which is illustrated in Figure 4.56.

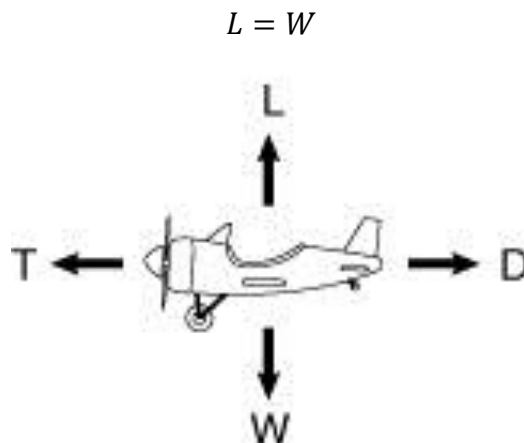


Figure 4.56 Steady level flight force balance [18]

It is assumed that there is no change in the weight of the aircraft during the flight, so that the lift force also doesn't change. Numerical results suggest that, during level flight, by changing the velocity of the airplane, the wing morphs into optimized shape at 14 m/s and morphed shapes at 10 m/s and 16.5 m/s free stream velocities in order to maintain the same lift, in this case 2.5 N.

Since all the wings have the same lift force values in these conditions, particular interest is to analyse the drag force. The drag curve of the wing models at 2.5 N value are presented in Figure 4.55 for this purpose. In the low Reynolds number aerodynamics, induced drag is much more prominent compared to parasite drag as discussed in Chapter 1. Furthermore, tip vortices are the main sources of induced drag.

Therefore, tip vortex measurements of the Base, Optimized 14, Morphed 10 and Morphed 16.5 wings are performed in order to analyse this behaviour and compare the tip vortex results with the drag curve results of the load cell measurements. By this way, the vortex behaviour of the wing models obtained by PIV measurements can validate the numerical results and the load cell experiment results.

#### **4.5.2 Results**

The mean velocity vectors obtained by averaging 300 images for the each case are plotted in vector maps. Moreover, Velocity Magnitude, Vorticity, Turbulence Kinetic Energy, and Reynolds Stress contours are presented for all of the wings at 14 m/s free stream velocity where they yield 2.5 N lift force in order to compare the PIV results with the drag curve results, which presented in Figure 4.55, of the load cell measurements. Then, by keeping  $x$  constant the velocity magnitude, vorticity, and turbulence kinetic energy values are plotted along  $y$  direction and the core radii of the tip vortices are compared. All the calculations are done and plots are prepared by using Tecplot 2012 software. The same analysis are performed for the wings at 15 m/s free stream velocity and the results are presented in Appendix A.

Some of the PIV measurements are performed for the additional velocities and angle of attack values of which their lift values are close to 2.5 N and also to compare angle

of attack or free stream velocity effects and they are presented in the Appendices B, C, D and E.

The free stream velocities and angle of attack values that can create 2.5 N lift force for all wings models at 14 m/s and 15 m/s are presented in Table 4.5.

Table 4.5 Angle of attack values at 14 m/s and 15m/s that create 2.5 N lift

	<i>14 m/s</i>	<i>15 m/s</i>
<i>Base Wing</i>	15°	12°
<i>Optimized 14 Wing</i>	8°	7°
<i>Morphed 10 Wing</i>	5°	4°
<i>Morphed 16.5 Wing</i>	11°	9°

### 4.5.3 Comparisons at 14 m/s Free Stream Velocity

#### 4.5.3.1 Velocity Magnitude Comparisons

For the final results of the vector maps, 300 images for each case is captured and analysed and the mean values of them are presented in this section. Since the analyses are performed on planes perpendicular to the free stream velocity, the analysis is 2D and there are two components of velocities. These velocities from instantaneous images are denoted by  $u$  and  $v$ . The mean velocities calculated from the 300 images are denoted by  $\bar{u}$  and  $\bar{v}$ . The vector maps for each case are composed of valid vectors not the substituted ones. Thus, all vector maps indicate purely the real physical characteristics of the flow field. The reason for the different locations of core of the velocity vectors in plots is because the planes that are captured are located at different downstream chord locations for the same wing (C and 2C) and for different mean chord values downstream for four half wing models. Therefore, their measurement plane is different and calibration is performed each time for the different planes at different downstream conditions.

The velocity magnitude contours have a good agreement with the theoretical understanding of the ideal tip vortex structure. However due to the wake of the wing, the results are not symmetrical as in the ideal case. The tangential velocity is zero at

the center and increases until it reaches to the core radius. Then, it decreases gradually to zero velocity, where the vortex size is defined. The velocity profile of a vortex is shown in Figure 4.57.

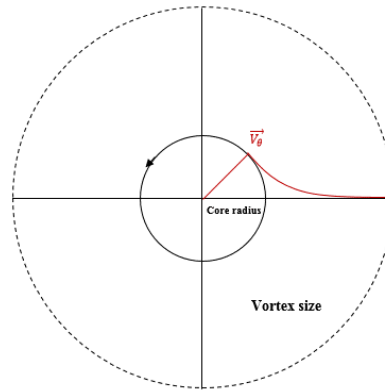


Figure 4.57 Vortex Velocity Profile

The Velocity Magnitude contours of the wings at 14 m/s at C and 2C locations are presented in Figures 4.58 and 4.59 respectively.

The full set of the experimental results for the velocity magnitude values of all wings are presented in Appendix B.

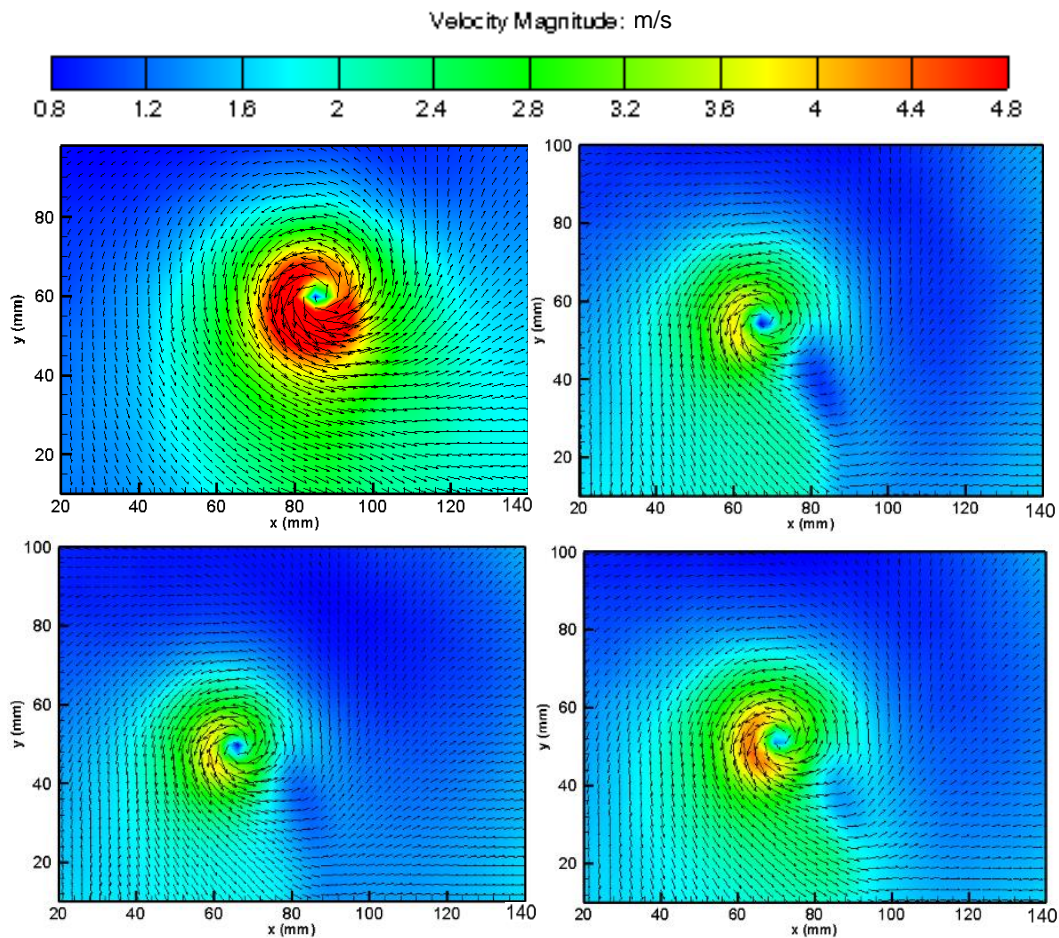


Figure 4.58 Velocity Magnitude Contours on one mean chord downstream plane at 14 m/s; Base Wing (Top Left), Optimized 14 Wing (Top Right), Morphed 10 Wing (Bottom Left) and Morphed 16.5 Wing (Bottom Right). Note that all cases are at different angles of attack as given in Table 4.5 but all producing the same 2.5 N lift force

It is very clear from the figures that, Base Wing has the biggest velocity magnitudes so the core radius of it is the biggest. Morphed 16.5 follows it as the second highest. It should be noted that these two wings have the smallest chord length and planform areas so the smallest Reynolds number values. They produce the required lift of 2.5N at higher angles of attack and lift coefficients compared to Morphed 10 and Optimized 14 wing, producing stronger vortices, which explains the large velocity magnitudes.



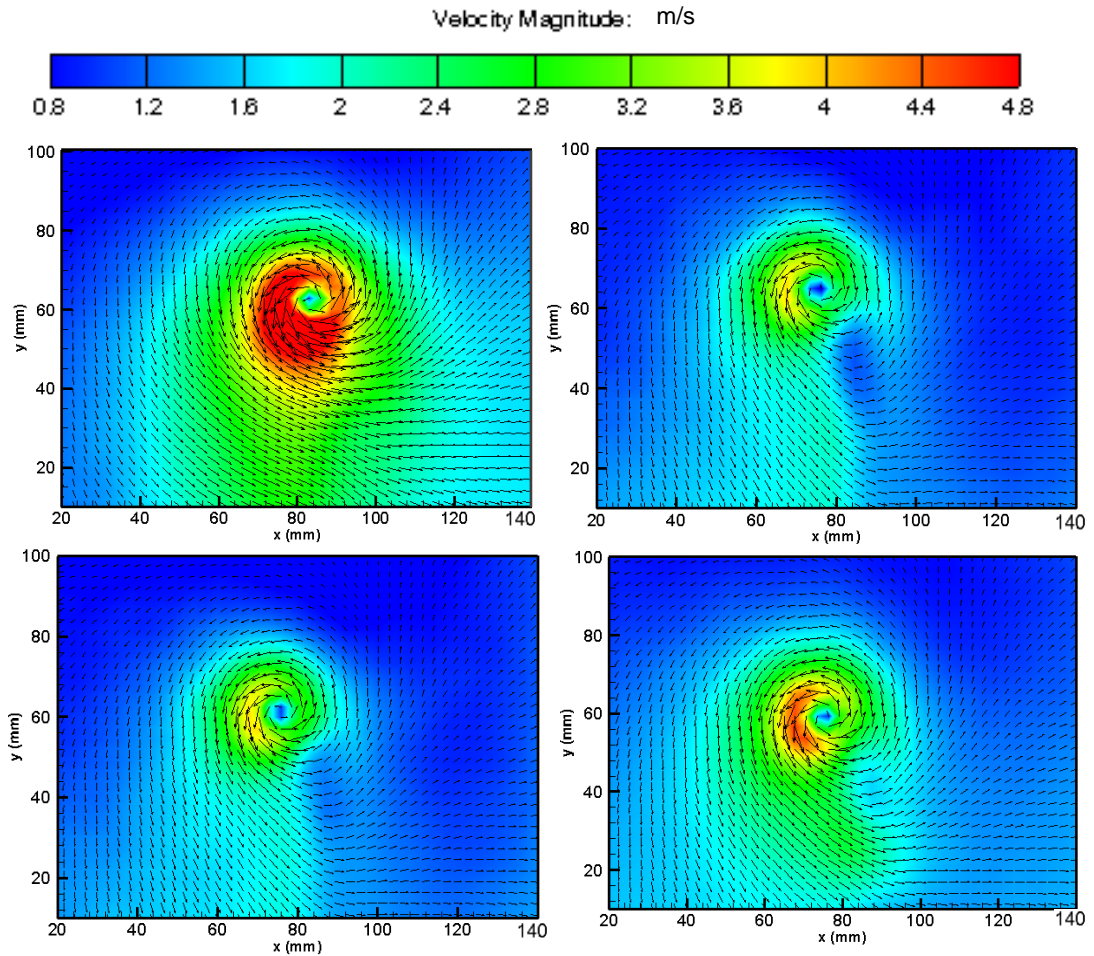


Figure 4.59 Velocity Magnitude Contours on two mean chord downstream plane at 14 m/s; Base Wing (Top Left), Optimized 14 Wing (Top Right), Morphed 10 Wing (Bottom Left) and Morphed 16.5 Wing (Bottom Right). Note that all cases are at different angles of attack as given in Table 4.5 but all producing the same 2.5 N lift force

The velocity Magnitude along the y direction by keeping x constant are plotted in Figures 4.60 and 4.61. The minimum velocity magnitude location in all cases are determined and subtracted from the y axis values according to the following Equation;

$$y' = y - y_c \quad (4.5)$$

By this way all the wings have minimum velocity magnitude at the center. This is done to make a comparison of the velocity field around the vortex core and to have an approximate idea about the vortex core radius. At the center, the velocity

magnitude is expected to be zero, whereas in the graphs it cannot reach to zero. This may be due to the grid resolution. It is seen that while the velocities away from the vortex in the measurement plane are approaching to zero, the region where the wing wake dominates does not reduce to zero value. It can be seen from the graphs that Optimized 14 Wing has the smallest velocity magnitude in both locations.

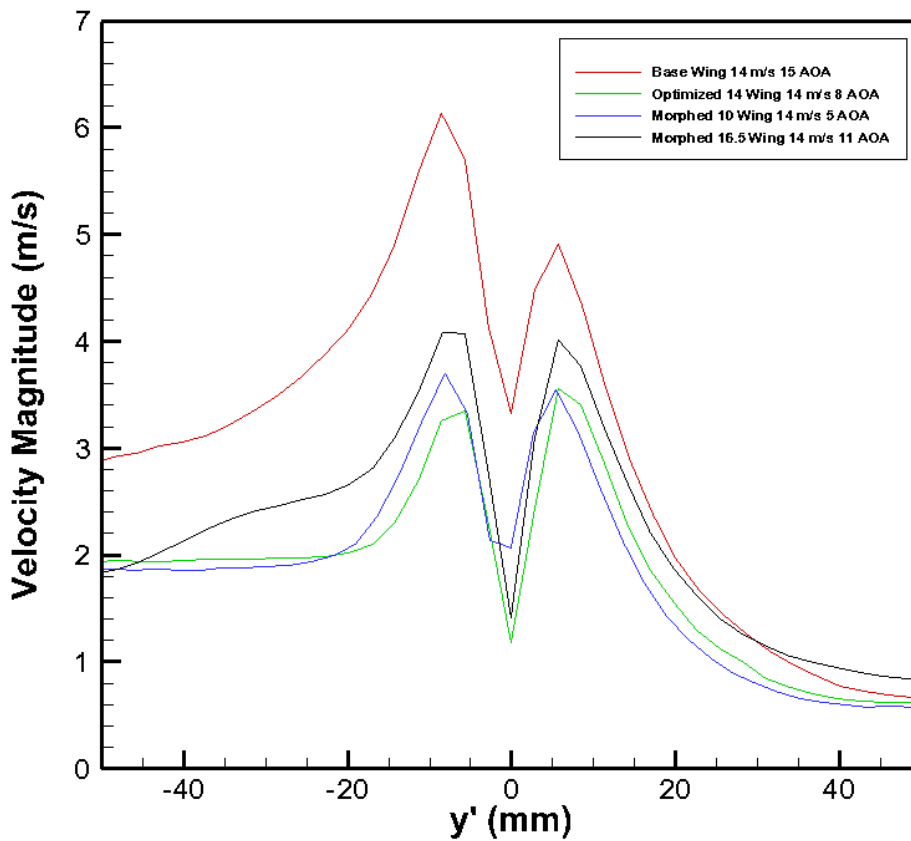


Figure 4.60 Velocity Magnitude at 14 m/s on one chord downstream plane

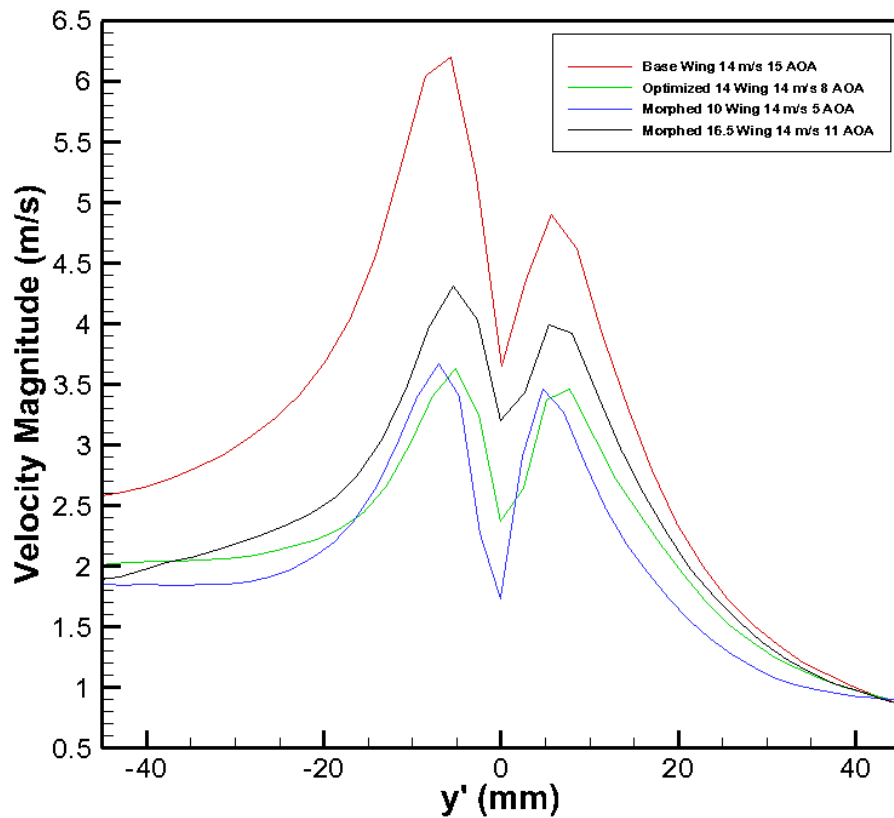


Figure 4.61 Velocity Magnitude at 14 m/s on two chord downstream plane

The distance between the two peaks of the velocity magnitude curves indicates the core radius of the vortex. The core radius values are listed in Table 4.6.

Table 4.6 Vortex Core Radius

<i>at 14 m/s</i>	<i>C (mm)</i>	<i>2C (mm)</i>
<i>Base Wing</i>	7,123	5,714
<i>Optimized 14 Wing</i>	5,676	6,412
<i>Morphed 10 Wing</i>	6,787	5,954
<i>Morphed 16.5 Wing</i>	6,364	5,387

Optimized 14 Wing has the minimum vortex core size among all the wings at C location as it has the lowest velocity magnitude, and according to the load cell results it has the minimum drag at 14 m/s, the velocity for which it is optimized for. Thus the two experimental approaches are in agreement. For the 2C location, Optimized 14

wing has bigger core radius than others where it has the lowest velocity magnitude, this may be caused by the vortex diffusion and will be discussed in the turbulence kinetic energy section.

#### 4.5.3.2 Vorticity Comparison

Vorticity is computed from the data of U and V velocities in the plane perpendicular to the free stream velocity. The vorticity is basically the curl of velocity as presented in Equation 4.6.

$$\mathbf{w} = \nabla \times \mathbf{V} \quad (4.6) \quad [51]$$

Since the analysis are 2D, there is only u and v components of the velocity in x and y directions. Thus x out of plane vorticity in z direction is found from the Equation 4.7.

$$w_z = \frac{\partial u}{\partial y} - \frac{\partial v}{\partial x} \quad (4.7)$$

Where  $w_z$  is the out of plane vorticity in z direction, u and v are the velocity components in x and y directions respectively.

In all the figures for all the half wing models, vorticity is maximum at the center of the vortex and approaches to zero gradually outside of the core region. In all images, it is observed that outside the core region, wake of the wing is dominating the flow field.

The mean out of plane vorticity contours according to PIV Results at C and 2C locations are presented in Figure 4.62 and 4.63 respectively. The vorticity contours are calculated at 14 m/s for each wing at the angle of attack values that yields 2.5 N lift force, as introduced in Table 4.5. The tip vortex and wake of the wing are shown in Figure 4.62. The wake distributions of the wings have different shapes since the span and the angle of attack values are different for the four half wing models.

The whole set of the experimental results for the vorticity contours are presented in Appendix C.

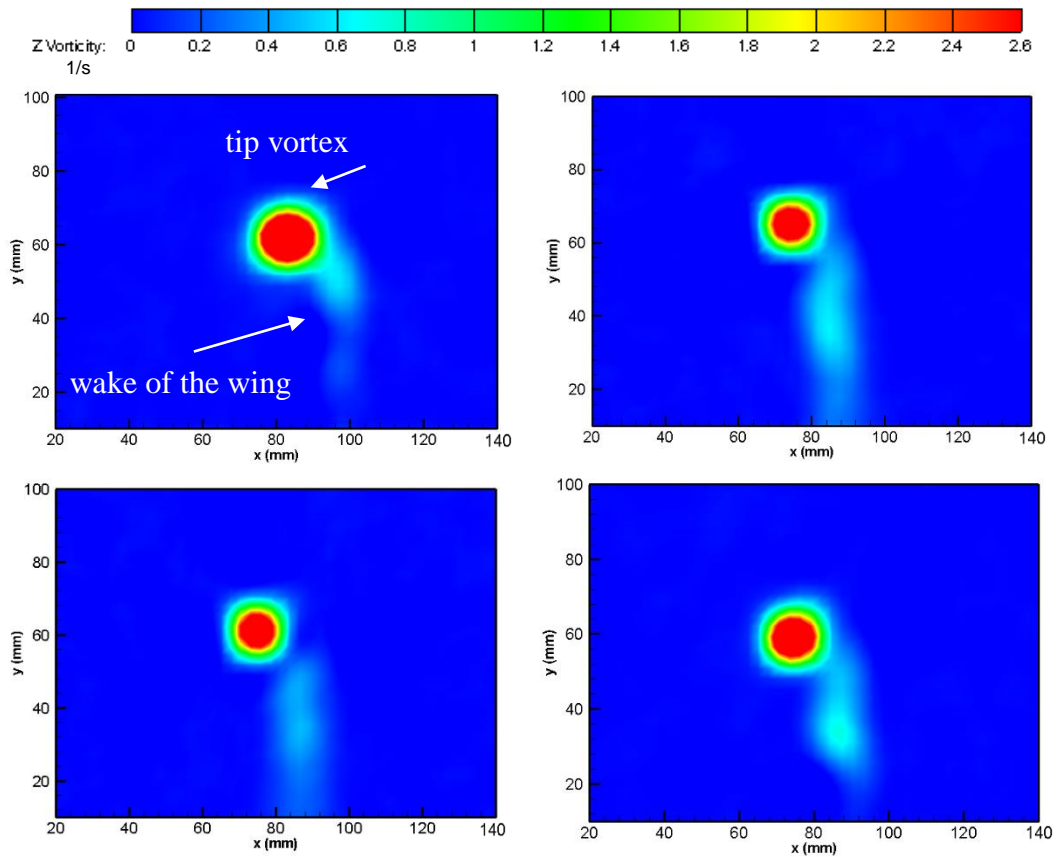


Figure 4.62 Vorticity Contours on one mean chord downstream plane at 14 m/s; Base Wing (Top Left), Optimized 14 Wing (Top Right), Morphed 10 Wing (Bottom Left) and Morphed 16.5 Wing (Bottom Right). Note that all cases are at different angles of attack as given in Table 4.5 but all producing the same 2.5 N lift force

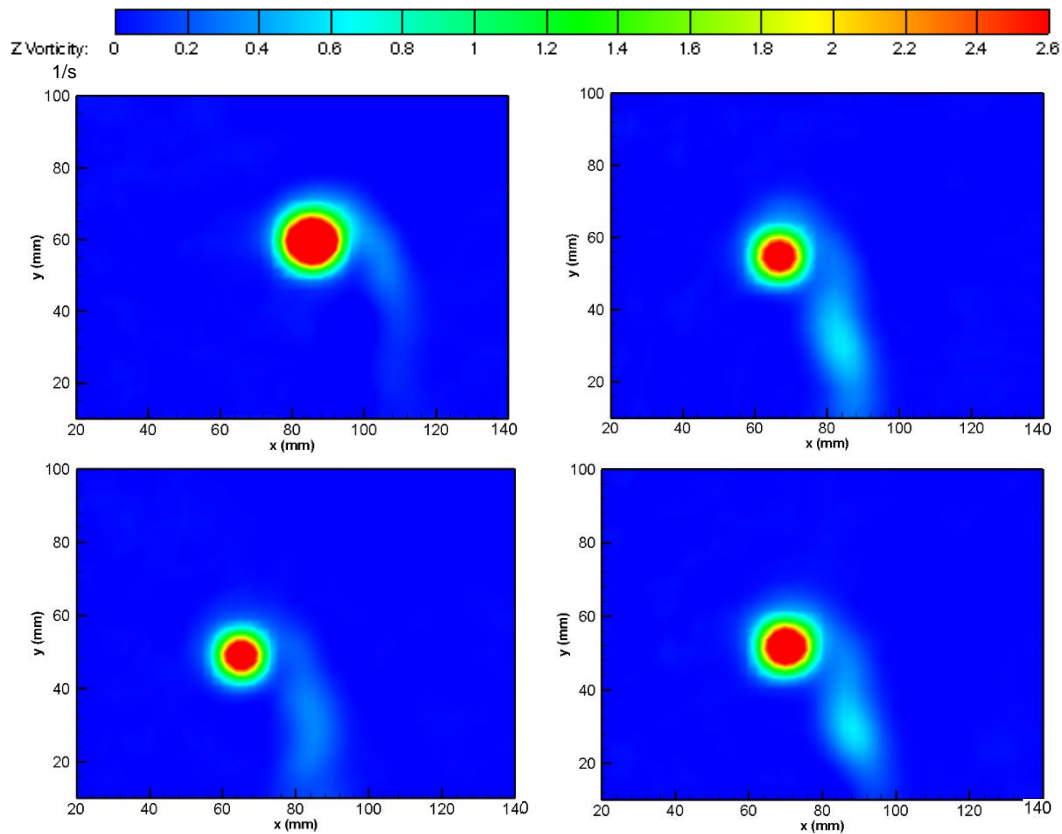


Figure 4.63 Vorticity Contours on two mean chord downstream plane at 14 m/s; Base Wing (Top Left), Optimized 14 Wing (Top Right), Morphed 10 Wing (Bottom Left) and Morphed 16.5 Wing (Bottom Right). Note that all cases are at different angles of attack as given in Table 4.5 but all producing the same 2.5 N lift force

In order to analyse vorticity magnitudes and vortex size, vortex core centre, x location is determined in Tecplot software. Then, a cut parallel to y axis is taken by keeping x (the core location value) constant. In order to get the vorticity centers at the same location for all the wings, y' values are obtained and vorticity magnitudes vs y' graphs are plotted accordingly. The results are presented in Figures 4.64 and 4.65. At 14 m/s free stream velocity, Optimized 14 Wing has the smallest vorticity, so the smallest drag value at both one chord and two chord locations as predicted by the load cell measurements. The vorticity values of the other wings are also in agreement with the drag curve obtained by load cell measurements. Moreover, the vorticity outside the vortex size approaches to zero for all the wings as suggested in the previous sections.

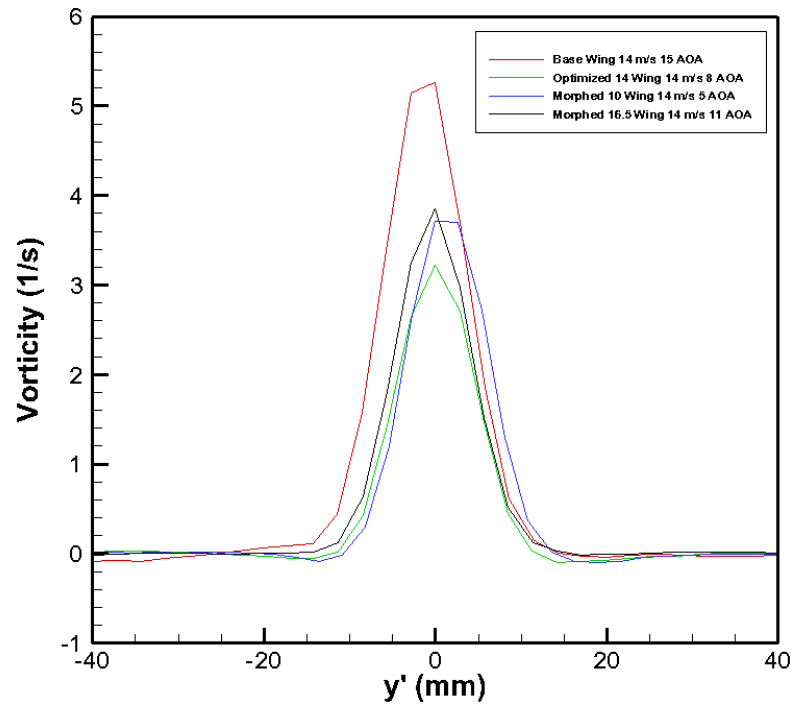


Figure 4.64 Mean out of Plane Vorticity along the Vortex on one mean chord downstream plane at 14 m/s

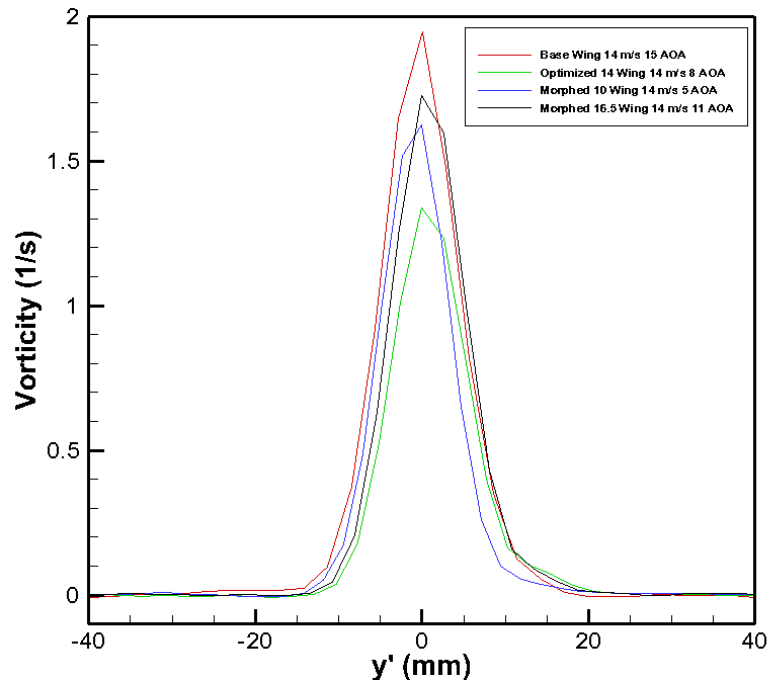


Figure 4.65 Mean out of Plane Vorticity along y direction on two mean chord downstream plane 2C Location at 14 m/s

### 4.5.3.3 Turbulence Kinetic Energy Comparisons

The data obtained from PIV results are the instantaneous velocity vectors for 300 images. By vector statistics analysis, the mean of these 300 images for each case is found. The instantaneous velocities are the sum of mean and fluctuating velocities as presented in Equation (4.8), which is called Reynolds decomposition.

$$u = \bar{u} + u' \quad (4.8)$$

where  $u'$  is fluctuating velocity,  $u$  is instantaneous, and  $\bar{u}$  is the mean velocity. When the average flow is steady, eddy motion in turbulent flow causes significant fluctuations [52]. Random behaviour of the flow is highly related with the turbulence characteristics.

Turbulence kinetic Energy is calculated according to the Equation 4.9.

$$k = \frac{1}{2} * (\overline{u'^2} + \overline{v'^2} + \overline{w'^2}) \quad (4.9)$$

The PIV analysis are 2D so there is no  $w$  component of velocity. Therefore, turbulent kinetic energy formula reduces into in plane turbulent kinetic energy in Equation 4.10.

$$k_{ip} = \frac{1}{2} * (\overline{u'^2} + \overline{v'^2}) \quad (4.10)$$

Turbulent kinetic energy is the mean kinetic energy per unit mass in fluctuating velocity field. It is a measure of interaction between the ambient air and the flow. Thus higher  $k$  means higher interaction and mixing [53].

Unsteadiness coming from the turbulence is not the only source, but wing tip vortices also exhibit some unsteadiness because of wandering [54]. Thus, the center of the core in vorticity and turbulence kinetic energy contours are compared and found to be almost at the same location for both. In the scope of this study, significant wandering has not been observed. Therefore, the wandering has no critical role in the turbulence kinetic energy contours for the scope of this study. In other words, the turbulence kinetic energy distribution is highly dominated by the wing tip vortices itself, the wing wake and unsteadiness of the flow caused by the wind tunnel turbulence.



Due to the high turbulence of all velocity components within the core, the peak in the turbulence kinetic energy of the vortex center is expected [55]. The peak of turbulence kinetic energy at the vortex center also indicates a non-laminar core. While moving away from the vortex core and wake of the wing, the turbulence kinetic energy reduces with the effect of dissipation.

The turbulent energy contours according to PIV Results at C and 2C locations are presented in Figures 4.66 and 4.67 respectively. The turbulent kinetic energy of the base wing is the highest among all the wings. Moreover, at C location, Morphed 16.5 Wing has the lowest turbulence kinetic energy whereas at 2C location morphed 10 wing has. It is observed that at C location, the wings with bigger chords and areas which are Optimized 14 and Morphed 10 Wings, have much more turbulence fluctuations in the surrounding flow of the vortex compared to Base Wing and Morphed 16.5 Wing. Moreover, another remark is that the wings with smaller planform area and chord (Morphed 16.5 and Base Wing) are exposed to higher wing wake caused turbulences.

The whole set of the experimental results for the turbulence kinetic energy contours are presented in Appendix D.

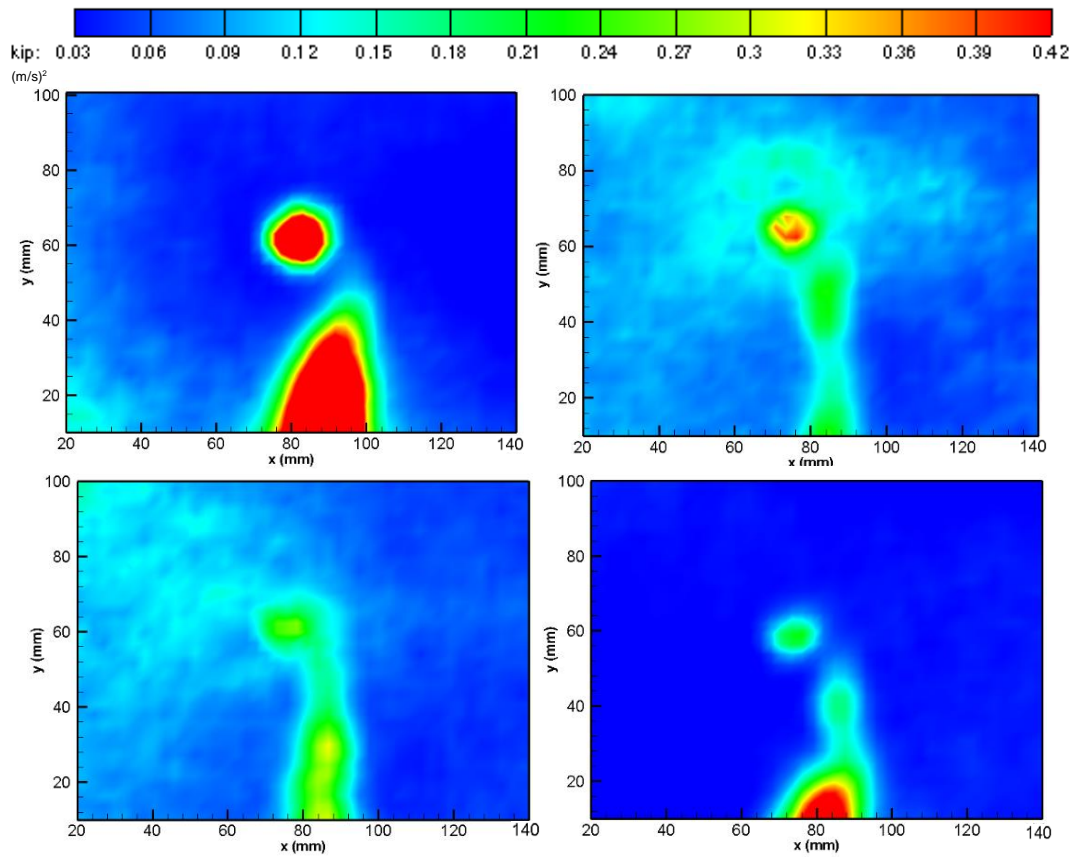


Figure 4.66 In-Plane Turbulence Kinetic Energy Contours on one mean chord downstream plane at 14 m/s; Base Wing (Top Left), Optimized 14 Wing (Top Right), Morphed 10 Wing (Bottom Left) and Morphed 16.5 Wing (Bottom Right). Note that all cases are at different angles of attack as given in Table 4.5 but all producing the same 2.5 N lift force

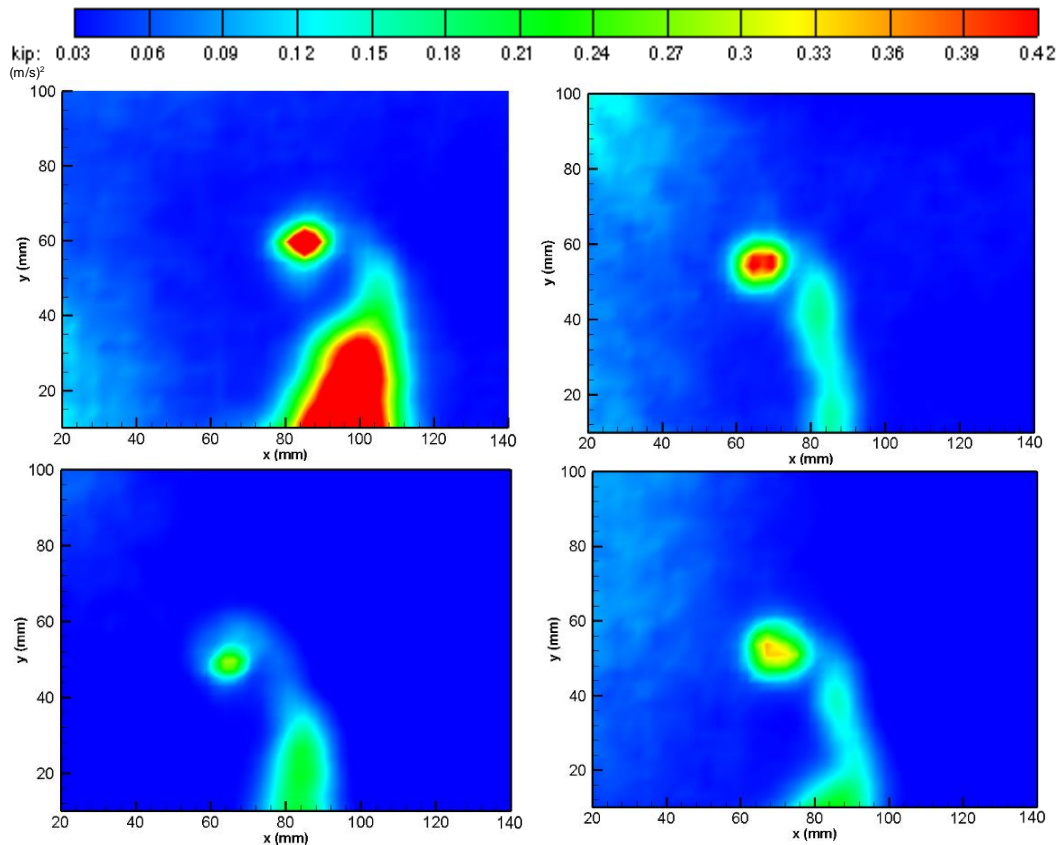


Figure 4.67 In-Plane Turbulence Kinetic Energy Contours on two mean chord downstream plane at 14 m/s; Base Wing (Top Left), Optimized 14 Wing (Top Right), Morphed 10 Wing (Bottom Left) and Morphed 16.5 Wing (Bottom Right).

Note that all cases are at different angles of attack as given in Table 4.5 but all producing the same 2.5 N lift force

The turbulence kinetic energy values along y direction, which are presented in Figures 4.68 and 4.69, are plotted at a constant x value that passes through the vortex center. The wake of the wings can be seen in the plots at low y values. As moving far from the vortex, the turbulent kinetic energies approaches to zero. Although Optimized 14 Wing has the lowest vorticity, it has the second biggest turbulent kinetic energy value among the wing models. The vortex core radius of the Optimized 14 Wing increases from C to 2C, while its velocity magnitude and vorticity value decreases. This may be the indication of the faster dissipation and enhanced mixing of the tip vortex compared to other wings, which is an advantage in terms of aerodynamic performance for Optimized 14 Wing at 14 m/s free stream velocity at which it is designed for.

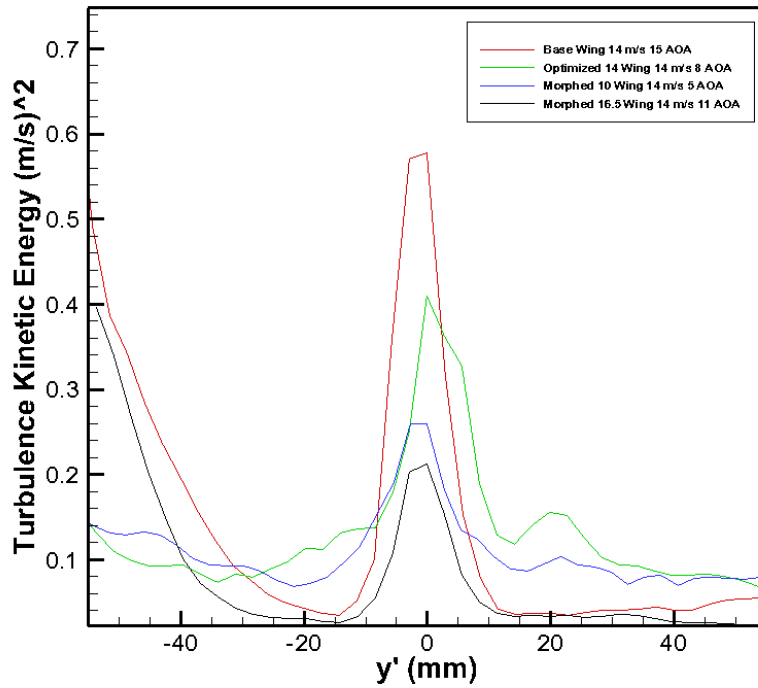


Figure 4.68 In Plane Turbulence Kinetic Energy along y direction at 14 m/s on one mean chord downstream plane

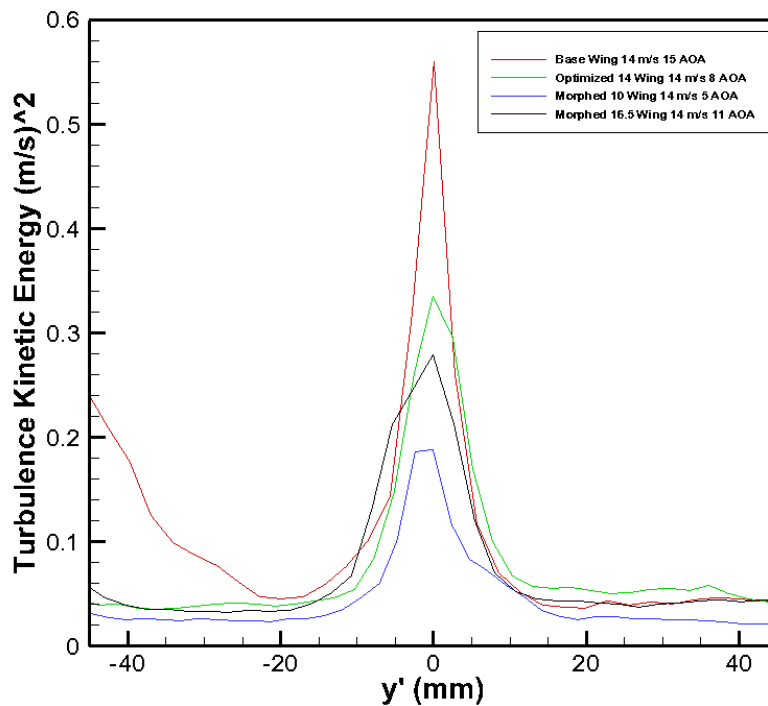


Figure 4.69 Turbulence Kinetic Energy along y direction at 14 m/s on two mean chords downstream plane

#### 4.5.3.4 Reynolds Stress Component Comparisons

For the turbulence models, steady Navier Stokes equations (presented in Equation 4.11 [52]) are replaced by Reynolds-Averaged Navier Stokes (RANS) equations (shown in Equation 4.12 [52]).

$$(\vec{V} \cdot \vec{\nabla}) * \vec{V} = -\frac{1}{\rho} * \vec{\nabla}P + \nu * \nabla^2 \vec{V} \quad (4.11)$$

$$(\vec{V} \cdot \vec{\nabla}) * \vec{V} = -\frac{1}{\rho} * \vec{\nabla}P + \nu * \nabla^2 \vec{V} + \vec{\nabla} \cdot (\tau_{ij,turbulent}) \quad (4.12)$$

The additional term here is  $\vec{\nabla} \cdot (\tau_{ij,turbulent})$  which accounts for the turbulent fluctuations.  $\tau_{ij,turbulent}$  is the tensor known as Reynolds stress tensor. The Reynolds stress tensor in Cartesian coordinates is shown in Equation 4.13 [52].

$$\tau_{ij,turbulent} = - \begin{pmatrix} \overline{u'^2} & \overline{u'v'} & \overline{u'w'} \\ \overline{u'v'} & \overline{v'^2} & \overline{v'w'} \\ \overline{u'w'} & \overline{v'w'} & \overline{w'^2} \end{pmatrix} \quad (4.13)$$

In this study, only the plane perpendicular to the free stream velocity is analysed so that 2D analysis is performed. The velocities in this plane are considered to be u and v. Thus the Equation 4.13 reduces to Equation 4.14.

$$\tau_{ij,turbulent,ip} = - \begin{pmatrix} \overline{u'^2} & \overline{u'v'} \\ \overline{u'v'} & \overline{v'^2} \end{pmatrix} \quad (4.14)$$

Only the shear stress term  $\overline{u'v'}$  can be analysed using the 2D PIV data obtained in this study.

Fluctuations in the flow are characterised by the Reynolds stresses [56]. Eddies having turbulence kinetic energy are responsible for the Reynolds Stress fluctuations. Wandering causes higher Reynolds stresses in the vortex core [56]. Since the occurrence of wandering is more possible in far field, Increasing of the location from C to 2C may have resulted in the increase of  $\overline{u'v'}$  although notable wandering is not observed during the experiments and after in the analysis.

Since the wake of the wing is very dominant, the  $\overline{u'v'}$  on the vortex region is not clearly visible for some of the cases. Reynolds Stress component  $\overline{u'v'}$  at the wing location decreases as the distance from the trailing edge increases from C to 2C for all the wings and all conditions.

The four leafed clover shape of the Reynolds stresses at the vortex location is what is expected to be seen. The four lobbed pattern of the tip vortices is also presented in previous studies. From the outer region of the vortex core the tangential velocity decreases and Reynolds stress tends to zero [55]. In all the obtained images for all wings, the Reynolds stresses of the flow field away from the vortex core and the wing wake is zero.

The increase in Reynolds Stress component  $\overline{u'v'}$  from C to 2C indicates a development of the axisymmetric vortex with a turbulent vortex core.

In contrast, in the images that show a decrease in Reynolds stress component  $\overline{u'v'}$  from C to 2C may be because of the interaction between primary and secondary vortices. Turbulence diminishes in these conditions by the effect of the relaminarization of the vortex core by the centrifugal forces. This can also be seen in some of the Turbulence Kinetic Energy Contours presented in the previous section.

It is observed that the turbulence kinetic energy contours and the Reynolds Stress component  $\overline{u'v'}$  contours has the same trend for all wings and at all conditions. This is because the high turbulence levels causes high Reynolds stresses and development of the axisymmetric vortices with turbulent vortex core. On the other hand, low turbulence levels and the relaminarization of the vortex core leads to low Reynolds stresses.

The whole set of the experimental results for the in plane Reynolds Stress component  $\overline{u'v'}$  are presented in Appendix E.

Reynolds Stress component  $\overline{u'v'}$  of the four half wing models are presented in Figures 4.70 and 4.71.

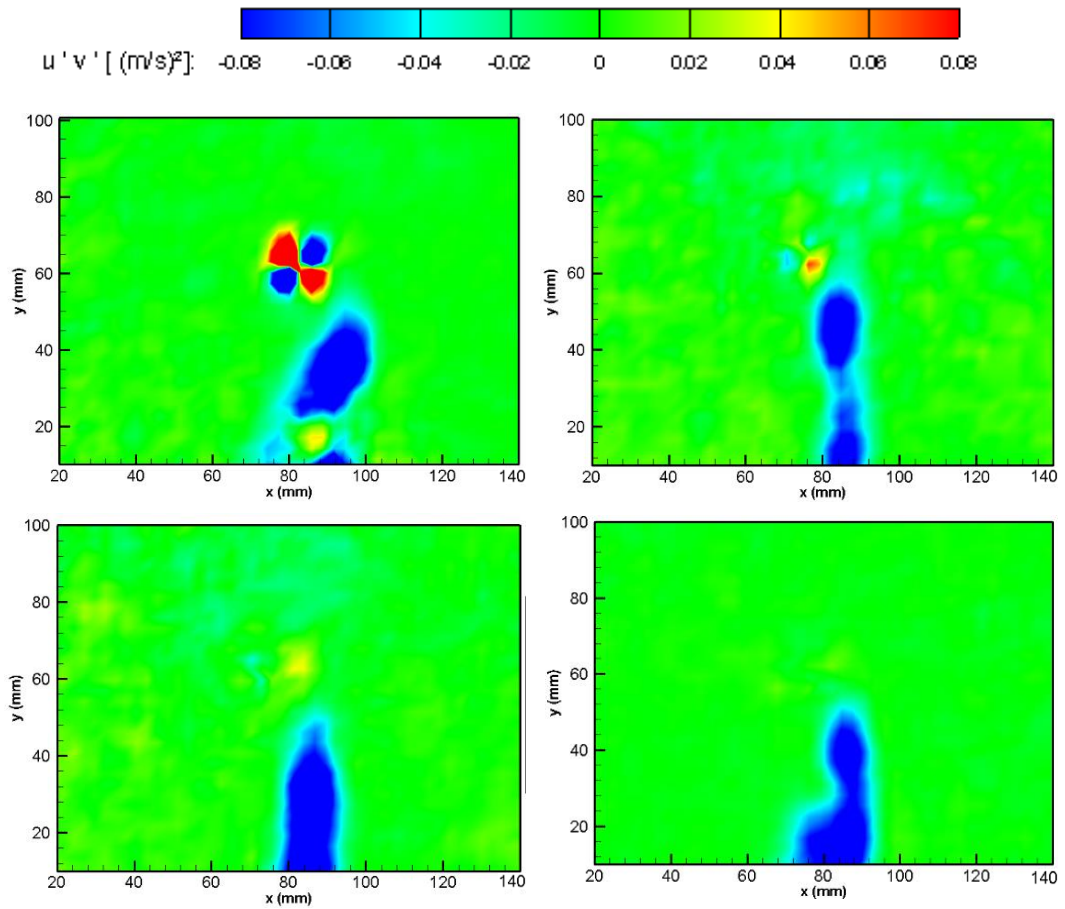


Figure 4.70  $\overline{u'v'}$  Contours on one mean chord downstream plane at 14 m/s; Base Wing (Top Left), Optimized 14 Wing (Top Right), Morphed 10 Wing (Bottom Left) and Morphed 16.5 Wing (Bottom Right). Note that all cases are at different angles of attack as given in Table 4.5 but all producing the same 2.5 N lift force

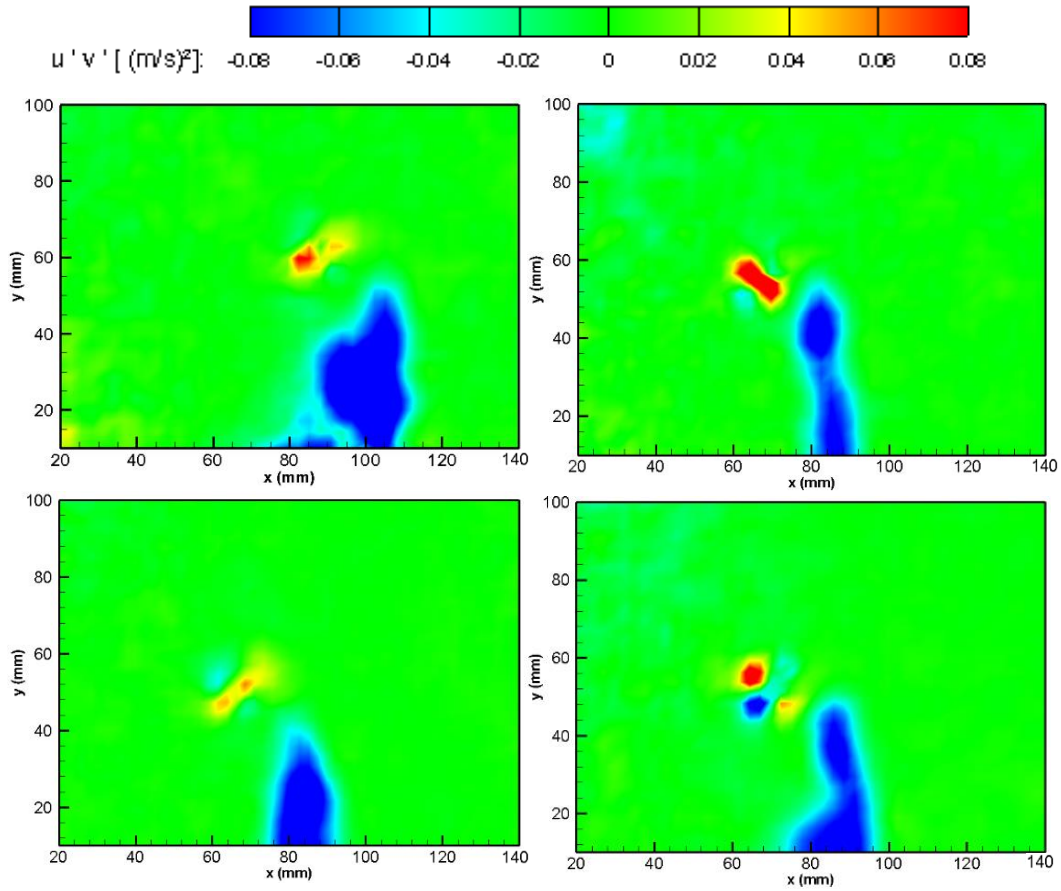


Figure 4.71  $\overline{u'v'}$  Contours on two mean chord downstream plane at 14 m/s; Base Wing (Top Left), Optimized 14 Wing (Top Right), Morphed 10 Wing (Bottom Left) and Morphed 16.5 Wing (Bottom Right). Note that all cases are at different angles of attack as given in Table 4.5 but all producing the same 2.5 N lift force

#### 4.5.3.5 Induced Drag Comparison

Induced Drag values of the tip vortices are calculated from the PIV data according to the following formula [21], [57];

$$D_i = \iint_S \frac{1}{2} \rho_\infty (u^2 + v^2) dx dy \quad (4.15)$$

Where S is the area of the measurement plane where the out of plane tip vortex is located. The induced drag of the tip vortices of the half wing models are presented in Table 4.6.



Table 4.7 Induced Drag of the Tip Vortices at 14 m/s

<i>Induced Drag (Newton)</i>	<i>Induced Drag at 14 m/s at C (PIV)</i>	<i>Induced Drag at 14 m/s at 2C (PIV)</i>	<i>Total Drag (Load Cell)</i>
Base Wing	0,0382	0,0378	0,2498
Optimized 14 Wing	0,0194	0,0213	0,1702
Morphed 10 Wing	0,0181	0,0167	0,1776
Morphed 16.5 Wing	0,0256	0,0251	0,2062

As it can be seen from the Table 4.7, Morphed 10 and Optimized 14 Wing have lowest induced drag values of the tip vortices. In the load cell experiments the total drag values of these two wing models are also very close and have the lowest total drag values.

#### 4.6 Conclusion

In this section the results of the tip vortex analysis performed by Particle Image Velocimetry is presented. Mean velocity vectors and mean velocity magnitude contours, out of plane vorticity and in-plane turbulence kinetic energy contours, and Reynolds stress component contours of the wings are presented at angle of attack values and free stream velocities that yield 2.5 N lift force.

Vortex Meandering is also taken into account, and 300 instantaneous images are analysed in order to investigate this problem. It is seen that the vortex location is very stable which is also observed during the experiments. Moreover, the effect of meandering is much more dominant and significant in the far field region [58]. Therefore, for the region of interest of this study, which is the near field, the meandering does not affect the averaged flow properties.

In 2D- PIV measurements, 90% of the uncertainty comes from the determination of the displacement pixels from raw images and 10% of is due to camera calibration [59]. The correlation peaks and image densities are checked after every measurement and the best ones are selected so that very explicit vector maps are obtained.

High turbulence levels within core and wing wake region is observed for all wings. It is seen that Reynolds stresses has the same trend with the Turbulence Kinetic Energy contours.

The small wake region at the downstream of the airfoil indicates a small drag force [45]. The increase of lift results an increase in induced drag so that the peak values of vorticity and velocity magnitude is increased.

The drag curve obtained from the load cell measurements is compared with the PIV results at 14 m/s free stream velocity for the four half wing models. The out of plane mean vorticity, in-plane turbulence kinetic energy, and mean velocity magnitude of the wings are compared by looking at the plots taken along y direction passes through the vortex core center. Tip vortex core radius values are also compared in order to validate optimized wing shapes at these velocities. Finally, induced drag values are calculated from the PIV results and compared with the total drag values of the load cell experiment results.

## CHAPTER 5

### CONCLUSION

Improvements in manufacturing technology on aircraft materials, actuators, sensors and other mechanisms raised the interest in morphing wing and with the increasing role of the unmanned aerial vehicles in military and civil applications, where the morphing wing technologies are mostly applied has resulted in a growing interest in low Reynolds number aerodynamics. Thus, this study mostly focused on low Reynolds number aerodynamic experiments of morphing wings.

The load cell experiments for the four half wing models at eight velocities and twenty angle of attack values are performed and compared with the previous experiment, numerical results obtained by Panel Method + 2D Boundary Layer solver and Fluent results. Repeating the experiments with a different data acquisition system and wing attachment set-up by changing the wind tunnel motor shaft balance and stabilization of the wind tunnel, experimental results are improved. Experimental drag and lift force values of the wings are found to be compatible with the numerical results. Numerical results can be improved by adding prediction tools for lower surface trailing edge separations at low angles of attack. Moreover, a predicting tool for the laminar separation on the upper surface at high angle of attack values can be enhanced.

Oil flow visualizations are performed to support the conclusions drawn from the load cell results. According to the experimental results, it seen that the wings that are manufactured according to the numerical results operate properly in the free stream velocities that they are designed for. While maintaining the same lift value in a level flight, experiment results show that the minimum drag values are obtained for the Morphed 10 Wing at 10 m/s, Morphed 16.5 Wing at 16.5 m/s and Optimized 14 Wing at 14 m/s as suggested by the numerical results.

Creation of the lift results in trailing vortices behind the wings, which creates a downwash on the aircraft wing and causes a reduction in lift and increase in drag

forces. Wing tip vortices are the main indicator of the induced drag. An improved comprehension of the tip vortex behavior and its control results in an aerodynamic advantage through reduction in induced drag [21].

Therefore, Particle Image Velocimetry (PIV) experiments are performed in two downstream locations for each wing in the planes perpendicular to the free stream velocity in order to analyze tip vortices. The velocity vector maps, velocity magnitude, vorticity, turbulence kinetic energy, and Reynolds stress contours of the wings are analysed at angle of attack values and free stream velocities that yields 2.5 N lift force. The drag curve obtained from the load cell measurements is compared with the results of velocity magnitude, vorticity, and turbulence kinetic energy, vortex core radius and induced drag.

As predicted by the numerical results and supported by the load cell experiments, It is finally approved by the PIV measurements that three half wing models optimized and morphed from the base wing are the optimum shapes at the conditions they are designed for. These optimized and morphed wing shapes can be operated in cruise, landing and high speed cruise mission segments so that the aircraft performance enhances with the morphing mechanism.

With an extensive knowledge of the wake of aircrafts by understanding of the physics of trailing vortex phenomenon can help to improve future aircraft designs [15]. With the morphing mechanism, wings can change their shapes at the velocities they are designed for and yield the minimum induced drag generated by tip vortices at those velocities. By this way, the performance of the aircraft is improved with a smoother flow around the wing, increasing lift, decreasing drag, reducing the empty weight so that increase in payload capacity, reducing the cost and fuel consumption by morphing mechanism.

## REFERENCES

- [1] D. Lentink and A. A. Biewener, “Nature-inspired flight-beyond the leap,” IOP Publishing, 2010.
- [2] D. T. Grant, M. Abdulrahim and R. Lind, “Design and analysis of biomimetic joints for morphing of micro air vehicles,” IOP Science Publication, 2010.
- [3] T. Mueller, “Aerodynamic Measurements at Low Reynolds Numbers for Fixed Wing Micro-Air Vehicles,” in *RTO AVT Course (RTO EN-9)*, Rhode-Saint-Genèse, Belgium, 2006.
- [4] G. C. N. Chattopadyay, B. Jony and A. Acharya, “An Analysis on Morphing Wing,” in *Global Engineering, Science and Technology Conference*, Dhaka, Bangladesh, 2012.
- [5] R. D. Breuker, M. M. Abdalla and Z. Gürdal, “A Generic Morphing Wing Analysis and Design Framework,” *Journal of Intelligent Material Systems and Structures*, 2011.
- [6] M. D. Skillen and W. A. Crossley, “Modeling and Optimization for Morphing Wing Concept Generation,” NASA, Indiana, 2007.
- [7] L. Nan, *The Methods of Drag Force Measurement in Wind Tunnels*, M.Sc. Dissertation: University of Gävle, 2013.
- [8] S. Tavoularis, *Measurement in Fluid Mechanics*, New York: Cambridge University Press, 2005.
- [9] Cameron Tropea, Alexander Yarin, John F. Foss, Editors, *Handbook of Experimental Fluid Dynamics*, Springer, 2007.
- [10] M.R. Hassani Ahangar, M.R. Kangavari, Khodadad Vahedi, “Reliability Model of A Wind Tunnel Balance System,” TÜBİTAK, 2010.
- [11] Jorge Colman Lerner, Ulfilas Boldes, *Wind Tunnels and Experimental Fluid Dynamics Research*, InTech, 2011.

- [12] Michael S. Selig, Robert W. Deters, Gregory A. Williamson, "Wind Tunnel Testing Airfoils at Low Reynolds Numbers," in *49th AIAA Aerospace Sciences Meeting*, Orlando, FL, 2011.
- [13] M. A. Gonzalez, J. M. Ezquerro and V. Lapuerta, "Components of a Wind Tunnel Balance : Design and Calibration," in *Wind Tunnels and Experimental Fluid Dynamics Research*, pp. 115-134.
- [14] H. Shah, J. Kitaba, S. Mathew and C. M. Lim, "Experimental Flow Visualization Over a Two-Dimensional Airfoil at Low Reynolds Number," in *Brunei International Conference on Engineering and Technology*, Brunei Darussalam, 2014.
- [15] O. A. Alsayed, W. Asrar and A. A. Omar, "Evaluation of Aircraft Wing-Tip Vortex Using PIV," in *The 10th Asian International Conference on Fluid Machinery*, 2010.
- [16] A. Shekarriz, T. Fu and J. Katz, "Near Field Behavior of a Tip Vortex," *AIAA*, vol. 31, no. 1, pp. 112-117, 1993.
- [17] D. Raymer, *Aircraft Design : A Conceptual Approach*, AIAA Education Series, 2002.
- [18] "MIT OCW," [Online]. Available: <http://ocw.mit.edu/ans7870/16/16.unified/propulsionS04/UnifiedPropulsion4/UnifiedPropulsion4.htm>. [Accessed 08 2015].
- [19] H. Ashley and M. Landahl, *Aerodynamics of Wings and Bodies*.
- [20] J. A. Posada, *Numerical Study of Wingtip Shear Vorticity Reduction by Wing Boundary Layer Control*, PhD Dissertation: West Virginia University, 2007.
- [21] D. Birch, T. Lee, F. Mokhtarian and F. Kafyeke, "Structure and Induced Drag of a Tip Vortex," *Journal of Aircraft*, vol. 41, no. 5, pp. 1138-1145, 2004.
- [22] R. Wlezien, G. Horner, A. McGowan, S. Padula, M. Scott, R. Silcox and J. Simpson, "The Aircraft Morphing Program," in *39th Structures, Structural Dynamics, and Materials Conference and Exhibit*, Long Beach, CA, 1998.

- [23] S. Körpe, Aerodynamic Modelling and Optimization of Morphing Wings, Ph.D. Dissertation: Middle East Technical University, 2014.
- [24] “Aluminium Alloy - Commercial Alloy - 6061 - T6 Extrusions,” Aalco, [Online]. Available: [http://www.aalco.co.uk/datasheets/Aluminium-Alloy-6061-T6-Extrusions\\_145.ashx](http://www.aalco.co.uk/datasheets/Aluminium-Alloy-6061-T6-Extrusions_145.ashx). [Accessed 3 July 2015].
- [25] Y. Ostovan, Experimental Investigation of Waveform Tip Injection on the Characteristics of the Tip Vortex, M.Sc. Dissertation: METU, 2011.
- [26] “Model 471B Thermo-Anemometer Test Instrument,” Dwyer Instruments International, [Online]. Available: <http://www.dwyerinst.com/Product/TestEquipment/Thermo-Anemometers/Model471B>. [Accessed 04 July 2015].
- [27] M. H. Özkanaktı, Measurement of Lift and Drag in Morphing Wings Using a High Precision Load Cell, M.Sc. Dissertation: Middle East Technical University, 2015.
- [28] ATI Industrial Automation, 2010. [Online]. Available: [http://www.atia.com/products/ft/ft\\_models.aspx?id=Gamma](http://www.atia.com/products/ft/ft_models.aspx?id=Gamma). [Accessed 2015].
- [29] G. Barden, Development of A Wind Tunnel Force Balance and Related Practical Exercise Manual, B.Eng. Dissertation: Charles Darwin University, 2014.
- [30] “National Instruments,” [Online]. Available: <http://www.ni.com/pdf/manuals/371747f.pdf>. [Accessed 16 08 2015].
- [31] National Instruments, [Online]. Available: <http://sine.ni.com/nips/cds/view/p/lang/en/nid/208800>. [Accessed 17 08 2015].
- [32] S. Bell, “A Beginner's Guide to Uncertainty of Measurement,” *National Physical Laboratory*, vol. 11, no. 2, March 2001.
- [33] J. B. Barlow, W. H. Rae, Jr. and A. Pope, *Low-Speed Wind Tunnel Testing*, New York: John Wiley & Sons, 1999.
- [34] “Error Analysis,” [Online]. Available: <http://teacher.nsl.rochester.edu>

/phy\_labs/AppendixB/AppendixB.html. [Accessed 08 2015].

- [35] A. Mukasyan, "Data and Error Analysis," [Online]. Available: [http://www3.nd.edu/~amoukasi/CBE358\\_Lab1/Data\\_Error\\_analysis.pdf](http://www3.nd.edu/~amoukasi/CBE358_Lab1/Data_Error_analysis.pdf). [Accessed 08 2015].
- [36] H. Zhang, Y. Zhou and J. Whitelaw, "Nier-Field Wing-Tip Vortices and Exponential Solution," *Journal of Aircraft*, vol. 43, no. 2, pp. 445-449, 2006.
- [37] "Dynamic Studio User Guide," Dantec Dynamics, Skovlunde, 2015.
- [38] J. McArthur, Aerodynamics of Wings at Low Reynolds Numbers, PhD Dissertation: University of Southern California, 2007.
- [39] "Aerospace and Ocean Engineering, Virginia Tech," [Online]. Available: <http://www.dept.aoe.vt.edu/~lutze/AOE3104/airfoilwings.pdf>. [Accessed 08 2015].
- [40] "Weather Underground," [Online]. Available: <http://www.wunderground.com> [Accessed 08 2015].
- [41] "Flow of Fluids Through Valves Fittings and Pipe Technical Paper No. 410," Crane, Connecticut, 2010.
- [42] e. David R. Lide, CRC Handbook of Chemistry and Physics, Florida: CRC Internet Version, 2005.
- [43] P. M. Bagade, S. B. Krishnan and T. K. Sengupta, "DNS of Low Reynolds Number Aerodynamics in the Presence of Free Stream Turbulence," *Frontiers in Aerospace Engineering*, vol. 4, no. 1, pp. 20-34, May 2015.
- [44] T. K. Sengupta, Theoretical and Computational Aerodynamics, John Wiley & Sons, 2014.
- [45] H. Hu and Z. Yang, "An Experimental Study of the Laminar Flow Separation on a Low-Reynolds-Number Airfoil," *Journal of Fluids Engineering*, vol. 130, 2008.



- [46] C. S. Lee, D.-B. Wang, F.-B. Hsiao, Y. H. Lim and S. Srigrarom, "Classification of Airfoils by Abnormal Behavior," in *24TH International Congress of the Aeronautical Sciences*, 2004.
- [47] D. F.R.S., *The Aerodynamic Design of Aircraft*, Pergamon, 1978.
- [48] W. Chen and L. P. Bernal, "Design and Performance of Low Reynolds Number Airfoils for Solar Powered Flight," in *46th AIAA Aerospace Sciences Meeting and Exhibit*, Reno, Nevada, 2008.
- [49] M. P. Thake, Investigation of a Laminar Airfoil with Flow Control and the Effect of Reynolds Number, MSc Dissertation: The Ohio State University, 2011.
- [50] A. Jones, N. Bakhtian and H. Babinsky, "Low Reynolds Number Aerodynamics of Leading Edge Flaps," University of Cambridge.
- [51] J. Wu, *Elements of Vorticity Aerodynamics*, Springer, 2005.
- [52] Y. A. Çengel and J. M. Cimbala, *Fluid Mechanics, Fundamentals and Applications*, New York: McGraw-Hill, 2006.
- [53] N. E. Öçer, G. Taşar, O. Uzol and S. Özgen, "Flow Structure and Turbulence in Near Fields of Circular and Non-Circular Jets," *EUCASS Proceedings Series*, vol. 3, no. 41-52, 2012.
- [54] O. A. Alsayed, W. Asrar, A. Omar, K. Kwon and H. Jung, "Experimental Investigation of Plain and Flapped Wing Tip Vortices," *Journal of Aircraft*, vol. 46, no. 1, pp. 254-561, 2009.
- [55] G. Michea, Formation and Early Development of Wing Tip Vortices, PhD Dissertation: University of Glasgow, 2013.
- [56] A. Heyes, R. Jones and D. Smith, "Wandering of wing-tip vortices," London.
- [57] E. Maskell, "Progress Towards a Method for the Measurement of the Components of a Wing of Finite Span," Royal Aircraft Establishment, 1973.
- [58] B. R. Ramaprian and Y. Zheng, "Measurements in Rollup Region of the Tip Vortex," *AIAA*, vol. 35, no. 12, pp. 1837-1843, 1997.

- [59] C. Brossard, J. Monnier, P. Barricau, F. Vandernoot, Y. Le Sant, F. Champagnat and G. Le Besnerais, “Principles and Applications of Particle Image Velocimetry,” *AerospaceLab*, vol. December, no. 1, 2009.
- [60] W. R. Quinn, “Measurements in the near flow field of an isosceles triangular turbulent free jet,” *Experiments in Fluids*, vol. 39, pp. 111-126, 2005.
- [61] D. Hepperle, “JavaFoil,” [Online]. Available: <http://www.mh-aerotoools.de/airfoils/java/JavaFoil%20Users%20Guide.pdf>.
- [62] K. Hansen, R. Kelso, A. Choudhry and M. Arjomandi, “Laminar Separation Bubble Effect on the Lift Curve Slope of an Airfoil,” in *19th Australasian Fluid Mechanics Conference*, Melbourne, 2014.
- [63] M. Gaster, “The Structure and Behaviour of Laminar Separation Bubbles,” Aeronautical Research Council Reports and Memoranda, London, 1969.
- [64] D. P. Raymer, *Aircraft Design : A Conceptual Approach*, Washington: AIAA, 1992.
- [65] “Infrared Thermo-Dynamic Research at University of Ancona,” Azo Materials, [Online]. Available: <http://www.azom.com/article.aspx?ArticleID=7895>. [Accessed 08 2015].
- [66] B. R. Munson, D. F. Young and T. H. Okiishi, *Fundamentals of Fluid Mechanics*, John Wiley & Sons, 1994.
- [67] J. D. Anderson, *Fundamentals of Aerodynamics*, McGraw-Hill, 2007.
- [68] “Basics of Turbulent FLOW,” [Online]. Available: <http://www.mit.edu/course/1/1.061/www/dream/SEVEN/SEVENTHEORY.PDF>. [Accessed 08 2015].
- [69] R. Ma and P. Liu , “Numerical Simulation of Low-Reynolds-Number and High-Lift Airfoil S1223,” in *World Congress on Engineering*, London, 2009.
- [70] “ANSYS Fluent User Guide,” Fluent Inc., 2006. [Online]. Available: <https://www.sharcnet.ca/Software/Fluent6/html/ug/node469.htm>. [Accessed 08 2015].

## APPENDIX A

### COMPARISON AT 15 M/S

#### At 15 m/s

The same procedure is repeated for all the wings for the angle of attack values that yields 2.5 N lift force at 15 m/s free stream velocity.

#### Velocity Magnitude Comparison

The in-plane mean velocity magnitude contours of the wings for 15 m/s free stream velocity at C and 2C Locations are presented in Figures A.1 and A.2

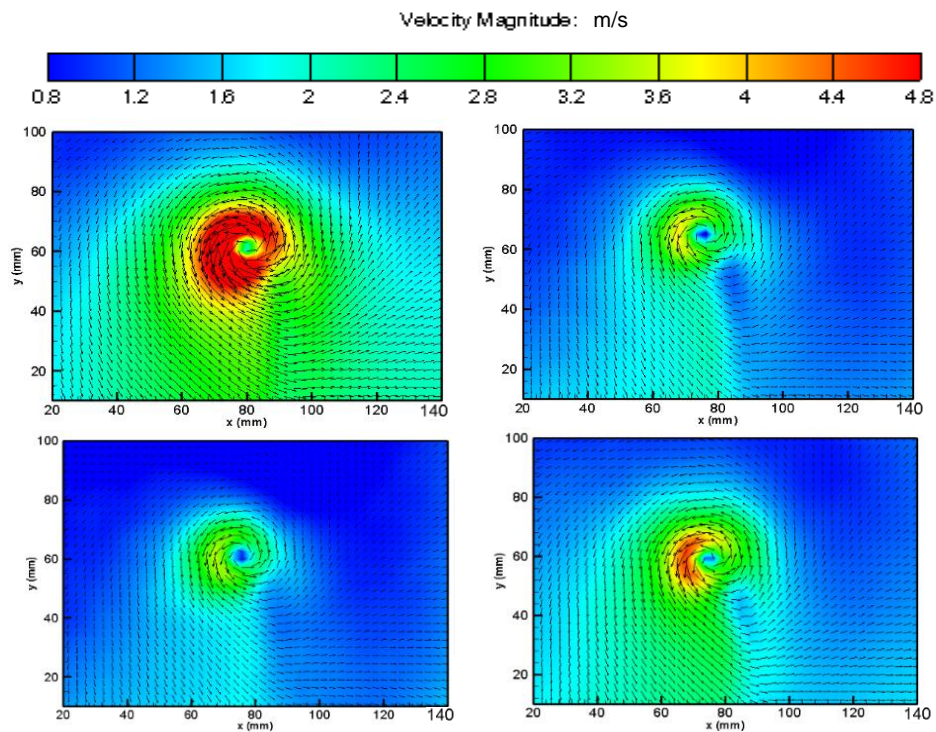


Figure A. 1 Velocity Magnitude Contours on one mean chord downstream plane at 15 m/s; Base Wing (Top Left), Optimized 14 Wing (Top Right), Morphed 10 Wing (Bottom Left) and Morphed 16.5 Wing (Bottom Right). Note that all cases are at different angles of attack as given in Table 4. but all producing the same 2.5 N lift force

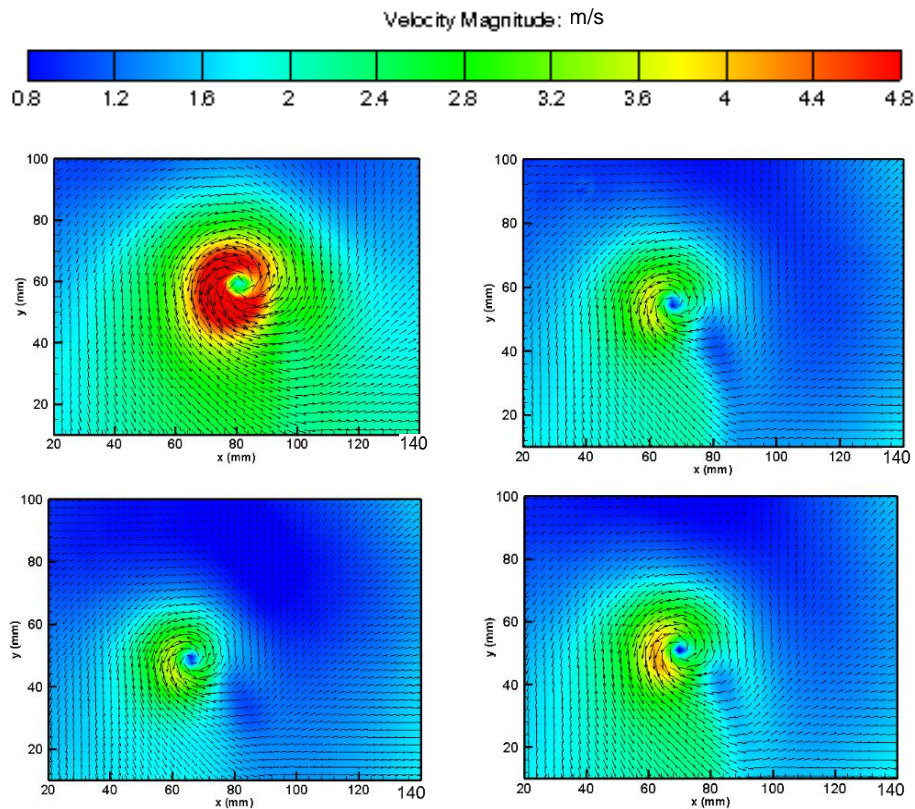


Figure A. 2 Velocity Magnitude Contours on two mean chord downstream plane at 15 m/s; Base Wing (Top Left), Optimized 14 Wing (Top Right), Morphed 10 Wing (Bottom Left) and Morphed 16.5 Wing (Bottom Right). Note that all cases are at different angles of attack as given in Table 4.5 but all producing the same 2.5 N lift force

It is seen that the Base wing has the highest velocity magnitude and followed by Morphed 16.5 Wing. Moreover, the velocity magnitude of Optimized 14 Wing and Morphed 10 Wing seems similar and will be distinguished by looking at the magnitude graphs. In all images it is observed that the wing wake causes drops in the velocity near the vortex location.

The velocity magnitude plots along y direction are presented in Figures A.3 and A.4. It is observed that at C location, Morphed 10 wing has the smallest velocity magnitude and it is followed by Optimized 14 Wing. At 2C Location, their peak magnitudes are almost the same where, the Base Wing and Morphed 16.5 wing has higher velocity magnitudes.

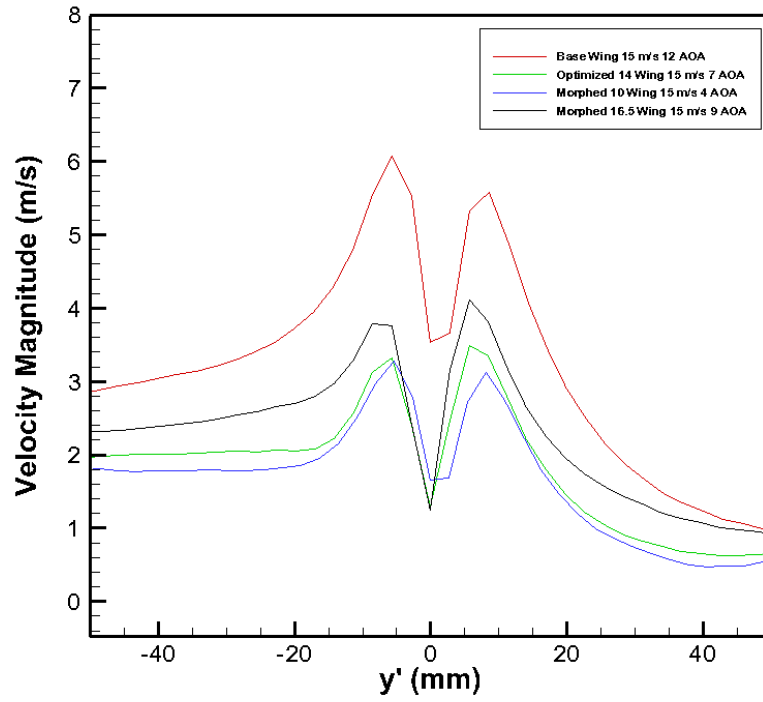


Figure A. 3 Velocity Magnitude along y direction at 15 m/s on one mean chord downstream plane

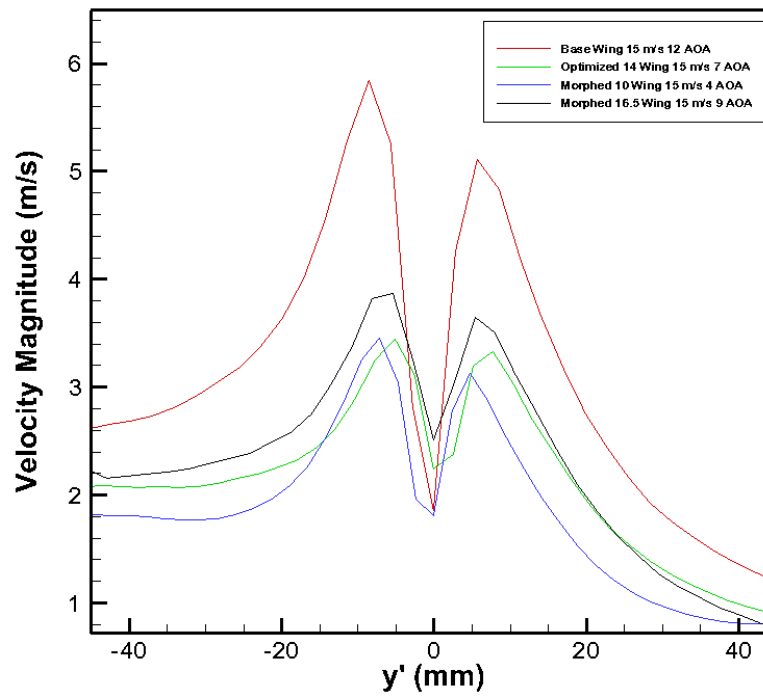


Figure A. 4 Velocity Magnitude along y direction at 15 m/s at two mean chord downstream plane

The distance between the two peaks of the velocity magnitude curves indicates the core radius of the vortex. The core radius values are listed in Table A.1.

Table A. 1 Vortex Core Radius

<i>at 15 m/s</i>	<i>C (mm)</i>	<i>2C (mm)</i>
<i>Base Wing</i>	8,545	7,092
<i>Optimized 14 Wing</i>	5,372	6,411
<i>Morphed 10 Wing</i>	7,664	5,934
<i>Morphed 16.5 Wing</i>	6,371	5,388

Looking at the vortex core radius of the four half wing models, it is seen that at 15 m/s at C location, Optimized Wing has the smallest tip vortex core radius where it has the second lowest velocity magnitude. According to load cell experimental results, Optimized 14 Wing has the lowest drag value. Thus having the smallest vortex core radius, and second lowest velocity magnitude the Optimized 14 Wing is found to be operating well at 15 m/s free stream velocity. At 2C Location, as in the case of 14 m/s the core radius of the Optimized 14 Wing increases in contrary to the other half wing models. Since its magnitude decreases, this may be the indication of fast diffusion of the vortex.

**Vorticity Comparison**

The vorticity contours of the wings at 15 m/s at C and 2C locations are presented in Figures A.5 and A.6. It is seen that the Base Wing has the highest vorticity region while Morphed 10 Wing has the lowest.

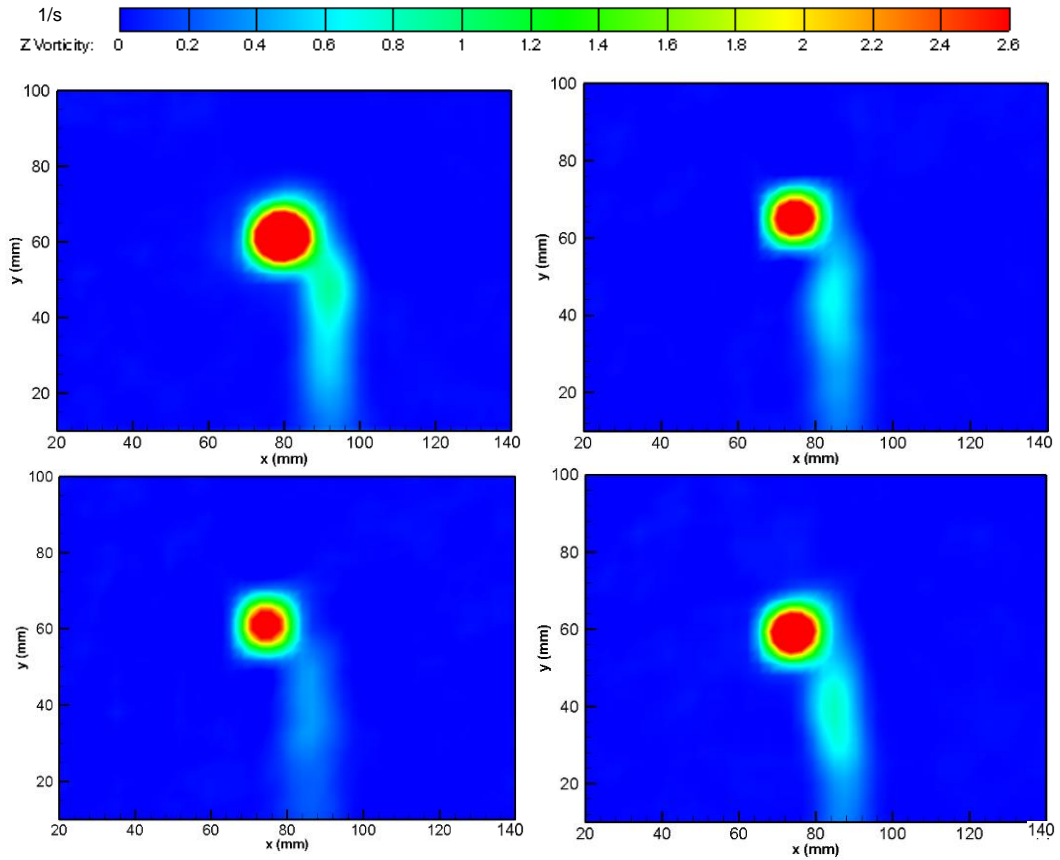


Figure A. 5 Vorticity Velocity Magnitude Contours on one mean chord downstream plane at 15 m/s; Base Wing (Top Left), Optimized 14 Wing (Top Right), Morphed 10 Wing (Bottom Left) and Morphed 16.5 Wing (Bottom Right). Note that all cases are at different angles of attack as given in Table 4.5 but all producing the same 2.5 N lift force

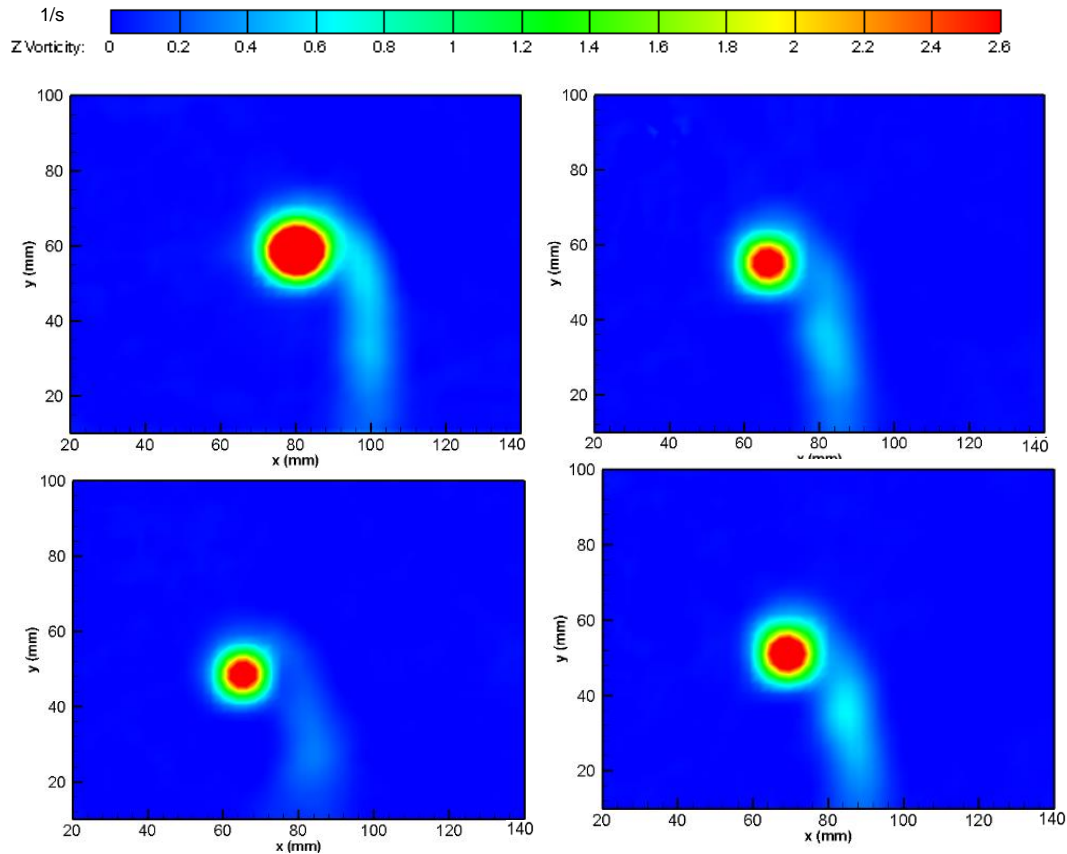


Figure A. 6 Vorticity Contours on two mean chord downstream plane at 15 m/s; Base Wing (Top Left), Optimized 14 Wing (Top Right), Morphed 10 Wing (Bottom Left) and Morphed 16.5 Wing (Bottom Right). Note that all cases are at different angles of attack as given in Table 4.5 but all producing the same 2.5 N lift force

The vorticity values along y direction at C and 2C locations are presented in Figures A.7 and A.8. Although Morphed 10 Wing at C locations seems to have the lowest vorticity in contour graphs. Moreover, moving away from the vortex, the velocity approaches zero as expected for all the half wing models. At 2C Location, Morphed 10 Wing and Optimized 14 Wing has the lowest vorticity magnitudes. It should be noted that the grid resolution may have effected plots.



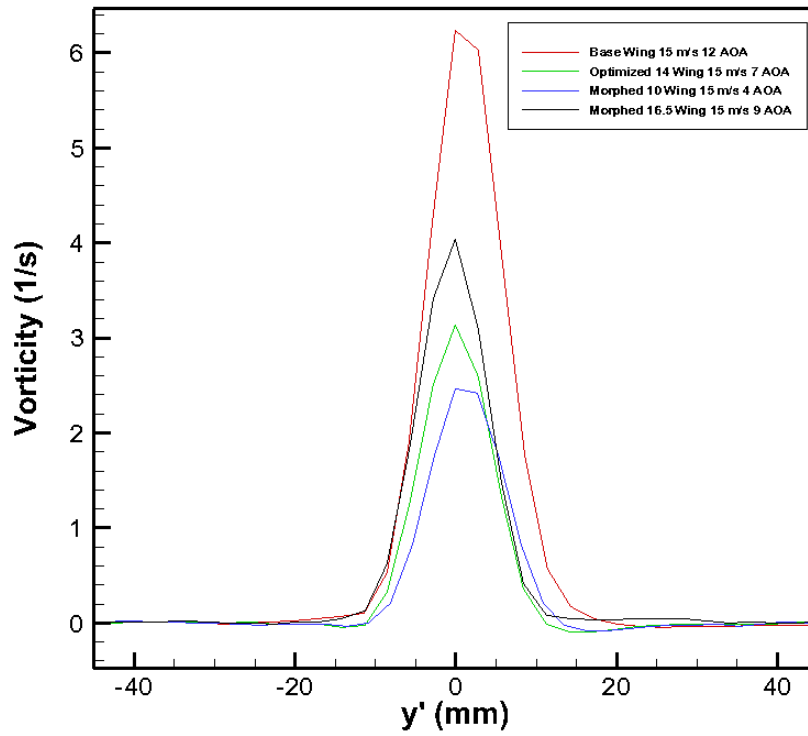


Figure A. 7 Vorticity along y direction at 15 m/s on one mean chord downstream

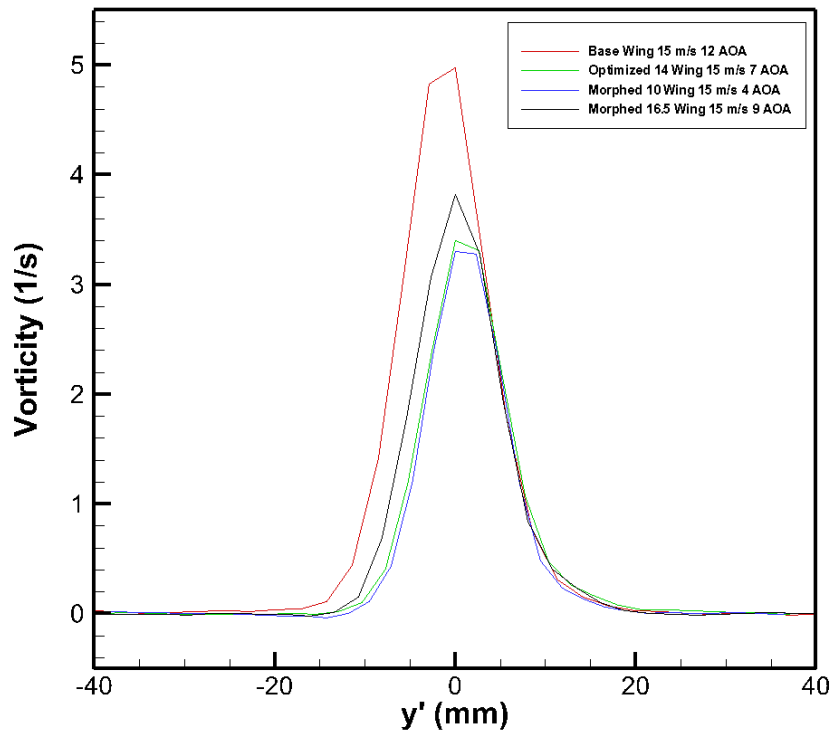


Figure A. 8 Vorticity along y direction at 15 m/s on two mean chord downstream

### Turbulence Kinetic Energy Comparison

The turbulence kinetic energy contours of the wings at C and 2C locations are presented in Figures A.9 and A.10. The Base wing has the maximum kinetic energy value while Optimized 14 Wing has the lowest at C location. This may cause low dissipation and result in high vorticity magnitude for Optimized 14 Wing as presented in previous section. The noise in the data of Optimized 14 Wing at 2C location is because of the instantaneous velocity fields of the acquired PIV data.

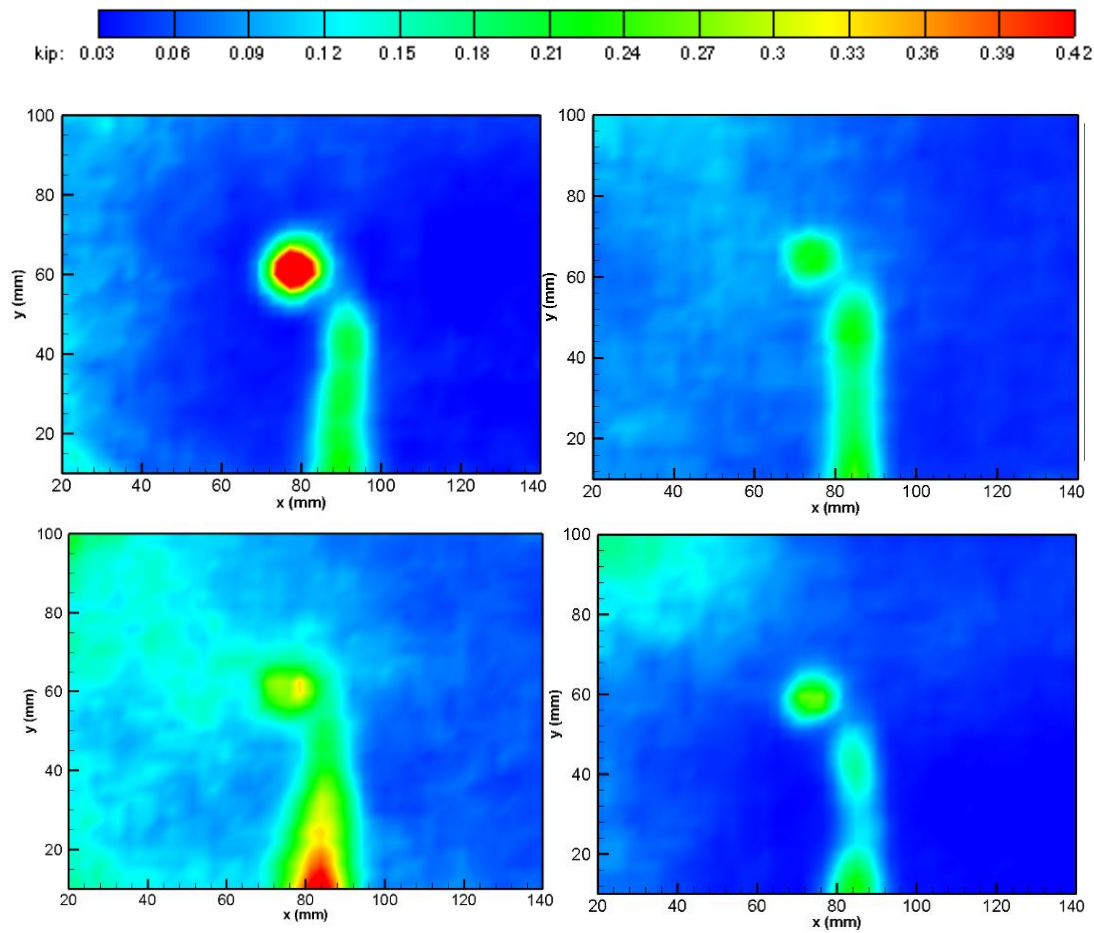


Figure A. 9 Turbulence Kinetic Energy Contours on one mean chord downstream plane at 15 m/s; Base Wing (Top Left), Optimized 14 Wing (Top Right), Morphed 10 Wing (Bottom Left) and Morphed 16.5 Wing (Bottom Right). Note that all cases are at different angles of attack as given in Table 4.5 but all producing the same 2.5 N lift force

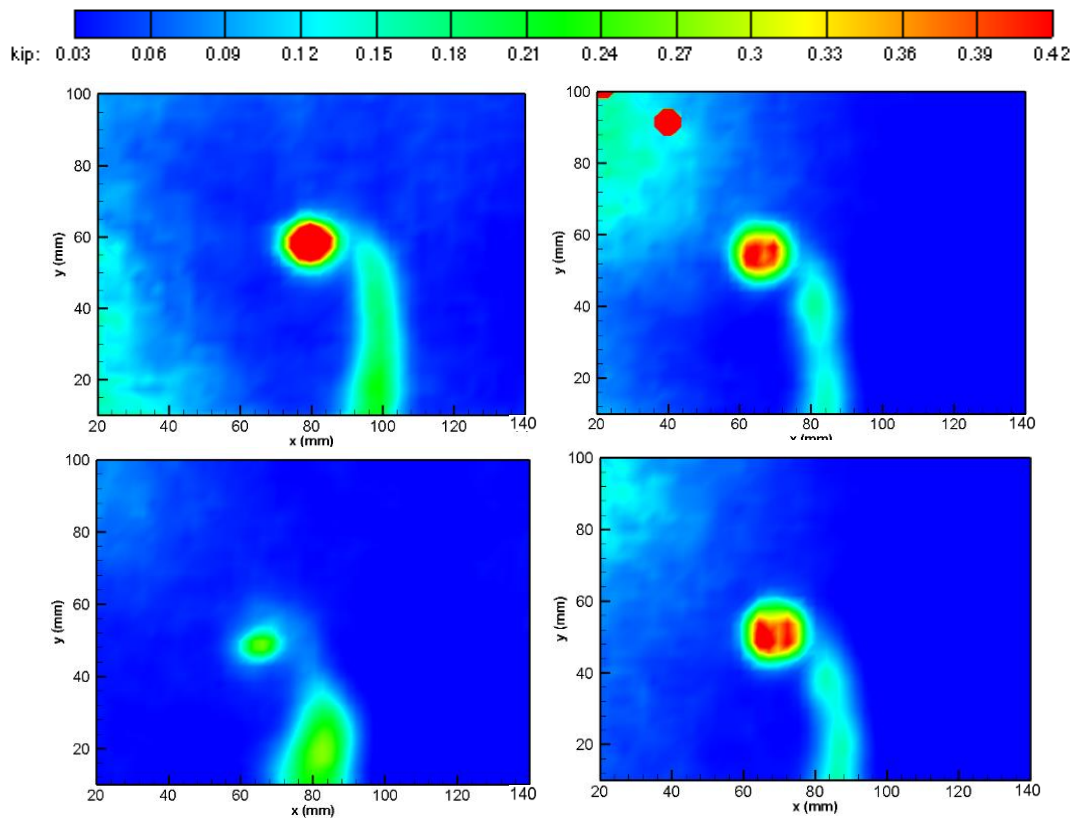


Figure A. 10 Turbulence Kinetic Energy Contours on two mean chord downstream plane at 15 m/s; Base Wing (Top Left), Optimized 14 Wing (Top Right), Morphed 10 Wing (Bottom Left) and Morphed 16.5 Wing (Bottom Right). Note that all cases are at different angles of attack as given in Table 4.5 but all producing the same 2.5 N lift force

The turbulent kinetic energy values along the y direction at C and 2C locations are presented in Figures A.11, and A.12. The turbulence fluctuations caused by the wake of the wing can be seen at low y values. The wings with higher planform area and chord (Morphed 10 and Optimized 14 Wing) is exposed to the wing wake more. The Optimized 14 Wing has the lowest turbulence kinetic energy values followed by Morphed 16.5 Wing. Thus, the performance of the Optimized 14 Wing reduced at 15 m/s compared to its designed velocity of 14 m/s considering the vorticity and turbulence kinetic energy results.

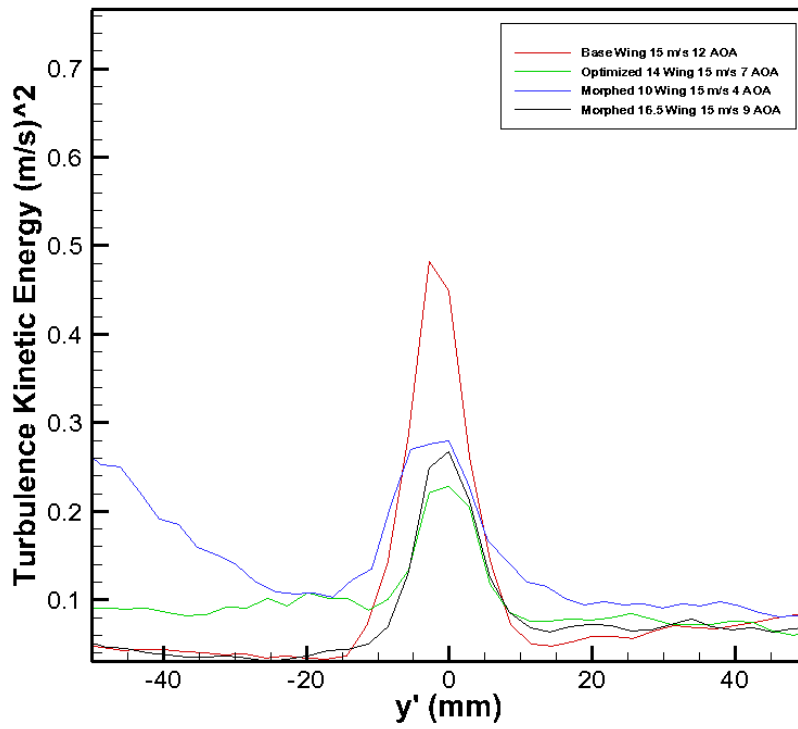


Figure A. 11 Turbulence Kinetic Energy along y direction at 15 m/s on one mean chord downstream plane

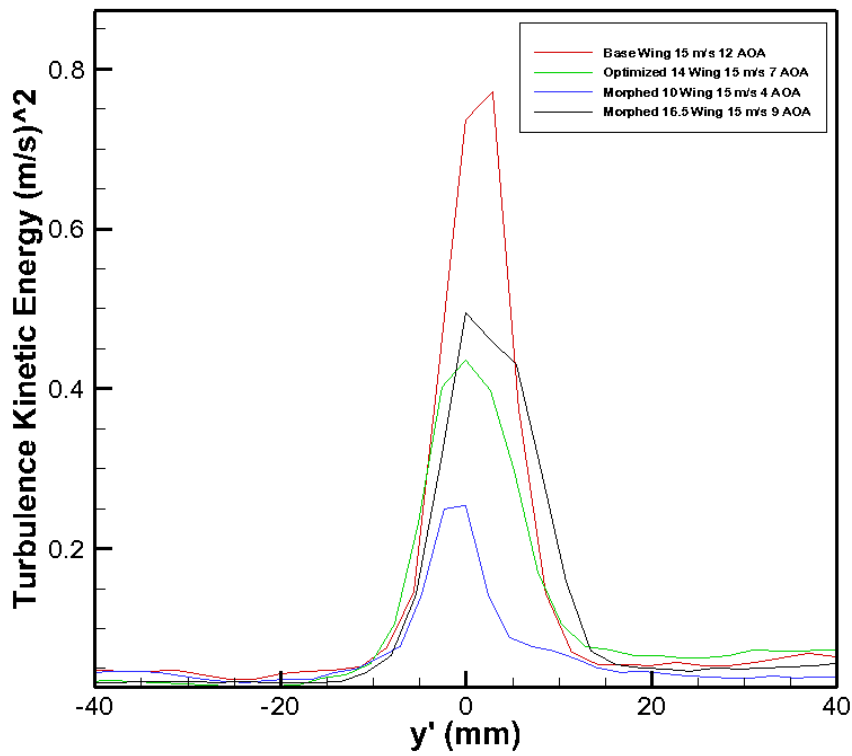


Figure A. 12 Turbulence Kinetic Energy along y direction at 15 m/s on two mean chord downstream plane

## Reynolds Stress Component Comparison

Reynolds Stress Component of the four half wing models at 15 m/s at one chord and two chord downstream locations are presented in Figures A.13 and A.14.

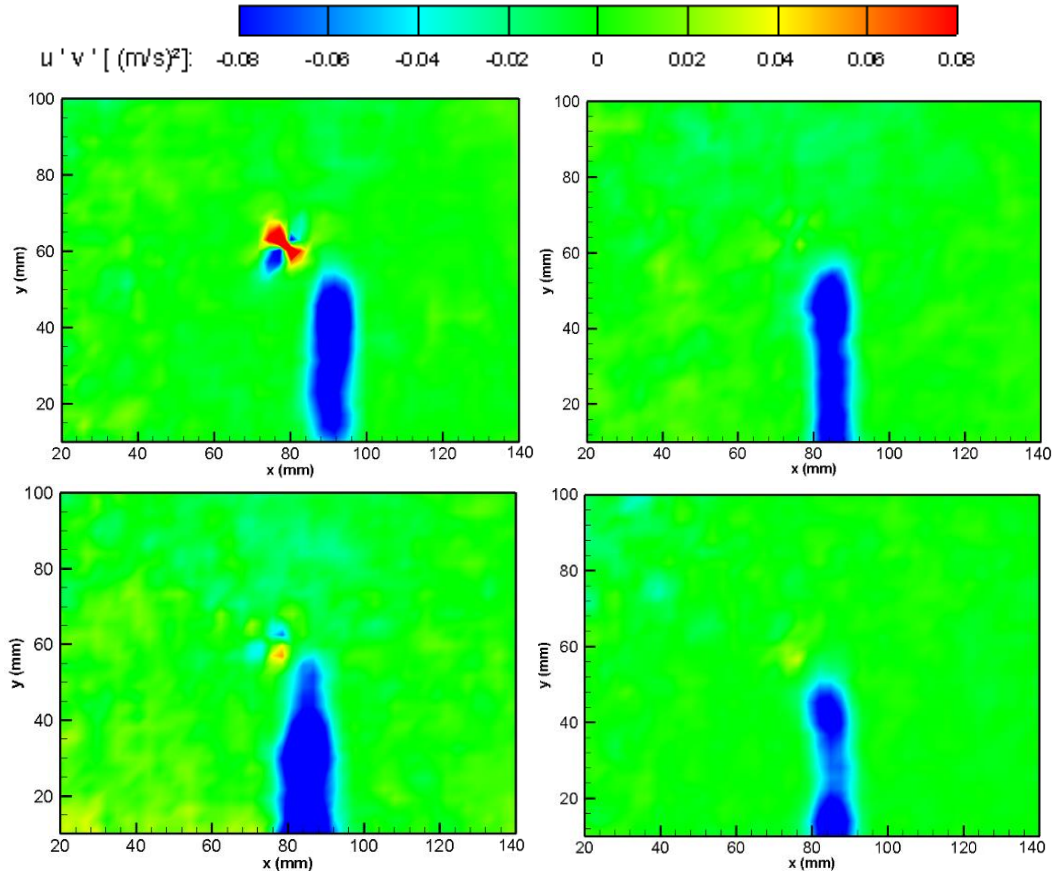


Figure A. 13  $\overline{u'v'}$  Contours on one mean chord downstream plane at 15 m/s; Base Wing (Top Left), Optimized 14 Wing (Top Right), Morphed 10 Wing (Bottom Left) and Morphed 16.5 Wing (Bottom Right). Note that all cases are at different angles of attack as given in Table 4.4 but all producing the same 2.5 N lift force

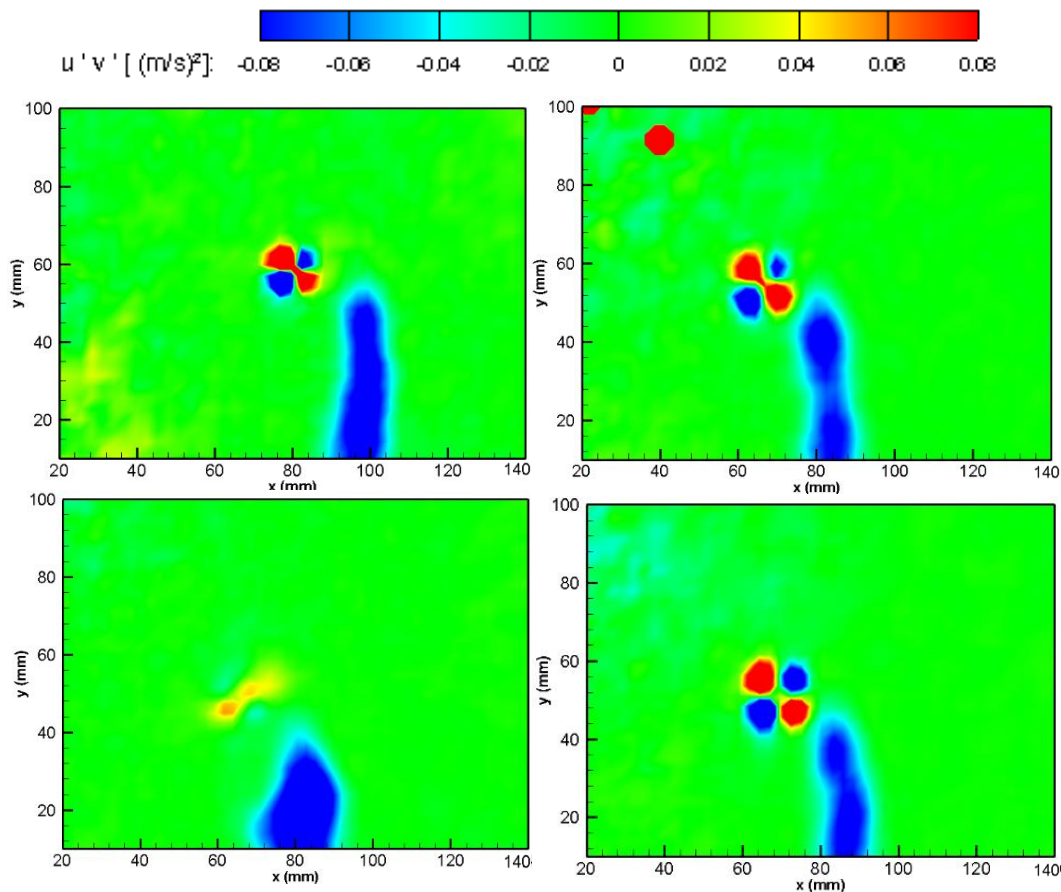


Figure A. 14  $\overline{u'v'}$  Contours on two mean chord downstream plane at 15 m/s; Base Wing (Top Left), Optimized 14 Wing (Top Right), Morphed 10 Wing (Bottom Left) and Morphed 16.5 Wing (Bottom Right). Note that all cases are at different angles of attack as given in Table 4.4 but all producing the same 2.5 N lift force

### Induced Drag Comparisons

Induced drag of the tip vortices of the half wing models are presented in Table A.2.

Table A. 2 Induced Drag of the Tip Vortices at 15 m/s

<i>Induced Drag (Newton)</i>	<i>Induced Drag at 15 m/s at C (PIV)</i>	<i>Induced Drag at 15 m/s at 2C (PIV)</i>	<i>Total Drag (Load Cell)</i>
Base Wing	0,0475	0,0461	0,2337
Optimized 14 Wing	0,0212	0,0223	0,1469
Morphed 10 Wing	0,0169	0,0159	0,1551
Morphed 16.5 Wing	0,0289	0,0260	0,1871

As it can be seen from the table, Morphed 10 Wing has the lowest induced drag and Optimized 14 Wing has the second lowest. Looking at the drag curve of load cell results, it can be seen that the total drag values are very close for these wings and they have the lowest total drag values among the four half wing models.





## APPENDIX B

### VECTOR MAPS AND VELOCITY MAGNITUDE

Looking at the velocity magnitude with vector map graphs, as the angle of attack increases, the peak values of the velocity magnitude is also increasing. From the results of velocity magnitude contours for all wings it is seen that the center size of the core of the vortex which has zero magnitude of velocity reduces with the increasing angle of attack and increasing free stream velocity. Although the zero velocity magnitude region of the center decreases, the magnitude of the highest regions of the velocity increases with increasing angle of attack values.

It is observed in all the wings in all conditions that, increasing the angle of attack or the free stream velocity results in an increase in velocity magnitude.

#### Base Wing

The Velocity Magnitude Contours with velocity vectors of the Base Wing are presented in Figures B.1, B.2 and B.3.

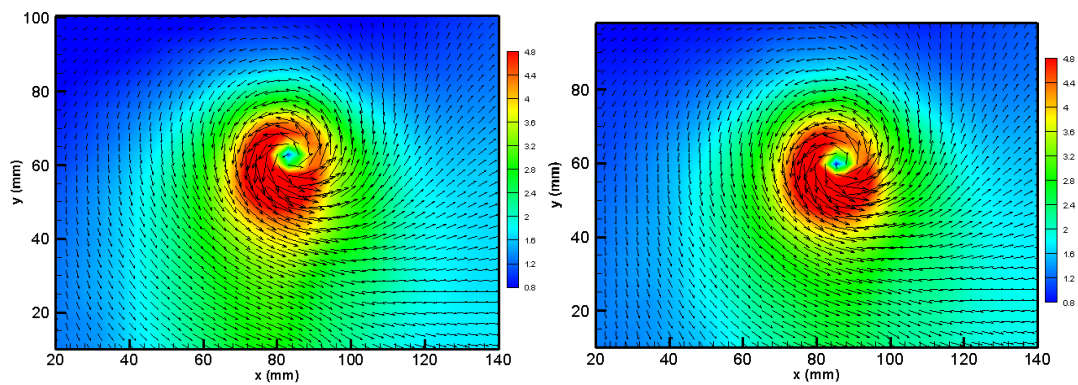


Figure B. 1 Velocity Magnitude of Base Wing at 14 m/s 15 AOA at C (left) and 2C (right) location

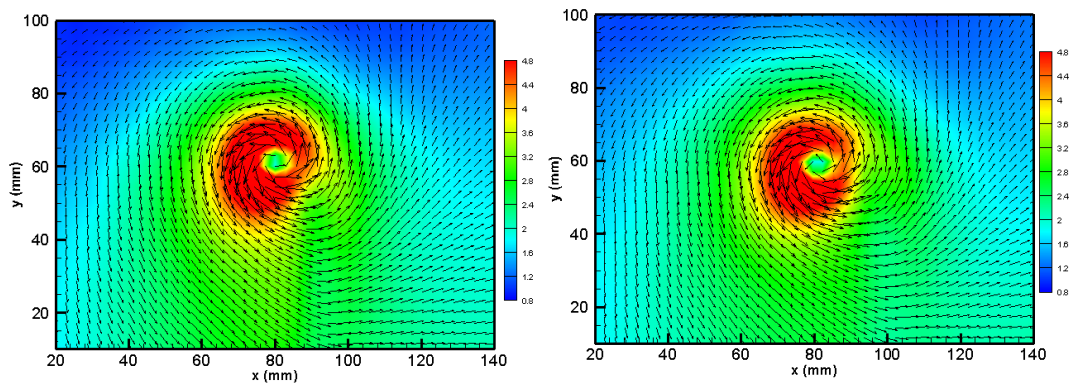


Figure B. 2 Velocity Magnitude of Base Wing at 15 m/s 12 AOA at C (left) and 2C (right) location

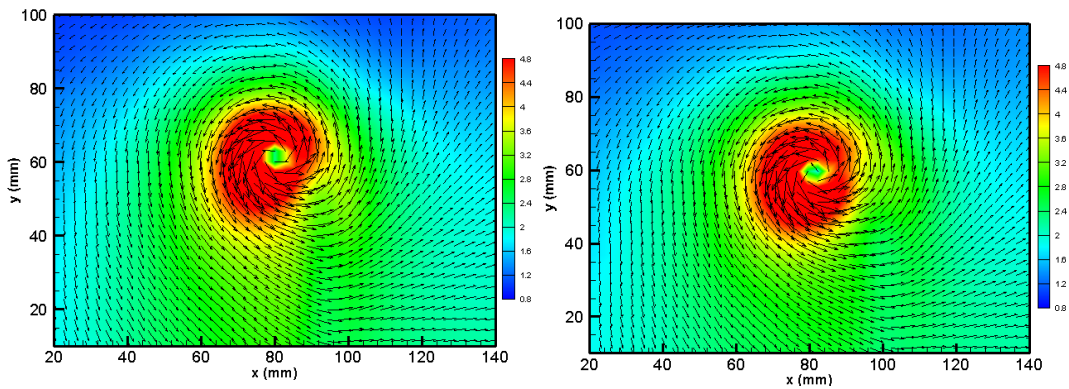


Figure B. 3 Velocity Magnitude of Base Wing at 15 m/s 13 AOA at C Location

### Optimized 14 Wing

The Velocity Magnitude Contours with velocity vectors of the Optimized 14 Wing are presented in Figures B.4, B.5, B.6 and B.7.

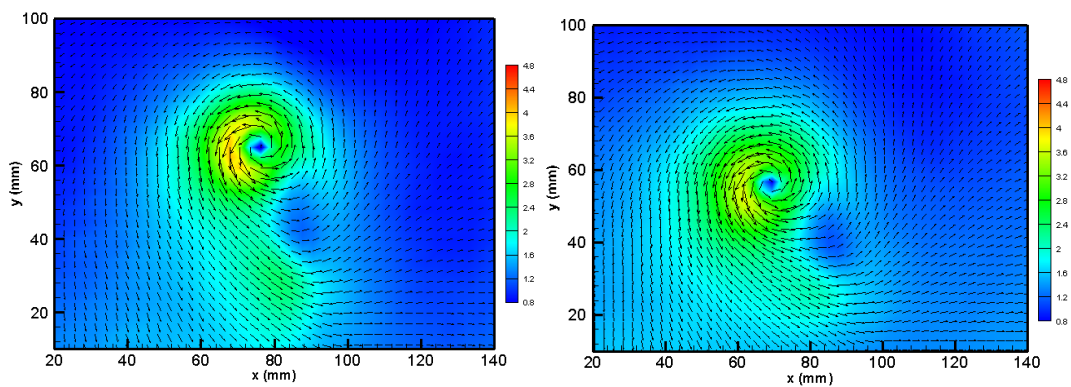


Figure B. 4 Velocity Magnitude of Optimized 14 Wing at 13 m/s 10 AOA at C (left) and 2C (right) location

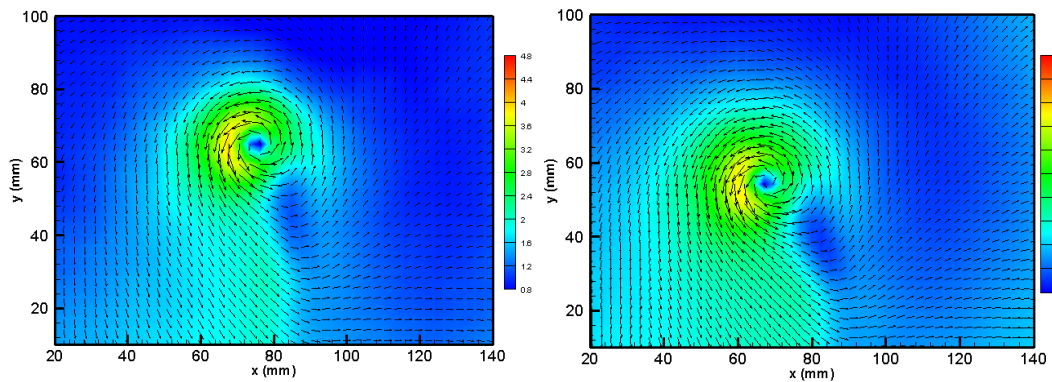


Figure B. 5 Velocity Magnitude of Optimized 14 Wing at 14 m/s 8 AOA at C (left) and 2C (right) location

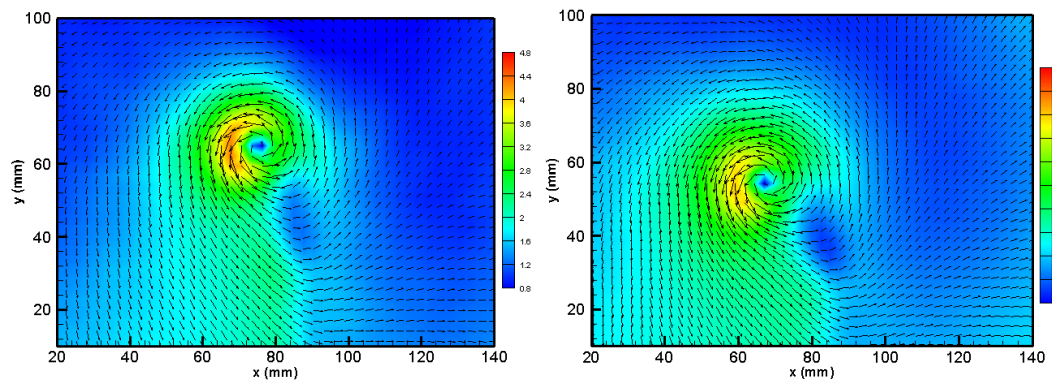


Figure B. 6 Velocity Magnitude of Optimized 14 Wing at 14 m/s 9 AOA at C (left) and 2C (right) location

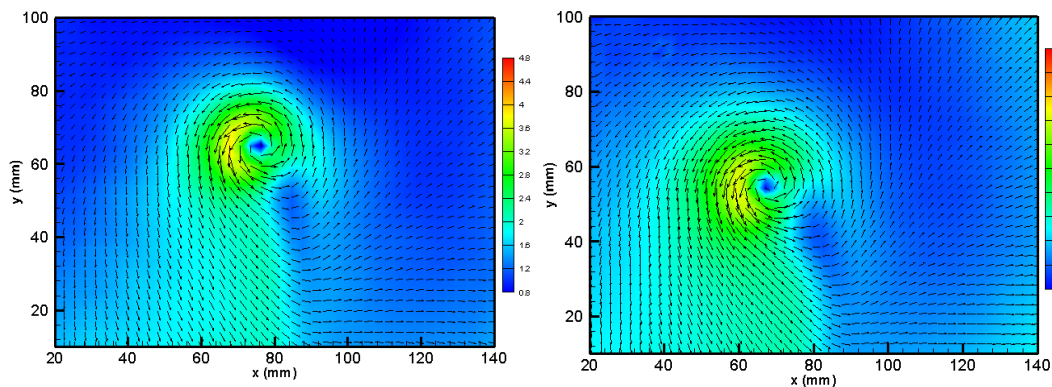


Figure B. 7 Velocity Magnitude of Optimized 14 Wing at 15 m/s 7 AOA at C (left) and 2C (right) location

#### 4.6.1 Morphed 10 Wing

The Velocity Magnitude Contours with velocity vectors of the Optimized 14 Wing are presented in Figures B.8, B.9, B.10, B.11, B.12, B.13, B.14 and B.15.

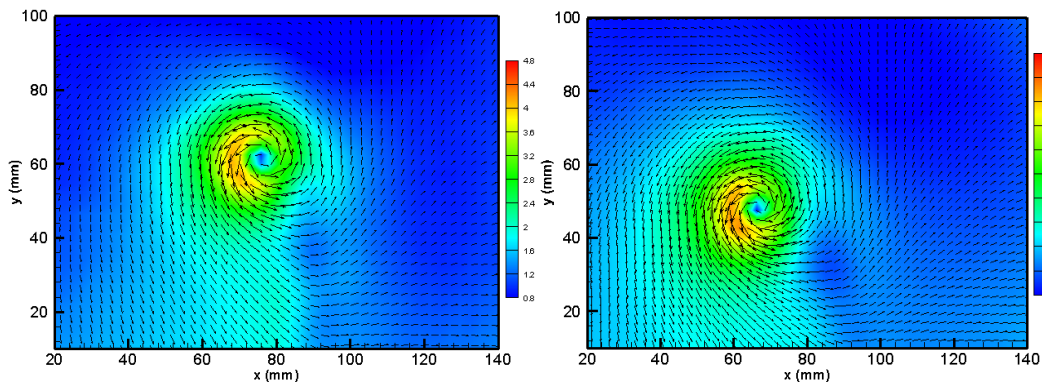


Figure B. 8 Velocity Magnitude of Morphed 10 Wing at 12 m/s 7 AOA at C (left) and 2C (right) location

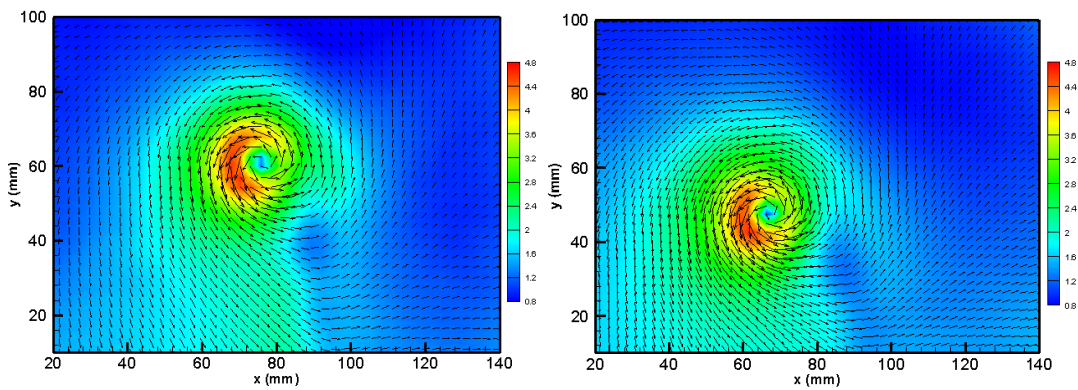


Figure B. 9 Velocity Magnitude of Morphed 10 Wing at 12 m/s 8 AOA at C (left) and 2C (right) location

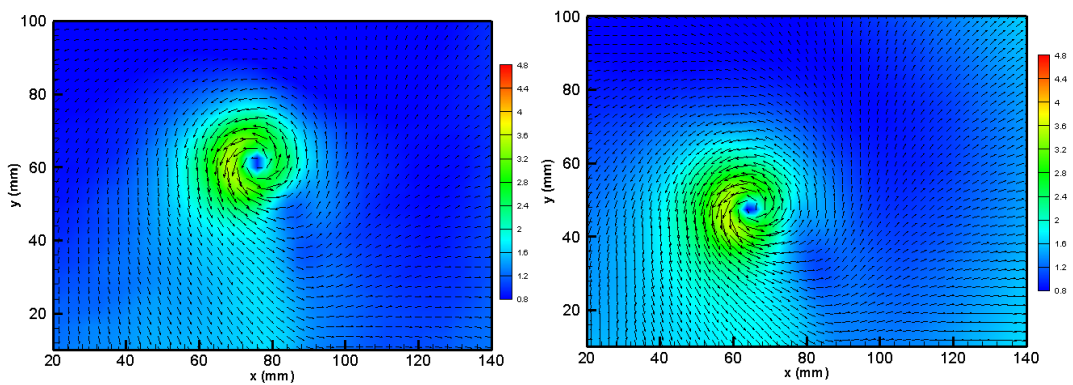


Figure B. 10 Velocity Magnitude of Morphed 10 Wing at 13 m/s 5 AOA at C (left) and 2C (right) location

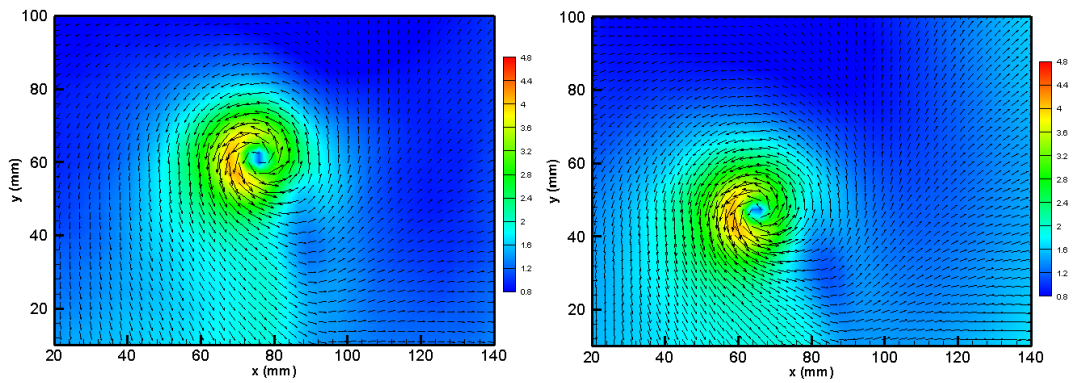


Figure B. 11 Velocity Magnitude of Morphed 10 Wing at 13 m/s 6 AOA at C (left) and 2C (right) location

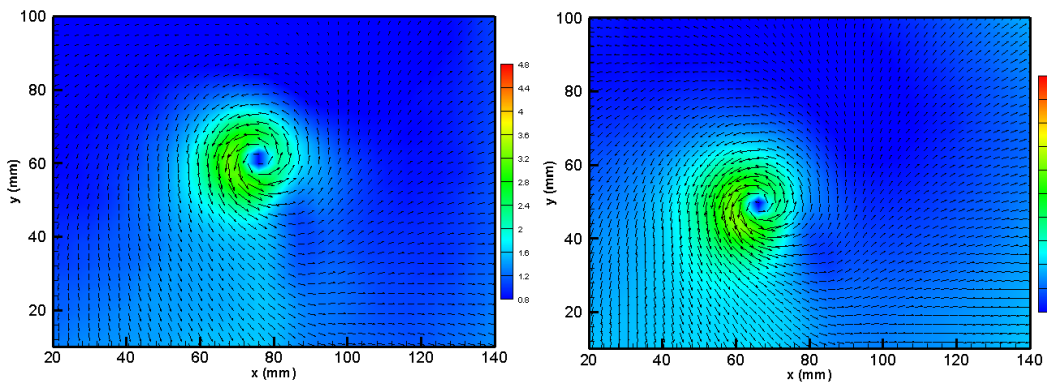


Figure B. 12 Velocity Magnitude of Morphed 10 Wing at 14 m/s 4 AOA at C (left) and 2C (right) location

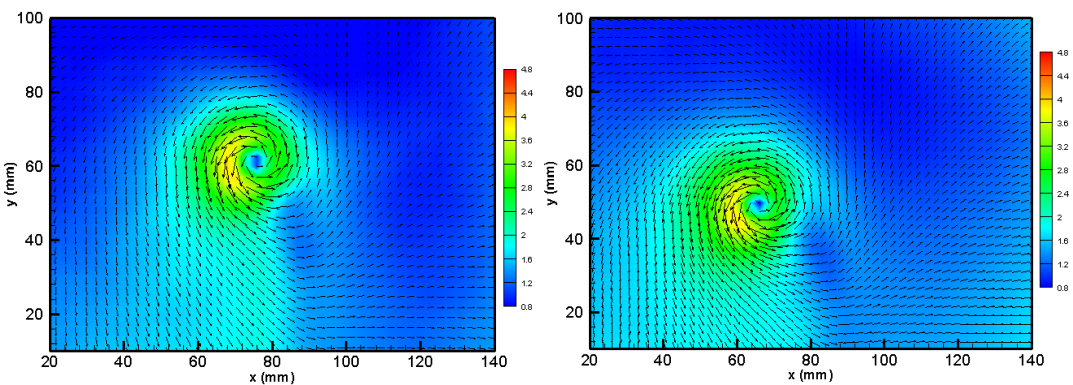


Figure B. 13 Velocity Magnitude of Morphed 10 Wing at 14 m/s 5 AOA at C (left) and 2C (right) location

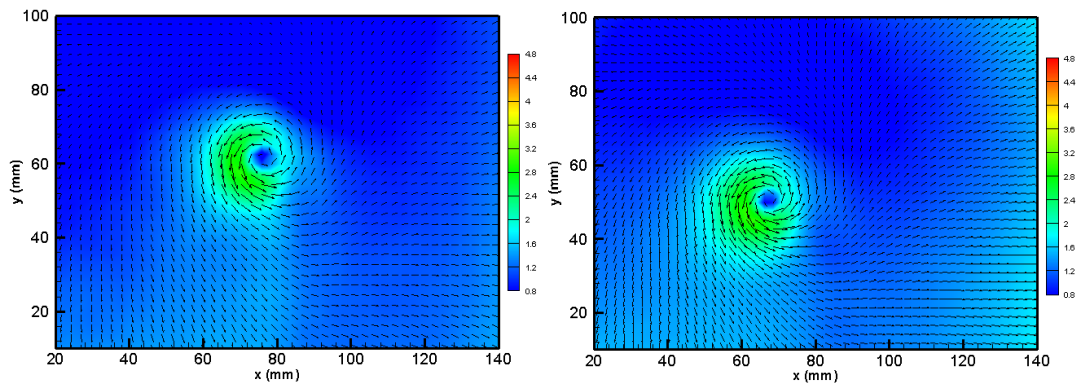


Figure B. 14 Velocity Magnitude of Morphed 10 Wing at 15 m/s 3 AOA at C (left) and 2C (right) location

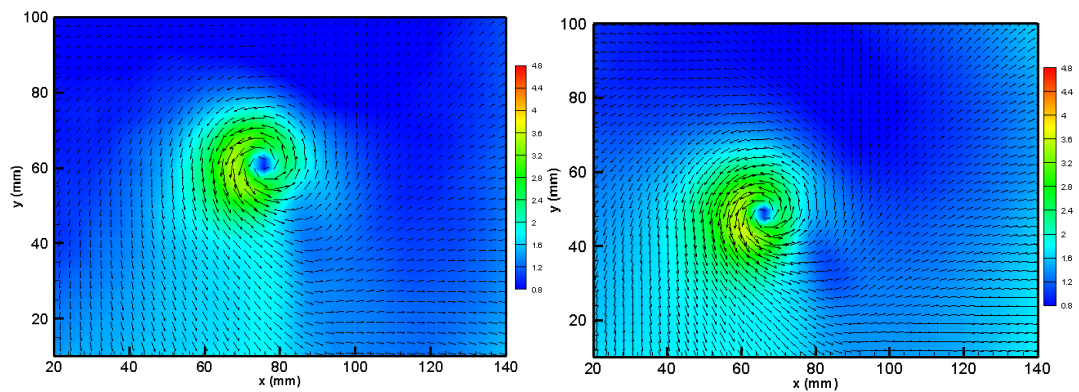


Figure B. 15 Velocity Magnitude of Morphed 10 Wing at 15 m/s 4 AOA at C (left) and 2C (right) location

### Morphed 16.5 Wing

The Velocity Magnitude Contours with velocity vectors of the Morphed 16.5 Wing are presented in Figures B.16, B.17, and B.18.

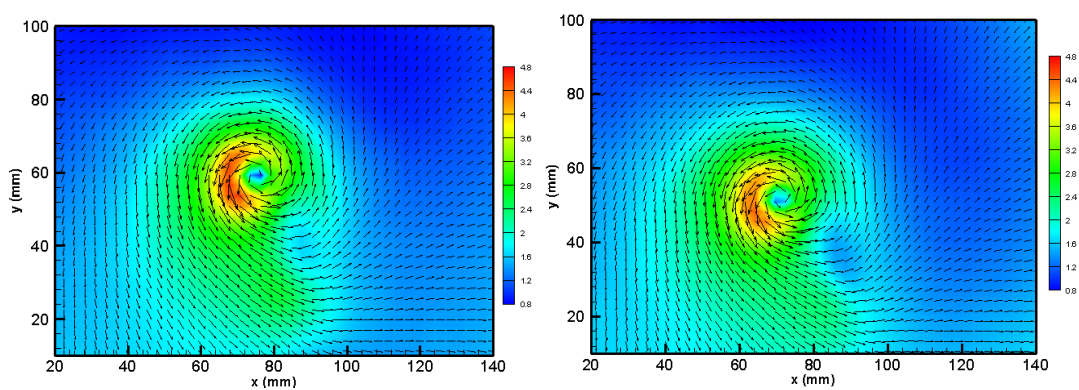


Figure B. 16 Velocity Magnitude of Morphed 16.5 Wing at 14 m/s 11 AOA at C (left) and 2C (right) location

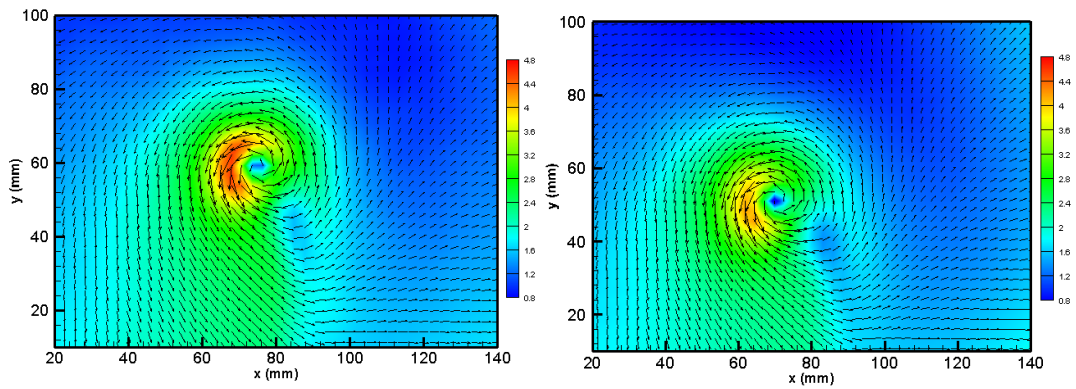


Figure B. 17 Velocity Magnitude of Morphed 16.5 Wing at 15 m/s 9 AOA at C (left) and 2C (right) location

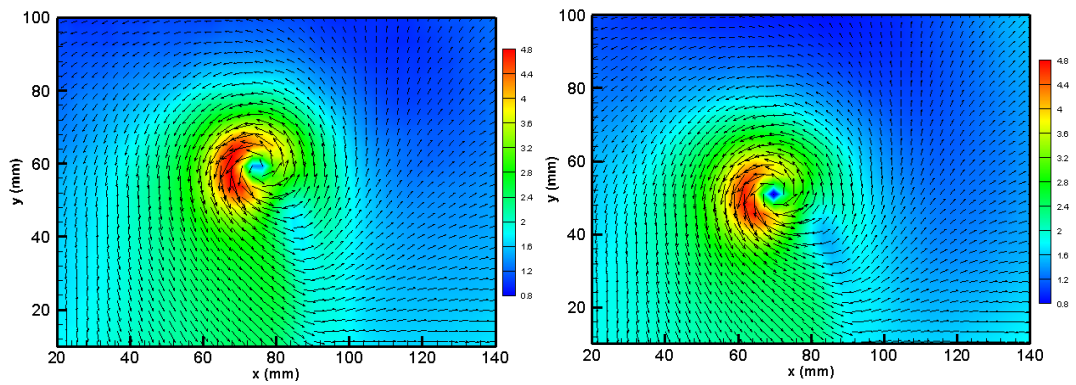


Figure B. 18 Velocity Magnitude of Morphed 16.5 Wing at 15 m/s 10 AOA at C (left) and 2C (right) location





## APPENDIX C

### VORTICITY CONTOURS

As the angle of attack increases, increase in lift force results in increase in peak values of the vorticity [21]. This phenomena is observed in all the wings.

#### Base Wing

The vorticity contours of the Base Wing are presented in Figures C.1, C.2, C.3, C.4, C.5, and C.6.

By comparing the vorticities of 15 m/s at 12 degree and 13 degree angle of attack values, it is seen that when the angle of attack increases, the wake of the wing also increases. Moreover, as the angle of attack increases, the region of high vorticity increases. Velocity comparisons are not applicable for this wing but will be discussed in the next sections for vorticity contours of the other wings.

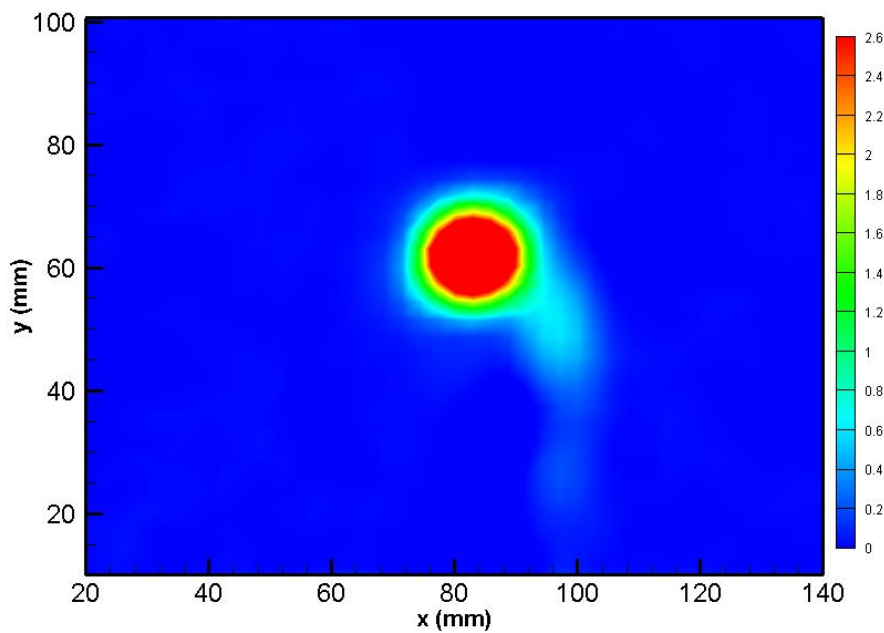


Figure C. 1 Base Wing Vorticity Contour at 14 m/s 15 AOA at C Location

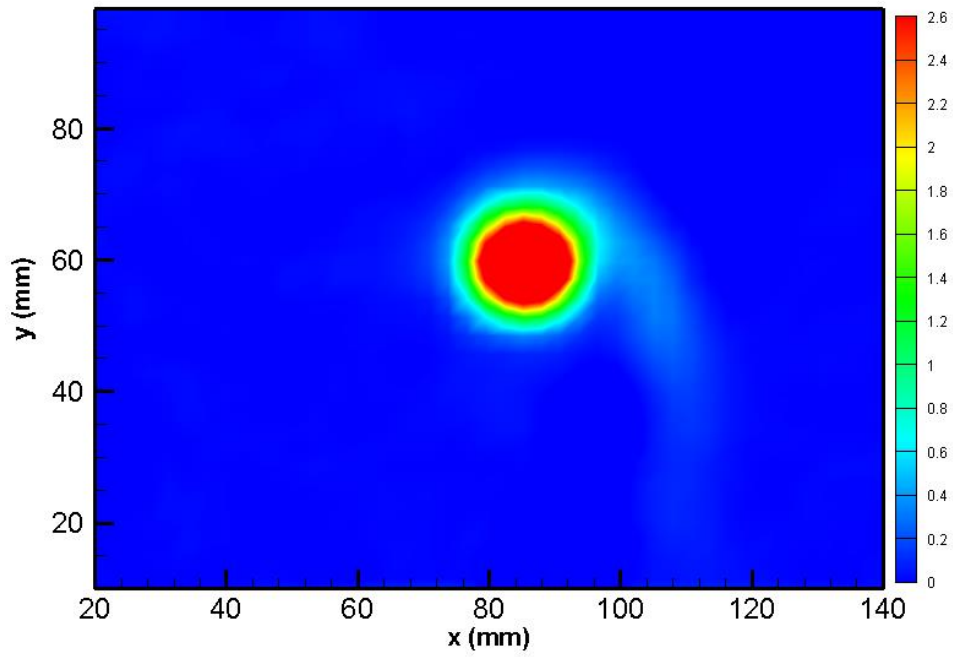


Figure C. 2 Base Wing Vorticity Contour at 14 m/s 15 AOA at 2C Location

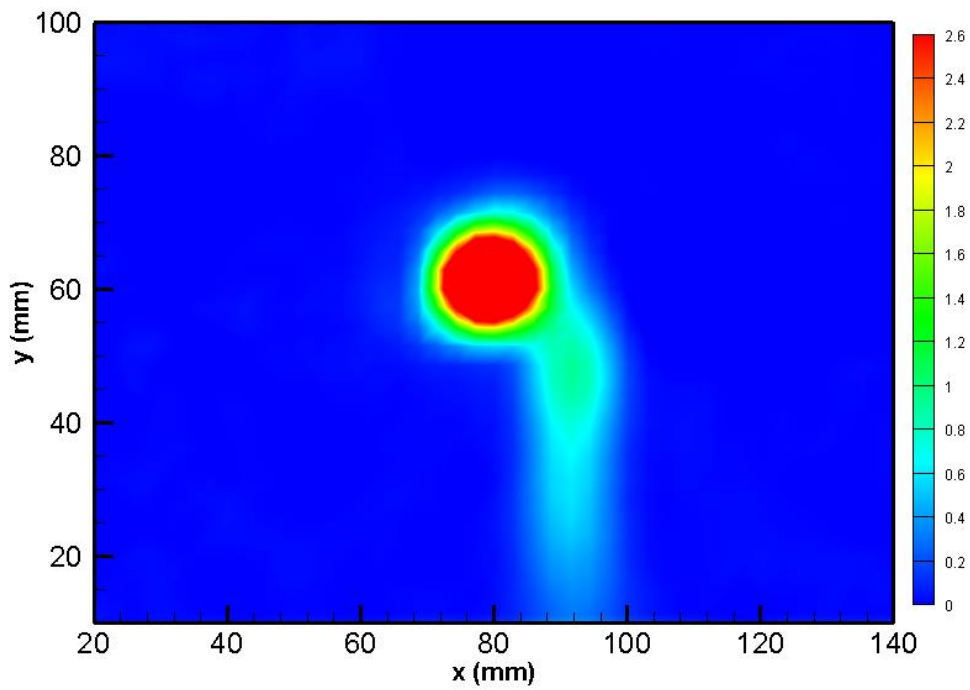


Figure C. 3 Base Wing Vorticity Contour at 15 m/s 12 AOA at C Location

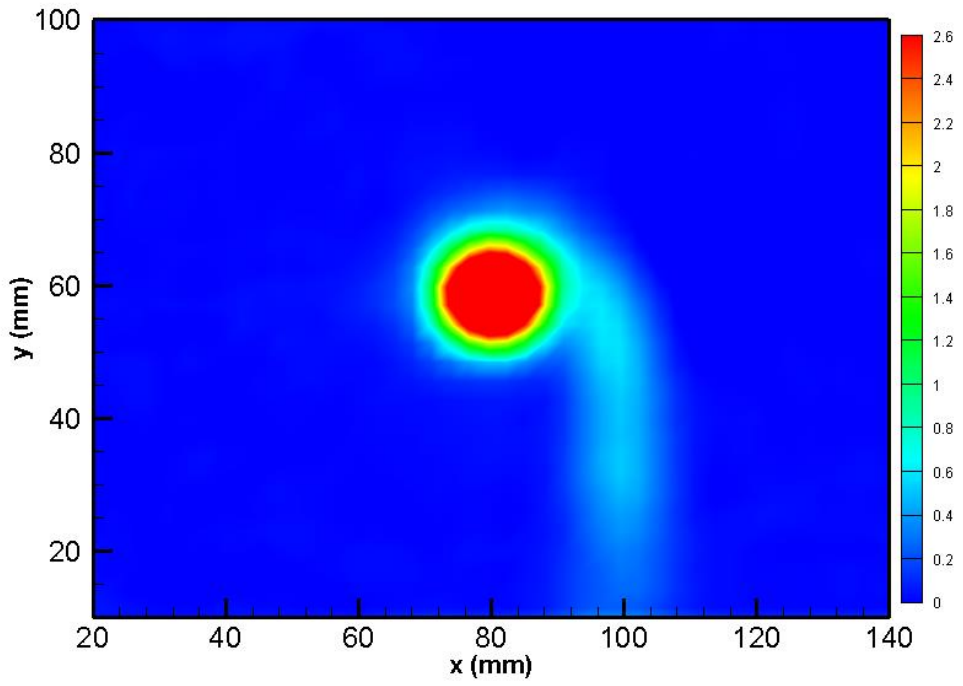


Figure C. 4 Base Wing Vorticity Contour at 15 m/s 12 AOA at 2C Location

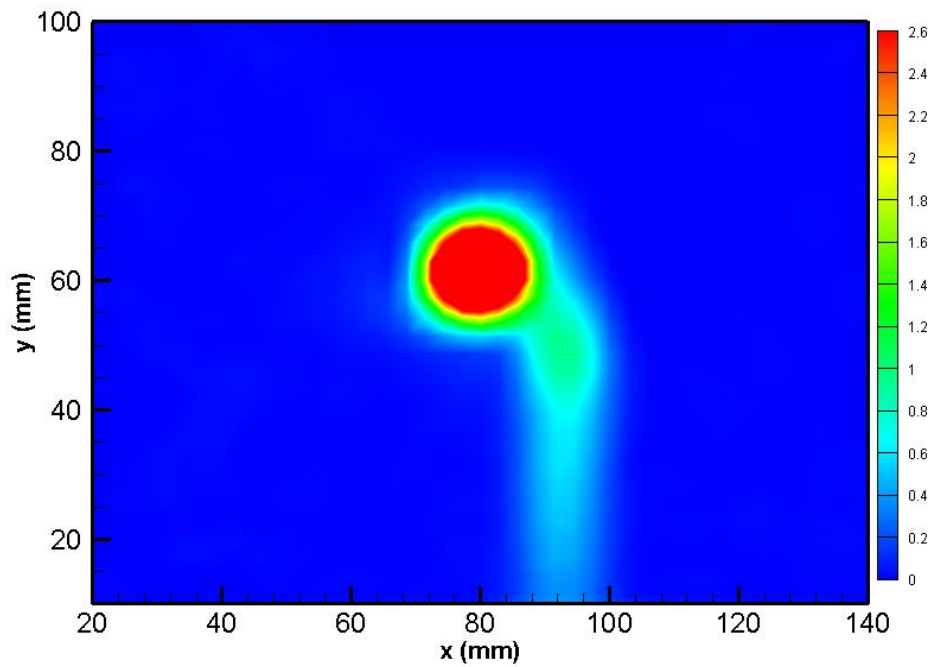


Figure C. 5 Base Wing Vorticity Contour at 15 m/s 13 AOA at C Location

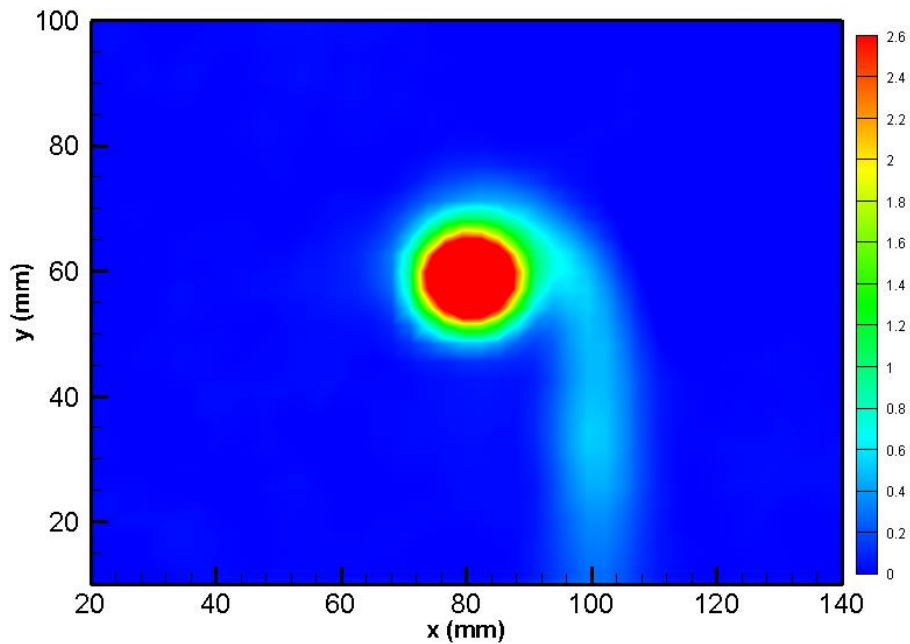


Figure C. 6 Base Wing Vorticity Contour at 15 m/s 13 AOA at 2C Location

### Optimized 14 Wing Vorticity Contours

Vorticity contours of the Optimized 14 Wing are presented in Figures C.7, C.8, C.9, C.10, C.11, C.12, C.13 and C.14.

The vorticity decreases gradually from the maximum to nearly zero in the outer part of the vortex. At 14 m/s, the wake of the wing increases as the angle of attack increases from 8 degrees to 9 degrees. Moreover, the vorticity also increases when the angle of attack increases at this velocity. Comparing with the load cell experimental results, there is also increase in lift so that increase in induced drag and resultant increase in the vorticity which is supported by PIV results. Another remark is that when the angle of attack increases from 8 to 9 at 14 m/s, the vorticity contours are getting closer, which means less vortex diffusion is present in the flow field.

Although both the velocity and angle of attack increase leads to an increase in vorticity, the angle of attack effect found to be more dominant by looking at the 14 m/s 8 AOA and 15 m/s 7 AOA graphs. Although the free stream velocity increases from 14 m/s to 15 m/s, since the angle of attack value is 1 degree less for 15 m/s case, the higher vorticity region is larger for 14 m/s free stream velocity.

The highest vorticity regions decreases as proceeding from one chord downstream to two chords downstream for all the cases. The vortex diffusion is found to be increasing with the increasing downstream location by looking at the contour distances for all cases.

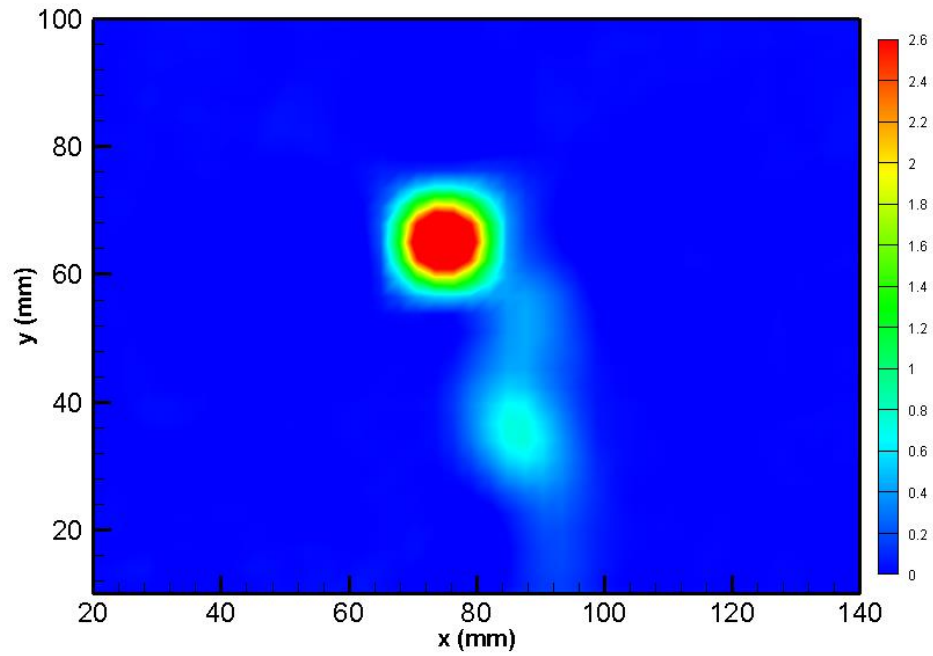


Figure C. 7 Optimized 14 Wing Vorticity Contour at 13 m/s 10 AOA C Location

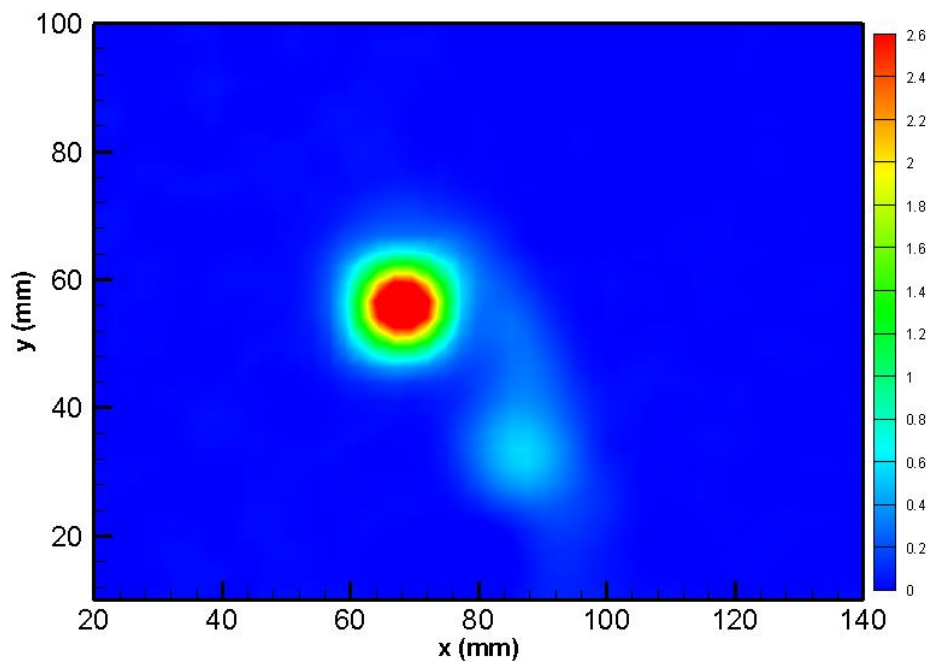


Figure C.8 Optimized 14 Wing Vorticity Contour at 13 m/s 10 AOA 2C Location

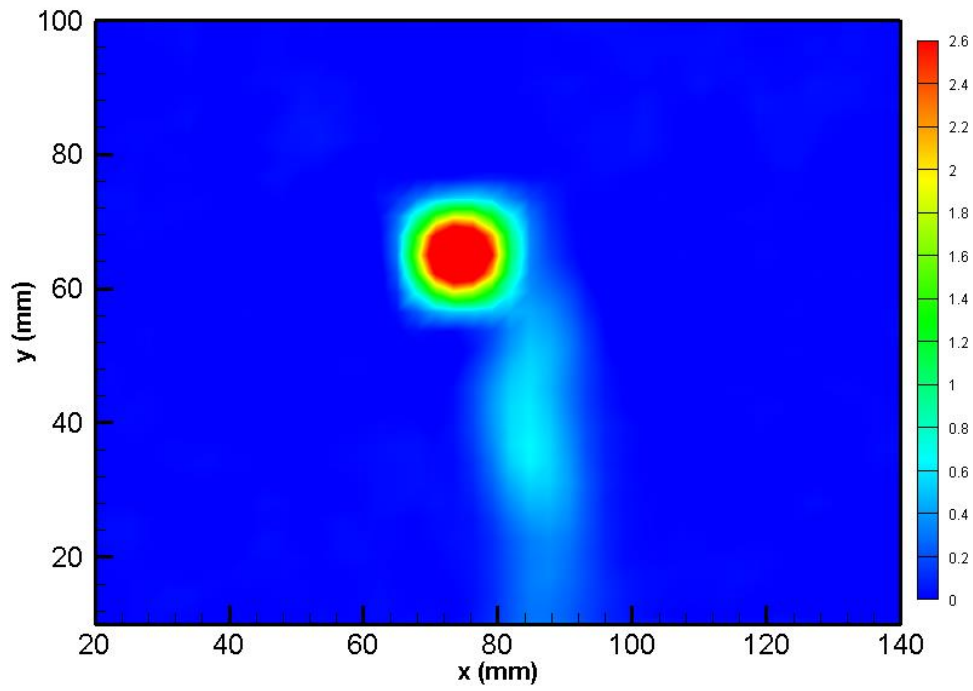


Figure C. 9 Optimized 14 Wing Vorticity Contour at 14 m/s 8 AOA C Location

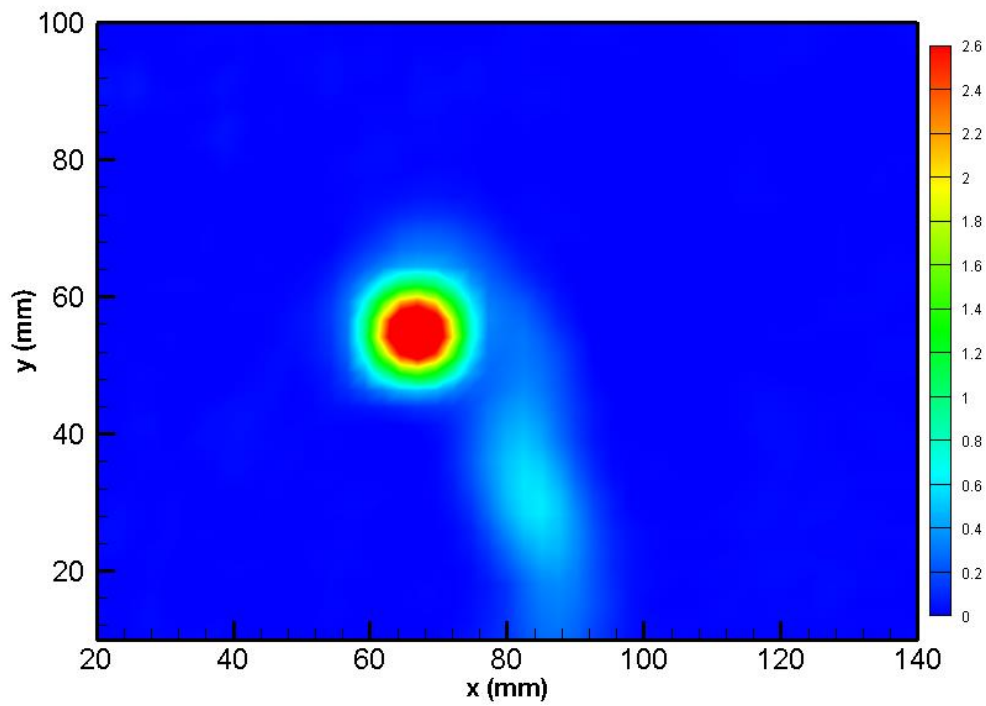


Figure C.10 Optimized 14 Wing Vorticity Contour at 14 m/s 8 AOA 2C Location

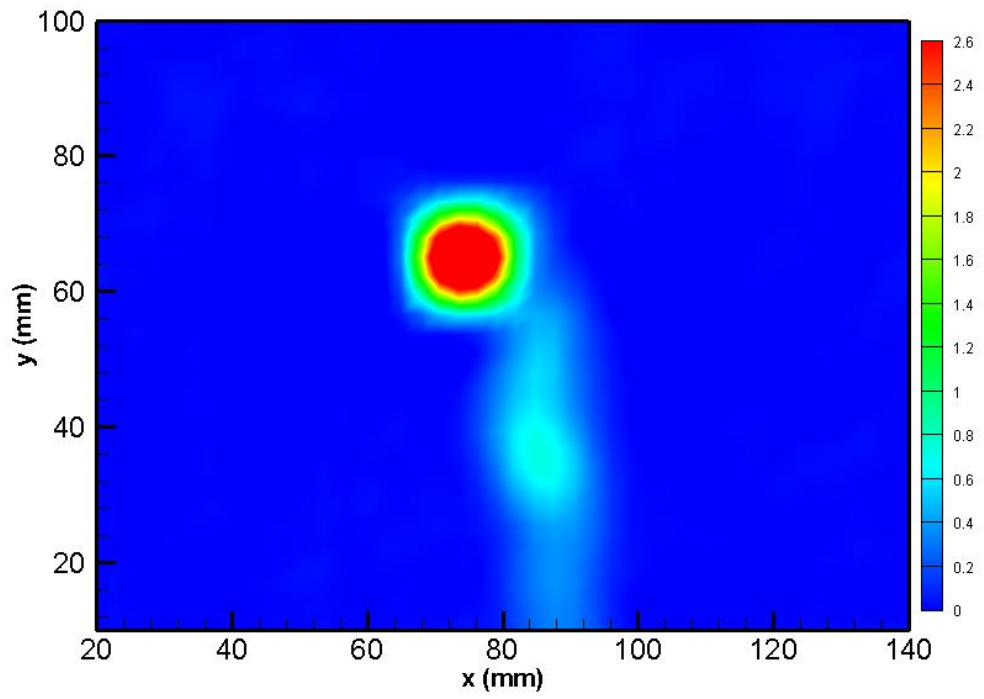


Figure C. 11 Optimized 14 Wing Vorticity Contour at 14 m/s 9 AOA C Location

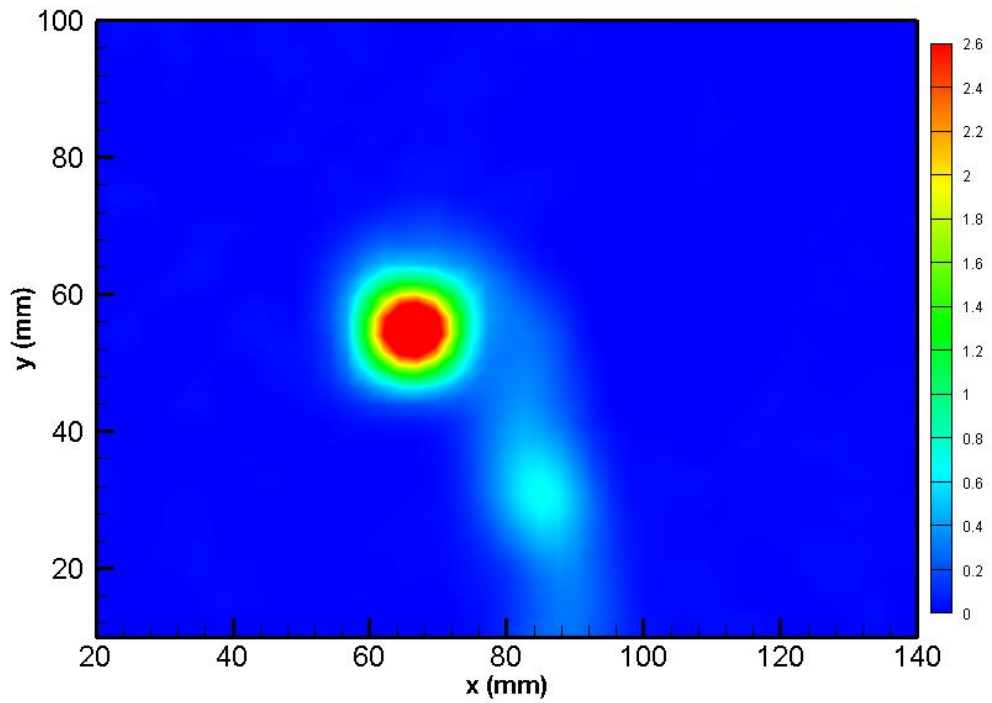


Figure C.12 Optimized 14 Wing Vorticity Contour at 14 m/s 9 AOA 2C Location

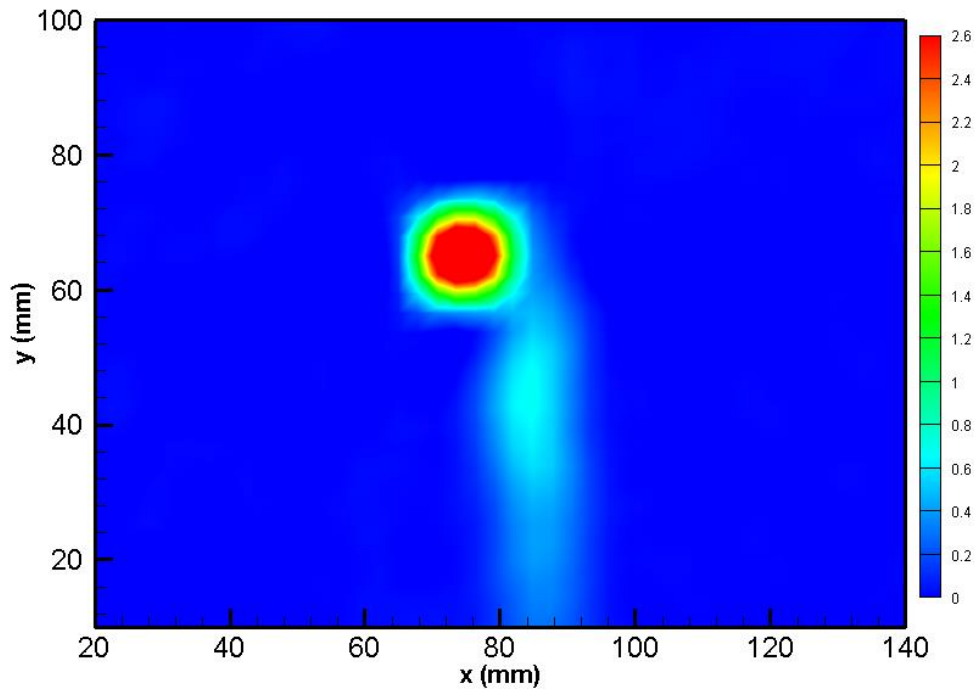


Figure C. 13 Optimized 14 Wing Vorticity Contour at 15 m/s 7 AOA C Location

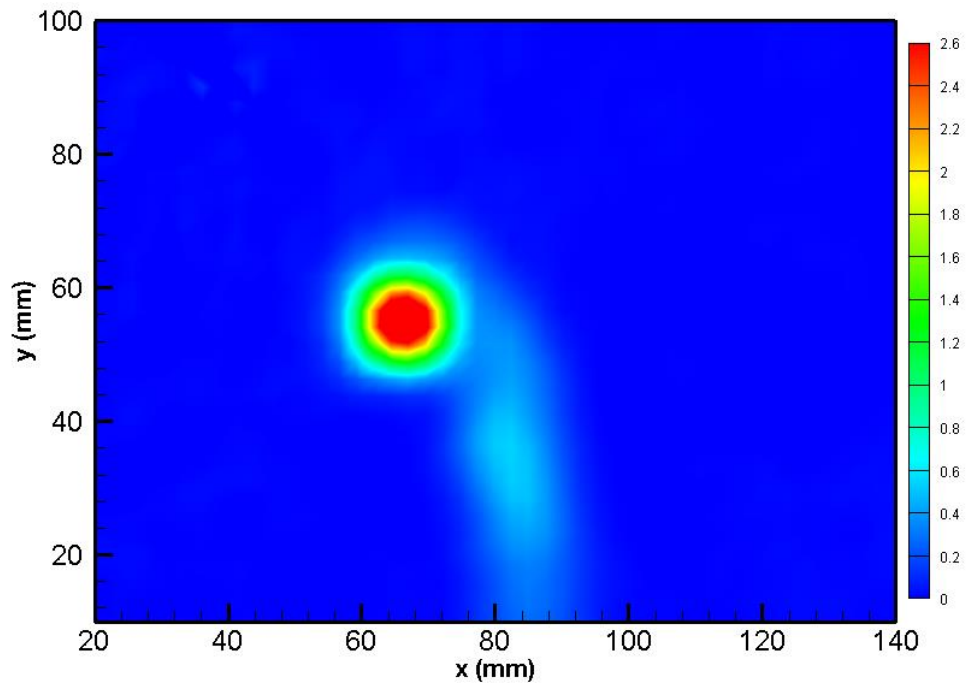


Figure C.14 Optimized 14 Vorticity Contour at Wing 15 m/s 7 AOA 2C Location



## **Morphed 10 Wing Vorticity Contours**

The vorticity contours of the Morphed 10 Wing are presented in Figures C.15, C.16, C.17, C.18, C.19, C.20, C.21, C.22, C.23, C.24, C.25, C.26, C.27, C.28, C.29 and C.30. More data is available for the Morphed 10 Wing compared to other wings because it has the highest Reynolds number and it can produce 2.5 N lift in many conditions.

The wake of the wing at C locations are higher than the wake at 2C locations. Furthermore, the vorticity contours are moving far away at 2C location compared to C location in all cases. This is an indication of vortex diffusion.

The vorticity increases as the angle of attack increases and this can be clearly seen in 13 m/s 5 AOA and 13 m/s 6 AOA conditions, caused by increase in lift and corresponding increase in drag in load cell results at these angles. Moreover, the wake of the wing increases as the angle of attack increases.

For the Morphed 10 Wing, the data for 13 m/s 5 AOA and 14 m/s 5 AOA is available so that the free stream velocity effect on vorticity can be deduced more precisely. According to the vorticity contours of this conditions, it is seen that the vorticity increases with the free stream velocity as suggested also by the load cell experimental results at these velocities.

Another conclusion can be drawn for the priority of angle of attack and free stream velocity effect at 14 m/s 5 AOA and 15 m/s 4 AOA conditions. Although velocity increases from 14 to 15 the angle of attack decreases for 5 to 4. It is clearly seen that the higher vorticity region in the 15 m/s 4 AOA case is lower than the 14 m/s 5 AOA case. This proves that the angle of attack effect on the vorticity magnitudes is bigger than the free stream velocity effect. This is also supported by the load cell experimental results that the lift and so the drag values of the 14 m/s 5 AOA case is higher than in the 15 m/s 4 AOA case.

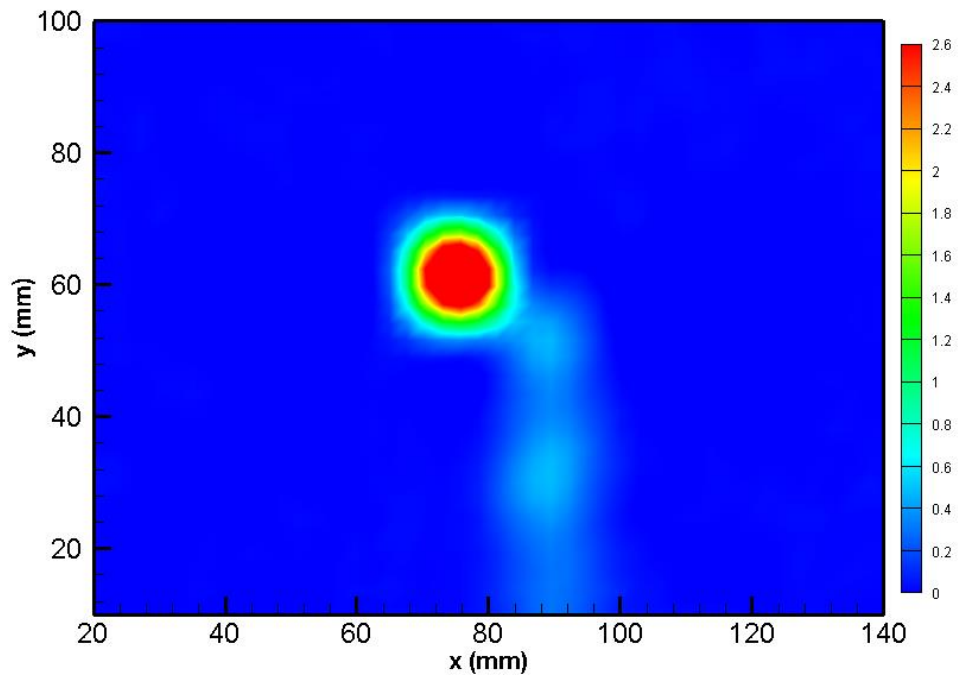


Figure C.15 Morphed 10 Wing Vorticity Contour at 12 m/s 7 AOA C Location

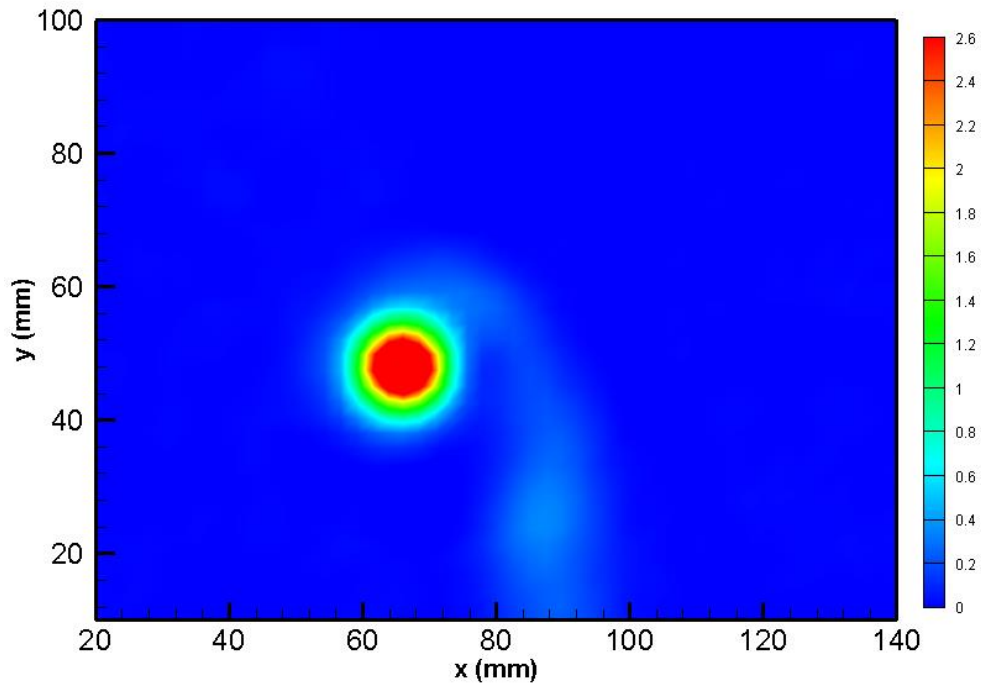


Figure C.16 Morphed 10 Wing Vorticity Contour at 12 m/s 7 AOA 2C Location

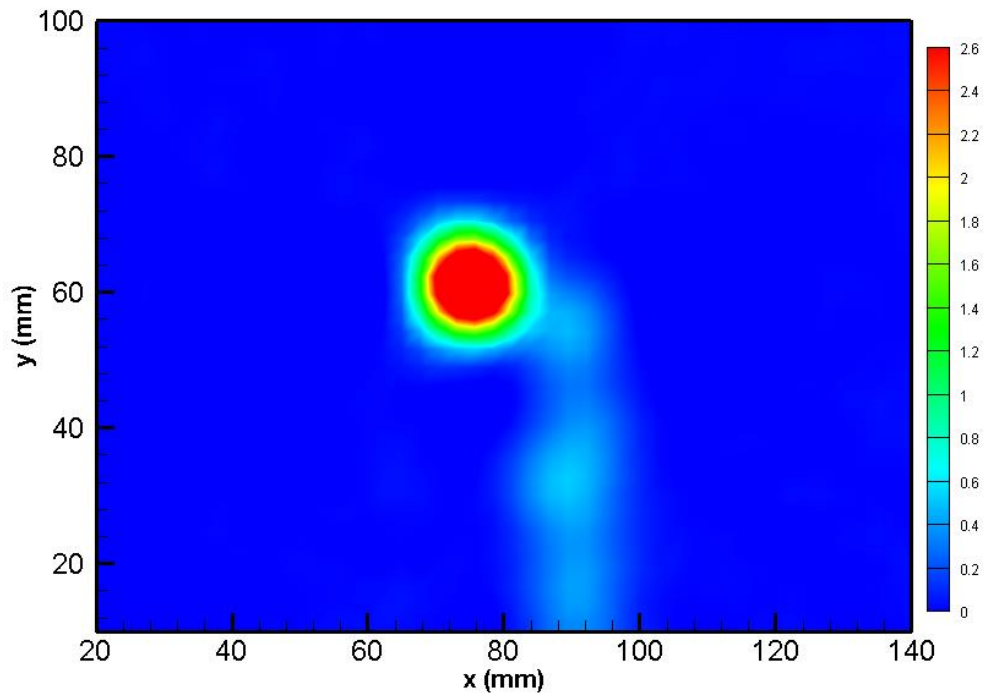


Figure C.17 Morphed 10 Wing Vorticity Contour at 12 m/s 8 AOA C Location

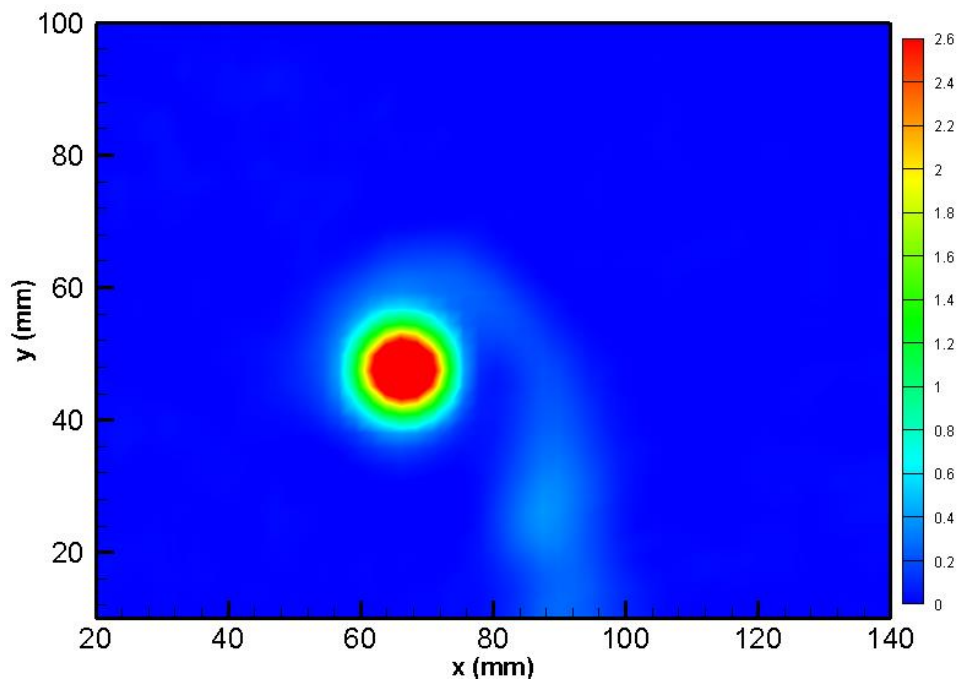


Figure C.18 Morphed 10 Wing Vorticity Contour at 12 m/s 8 AOA 2C Location

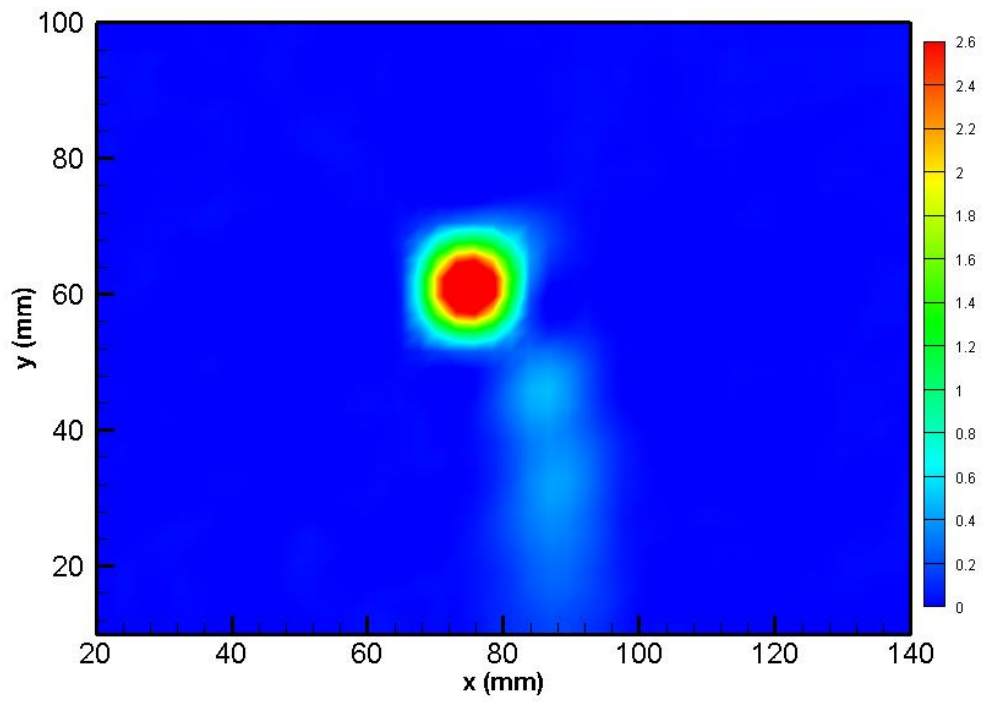


Figure C.19 Morphed 10 Wing Vorticity Contour at 13 m/s 5 AOA C Location

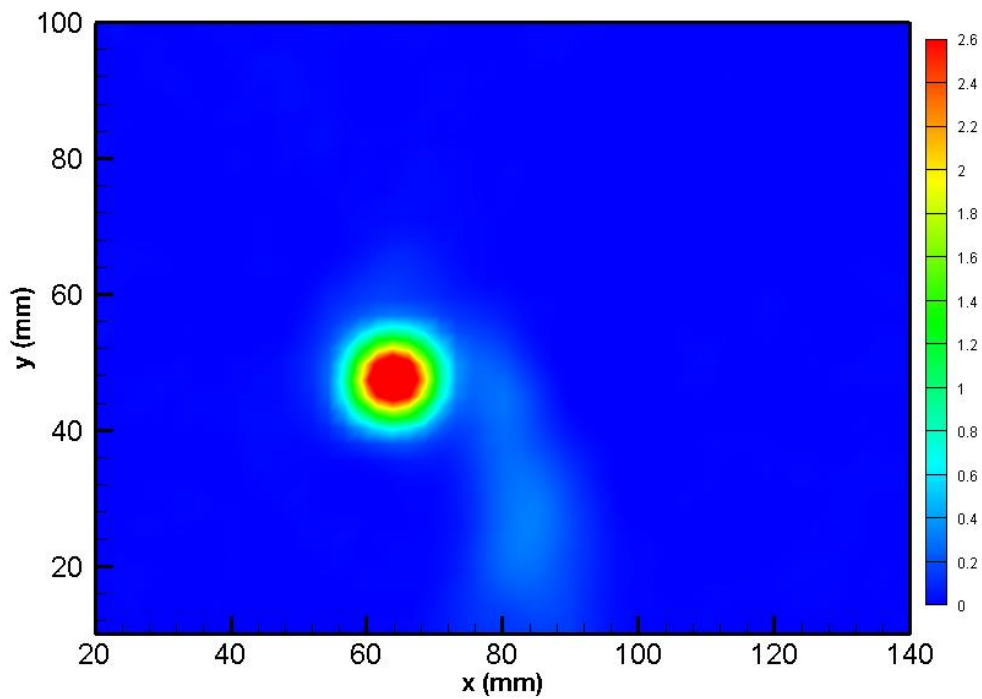


Figure C.20 Morphed 10 Wing Vorticity Contour at 13 m/s 5 AOA 2C Location

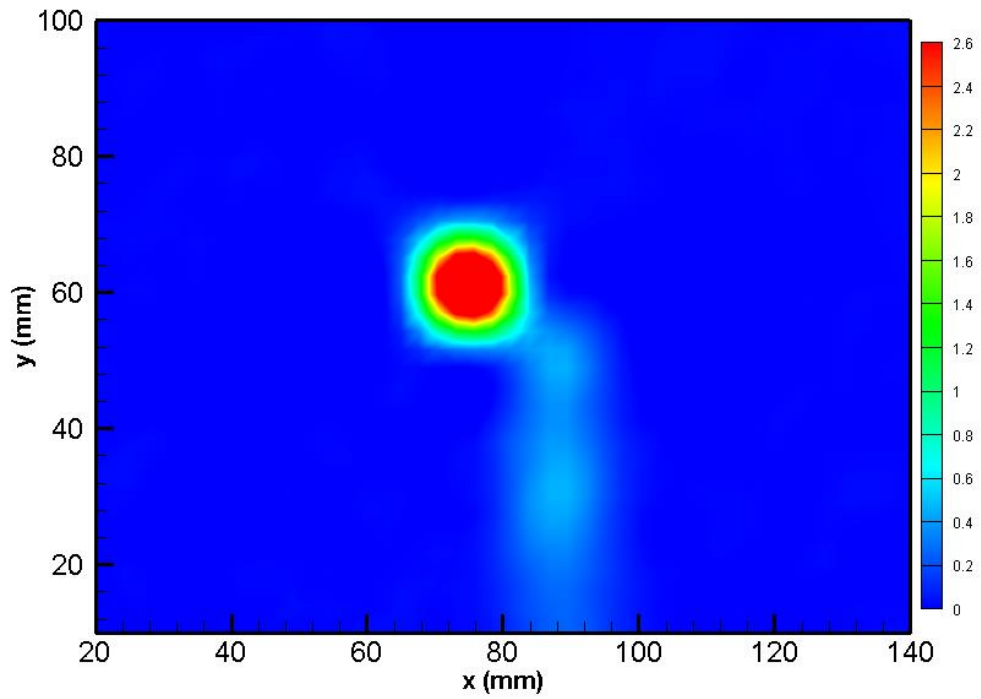


Figure C.21 Morphed 10 Wing Vorticity Contour at 13 m/s 6 AOA C Location

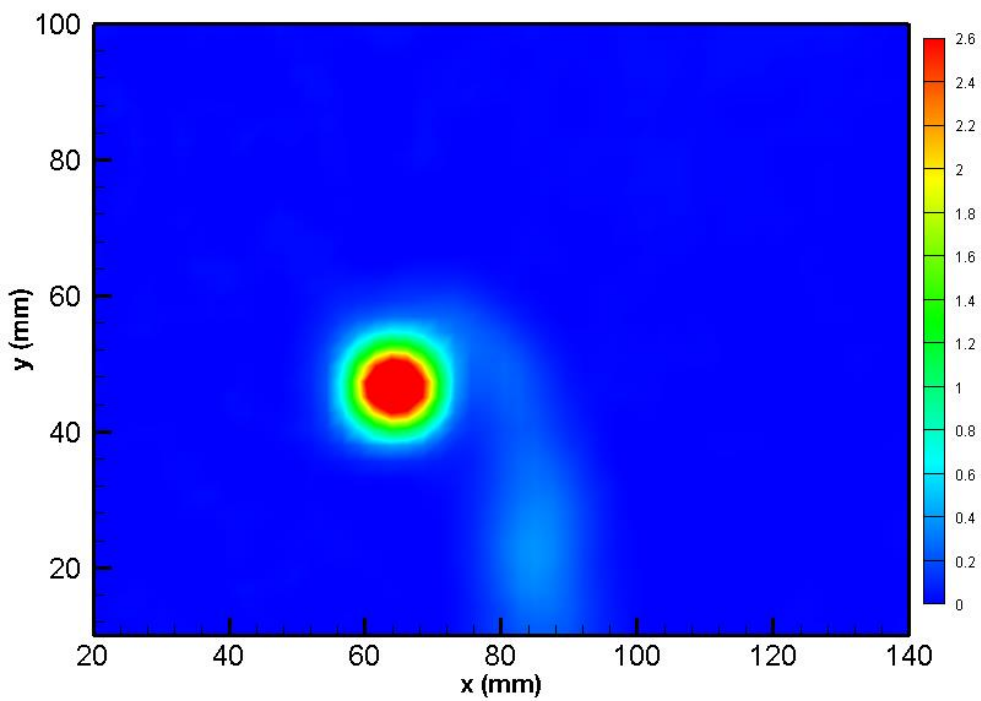


Figure C.22 Morphed 10 Wing 13 m/s 6 AOA 2C Location

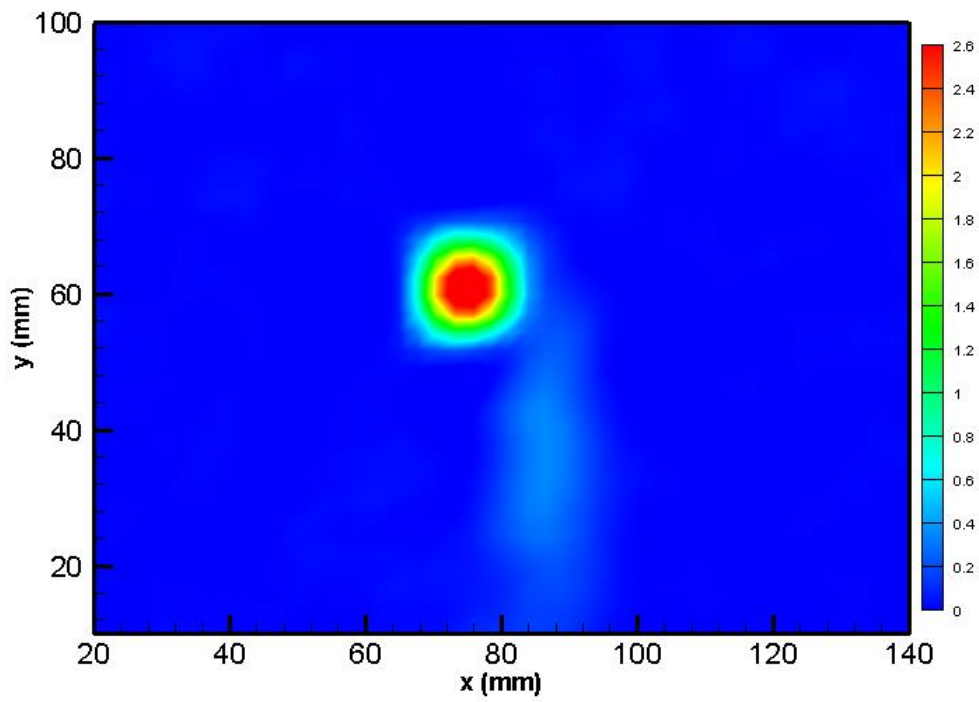


Figure C.23 Morphed 10 Wing Vorticity Contour at 14 m/s 4 AOA C Location

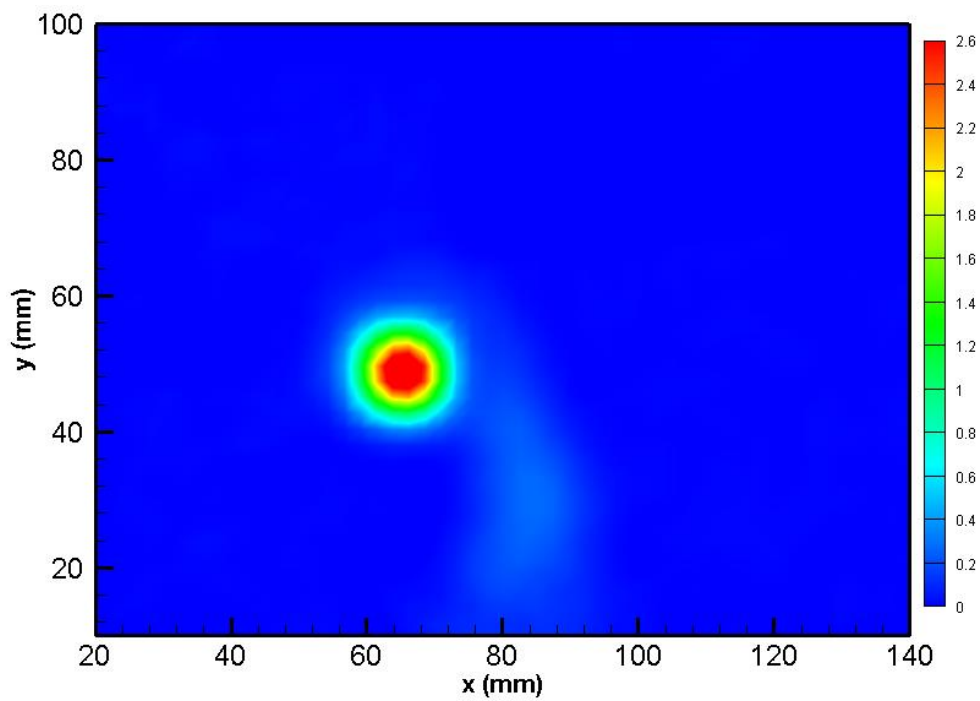


Figure C.24 Morphed 10 Wing Vorticity Contour at 14 m/s 4 AOA 2C Location

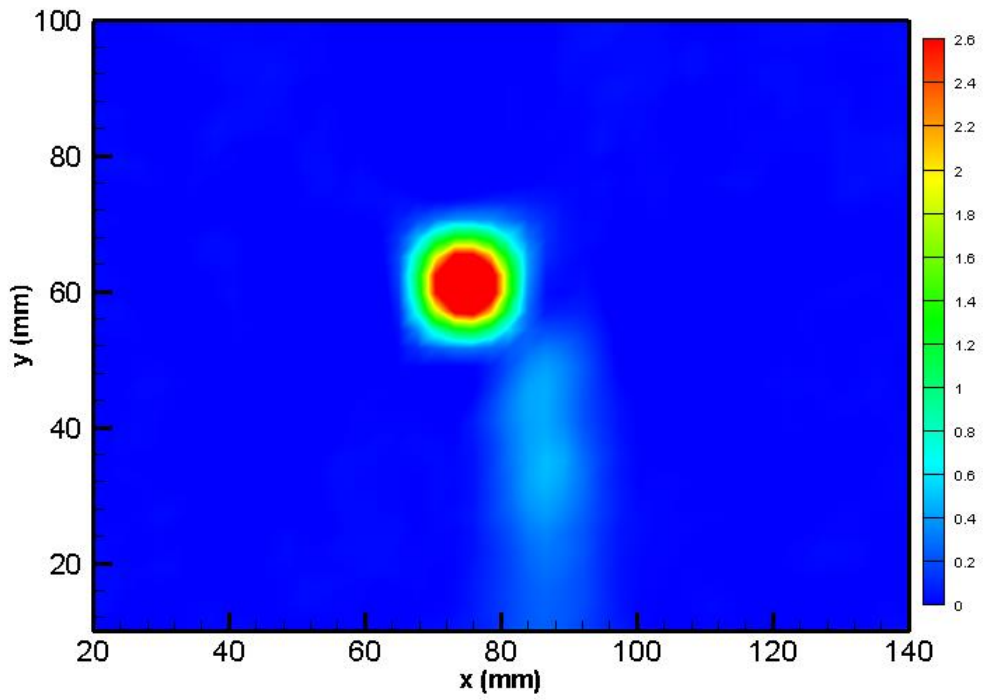


Figure C.25 Morphed 10 Wing Vorticity Contour at 14 m/s 5 AOA C Location

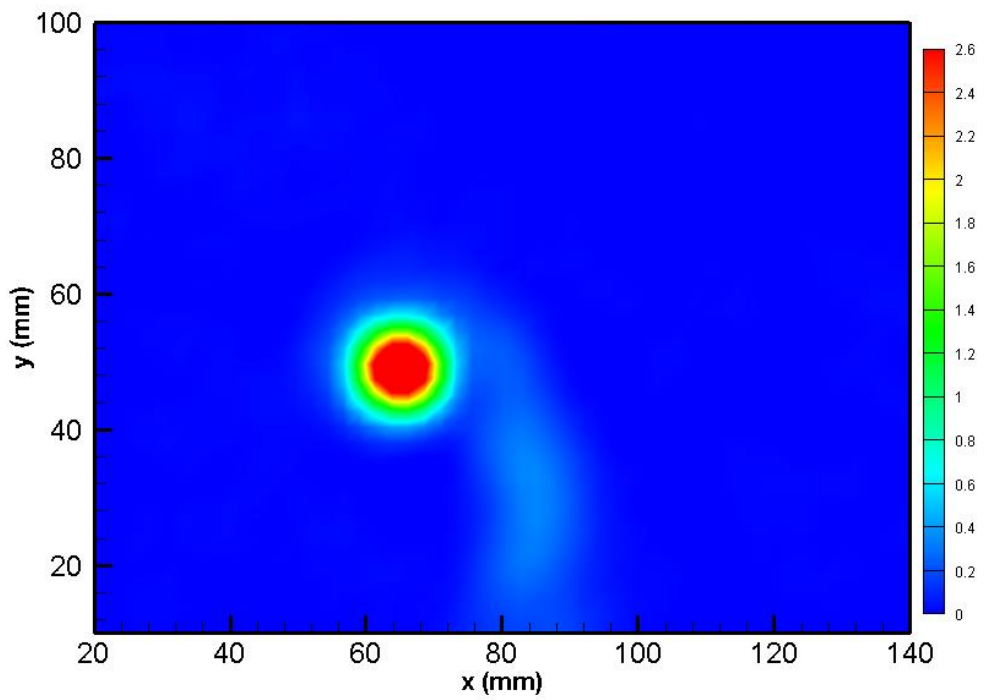


Figure C.26 Morphed 10 Wing Vorticity Contour at 14 m/s 5 AOA 2C Location

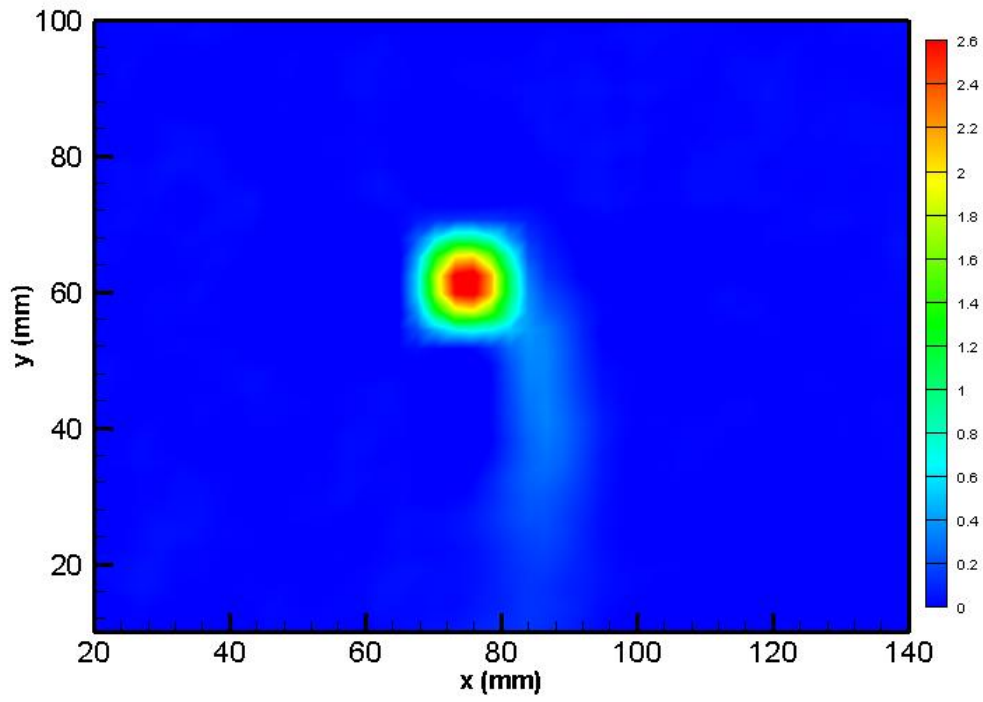


Figure C.27 Morphed 10 Wing Vorticity Contour at 15 m/s 3 AOA C Location

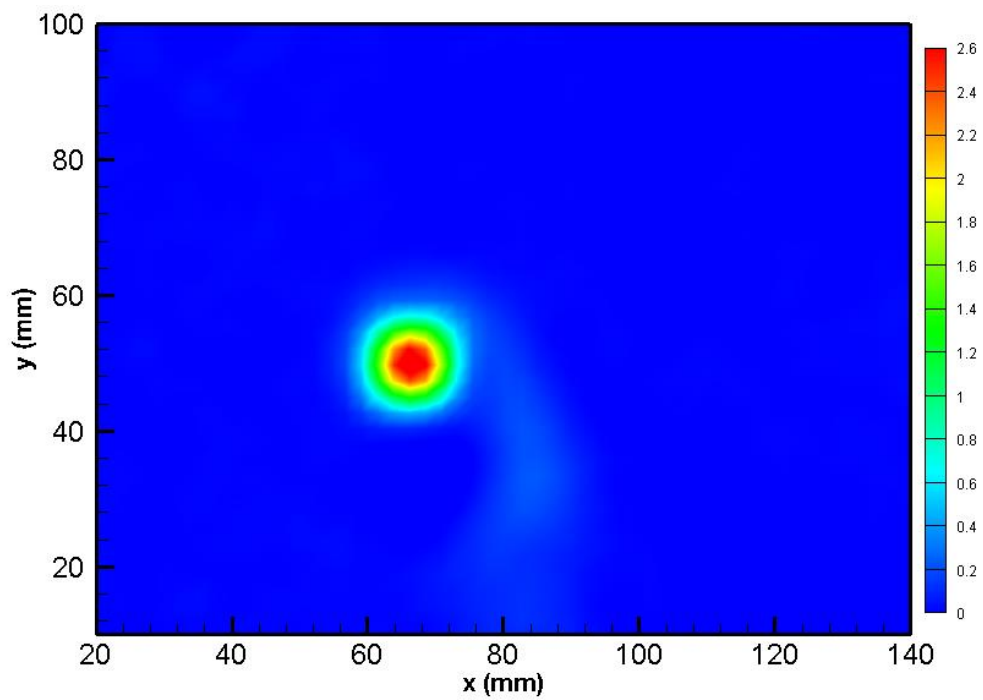


Figure C.28 Morphed 10 Wing Vorticity Contour at at 15 m/s 3 AOA 2C Location



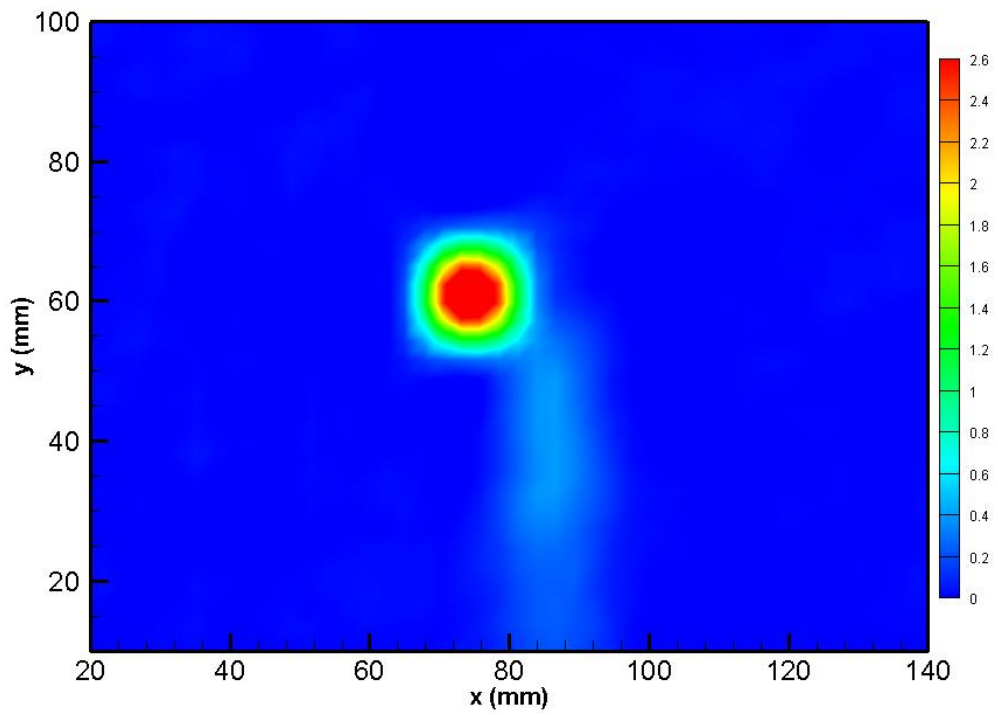


Figure C.29 Morphed 10 Wing Vorticity Contour at 15 m/s 4 AOA C Location

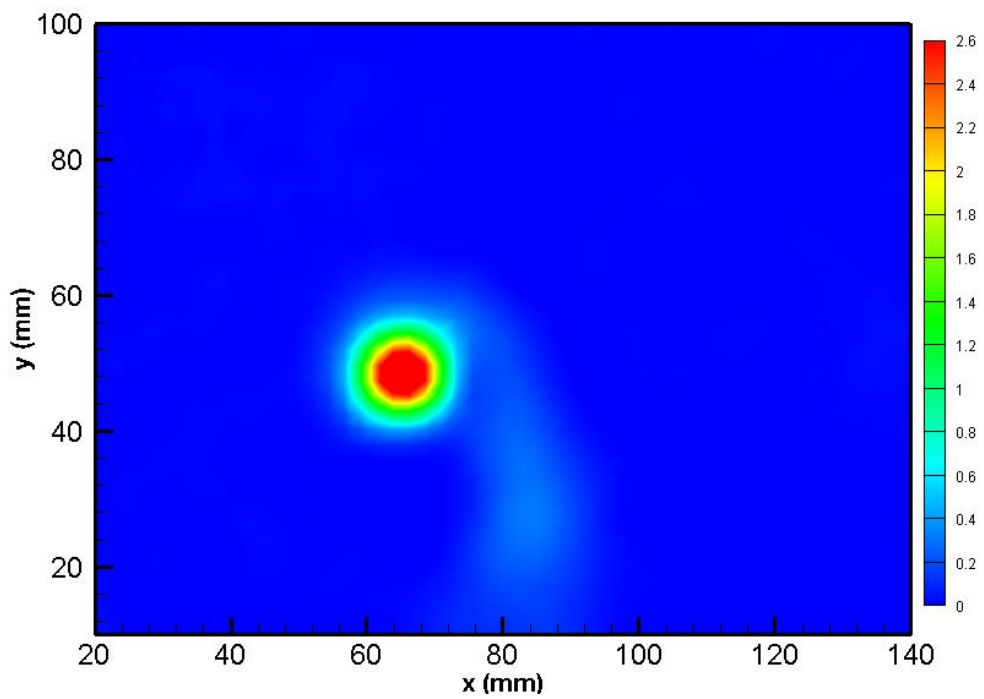


Figure C.30 Morphed 10 Wing Vorticity Contour at 15 m/s 4 AOA 2C Location

### Morphed 16.5 Wing Vorticity Contours

The vorticity contours of the Morphed 16.5 Wing are presented in Figures C.31, C.32, C.33, C.34, C.35, and C.36.

It is seen that when the angle of attack increases from 9 to 10 degrees angle of attack at 15 m/s, the vorticity also increases. This behaviour is also supported by the load cell experiments by the increase in lift so the drag values. At C locations the vorticity is higher than the ones at 2C location for all cases. Moreover, the wake of the wing decreases as the distance from the wing tip increases from C to 2C. It should be also noted that when the angle of attack increases, the wake of the wing becomes larger and this can be seen clearly in the vorticity contours of 15 m/s 9 degree and 15 m/s 10 degree at C Location.

Furthermore, the vorticity contours are moving far away from each other at 2C location compared to C location in all cases. This is an indication of vortex diffusion.

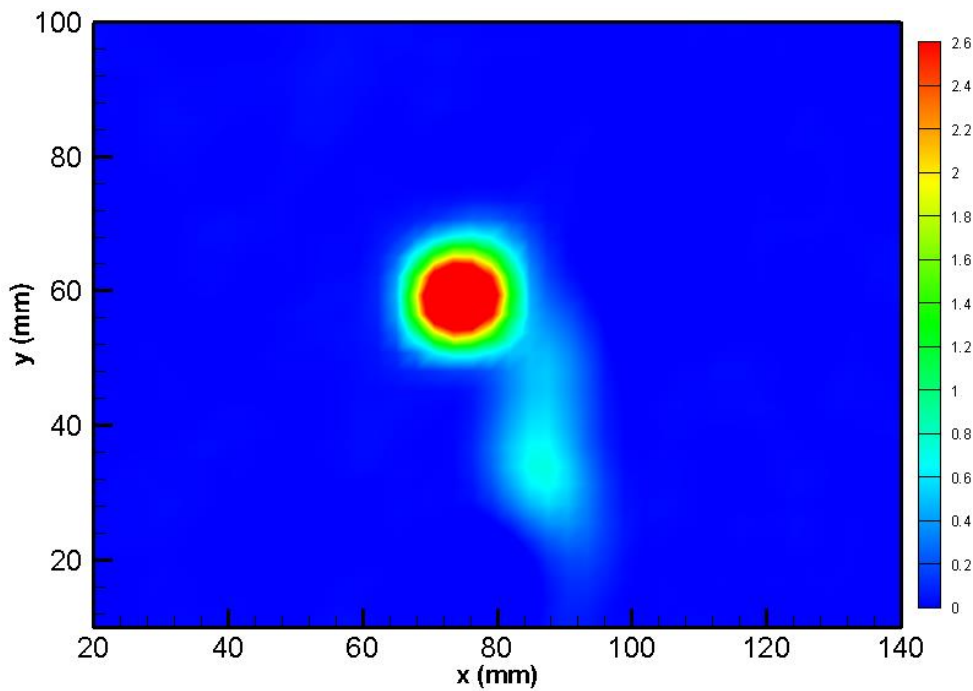


Figure C.31 Morphed 16.5 Wing Vorticity Contour at 14 m/s 11 AOA C Location

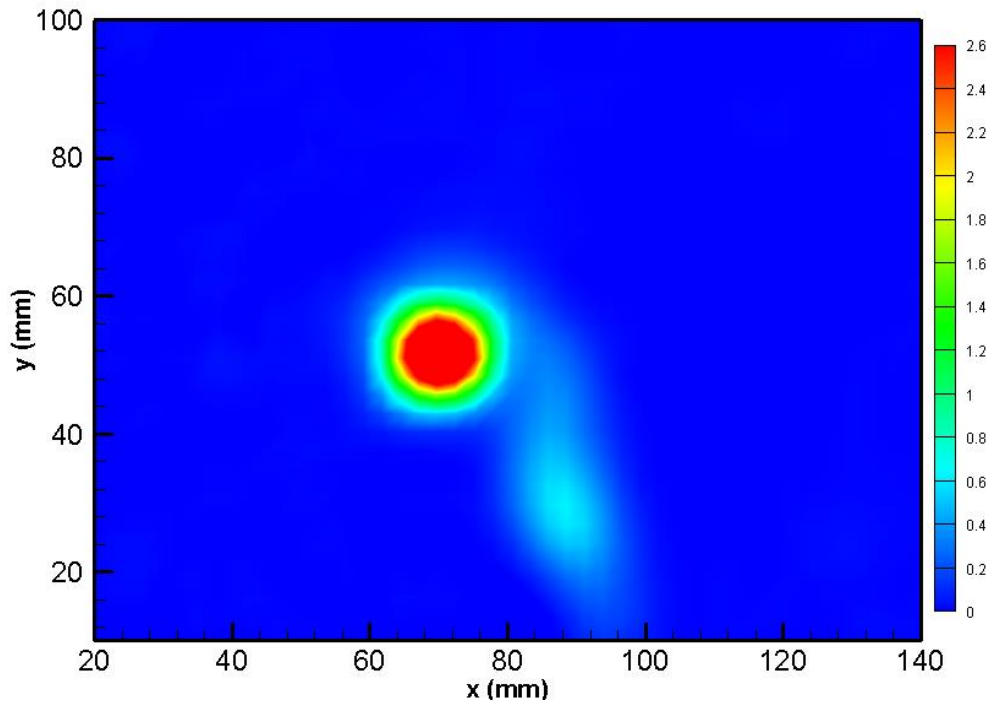


Figure C.32 Morphed 16.5 Wing 14 m/s Vorticity Contour at 11 AOA 2C Location

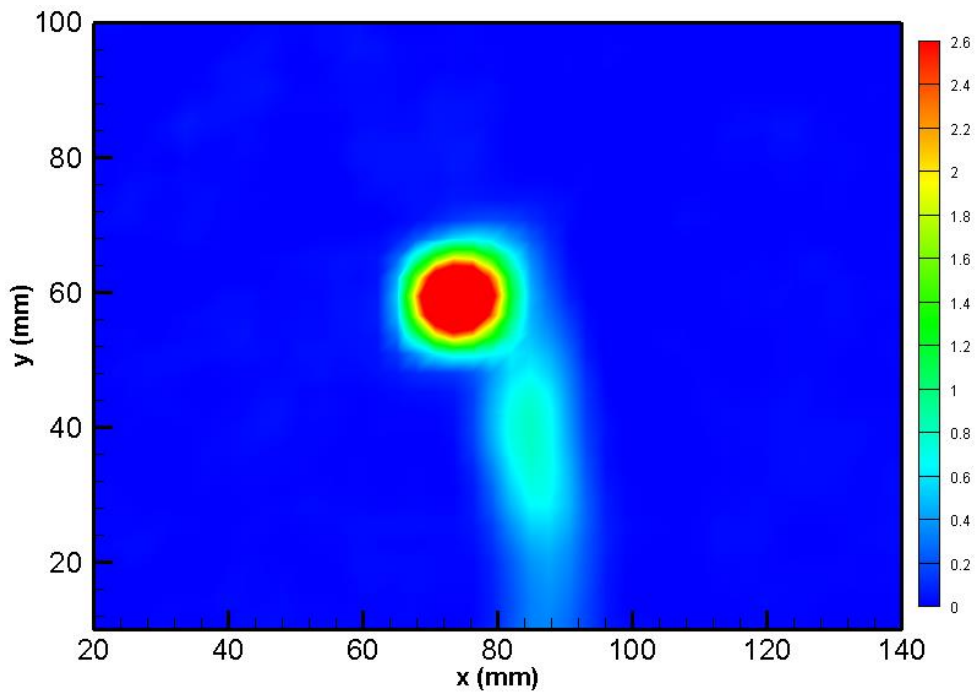


Figure C.33 Morphed 16.5 Wing Vorticity Contour at 15 m/s 9 AOA C Location

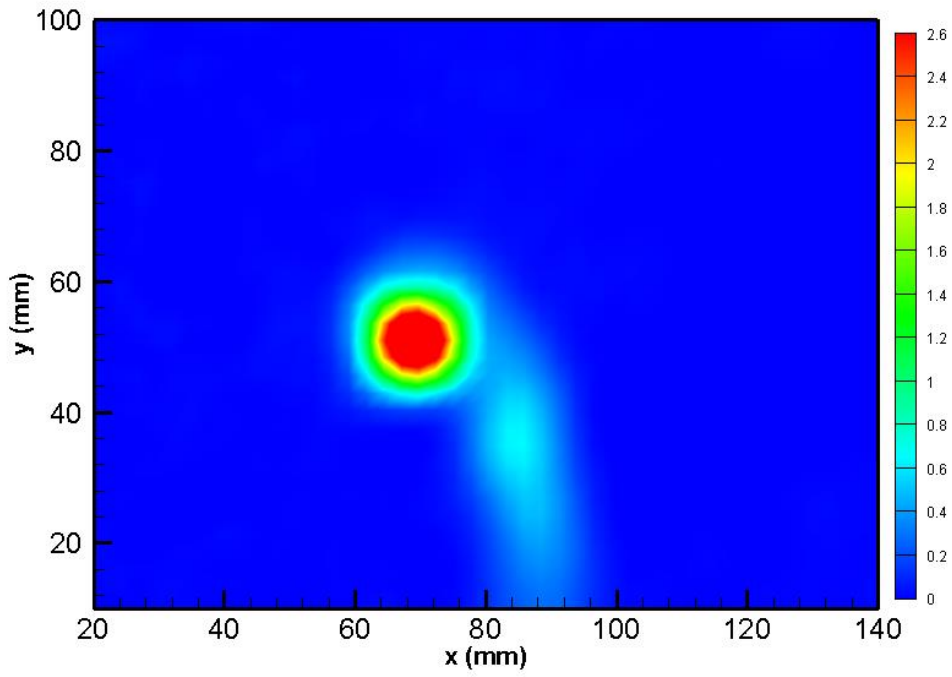


Figure C.34 Morphed 16.5 Wing Vorticity Contour at 15 m/s 9 AOA 2C Location

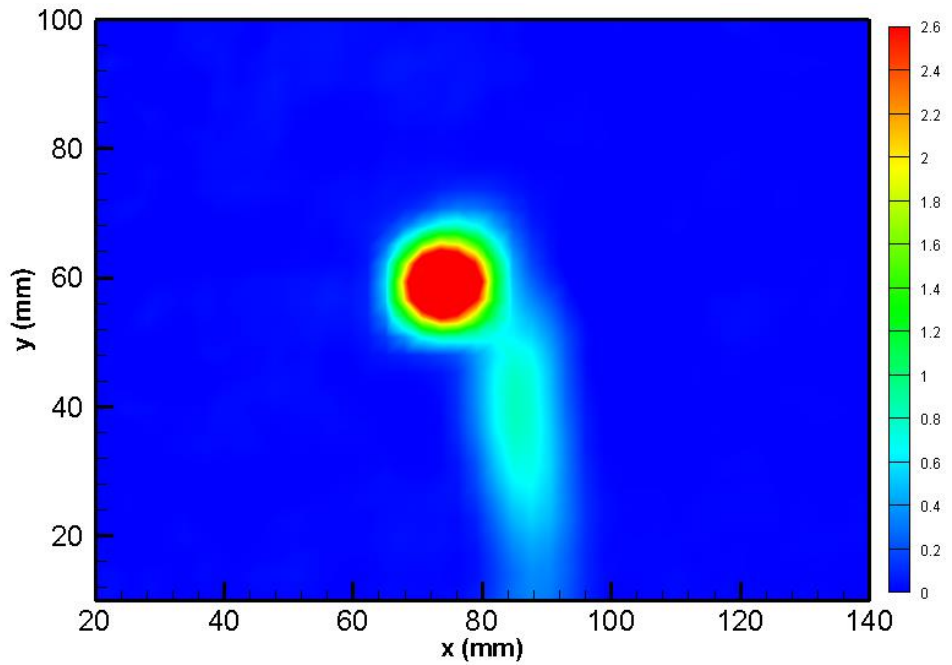


Figure C.35 Morphed 16.5 Wing Vorticity Contour at 15 m/s 10 AOA C Location

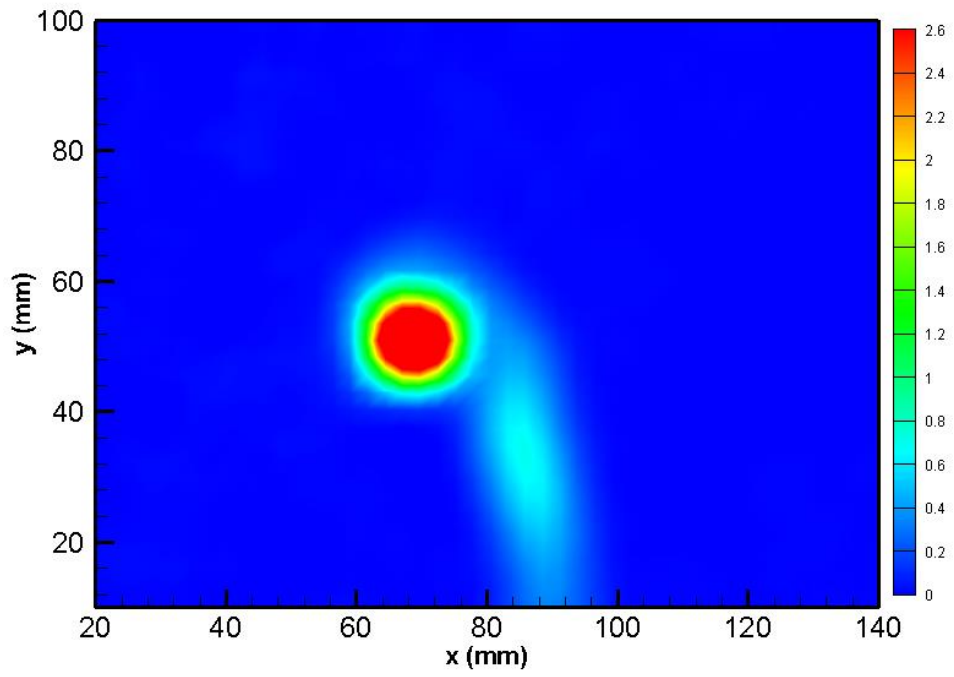


Figure C.36 Morphed 16.5 Wing 15 m/s Vorticity Contour at 10 AOA 2C Location



## APPENDIX D

### TURBULENCE KINETIC ENERGY CONTOURS

#### Base Wing

The base wing Turbulence Kinetic Energy Contours are presented in Figures D.1, D.2, D.3, D.4, D.5 and D.6.

The kinetic energy distribution of the wing wake reduces from one chord to two chord location due to moving away from the wing. It is seen that the turbulent kinetic energies are higher at C locations compared to 2C locations for 14 m/s 15 AOA and 15 m/s 13 AOA cases. These are the only conditions that turbulence kinetic energy decreases with distance among all the wings and conditions. Considering the load cell measurement results, this behaviour may be caused since the flow separates at these two conditions, the wake region at the downstream becomes small although separation bubble forms in the upper surface [45]

For 15 m/s 12 AOA case, increasing downstream location creates an increase in the high values of the contours as expected. Since it is observed in a previous study that turbulence kinetic energy increases with increasing streamwise distance [60]. Thus, closer to the wing tip trailing edge, the fluctuations, so the turbulence kinetic energies are lower.

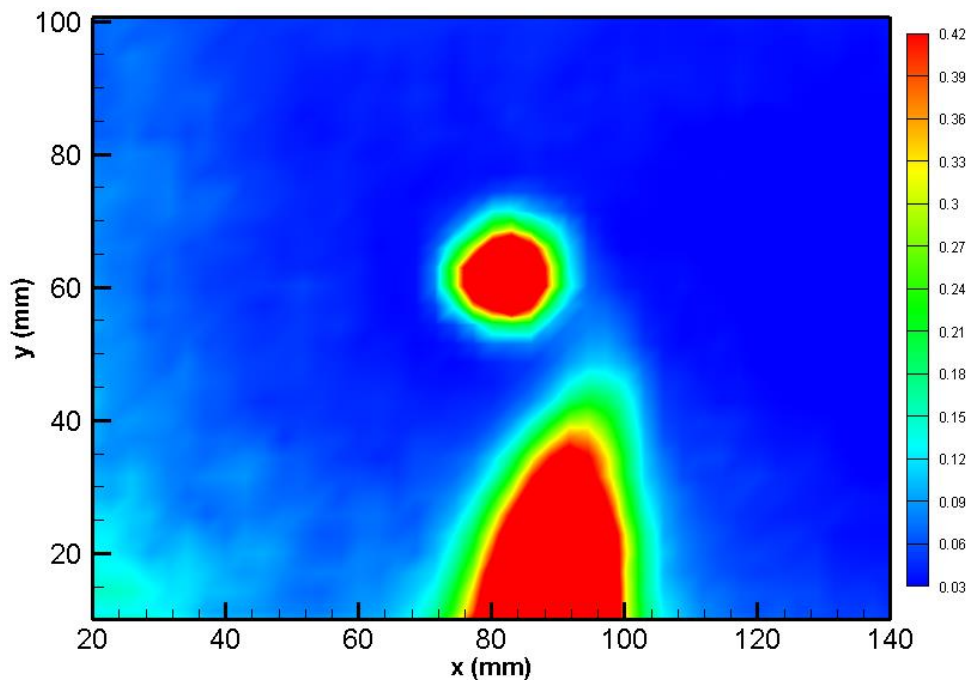


Figure D.1 Turbulence Kinetic Energy Contour of Base Wing 14 m/s 15 AOA at C Location

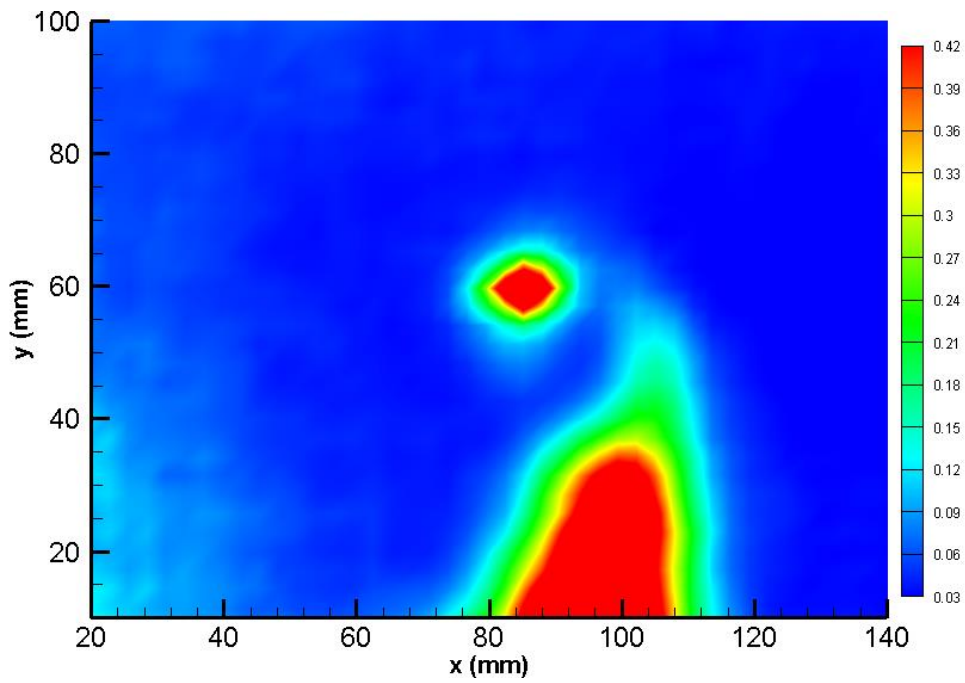


Figure D.2 Turbulence Kinetic Energy Contour of Base Wing 14 m/s 15 AOA at 2C Location



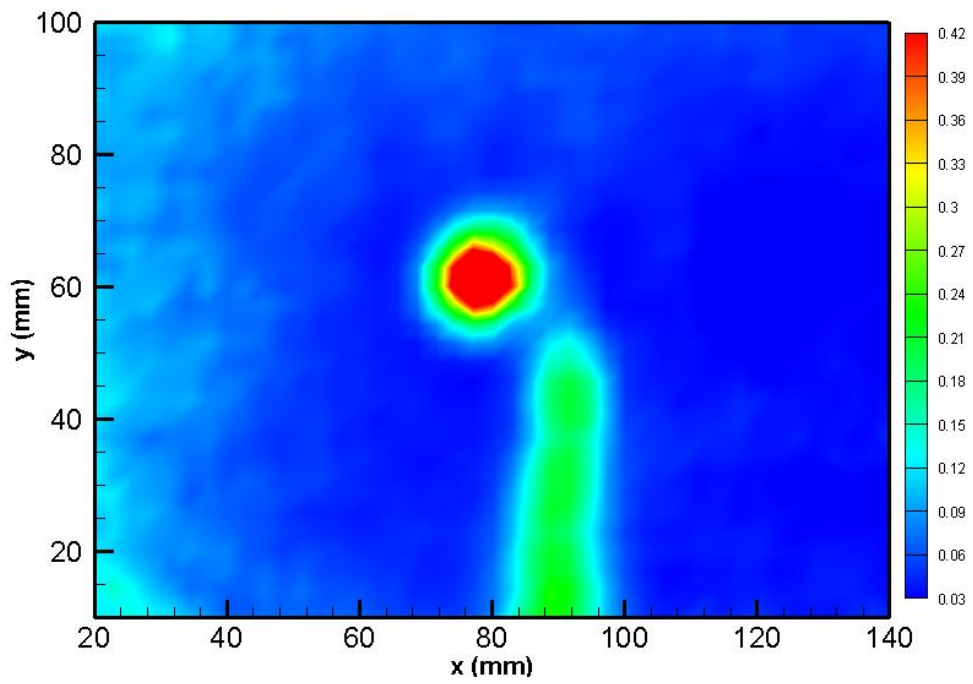


Figure D.3 Turbulence Kinetic Energy Contour of Base Wing 15 m/s 12 AOA at C Location

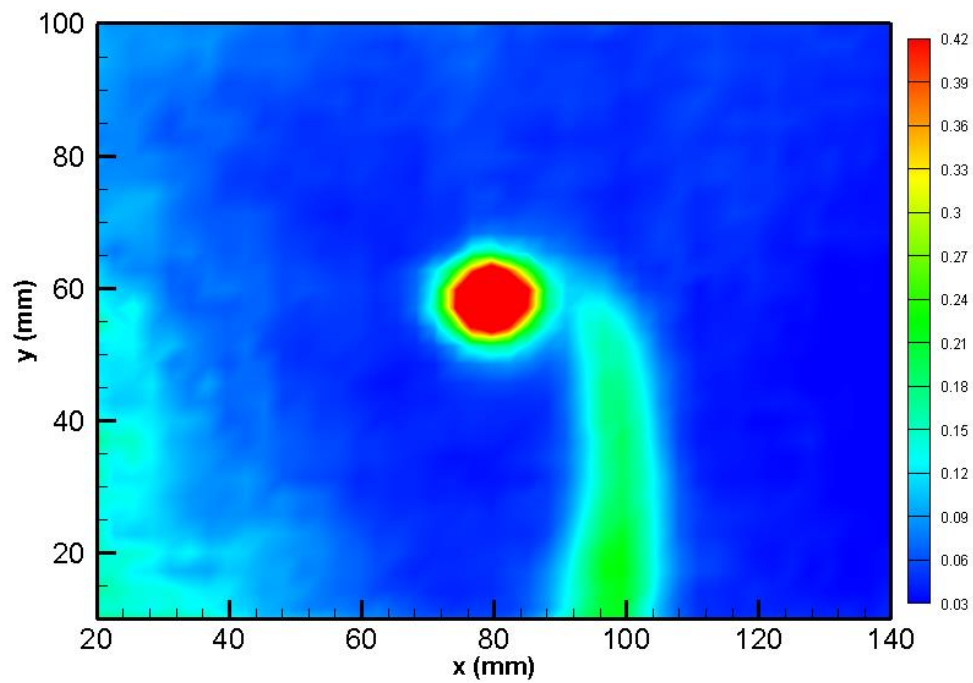


Figure D.4 Turbulence Kinetic Energy Contour of Base Wing 15 m/s 12 AOA at 2C Location

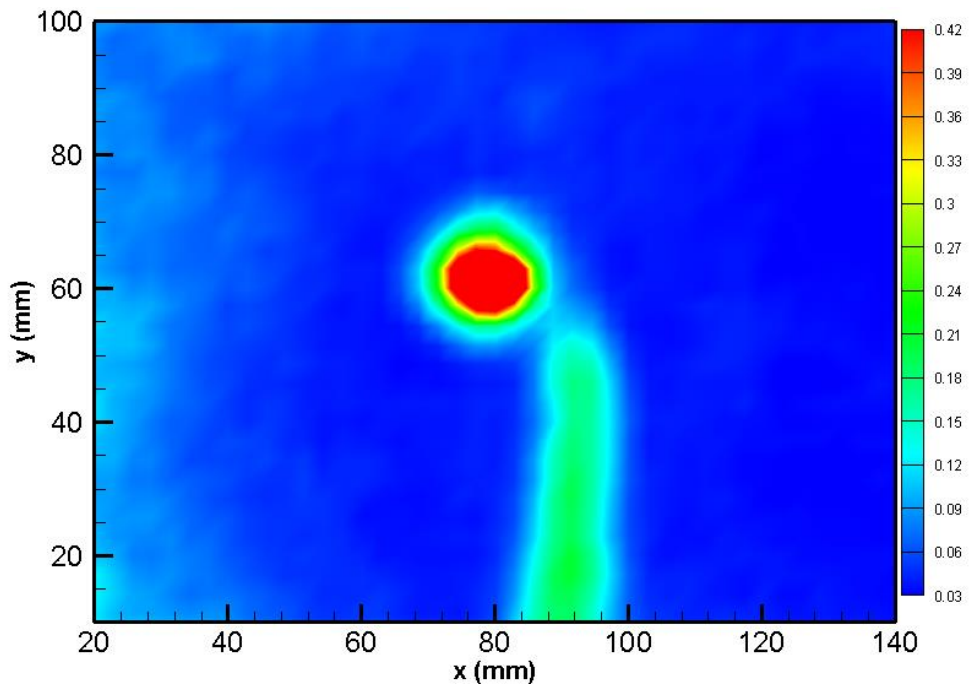


Figure D.5 Turbulence Kinetic Energy Contour of Base Wing 15 m/s 13 AOA at C Location

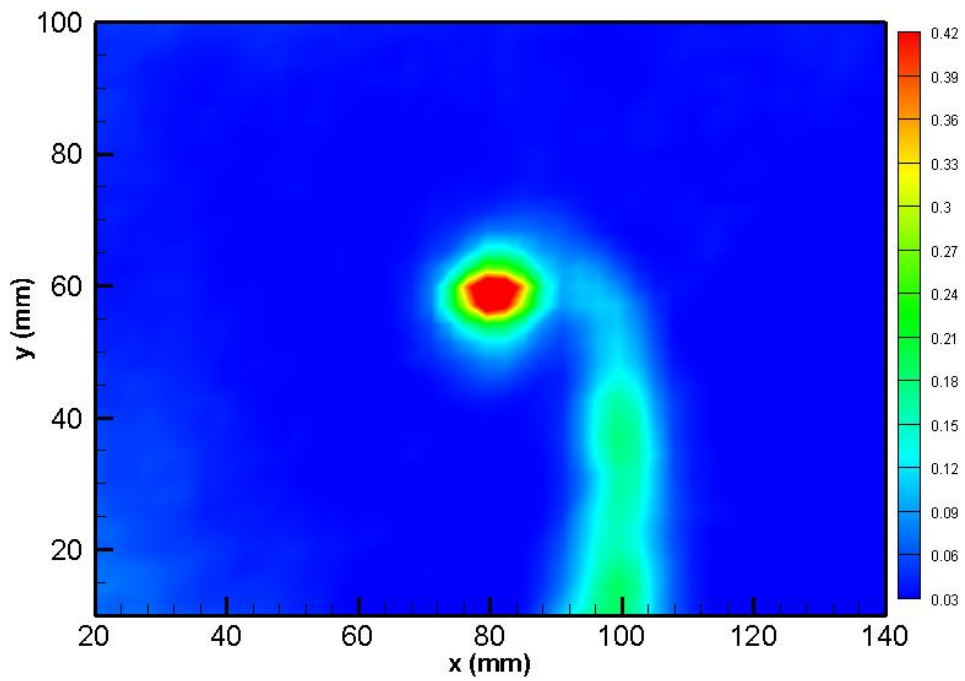


Figure D.6 Turbulence Kinetic Energy Contour of Base Wing 15 m/s 13 AOA at 2C Location

### Optimized 14 Wing

The Turbulence Kinetic Energy Contours of the Optimized 14 Wing are shown in Figures D.7, D.8, D.9, D.10, D.11, D.12, D.13 and D.14.

The behaviour observed in Base Wing for 15 m/s 12 AOA is also valid for the Optimized 14 Wing. While the wing wake dominates the fluctuation in velocity at C Location, as moving downstream, the effect of wake diminishes and the turbulence kinetic energy of the vortex increases significantly. It is seen that closer to the wing trailing edge the fluctuations in the flow increases not only in wing wake region but also in the neighbour regions.

It is seen that at C Location, as the angle of attack increases, the turbulence kinetic energy of the vortex decreases whereas at 2C Location, the turbulence kinetic energy increases with increasing angle of attack. In the 2C Location of 15 m/s 7 AOA data there is a noise in the image which may arise from instantaneous images.

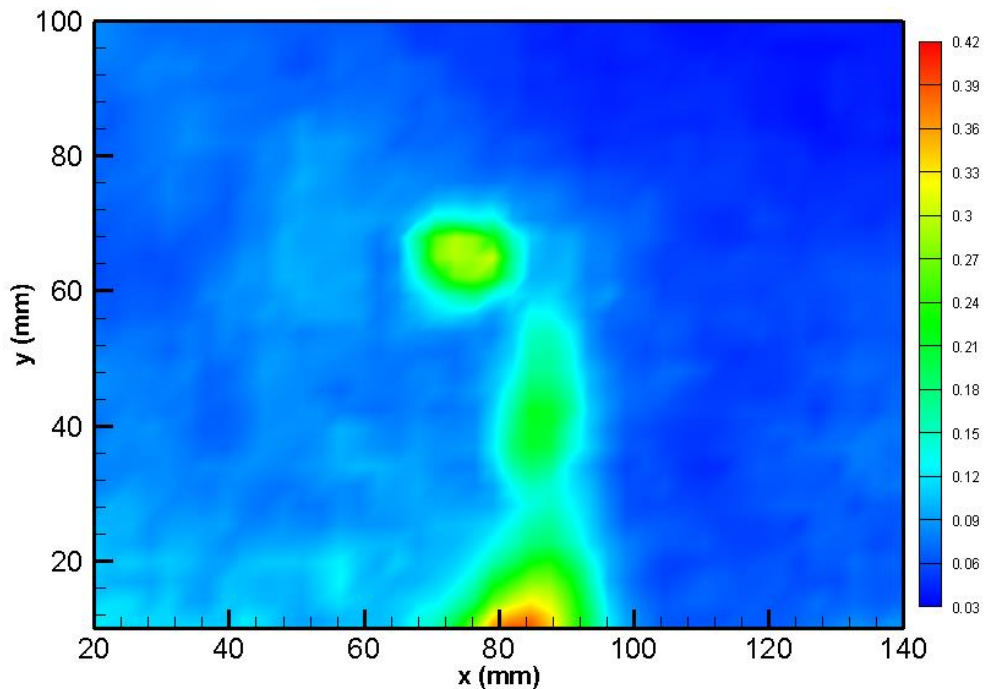


Figure D.7 Turbulence Kinetic Energy Contour of Optimized 14 Wing 13 m/s 10 AOA at C Location

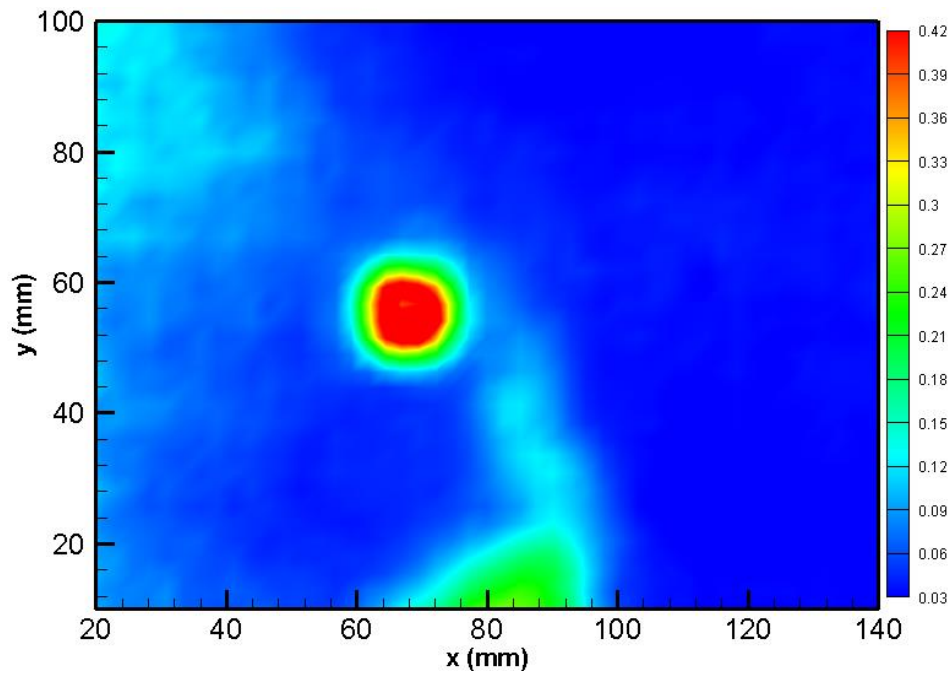


Figure D.8 Turbulence Kinetic Energy Contour of Optimized 14 Wing 13 m/s 10 AOA at 2C Location

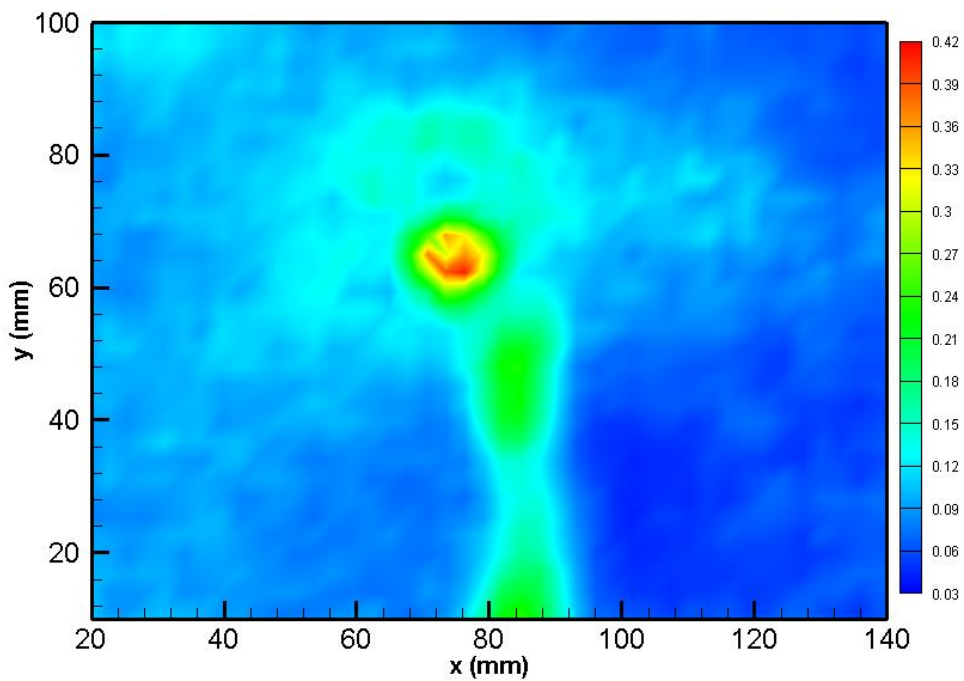


Figure D.9 Turbulence Kinetic Energy Contour of Optimized 14 Wing 14 m/s 8 AOA at C Location

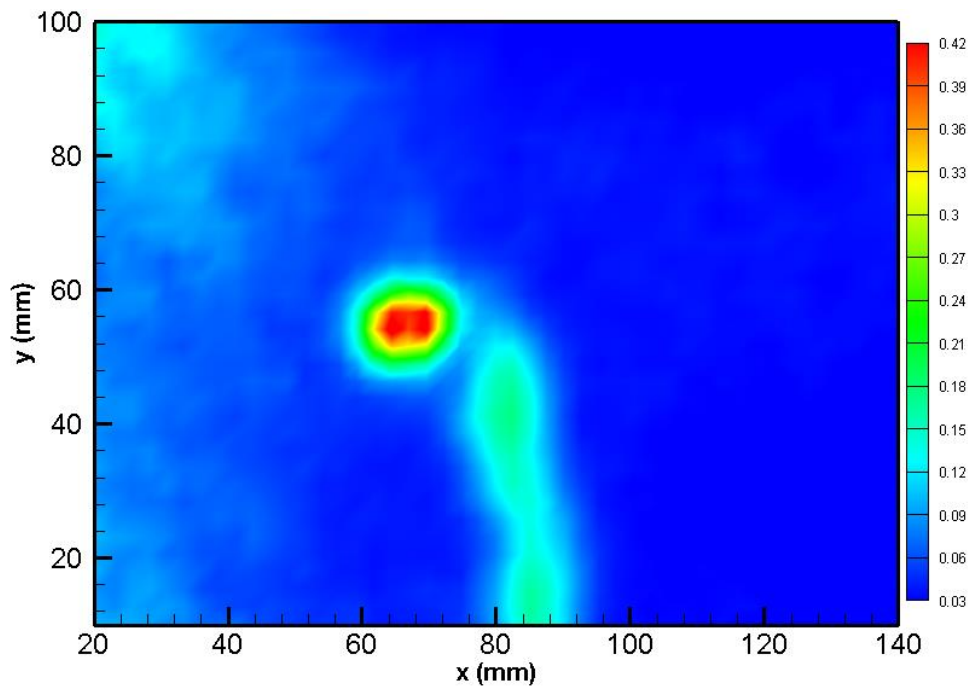


Figure D.10 Turbulence Kinetic Energy Contour of Optimized 14 Wing 14 m/s 8 AOA at 2C Location

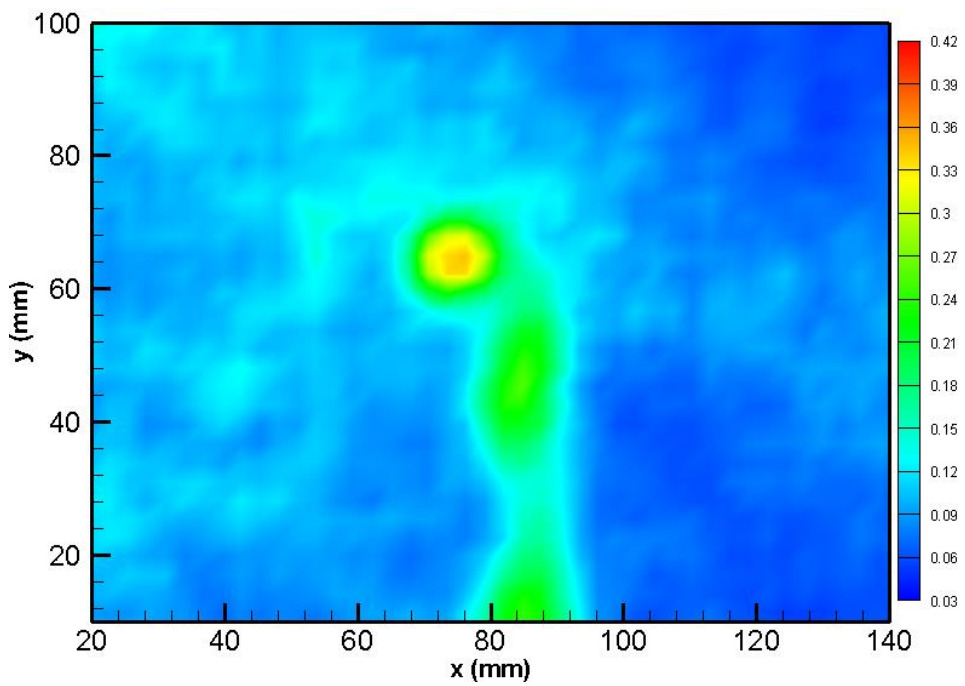


Figure D.11 Turbulence Kinetic Energy Contour of Optimized 14 Wing 14 m/s 9 AOA at C Location

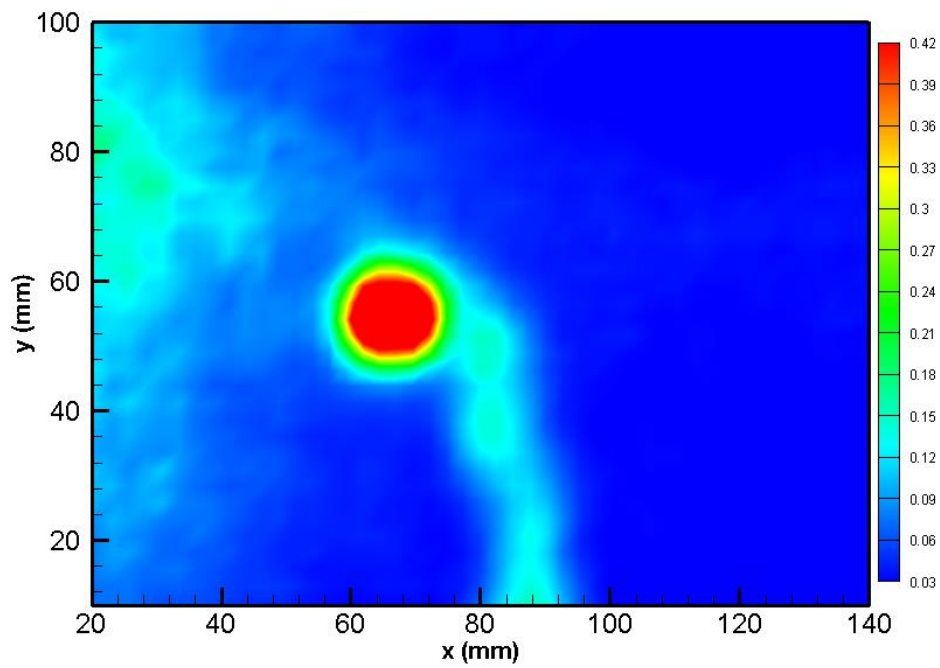


Figure D.12 Turbulence Kinetic Energy Contour of Optimized 14 Wing 14 m/s 9 AOA at 2C Location

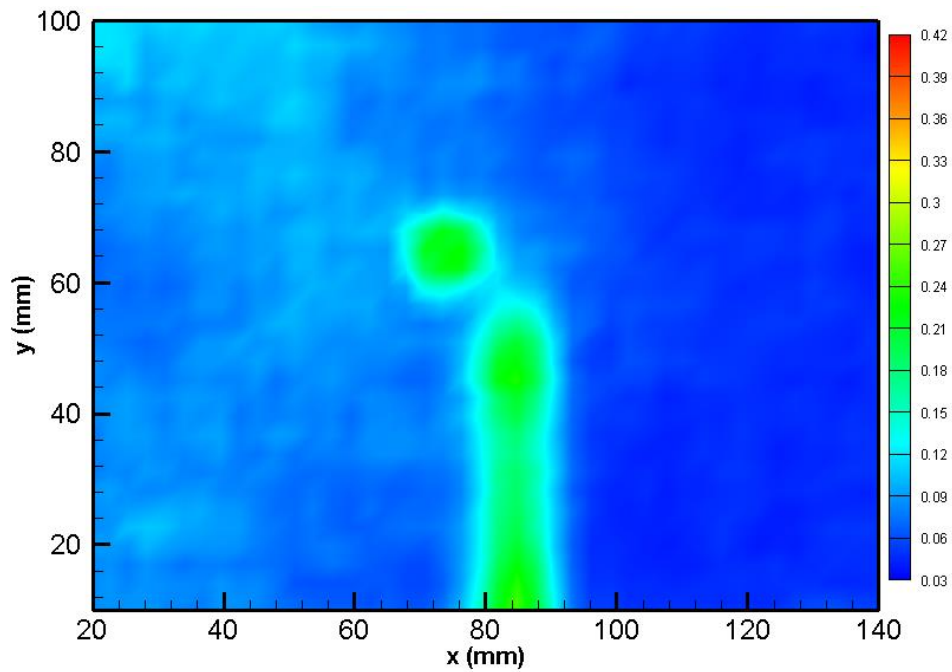


Figure D.13 Turbulence Kinetic Energy Contour of Optimized 14 Wing 15 m/s 7 AOA at C Location

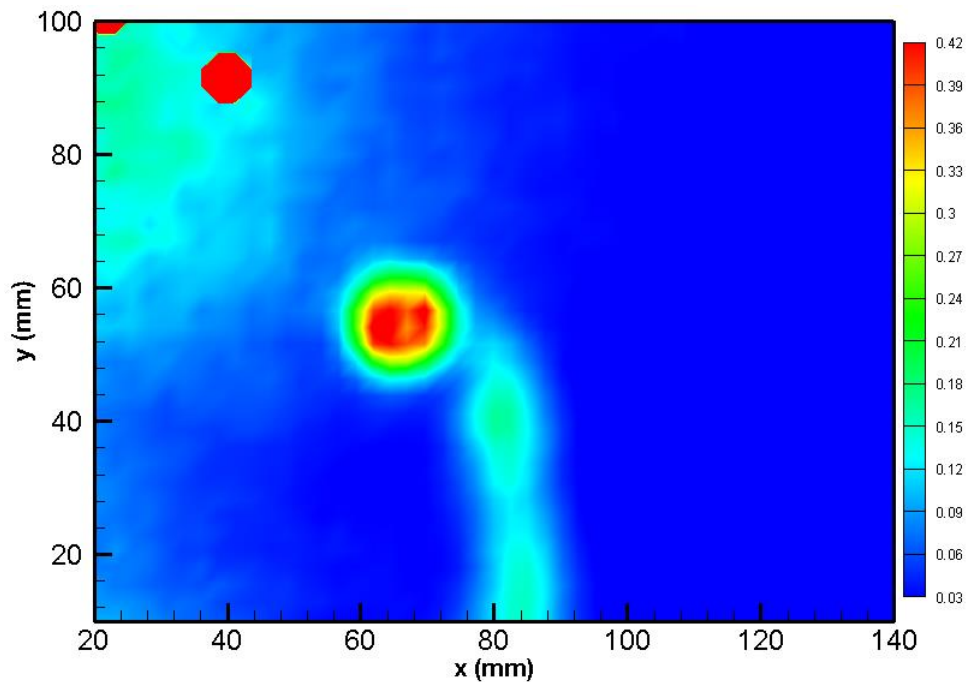


Figure D.14 Turbulence Kinetic Energy Contour of Optimized 14 Wing 15 m/s 7 AOA at 2C Location

### Morphed 10 Wing

The Turbulent Kinetic Energy Contours of the Morphed 10 Wing are presented in Figures D.15, D.16, D.17, D.18, D.19, D.20, D.21, D.22, D.23, D.24, D.25, D.26, D.28, D.29 and D.30.

It is observed that near the trailing edge at C location the wing wake and the fluctuations in the flow field are very dominant, while as moving downstream to 2C location, the turbulence kinetic energy of the vortex becomes more apparent. The highest values of the turbulence kinetic energy increases as distance from the trailing edge of the wing increases.

At C Locations when the angle of attack increases it is observed that the turbulence kinetic energy of the vortex increases for all velocities measured, 13 m/s, 14 m/s and 15 m/s, except 12 m/s. AT 2C Locations, turbulence kinetic energy increases as angle of attack increases for all cases.

For the free stream velocity changes, at C Locations, as the velocity increases, the highest values of turbulence kinetic energy of the vortex increases.

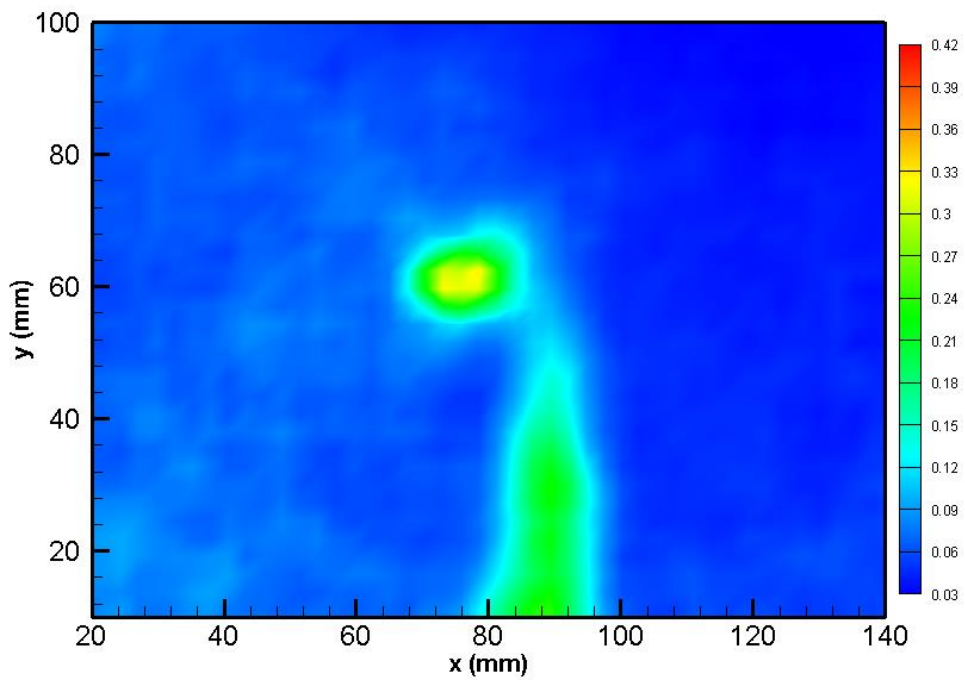


Figure D.15 Turbulence Kinetic Energy Contour of Morphed 10 Wing 12 m/s 7 AOA at C Location

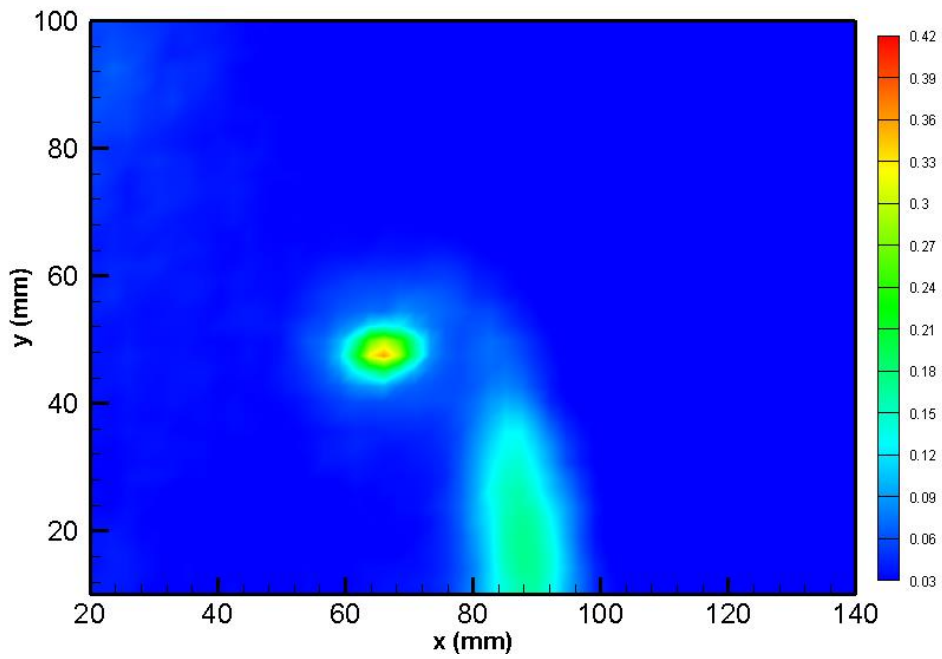


Figure D.16 Turbulence Kinetic Energy Contour of Morphed 10 Wing 12 m/s 7 AOA at 2C Location



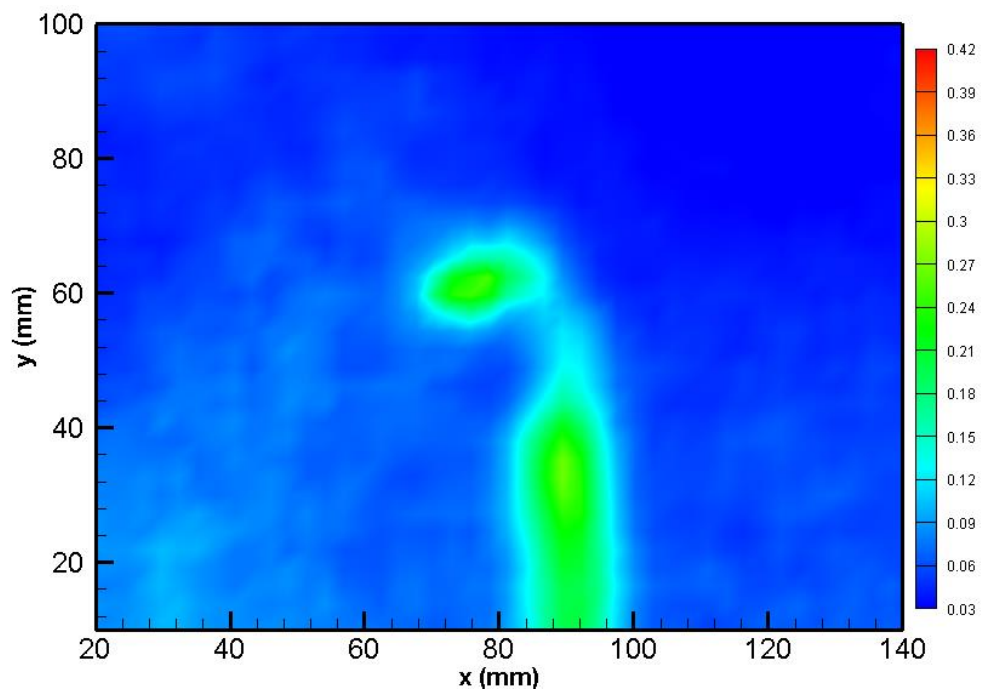


Figure D.17 Turbulence Kinetic Energy Contour of Morphed 10 Wing 12 m/s 8 AOA at C Location

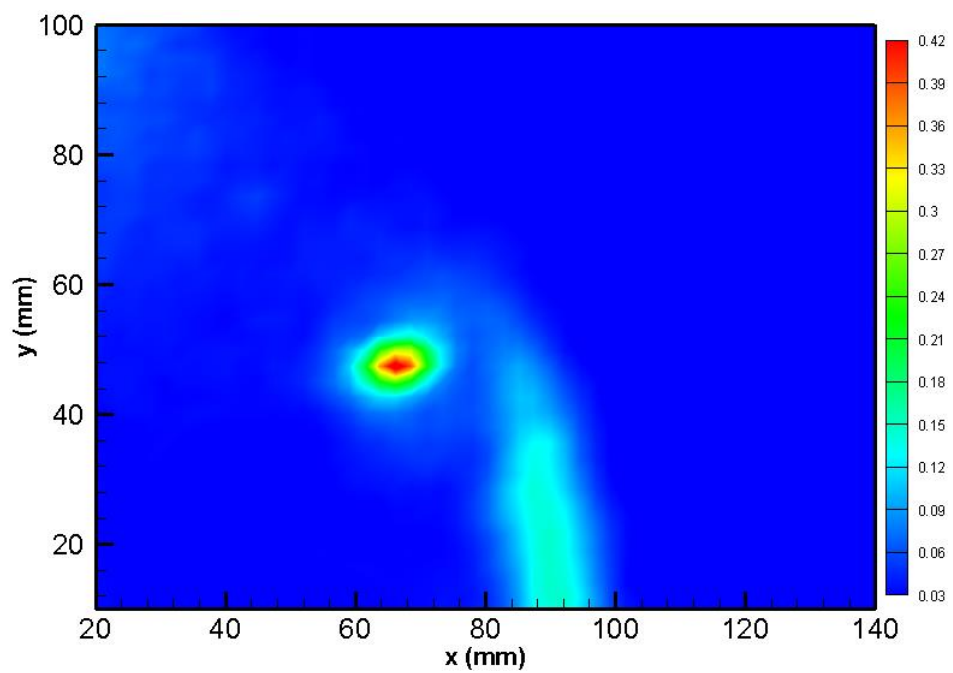


Figure D.18 Turbulence Kinetic Energy Contour of Morphed 10 Wing 12 m/s 8 AOA at 2C Location

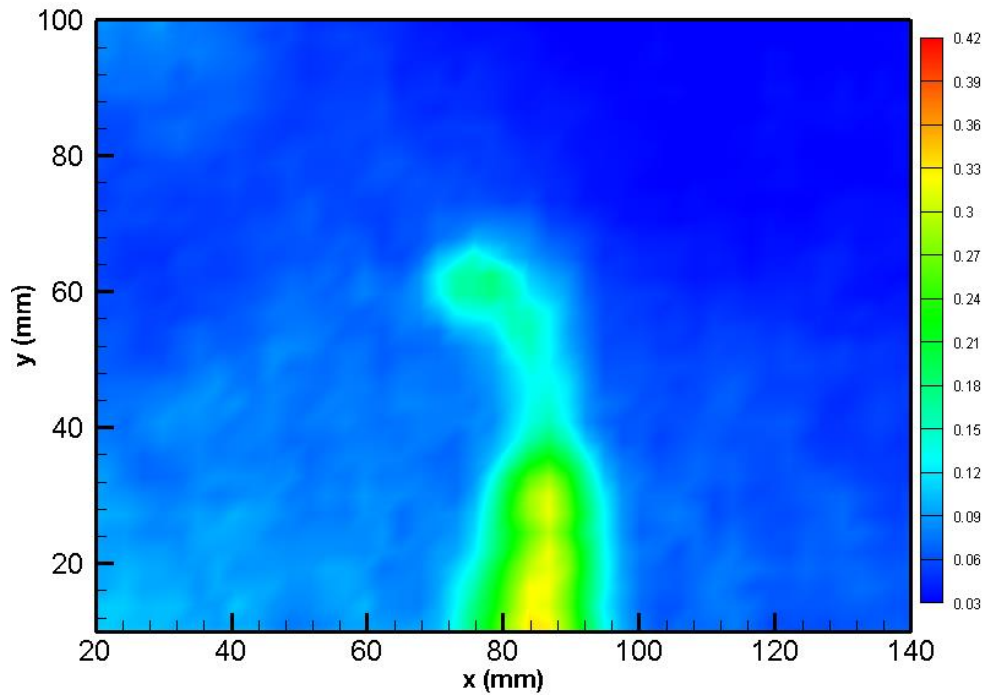


Figure D.19 Turbulence Kinetic Energy Contour of Morphed 10 Wing 13 m/s 5 AOA at C Location

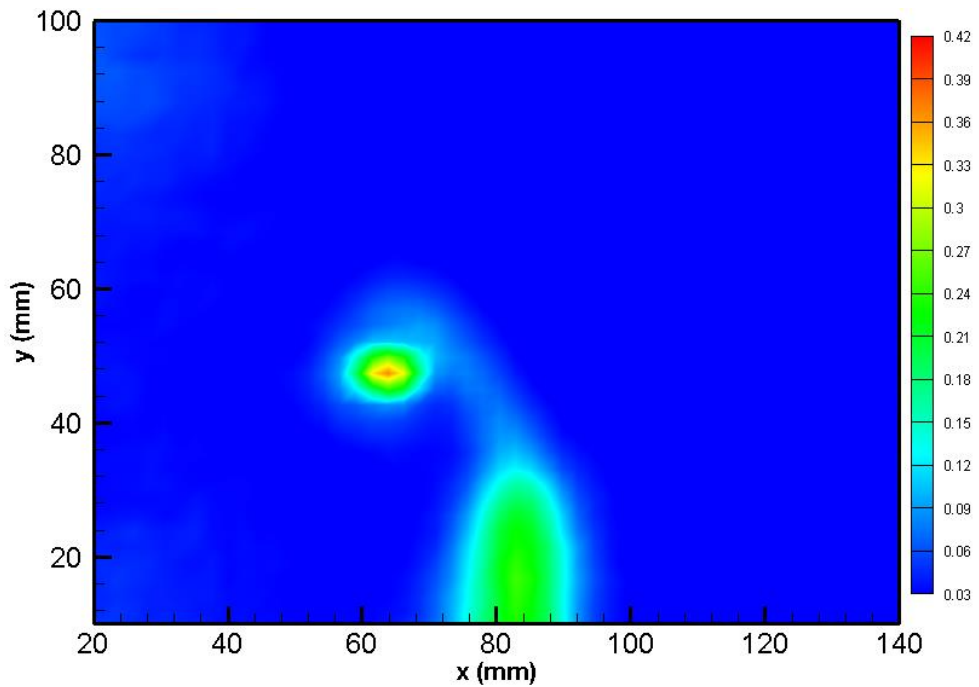


Figure D.20 Turbulence Kinetic Energy Contour of Morphed 10 Wing 13 m/s 5 AOA at 2C Location

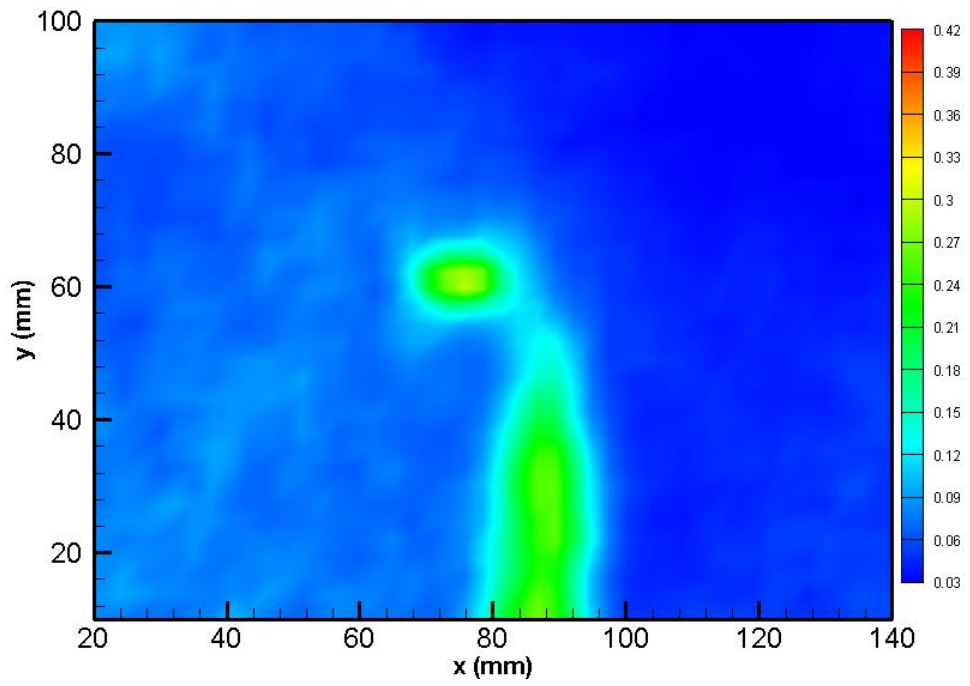


Figure D.21 Turbulence Kinetic Energy Contour of Morphed 10 Wing 13 m/s 6 AOA at C Location

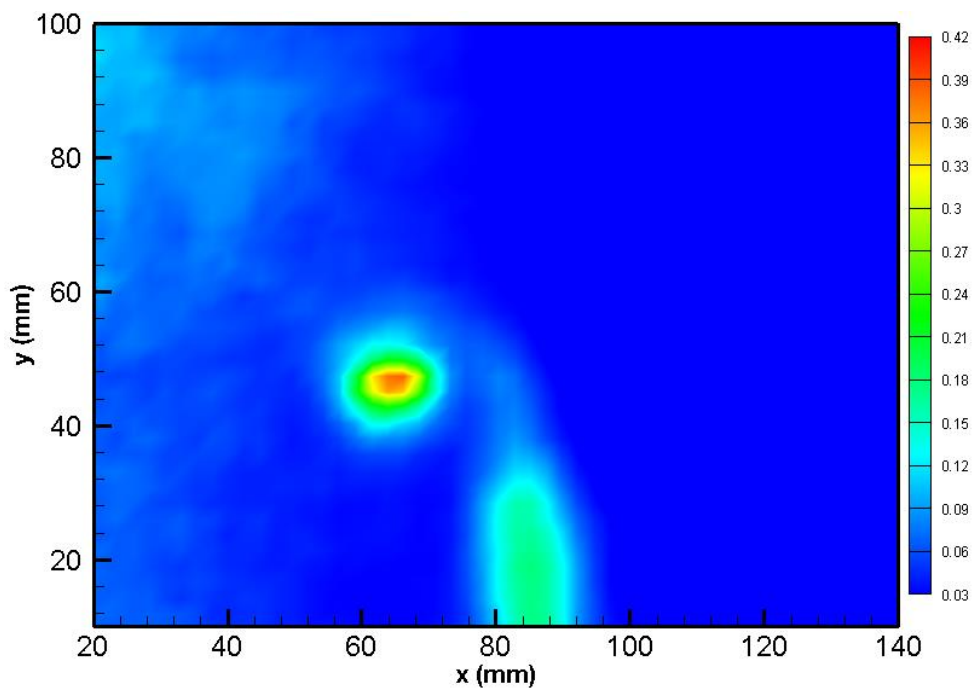


Figure D.22 Turbulence Kinetic Energy Contour of Morphed 10 Wing 13 m/s 6 AOA at 2C Location

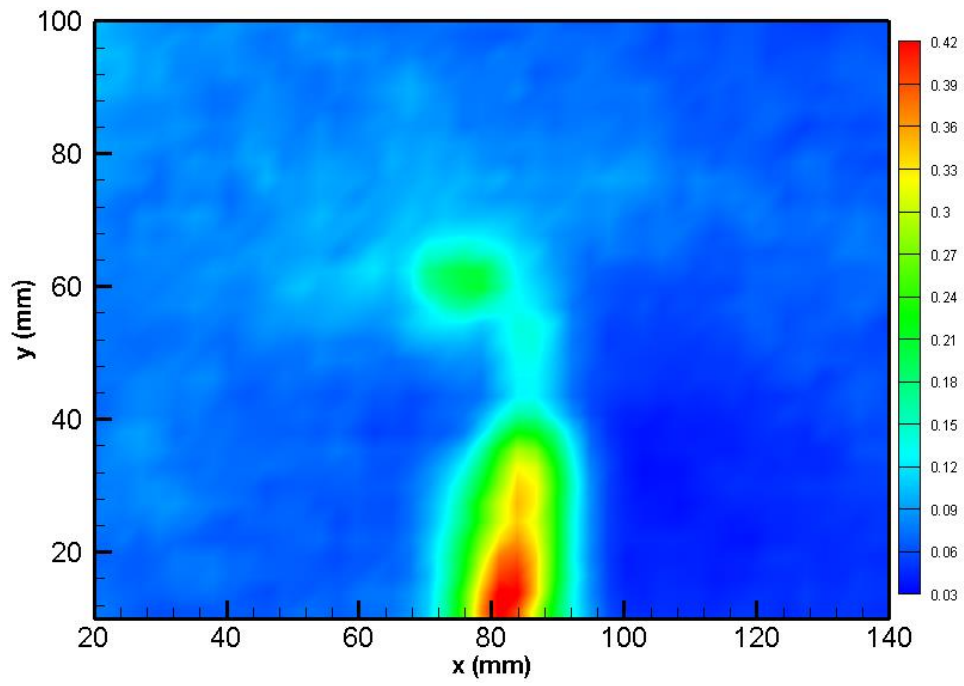


Figure D.23 Turbulence Kinetic Energy Contour of Morphed 10 Wing 14 m/s 4 AOA at C Location

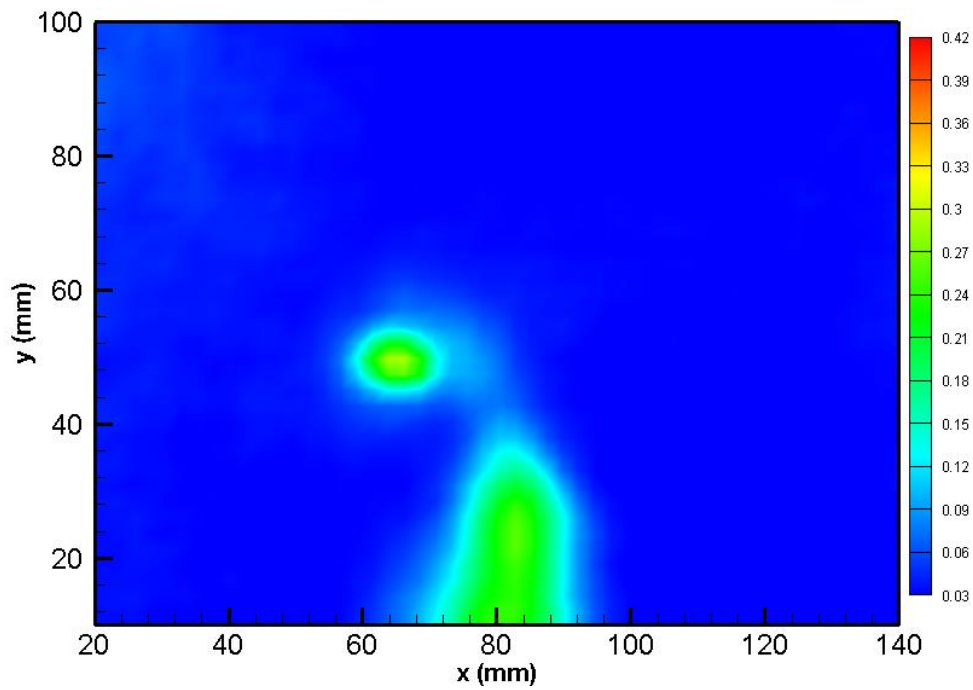


Figure D.24 Turbulence Kinetic Energy Contour of Morphed 10 Wing 14 m/s 4 AOA at 2C Location

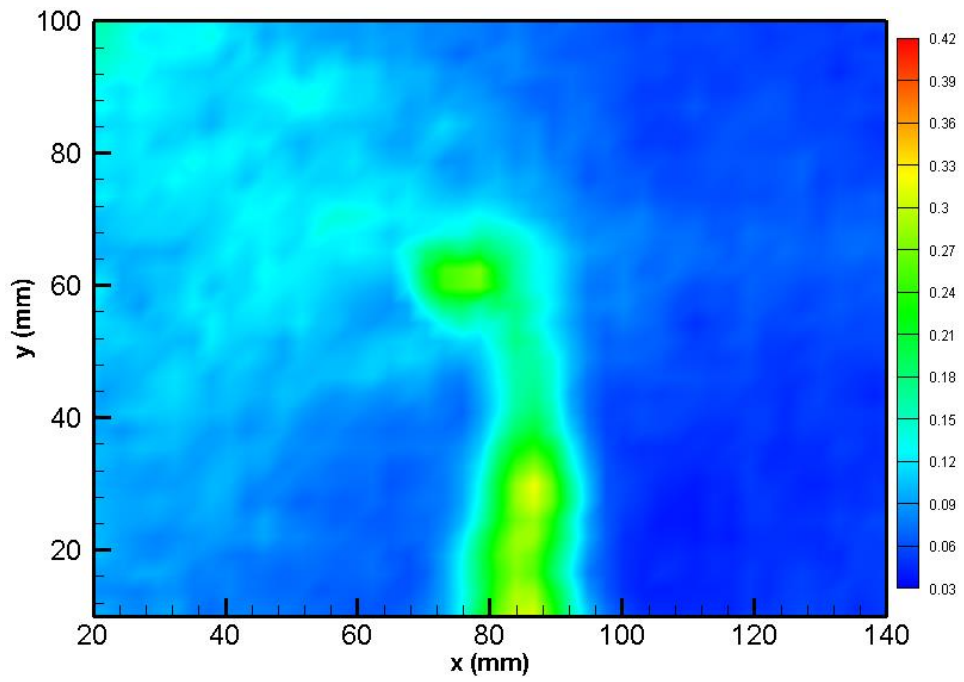


Figure D.25 Turbulence Kinetic Energy Contour of Morphed 10 Wing 14 m/s 5 AOA at C Location

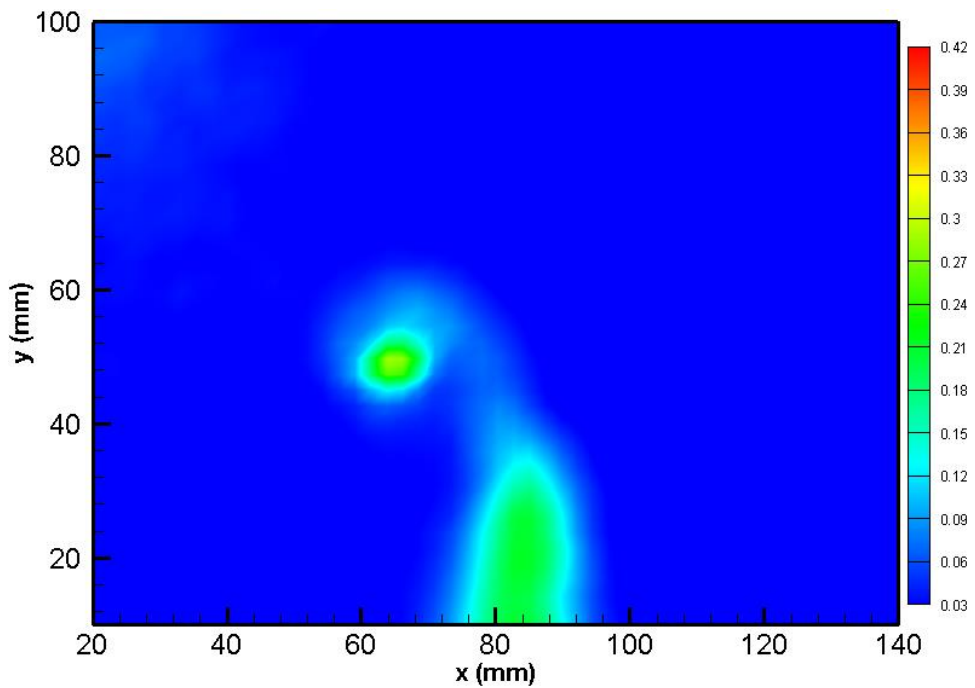


Figure D.26 Turbulence Kinetic Energy Contour of Morphed 10 Wing 14 m/s 5 AOA at 2C Location

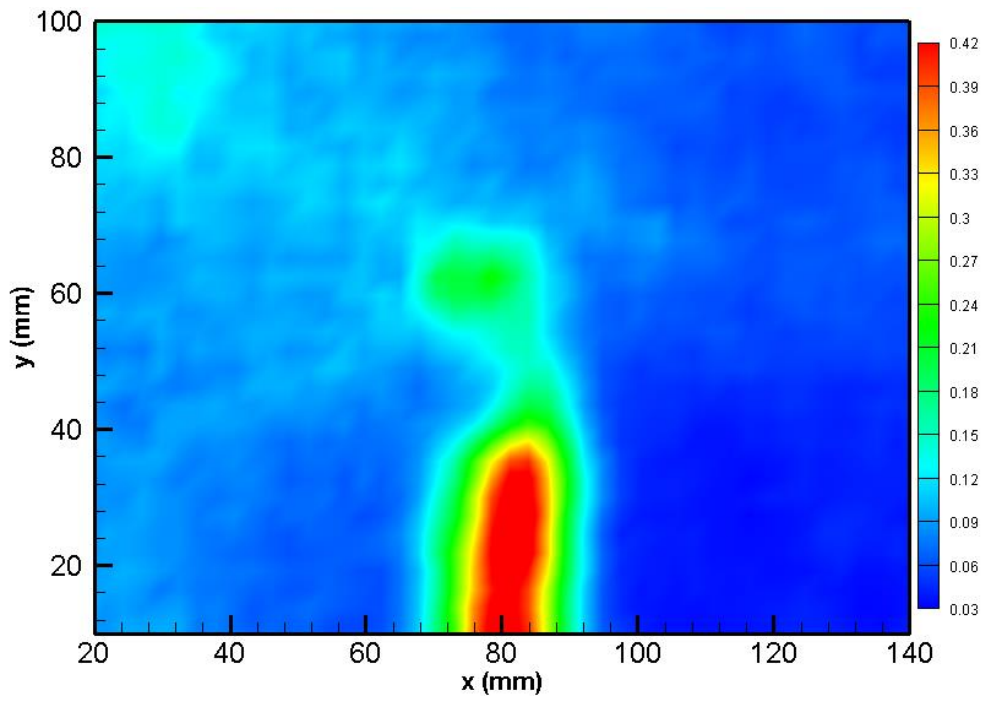


Figure D.27 Morphed 10 Wing 15 m/s 3 AOA at C Location

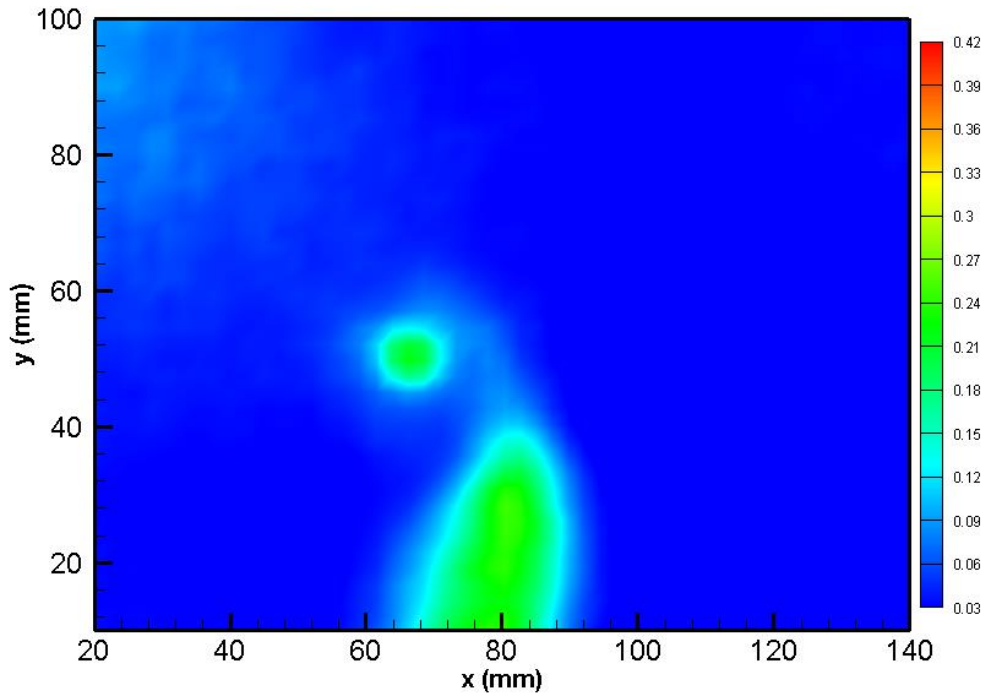


Figure D.28 Turbulence Kinetic Energy Contour of Morphed 10 Wing 15 m/s 3 AOA at 2C Location

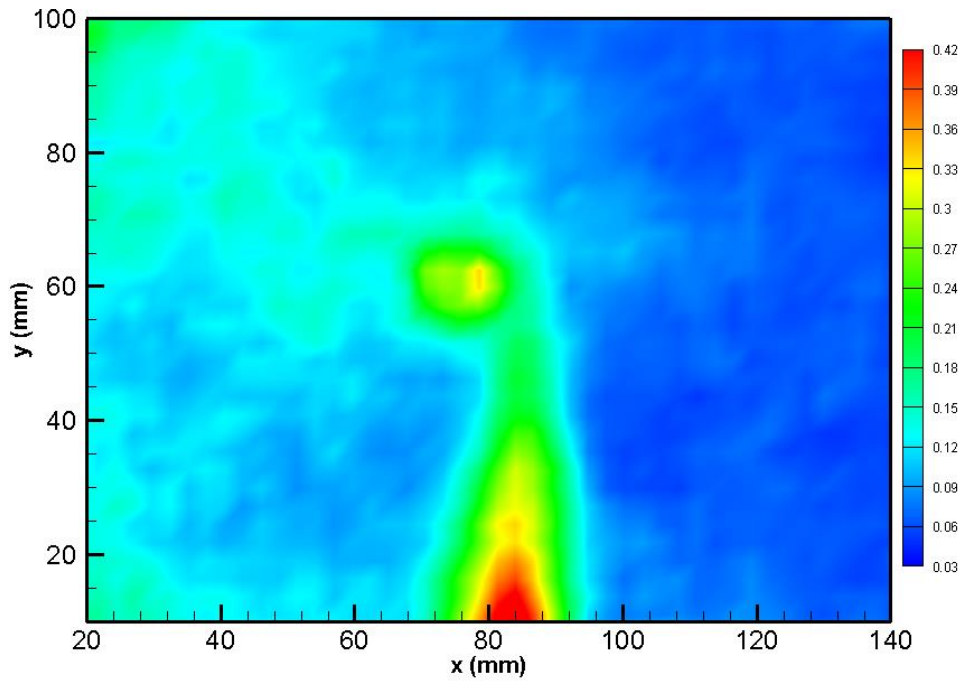


Figure D.29 Turbulence Kinetic Energy Contour of Morphed 10 Wing 15 m/s 4 AOA at C Location

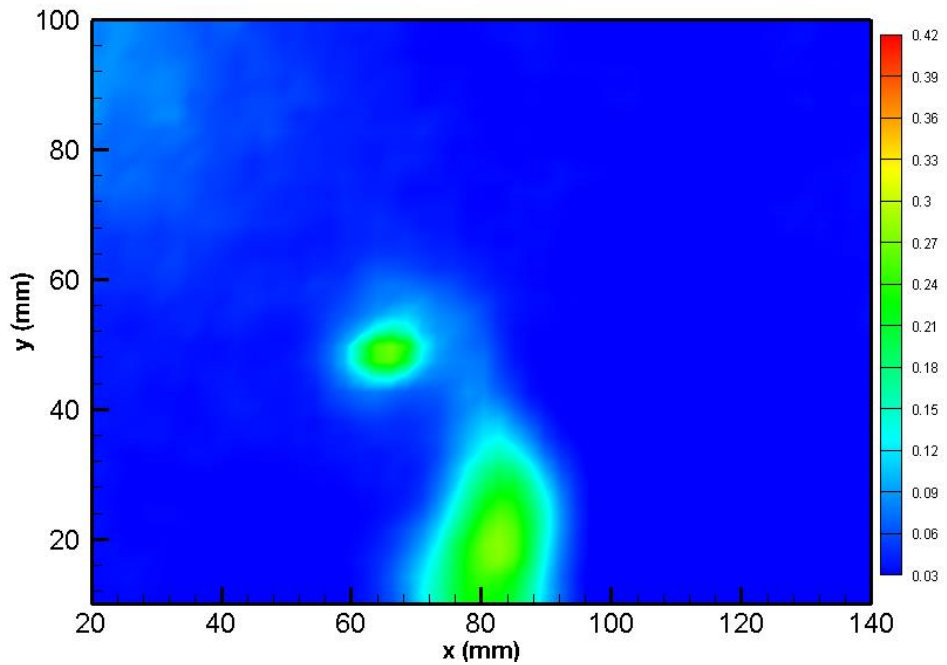


Figure D.30 Turbulence Kinetic Energy Contour of Morphed 10 Wing 15 m/s 4 AOA at 2C Location

### Morphed Wing at 16.5 m/s

The turbulence kinetic energy contours of the Morphed 16.5 Wing are presented in Figures D.31, D.32, D.33, D.34, D.35 and D.36

It is observed that, at C locations the wing wake is more dominant than in 2C locations so that higher turbulence kinetic energy levels are observed at C Location. While going downstream from C to 2C, the turbulence kinetic energy of the vortex becomes more apparent as the fluctuations caused by the wing wake diminishes. Thus turbulence kinetic energy increases with the increasing downstream location from wing trailing edge.

As angle of attack increases, the turbulence kinetic energy of the vortex increases in C Location. However, at 2C Location, the turbulence kinetic energy of the vortex decreases with increasing angle of attack.

At C locations, closer to wing trailing edge, the fluctuations in velocity of the neighbourhood of the vortex and wing in the flow field is very dominant.

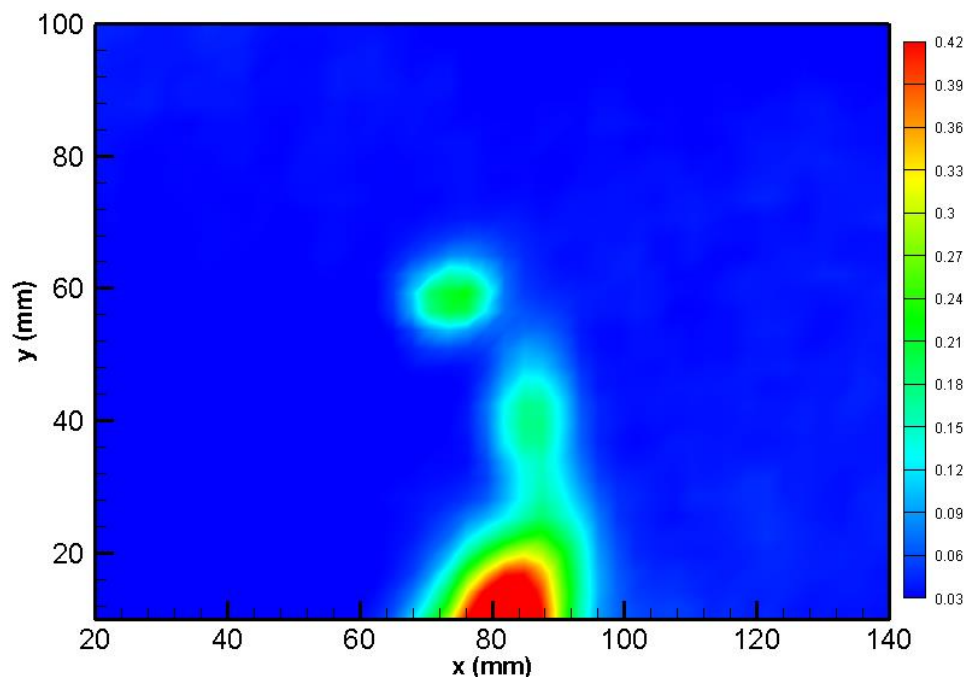


Figure D.31 Turbulence Kinetic Energy Contour of Morphed 16.5 Wing 14 m/s 11 AOA TKE at C Location



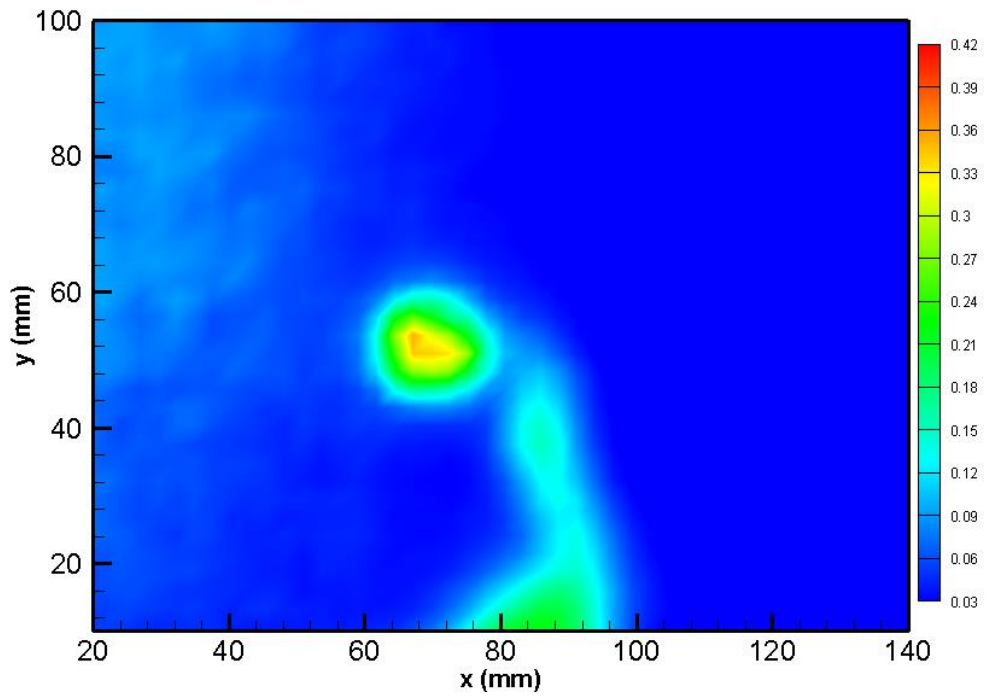


Figure D.32 Turbulence Kinetic Energy Contour of Morphed 16.5 Wing 14 m/s 11 AOA TKE at 2C Location

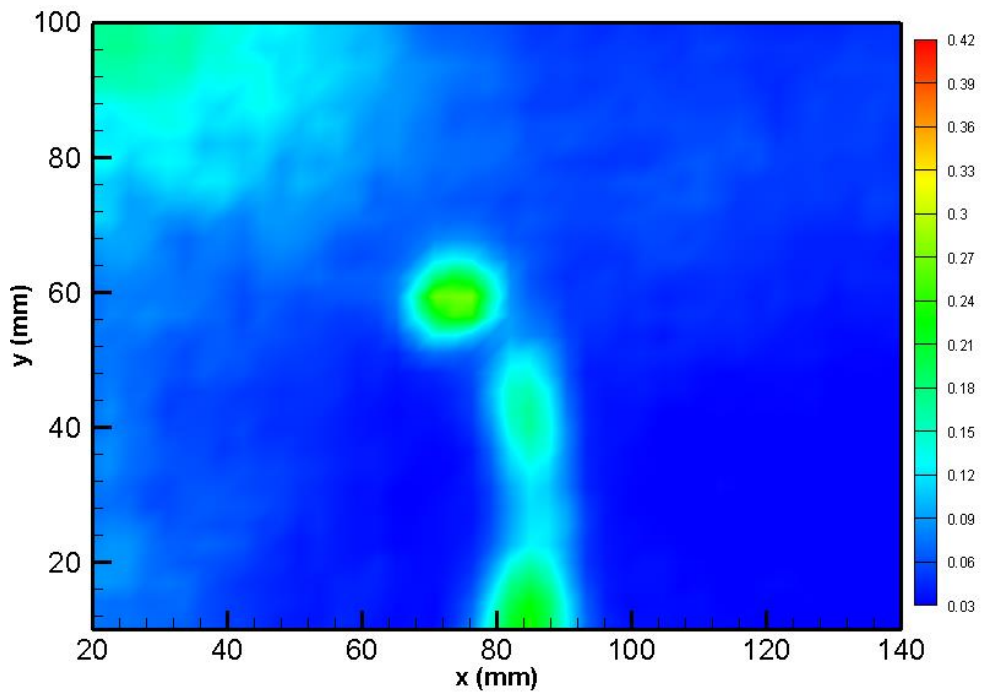


Figure D.33 Turbulence Kinetic Energy Contour of Morphed 16.5 Wing 15 m/s 9 AOA TKE at C Location

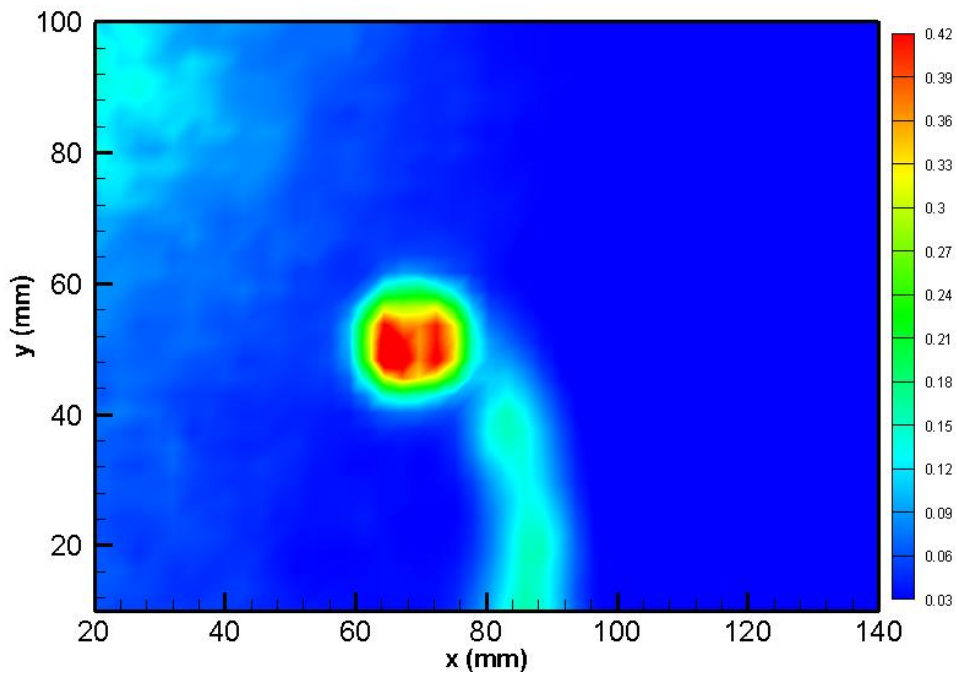


Figure D.34 Turbulence Kinetic Energy Contour of Morphed 16.5 Wing 15 m/s 9 AOA TKE at 2C Location

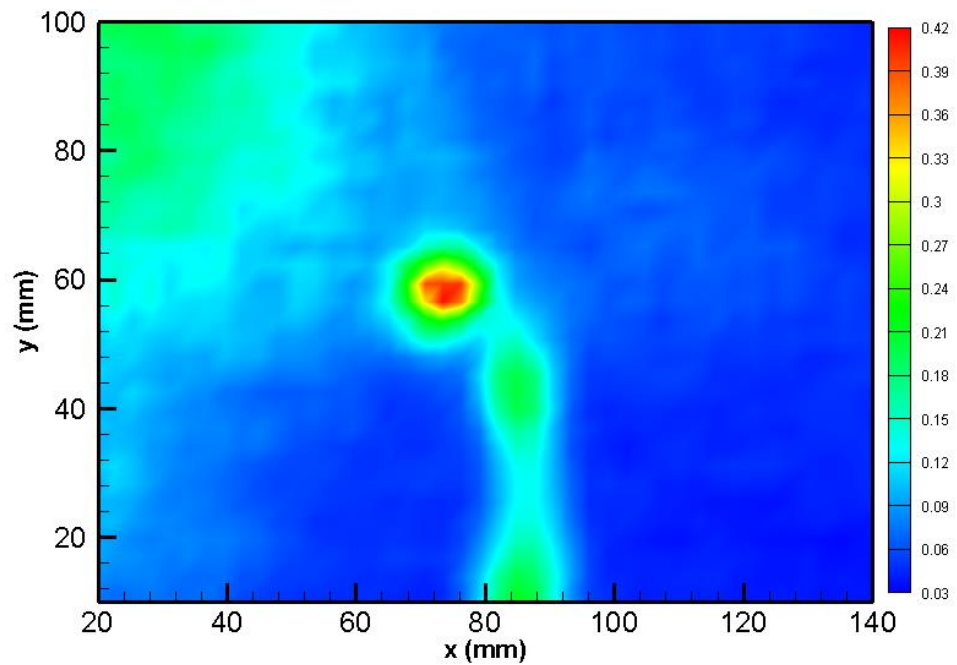


Figure D.35 Turbulence Kinetic Energy Contour of Morphed 16.5 Wing 15 m/s 10 AOA TKE at C Location

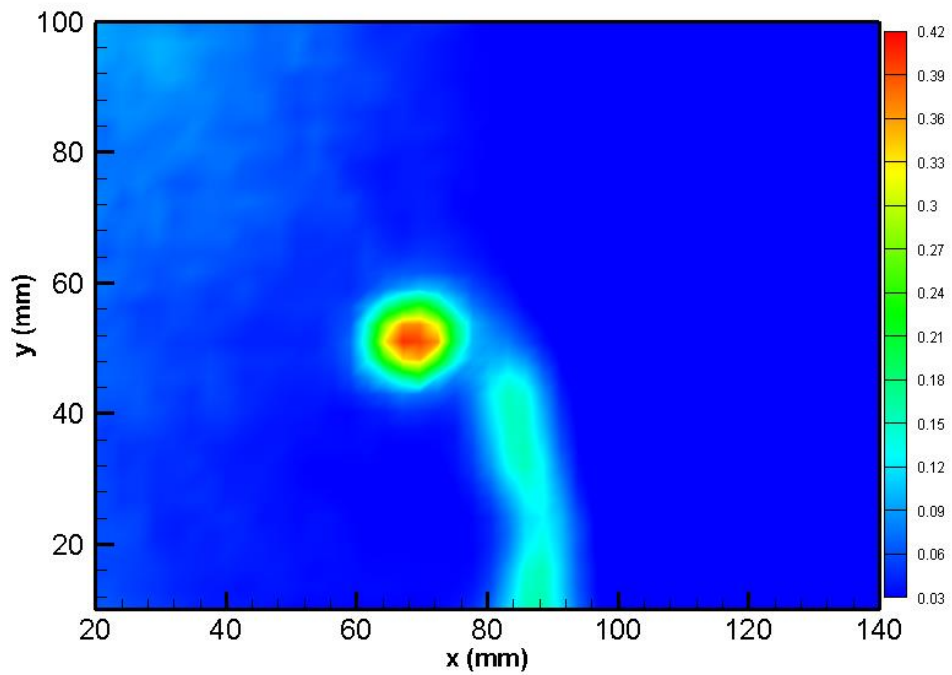


Figure D.36 Turbulence Kinetic Energy Contour of Morphed 16.5 Wing 15 m/s 10 AOA TKE at 2C Location

To illustrate the Base Wing at 14 m/s 15 AOA, the Reynolds stresses decreases from C to 2C and their turbulent kinetic energies also decreases. In contrast, for 15 m/s 14 AOA condition, the Reynolds stresses increase from C to 2C and so the turbulent kinetic energies.



## APPENDIX E

### REYNOLDS STRESS COMPONENT CONTOURS

#### Base Wing

Reynolds Stress Contours of the Base Wing are presented in Figures E.1, E.2 and E.3.

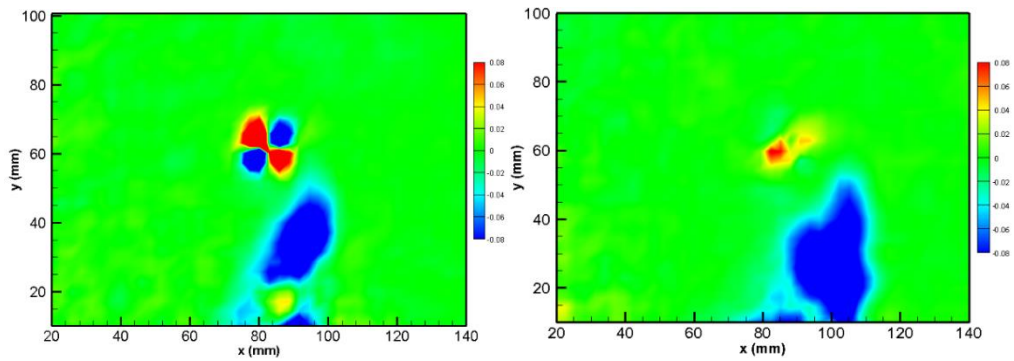


Figure E.1 Base Wing RS 14 m/s 15 AOA at C (left) and 2C (right) location

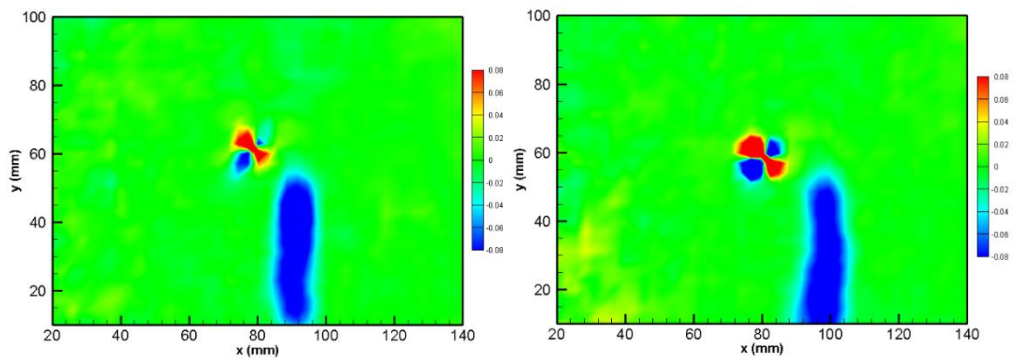


Figure E.2 Base Wing RS 15 m/s 12 AOA at C (left) and 2C (right) location

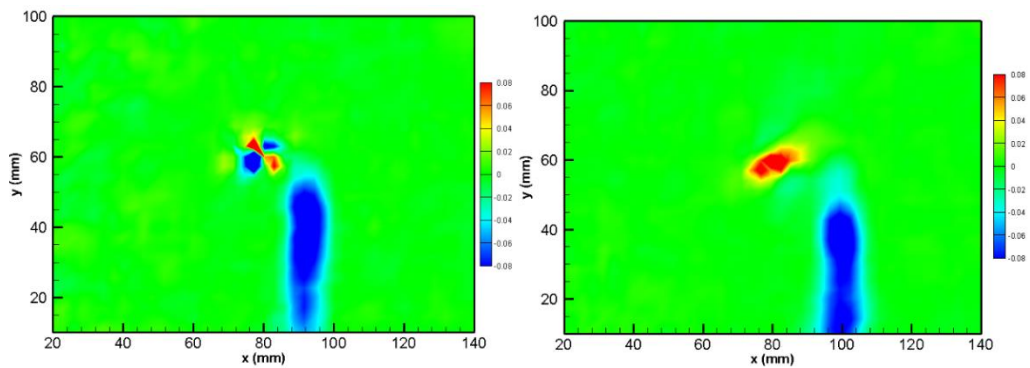


Figure E.3 1 Base Wing RS 15 m/s 13 AOA at C (left) and 2C (right) location

## Optimized 14 Wing

Reynolds Stress Contours of the Optimized 14 Wing are presented in Figures E.4, E.5, E.6, and E.7.

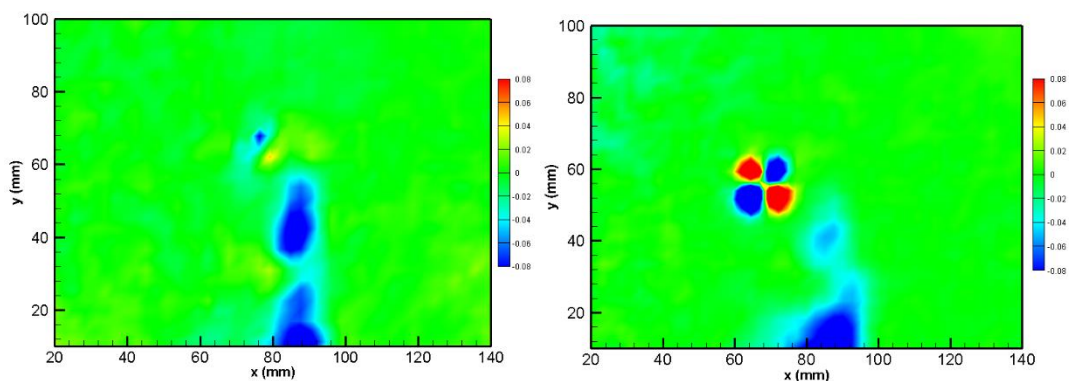


Figure E.4 Optimized Wing RS 13 m/s 10 AOA at C (left) and 2C (right) location

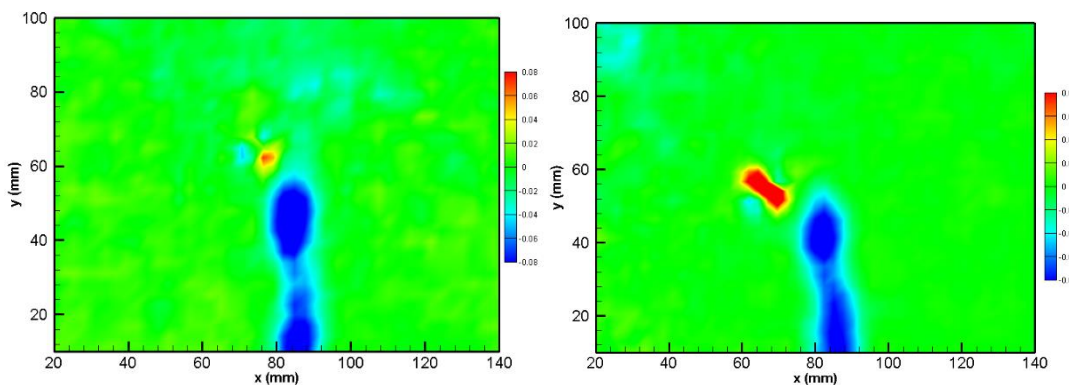


Figure E.5 Optimized Wing RS 14 m/s 8 AOA at C (left) and 2C (right) location

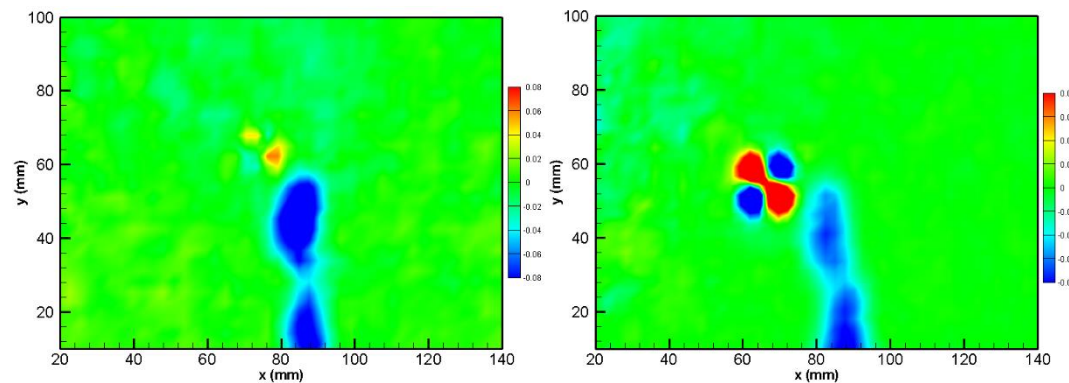


Figure E.6 Optimized Wing RS 14 m/s 9 AOA at C (left) and 2C (right) location

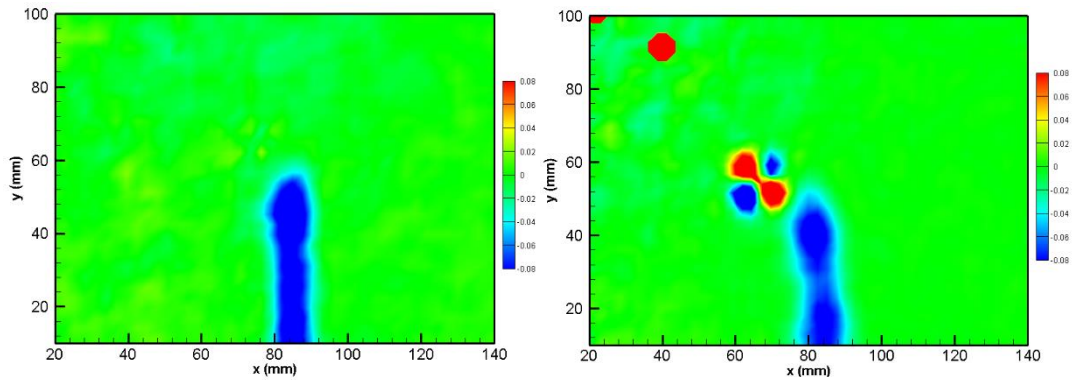


Figure E.7 Optimized Wing RS 15 m/s 7 AOA at C (left) and 2C (right) location

### Morphed 10 Wing

Reynolds Stress Contours of the Morphed 10 Wing are presented in Figures , E.8, E.9, E.10, E.11, E.12, E.13, E.14 and E.15.

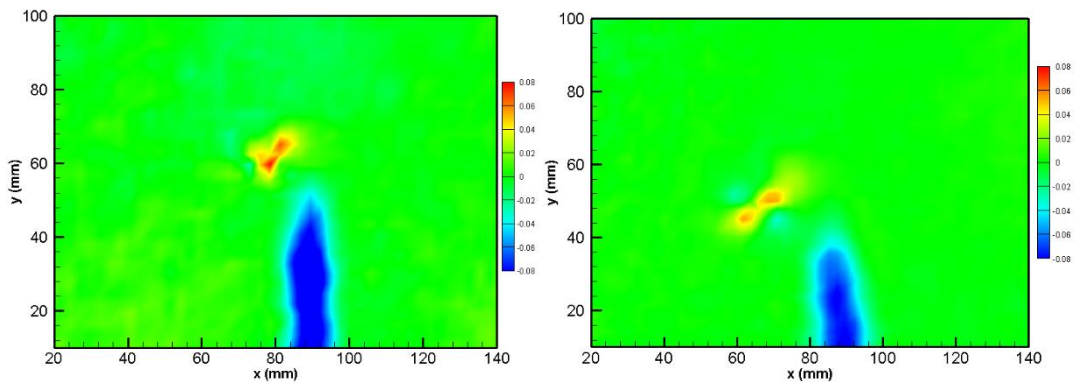


Figure E.8 Morphed 10 Wing RS 12 m/s 7 AOA at C (left) and 2C (right) location

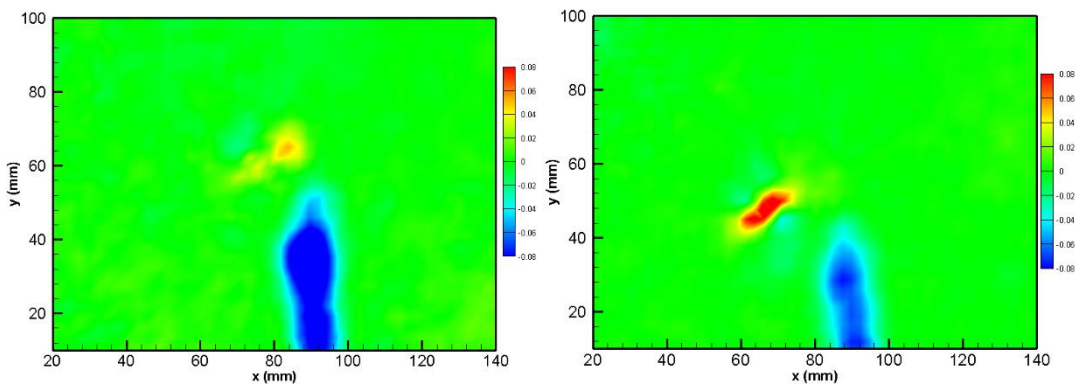


Figure E.9 Morphed 10 Wing RS 12 m/s 8 AOA at C (left) and 2C (right) location

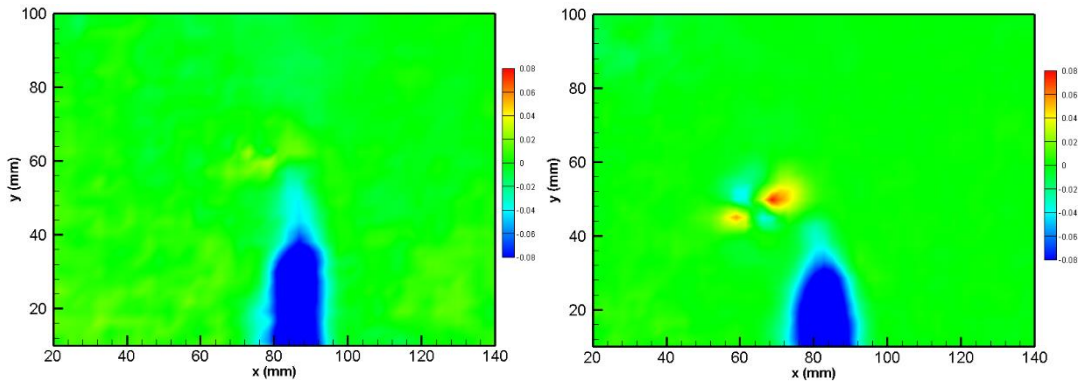


Figure E.10 Morphed 10 Wing RS 13 m/s 5 AOA at C (left) and 2C (right) location

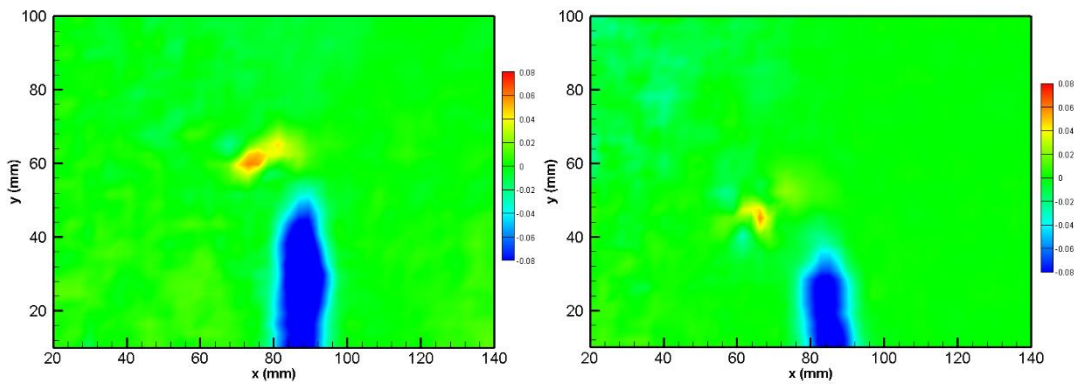


Figure E.11 Morphed 10 Wing RS 13 m/s 6 AOA at C (left) and 2C (right) location

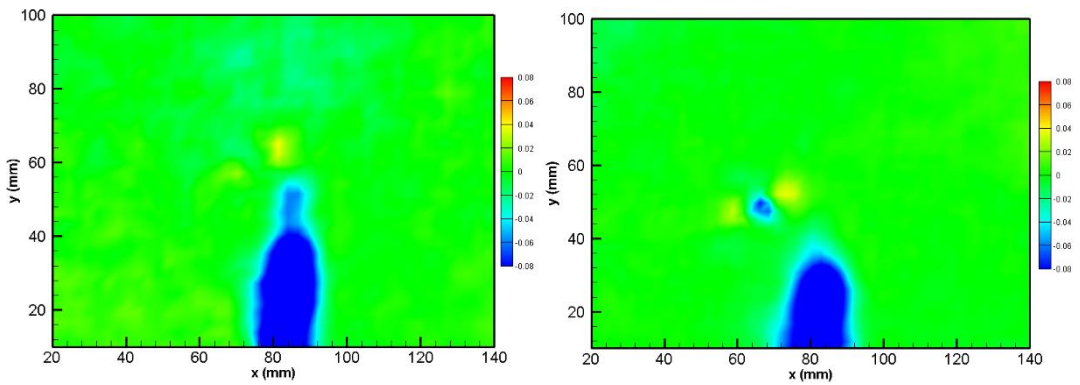


Figure E.12 Morphed 10 Wing RS 14 m/s 4 AOA at C (left) and 2C (right) location



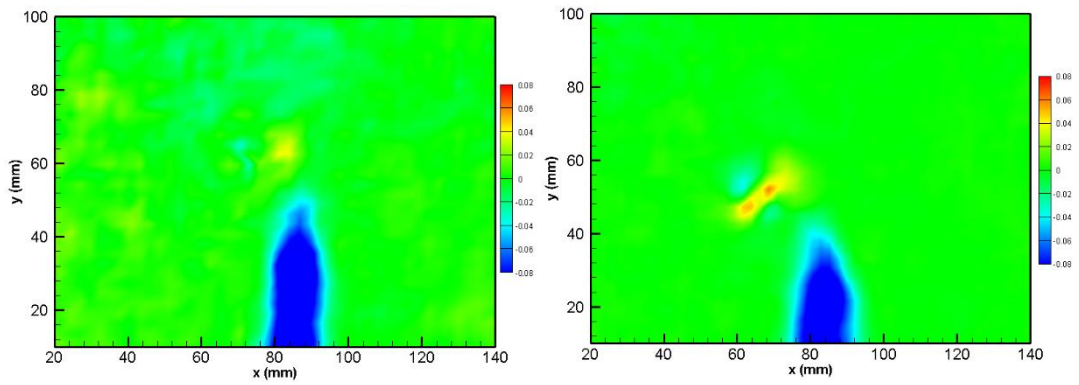


Figure E.13 Morphed 10 Wing RS 14 m/s 5 AOA at C (left) and 2C (right) location

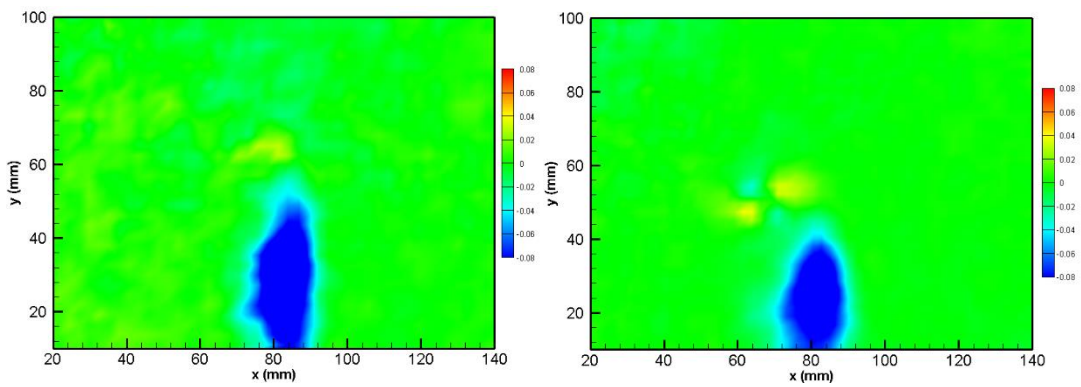


Figure E.14 Morphed 10 Wing RS 15 m/s 3 AOA at C (left) and 2C (right) location

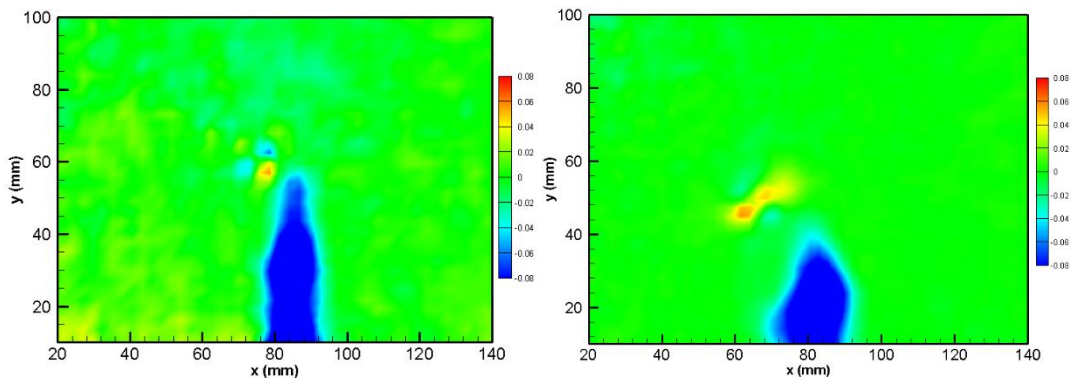


Figure E.15 Morphed 10 Wing RS 15 m/s 4 AOA at C (left) and 2C (right) location

### Morphed 16.5 Wing

Reynolds Stress Contours of the Morphed 16.5 Wing are presented in Figures E.16, E.17 and E.18.

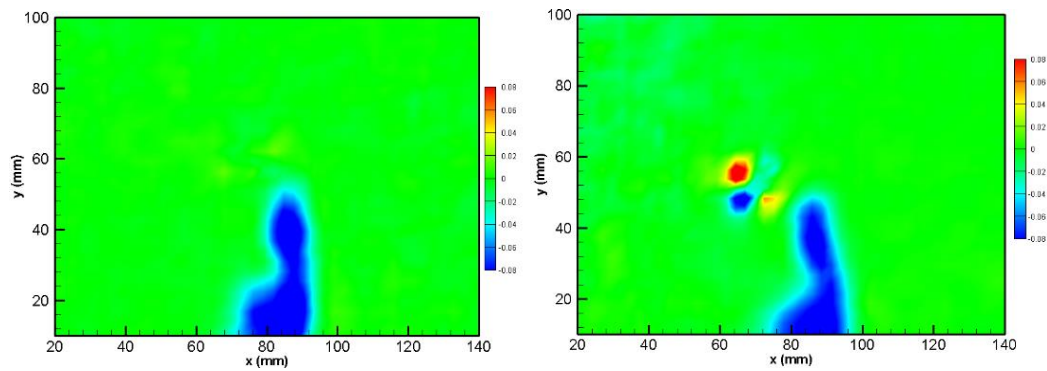


Figure E.16 Morphed 16.5 Wing RS 14 m/s 11 AOA at C (left) and 2C (right)

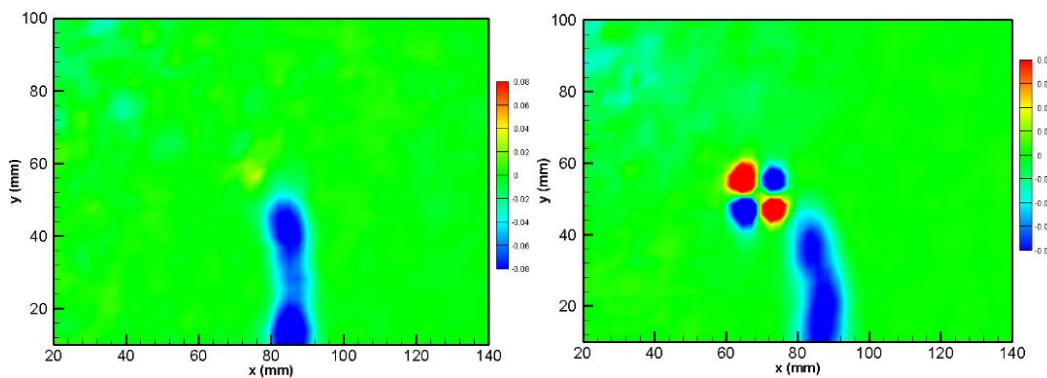


Figure E.17 Morphed 16.5 Wing RS 15 m/s 9 AOA at C (left) and 2C (right) location

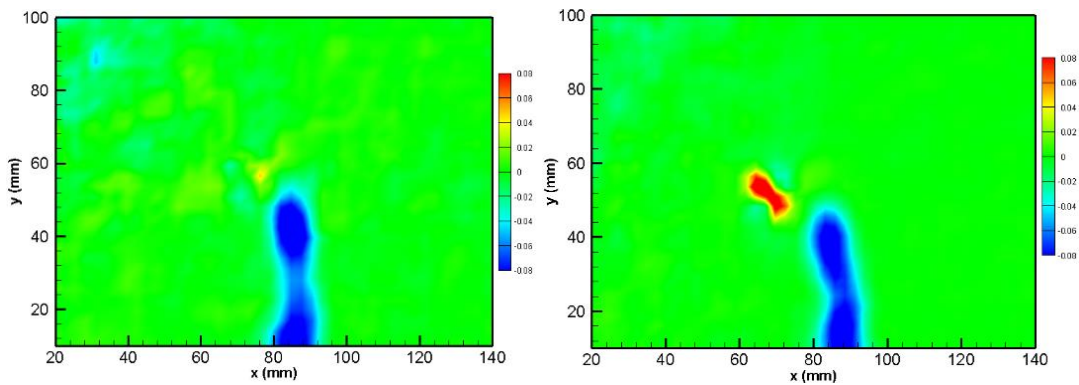


Figure E.18 Morphed 16.5 Wing RS 15 m/s 10 AOA at C (left) and 2C (right) location